Accelerated Corrosion Test Simulation: Lattice Model vs. Continuum Model

Yue Dai

Technische Universiteit Delft

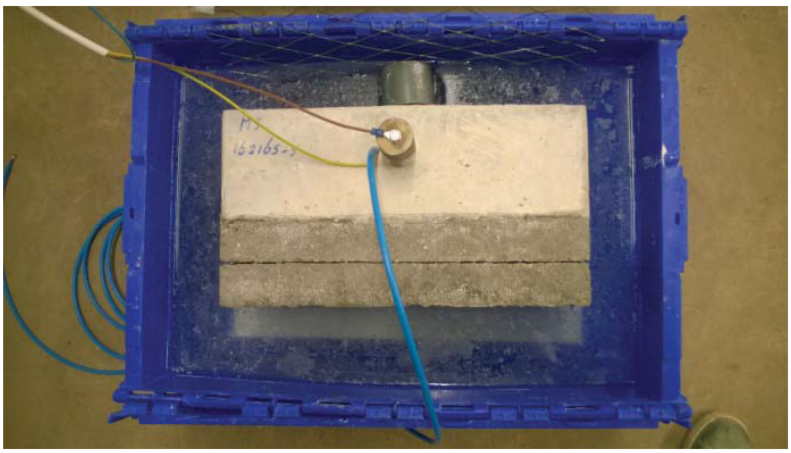

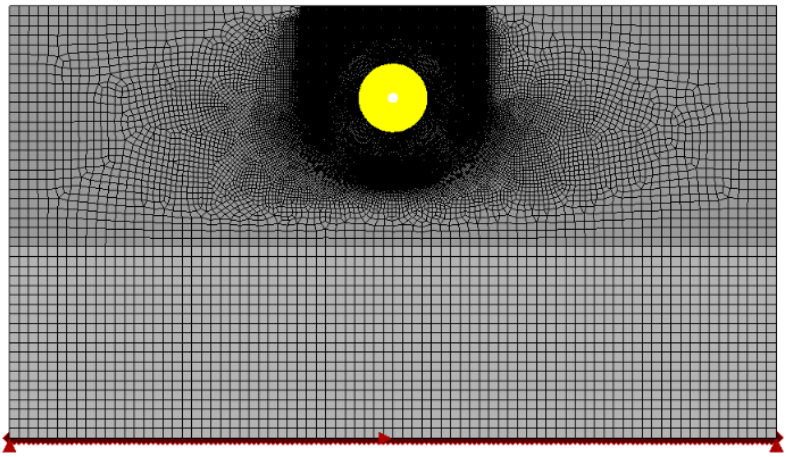

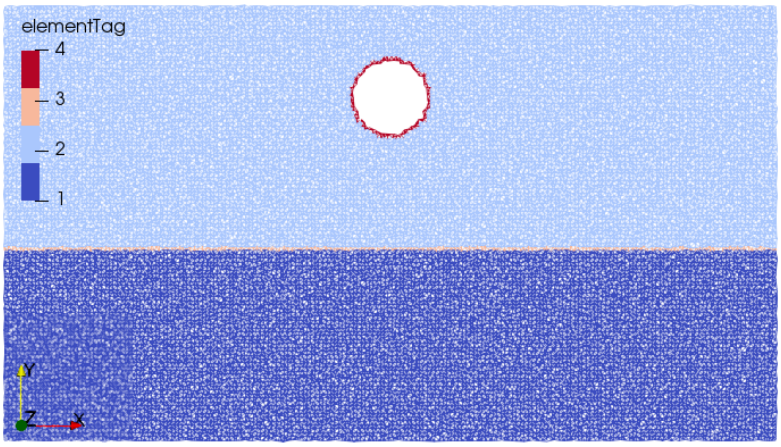

TU Delft Delft University of Technology

Challenge the future

Accelerated Corrosion Test Simulation: Lattice Model vs. Continuum Model

by

Yue Dai

in partial fulfillment of the requirements for the degree of

Master of Science
in
Structural Engineering

at the Delft University of Technology,
to be defended publicly on Wednesday November 28, 2018 at 15:00.

Supervisors:	Dr. Mladena Luković	TU Delft
	Ab van den Bos	DIANA FEA B.V.
Thesis Assessment Committee:	Prof. Dr. D.A. Hordijk	TU Delft, Chairman
	Dr. C. B. M. Blom	Gemeente Rotterdam & TU Delft
	Prof. Dr. E. Schlangen	TU Delft

An electronic version of this thesis is available at http://repository.tudelft.nl/.

ABSTRACT

A series of accelerated corrosion tests were done by SGS INTRON (commenced by Combinatie Aanpak Maastunnel, constructor of the Maastunnel project) to investigate for a proper repair material for the deteriorated concrete floor in the Maastunnel at Rotterdam. Five types of fiber reinforced mixtures with different tensile behavior ranging from SHCC (strain-hardening cementitious composite) to ON06 (similar tensile behavior as normal concrete) were designed, and their behavior as repair material under accelerated corrosion test was evaluated and compared. Different cracking behavior was observed due to the different tensile behavior in the repair mortar. It is of utmost importance to investigate if the cracking behavior can be simulated by numerical modeling and if in the future, the parametric analysis might be performed without large experimental series.

Two types of numerical models are implemented in this master thesis, namely the lattice model and the continuum model. Both types of model can simulate the distributed crack pattern of SHCC as obtained in the experiment with the help of certain randomness. The randomness of the lattice model comes from the inherent distribution of the lattice beams. A random field on the tensile strength is developed in the continuum model to take advantage of the randomness. The continuum model cannot show the behavior of decreasing number of cracks with decreasing fracture energy in the strain-softening materials due to the bifurcation problem brought by its incremental solution method. In contrast, the lattice model shows the ability to perform different crack pattern with different strain-softening concrete and avoid bifurcation problem because of its sequentially linear solution method. Moreover, the convergence problem in the continuum model after the localization of the cracks influences also the accuracy of the results. Although it can predict the damage pattern, the lattice model shows the trend to underestimate the crack width of the strain-softening material. The lattice model can predict the influence of the repair mortar-substrate bond strength on the crack pattern. Meanwhile, the continuum model always shows a complete failure in the repair mortar-substrate interface.

To summarize, the lattice model can simulate the crack pattern of different materials in the accelerated corrosion test. The continuum model has better performance in predicting the crack width. A combined model based on the continuum model and using sequentially linear solution method is proposed for further investigation.

A number of parameters and their influences were investigated. The boundary conditions at the bottom edge are observed to influence the direction of the bottom cracks. The edges of the specimen are kept free in the experiment. However, the repaired area is constrained by the surrounding concrete in reality. This indicates that the laboratory test may not represent the cracking behavior of the concrete floor in the tunnel accurately. The constrained edges are suggested for future research. SHCC is observed to be more sensitive to the repair mortar-substrate bond strength than material with lower stain capacity. Extra caution is advised at the repair mortar-substrate interface while applying SHCC in a concrete repair system.

From the material point of view, with increasing fracture energy and strain capacity, more but thinner cracks can be obtained in the accelerated corrosion test. SHCC material can exhibit the distributed crack pattern with a maximum crack width of 0.1 mm which is ten times smaller than normal concrete. This behavior of SHCC is very suitable for being applied to a concrete repair system. The distributed cracks with smaller crack width can effectively limit the possibility of further corrosion. It is observed that the materials with deflection-hardening behavior in the bending test can produce this distributed crack pattern. Besides SHCC, some strain-softening (under direct tension) materials can also show the deflection-hardening behavior in the bending test and produce the distributed crack pattern. This distributed crack pattern can decrease the crack width by around 90% which can limit the penetrating of chemicals into the repaired area after its cracking. SHCC and fiber reinforced concrete with deflection-hardening behavior in the bending test are advised to be used in the concrete repair system further.

PREFACE

This thesis project was developed to fulfill the requirements of the program Master of Science in Structural Engineering with specialization in concrete structures at the Delft University of Technology. I would like to thank people that helped me during this project. First and most importantly, I want to thank my supervisors Mladena Luković and Ab van den Bos of their unconditioned help. They are always there to discuss and share their knowledge with me whenever I have any problems. I would also like to thank Gerd-jan Schreppers for giving me this opportunity to do research at DIANA FEA BV. This will be one of the most precious memory in my life. Moreover, I would like to thank Kees Blom for introducing me into this topic and Dick Hordijk and Erik Schlangen for taking their time to present in my thesis committee. Also, I would like to thank Manimaran Pari and Panos Evangeliou for helping me in working with DIANA and many practical problems. Moreover, I would like to thank Angelo Garofano for his "Monday Express" to Arnhem.

A special thank goes to all members of the CHICKEN FIVE for our protein lunch tradition together. I will remember all the Fridays we spent together and I am sorry for the death of those fried chicken in our stomach. Furthermore, I would like to thank all my friends for being a listener and cheering me up every time I felt depressed. I would like to thank also my lovely cats Pidgey and Choco for their company. Most importantly, I would like to thank my girlfriend Ruoqing for her unconditioned love and support. You let me feel the strong support from a family member although I am thousands of kilometers away from home. You make me into a better man. Last but not least, I would like to thank my dear parents Zhijuan and Lijun for their support during my two-year study both economically and mentally. I cannot accomplish this without your help. I feel very fortunate to be your child. Thank you.

Yue Dai

Utrecht, November 2018

CONTENTS

NOMENCLATURE

Greek Symbols

α	Thermal expansion coefficient
α_l	Load factor
χ	Random variables vector
δ	Beam deflection
Δ_x	Leg distance
ϵ_{mb}	Elastic strain
$\epsilon^{cr}_{nn.ult}$	Normal ultimate tensile strain
ϵ_{nn}	Normal total strain
ϵ^{cr}_{nn}	Normal crack strain
ϵ_u	Ultimate tensile strain
$\gamma()$	Variance function
λ_{crit}	Scaling factor
μ	Mean value
ρ	Minimum correlation threshold value
$\rho()$	Correlation function
σ	Standard deviation
σ_r	Averaged load pressure
σ_l	Lower limit tensile strength
σ_{mb}	Upper limit tensile strength
σ^{cr}_{nn}	Normal crack stress

Latin Symbols

A	Voxel size
A_s	Reinforcement cross-section area

C_1, C_2	Experience parameter in the tension-softening relation proposed by Hordijk et al.
cmd_u	Ultimate crack mouth opening distance
D	Averaged random field domain
d_c	Correlation length
d_g	Model depth
d_m	Mesh size
d_R	Diameter of rebar
d_x	Correlation length in x direction / displacement in x direction
d_y	Correlation length in y direction
E	Young's modulus
E_g	Global structural stiffness
E_l	Local material Young's modulus
f	Force vector
f_c	Compressive strength
F_R	Reaction force
F_r	Distributed force
f_R	Bending stress
f_t	Tensile strength
$f_{t.ult}$	Ultimate tensile strength
G	Shear stiffness
G_h^I	Fracture energy
h	Crack band width
K	Stiffness matrix
k	Coefficient of Permeability
L	Decomposed correlation matrix
l_x	Model length
l_y	Model height

n_{lp}	Number of load points
R	Correlation matrix
r_c	Calibrated lattice beam radius
r_i	Input lattice beam radius
s	Sub-cell size
T	Tempreture
u	Displacement vector
w	Maximum crack width
w/c	Water cement ratio
$z_c(x)$	Spatially correlated random variables vector

Abbreviations

CMD	Covariance matrix decomposition method
CMOD	Crack mouth opening displacement
COV	Covariance length
FRC	Fiber reinforced concrete
FRCCON	Fiber reinforced concrete model defined by CIB-FIB working groups
FRCFAC	Fiber reinforce concrete scaling factor
ISMD	Integrated structures and materials design
LOP	Limit of proportionality
NLFEA	Nonlinear finite element analysis
RF	Reference location
RH	Relative Humidity
RM	Repair Mortar
SHCC	Strain-hardening cementitious composites
SLA	Sequentially linear analysis

List of Figures

List of Tables

1

INTRODUCTION

1.1. BACKGROUND

The Maastunnel in Rotterdam is the first immersed tunnel with a rectangular cross-section in Europe. The Maastunnel is finished in construction in 1942 and comes with a length of 1373 meters including access roads. Connecting the banks of the Nieuwe Maas, the tunnel consists of four tubes combined within a single section: two tubes for cars, one for cyclists and one for pedestrians (Figure 1.1). It is now temporarily closed and under renovation to extend its service life for some more years. The concrete of the tunnel is deteriorated. Chloride brought by de-icing salts has penetrated into concrete, and the reinforcement is heavily corroded because of the deeply penetrated chloride. Furthermore, the concrete cover has spalled off and disappeared in large sections of the tunnel (Figure 1.2a), especially at the floor of the tunnel [16]. The cross-section area of the reinforcements at the corroded spots also decreased enormously. The municipality of Rotterdam has proposed a practical repair strategy with the support from multiple research institutes to ensure that the concrete cover-zone can last for the remaining service life of the tunnel, without or with limited maintenance [16]. The repair strategy consists of the following:

- Remove the concrete in the cover zone with a depth of two times the original concrete cover depth plus reinforcement diameter.
- Clean the rebars by removing all the rust.
- Add a repair material which does not debond and crack.

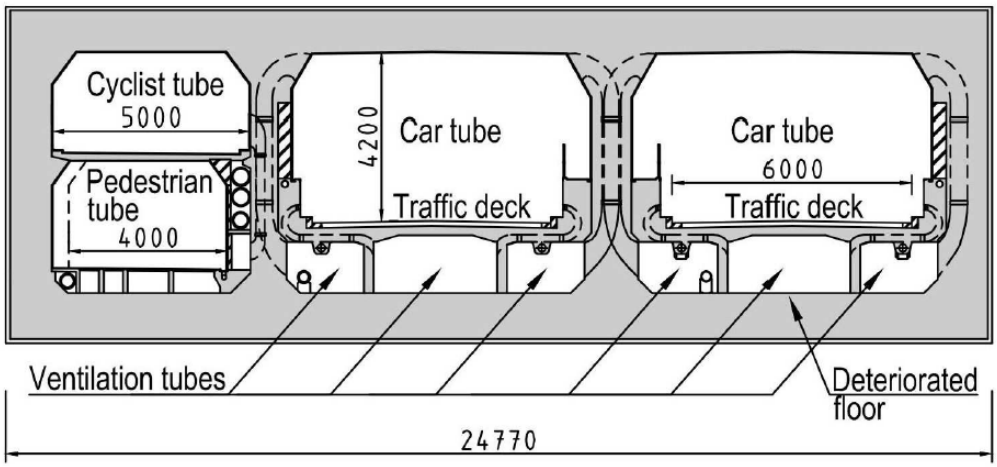

Figure 1.1: Cross Section of the Maastunnel [1]

(a) Inspected floor and ceiling

(b) Damage continuation in the previously repaired patches

Figure 1.2: Field inspection

There are still possibilities that the repaired patches may fail with time development even if the repairing process has been performed carefully. A good example of this is showed in Figure 1.2b. Therefore, the repairing material should be chosen carefully to fulfil the requirement of having no or limited maintenance during the service life of the tunnel. Besides normal concrete as a repair material, another type of repair material is taken into consideration: strain-hardening cementitious composites (SHCC) [17].

1.2. ACCELERATED CORROSION TEST BY SGS INTRON

In order to repair the severe damage on the floor of the Maastunnel caused by reinforcement corrosion, part of the floor will be restored. The complete upper surface of the floor will be removed and cleaned by high-pressure water jets. Then, the area will be covered

by repair mortar. For this purpose, the Combinatie Aanpak Maastunnel (CAM, constructor of the Maastunnel project) commission SGS INTRON BV to investigate for a proper mortar mixture to realize a durable and sustainable solution.

1.2.1. DESIGN AND PRODUCE COMPOSITES

Fibre reinforced concrete mixtures are considered in this project. The tensile and cracking behavior of fiber reinforced concrete can help limit crack width and prevent possible reinforcement corrosion in the future. In the experiment, five types of different fiber reinforced concrete mixtures are developed. The recipes used of these mixtures are displayed in Table 1.1.

Table 1.1: Recipes for test mixtures

Name	OG26	ON01	ON06	ON25	OG15
Code	M1	M2	M3	M4	M5
Cement (kg/m^3)	790	420	420	440	730
Limestone flour (kg/m^3)	790		65	65	
PPr-macrofibres "Istrice - iShots®29mm" (kg/m^3)			6	25	
PPr-microfibres "Bonar - Confiber 23" (kg/m^3)		1.35	0.90		
PVA-microfibres "Kuraray - RECS 15/8" (kg/m^3)	26				15
Sand 0/4 (kg/m^3)		753	727	895	456
Gravel 3/5 (kg/m^3)		160	154	281	97
Gravel 5/8 (kg/m^3)		240	231	422	145
Gravel 8/16 (kg/m^3)		599	578		363
Mixing Water (kg/m^3)	411	177	177	182	328
Cugla Cretoplast (kg/m^3)		1.26	1.26	1.45	
Cugla LR-9400 (kg/m^3)	2.40	1.04	1.04	1.36	1.10

Due to the presence of the fibres, the mortars were difficult to mix. Initially, they were mixed with a concrete mixer (Figure 1.3a), but this resulted in clustering of the fibres. Therefore, all the mixtures were then mixed in a mixing container with a mortar mixer (Figure 1.3b) except material M4 (ON25).

1.2.2. MIXTURE PROPERTY

In Table 1.2 and 1.3, some properties of the five mixtures are presented. The data are tested and recorded immediately after production (Table 1.2) and after 30 minutes (Table 1.3).

(a) Concrete Mixer

(b) Mortar Mixer

Figure 1.3: Mixing Equipment

Table 1.2: Measurements on Concrete Mix Immediately after Mixing

Composition	OG26	ON01	ON06	ON25	OG15
Theoretical air content (%)	6.8	5.0	2.8	0.4	1.7
Air content (%)	6.8	4.2	1.9	-	-
Density (kg/m^3)	1910	2270	2330	2340	2130
Temperature (°C)	20.7	21.7	22.3	22.3	21.8
Slump (mm)	260	100	130	78	141
Mobility (mm)	700	400	380	310	475

Table 1.3: Measurements on Concrete Mix 30 Minutes after Mixing

Composition	OG26	ON01	ON06	ON25	OG15
Theoretical air content (%)	3.4	4.1	4.0	0.4	1.7
Air content (%)	3.3	4.3	3.8	-	-
Density (kg/m^3)	1980	2290	1980	2340	2130
Slump (mm)	250	80	110	54	169
Mobility (mm)	635	375	380	285	500

1.2.3. COMPRESSION AND FLEXURAL TESTS ON MORTAR

Compression and flexural test were performed on these materials. The beam size for flexural test and hydration shrinkage measurement is $100 \times 100 \times 500\ mm$. Also cylinders with a size of $150 \times 300\ mm$ and cubes with a size of $150\ mm$ were produced for compression test.

Figure 1.4 shows the temperature change in the beams prior to the hydration shrinkage measurement.

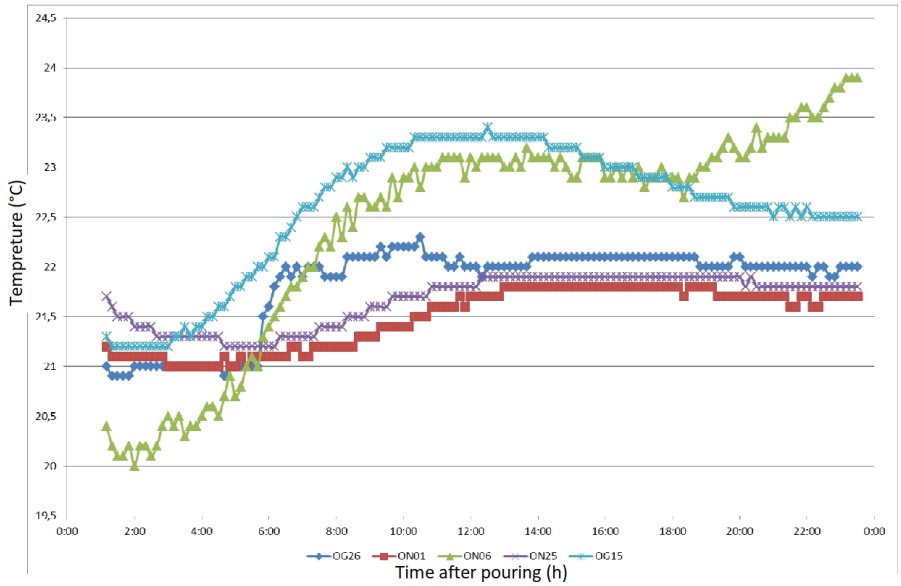

Figure 1.4: Temperature Change in the Beams Prior to Hydration Shrinkage Measurement

The hydration shrinkage of the beams under lab condition (20 °C and 65% RH) are measured and presented in Figure 1.5.

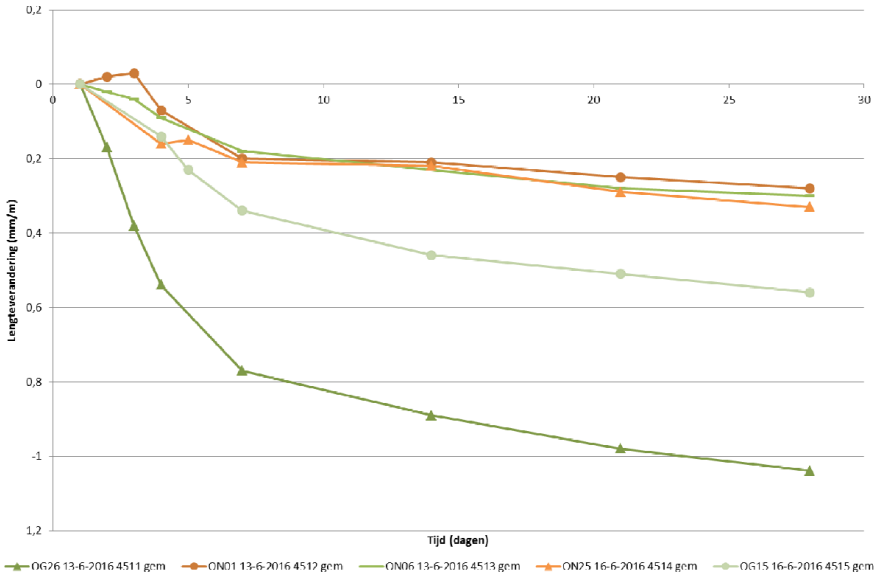

Figure 1.5: Hydration Shrinkage in the Beams under Lab Condition

The results obtained from compression test are measured up to 28 days and presented in Table 1.4.

Table 1.4: Compression Test Results up to 28 Days

Composition	OG26	ON01	ON06	ON25	OG15
Density (kg/m^3)	1950	2280	2300	2280	2100
Cubical 4-day strength (N/mm^2)	27.9	23.5	29.5	34.4	20.0
Cubical 7-day strength (N/mm^2)	37.4	32.6	39.0	44.7	28.9
Cubical 14-day strength (N/mm^2)	46.7	36.4	48.6	56.5	36.3
Cubical 28-day strength (N/mm^2)	53.1	48.1	56.2	61.6	44.4
Cylindrical 4-day strength (N/mm^2)	29.4	24.8	27.4	30.2	19.0
Cylindrical 7-day strength (N/mm^2)	37.7	32.1	34.0	36.9	28.3
Cylindrical 28-day strength (N/mm^2)	48.9	43.1	49.1	54.4	42.3
Young's modulus 4-day (N/mm^2)	14050	25550	26475	28125	15300
Young's modulus 7-day (N/mm^2)	14800	27400	30675	33100	15825
Young's modulus 28-day (N/mm^2)	18725	33550	37950	37575	37575

For mixtures ON01 and ON06, there are no 3-point or 4-point bending test done because there is no significant contributions from fibre reinforcements. They have low plastic tensile strain capacity and behave more similar to normal concrete. Part of the results of bending tests are lost due to ICT issues. All bending experiments were done in line with EN 14651 [18] (beam size is the only difference). An average value of the experiments at 28 days are showed in Table 1.5. All the recorded results are listed in Appendix A.

Table 1.5: Bending Test Results

Test Type	Three-Point Bending			Four-Point Bending		
Composite	OG26	ON25	OG15	OG26	ON25	OG15
LOP (N/mm^2)	6.35	-	5.70	-	-	6.25
f_R1 ($\delta 1 = 0.47\ mm$) (N/mm^2)	8.75	-	4.40	-	-	2.30
f_R2 ($\delta 2 = 1.32\ mm$) (N/mm^2)	6.45	-	1.50	-	-	0.60
f_R3 ($\delta 3 = 2.17\ mm$) (N/mm^2)	4.05	-	0.70	-	-	0.25
f_R4 ($\delta 4 = 3.02\ mm$) (N/mm^2)	2.65	-	0.40	-	-	0.15

1.2.4. EXPERIMENT SET-UP

The crack behavior (crack pattern, number of cracks and maximum crack width) of the five designed materials are different. Cracking behavior can significantly influence the durability of a repair system, which is the most important aspect of evaluating the performance of a repair mortar. Therefore, an accelerated corrosion test was designed and executed to test the cracking behavior of the repair mixtures. The design of the experiment specimens is shown in Figure 1.6. The test specimen is with a size of $400 \times 300 \times 226\ mm$. A $\phi 36\ mm$ reinforcement is embedded with a concrete cover of 30mm in the center of the specimen to imitate the corrosion condition that exists in the tunnel. The depth of substrate and repairing mortar are 100 mm and 126 mm respectively.

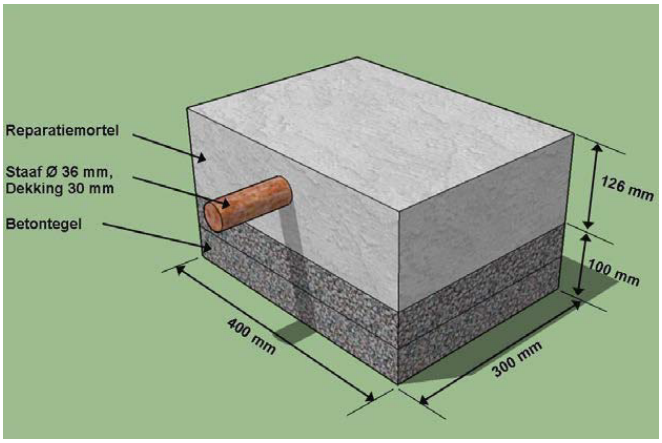

Figure 1.6: Design of Test Specimen

On the reinforcement, a reference electrode with 230 mV potential is fixed with plastic wraps. Wooden moulds were made for the manufacture of the experiment specimens. The moulds were filled in by two layers and compacted with a vibrator (Figure 1.7).

(a) Fill Moulds

(b) Compacting

Figure 1.7: Production of Test Specimens

After curing under lab condition, all the test pieces were placed in a container filled with saturated lime water. The test pieces extended about 30 mm from above the water level. During the test, the water was always replenished to maintain this level. Cathode (Ti-mesh) was placed next to the test piece with a PVC ring as spacer (Figure 1.8a). Then the cathode and anode (rod) were connected to a voltage-controlled power source (Figure 1.8b).

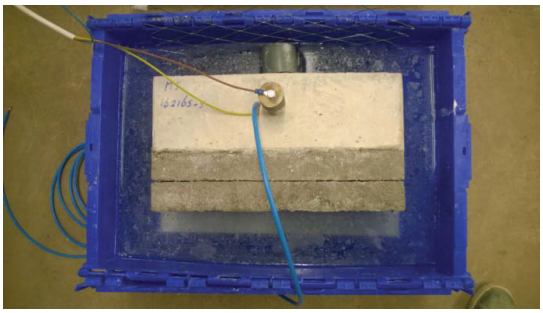

(a) Details of Specimen

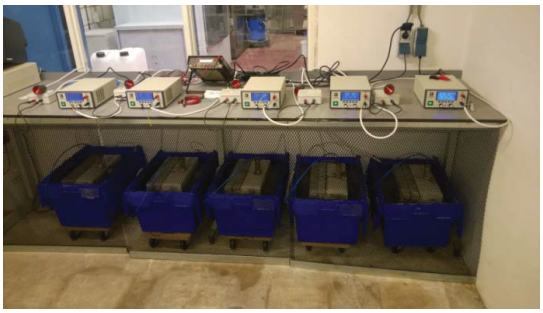

(b) Connection to Power Source

Figure 1.8: Experiment Set-up

Table 1.6 shows the phases of the accelerated corrosion test. The current density ($\mu A/cm_s^2$) was always held constant for 7 consecutive days. The required current is calculated from current density and steel surface ($A_s = 315.6\ cm^2$). The current and voltage were measured and adjusted at least once per day if needed.

Table 1.6: Accelerated Corrosion Test Phase

Phase	Current ($\mu A/cm_s^2$)	Current (mA)	Lasted Time (d)	Measurement Stage
1	50	15.8	7	
2	75	23.7	7	1
3A	100	31.6	7	
3B	100	31.6	7	
4A	175	55.2	7	
4B	175	55.2	7	
4C	175	55.2	7	
5A	300	94.7	7	
5B	300	94.7	7	2

1.2.5. OVERVIEW OF RESULTS

Every each phase of 7 days, the voltage was suspended temporarily and the specimens removed from the water and then visually inspected for cracks and marked if visible. After completion of the accelerated corrosion test, most part (around 95 mm) of the substrate layer was removed using a water-cooled saw (Figure 1.9). Before vacuum impregnation with fluorescent resin (Figure 1.10), the test pieces have been dried for 48 hours at 40°C. Then, the test piece is impregnated with a fluorescent resin under UV light. After curing of the resin (Figure 1.11), the impregnated test piece was cut at three depths (30, 100, and 200 mm)(see Figure 1.12).

Figure 1.9: Remove Substrate

Figure 1.10: Vacuum Impregnation

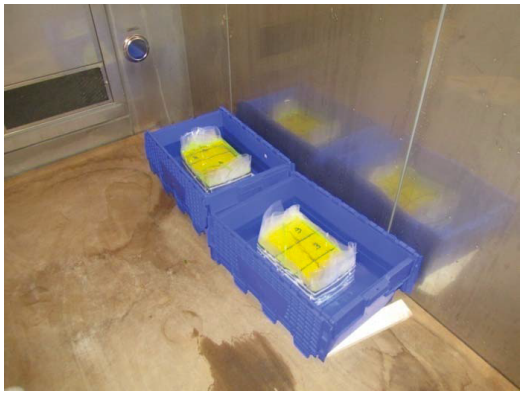

Figure 1.11: Resin Curing in Water at 4°C

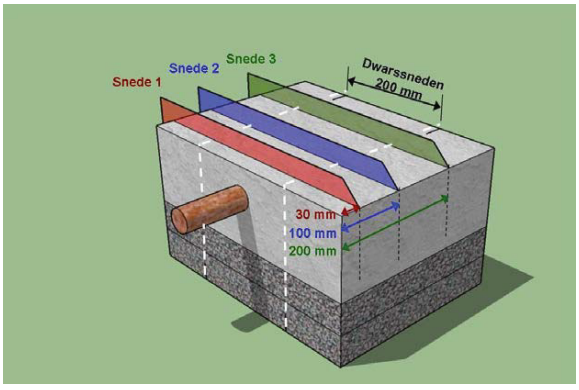

Figure 1.12: Saw Cut Depth

In Table 1.7, the cracking behaviour of the experimental specimens are summarized. This table includes: number of cracks, crack width range and corrosion layer thickness. The detailed crack pattern of the fluorescence examination of all specimens are listed in Appendix B. They are recorded under both normal light and UV light.

Table 1.7: Results of Cuts in Different Depth

Cut Depth (mm)	Item	OG26	ON01	ON06	ON25	OG15
30	No. of Crakcs	28	4	4	8	5
	Crack Width (mm)	0.1~0.2	0.1~1.0	0.1~0.8	0.1~0.7	0.1~0.7
	Maximum Crack Width (mm)	0.2	1.0	0.8	0.7	0.7
	Corrosion Layer Thickness (mm)	0.2	0.3	0.2	0.2	0.2
100	No. of Crakcs	22	4	5	6	7
	Crack Width (mm)	0.1~0.2	0.1~0.9	0.1~1.0	0.1~0.8	0.1~0.6
	Maximum Crack Width (mm)	0.2	0.9	1.0	0.8	0.6
	Corrosion Layer Thickness (mm)	0.3	0.3	0.1	0.2	0.2
200	No. of Crakcs	26	5	7	6	8
	Crack Width (mm)	0.1~0.2	0.1~0.7	0.1~1.0	0.1~0.8	0.1~0.8
	Maximum Crack Width (mm)	0.2	0.7	1.0	0.8	0.8
	Corrosion Layer Thickness (mm)	0.2	0.4	0.2	0.3	0.2

Based on the results from the experiments, the following conclusions can be drawn:

- The procedure used for accelerated corrosion is suitable for examining the crack pattern under uniform corrosion condition.
- Mixture OG26(SHCC) shows distributed crack pattern without any major concentrated cracks. However, the other four mixtures cannot show the distributed crack pattern.
- Mixture with higher fiber volume produces more cracks and smaller crack width.

1.3. PROBLEM STATEMENT

In the previous section, an introduction has been given about the accelerated corrosion test done by SGS INTRON BV. From the experimental results, different mixtures showed different cracking behavior. Especially mixture OG26 (SHCC) and mixture ON06 (material with the lowest fracture energy, can be regarded as normal concrete) shows a significant difference in the crack pattern in the experiment. The intention of the accelerated corrosion test

is to investigate a proper mortar for the repairing of the tunnel. Therefore, the length of the specimen (400 mm) and the radius of the reinforcement (18 mm) are at the similar level of the rebar spacing and radius in the concrete floor of the Maastunnel. However, the experiment is time-consuming. It is of utmost importance to investigate if the cracking behavior can be simulated by numerical modeling and if in the future, the parametric analysis might be performed without large experimental series.

There are two possible types of finite element model to simulate the cracking behavior of concrete, namely continuum model and lattice model. An obvious distinction between these two type of models is the geometric definition. Also, crack formation method and solution method are also important features for both of the models. A nonlinear incremental solution method is applied in the continuum model. However, a sequentially linear solution method is used in the lattice model. An overview of the comparison between the models is shown in Table 1.8.

Table 1.8: Overview of Numerical Models

Model	Geometry	Crack Formation	Solution Method	Method Type
Continuum	Continuum	Total Strain Based Cracking	Nonlinear Incremental	Iterative
Lattice	Discrete	Element Removal	Sequential Linear	Linear

The crack pattern is the key feature of different repair materials. With SHCC, distributed cracks with relatively small crack width are performed. With other fiber reinforced concrete (FRC), concentrated cracks with higher crack width are developed. The number of cracks also decreases with decreasing fracture energy. Therefore, the number of cracks and maximum crack width are the key features to evaluate the performance of a repair mortar. Thence, it is important to investigate the performance of both types of models in simulating the cracking behavior (crack pattern, number of cracks and maximum crack width) of different repair mortar.

Continuum model has been widely used in predicting the load capacity of concrete structures. The lattice model origins from a model in theoretical physics proposed by Herrmann [19]. It was developed by Schlangen for modeling fracture process on a very detailed level in material research [20]. The main cause of nonlinearity in concrete is cracking, which is

the result of the limited strain capacity of concrete in tension [21]. One primary goal of this project is to compare and conclude the pros and cons of the two models in simulating the cracking behavior of material with different fracture energy.

The purpose of the accelerated corrosion test done by SGS INTRON is to simulate the influence on the surrounding concrete due to the corrosion of the reinforcement. However, the boundary condition of the specimen in the experiment is not identical to the real scenarios. In the experiment, all the boundaries are entirely free. Nevertheless, the concrete floor in the tunnel is always constrained by the surrounding concrete. The influence of the change in boundary condition on the crack pattern is in doubt.

Moreover, the tensile strength of the mortar-substrate interface is also a critical parameter in concrete repair system. It can be regarded as a general "boundary condition". The change of the interface tensile strength can influence the stiffness matrix significantly which results in a different cracking behavior. However, this parameter is not examined in the experiment. Therefore, the influence of interface tensile strength on cracking behavior also needs to be examined.

In general, the main research problems of this thesis project can be summarized as:

- How are the performances of the lattice model and the continuum model in simulating the cracking behavior (crack pattern, number of cracks and maximum crack width) of repair mortar with different fracture energy in accelerated corrosion test? What are the pros and cons of both models?
- How is the influence of boundary conditions on the cracking behavior in accelerated corrosion test. What are the suggestions for boundary conditions in experiment design to simulate the real scenarios accurately?
- How is the influence of mortar-substrate interface tensile strength on the cracking behavior in accelerated corrosion test? Is this influence sensitive to the fracture energy of repair mortar?

1.4. RESEARCH CONTENT

Firstly, the influence of bottom edge boundary conditions on cracking behavior is studied in the continuum model. Material ON06 (material with least fracture energy, can be regarded as normal concrete) is implemented for this chapter. Two different types of boundary conditions are applied: free bottom edge (imitating the accelerated corrosion test) and constrained bottom edge (imitating the concrete floor in the Maastunnel). Moreover, the influence of different loading conditions on the cracking behavior is also investigated. Three different types of loading conditions are applied and compared: prescribed displacement (displacement control), thermal load (prescribed strain, indirect force control) and prescribed force (direct force control).

Following, two lattice models with constrained and free bottom respectively are developed and compared using ON06 as repair mortar. Then, the strain-hardening material SHCC is implemented in both types of models to investigate their performance in simulating the distributed crack pattern of SHCC.

In the next step, a parametric study is conducted on the fracture energy of repair mortar. Five different types of materials are defined with different fracture energy ranging between two extreme materials used in the previous chapters (SHCC and ON06). An extended comparison is carried out between these two types of models to investigate their pros and cons in simulating the cracking behavior of materials with different fracture energy and strain capacity.

Furthermore, a parametric study about the interface tensile strength is carried out. Four levels of interface tensile strength ranging between 10% and 100% of the tensile strength of repair mortar are applied to the mortar-substrate interface elements in both types of models. This parametric study is done with material SHCC and ON06 to investigate also its sensitivity of fracture energy and strain capacity in repair mortar.

Finally, the influence of substrate strength on the crack pattern is investigated. C30 and C60 concrete are applied respectively as repair mortar. Whether the substrate strength as a general "boundary condition" can influence the crack pattern is studied through the comparison between these models.

2

Literature Review

2.1. Strain-hardening Cementitious Composites (SHCC)

In the Microlab at TU Delft, new types of repairing material are under development [22] [23] [14] [24]. Also there are some ongoing research projects focusing on the chloride ingress and corrosion of rebars in cracked concrete [25] [26] [27]. Based on these researches several new repair materials are developed. These materials, which contain fiber reinforcements and show strain-hardening behavior under tension are named as strain-hardening cementitious composites (SHCC).

2.1.1. General Information

Although with the name "cementitious composites", SHCC is not concrete actually. It contains fine sand instead of coarse aggregates. Also, normally SHCC contains fiber reinforcements with a percentage of around 2%. Tensile behavior is a major difference that SHCC has in comparison to conventional concrete: SHCC comes with a strain-hardening behavior in tension. Therefore, the load carried by the SHCC specimen will not decrease after the ignition of the first crack. Moreover, the specimen will develop multiple small cracks instead of a big major crack. The specimen has a dramatically high deformation capacity in this way [2].

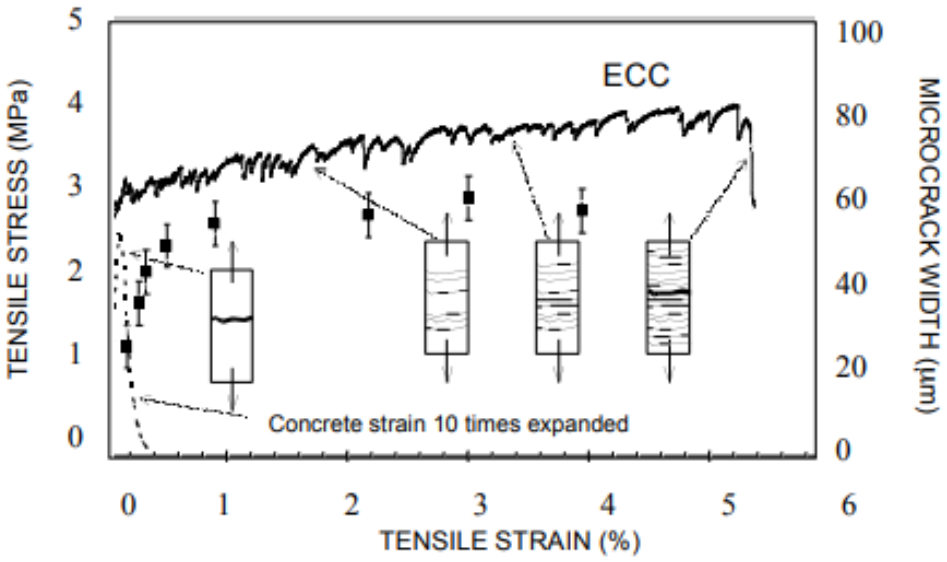

Figure 2.1: Strain Capacity of SHCC [2]

SHCC is famous for its high deformation capacity (Figure 2.1) and the ability in crack width control (produce multiple cracks with width normally smaller than $100\mu m$ instead of one major crack, Figure 2.2). This is because of the fine particle composite (only sand without aggregate) as well as the interaction between fiber reinforcements and mortar matrix. Instead of losing connection directly, the fibers will take over and hold the tensile stress after a crack opening. Extra external loads needed to break the bonding connection between fiber and the matrix. However, before broken the bonding connection or the fiber itself, another crack will be formed. Repeating this process, both the load capacity and ductility will get increased. This whole cracking-bridging-cracking process produces the strain-hardening behavior of SHCC.

2.1.2. MECHANICAL PROPERTY

SHCC is a series of cementitious based material. A summary of major mechanical properties is displayed in Table 2.1. The variance of the mechanical properties comes from the differences in ingredient and producing procedures. It should be emphasized that these properties are tailorable through the use of micro-mechanics tools [2].

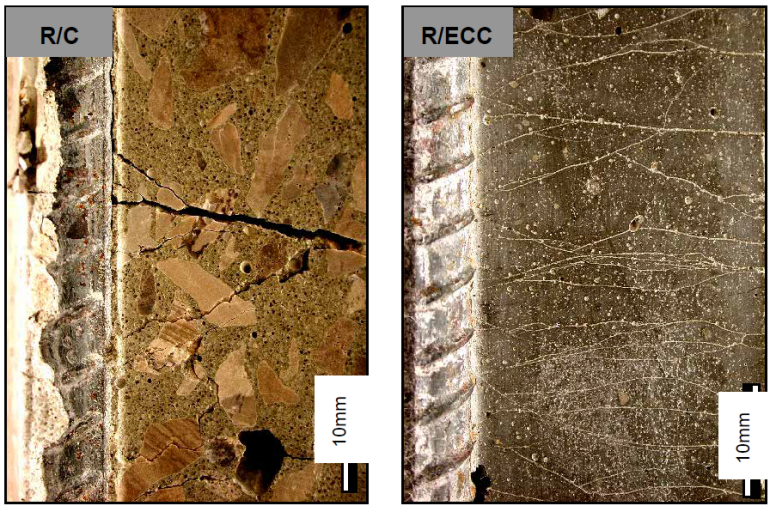

Figure 2.2: Comparison of crack pattern between SHCC and normal concrete [3]

Table 2.1: Major Mechanical Properties of SHCC [2]

Compressive Strength (MPa)	First Crack Strength (MPa)	Ultimate Tensile Strength (MPa)	Ultimate Tensile Strain (%)	Young's Modulus (GPa)	Flexural Strength (MPa)	Density (g/cc)
20 ~ 95	3 ~ 7	4 ~ 12	1 ~ 8	18 ~ 34	10 ~ 30	0.95 ~ 2.3

An important note from Table 2.1 is that the ultimate tensile strain of this type of material is dramatically larger than normal concrete ($100-800$ times larger). This shows the ductility of SHCC. Some researches ([6], [28] and [29]) showed that due to its small crack widths and ductility, SHCC patch repair can effectively restrain chloride penetration thus prevent the reinforcement from corrosion.

2.1.3. DURABILITY

In respect of structural durability, SHCC has advantages in three aspects in replacing normal concrete in reinforced concrete structures [7]:

- Use its micro-sized crack in delaying the reach of aggressive agents to steel reinforcements.
- Avoid pitting corrosion and slow down corrosion through its distributed cracking be-

havior instead of one large concentrating crack.

- Restrain concrete cover spalling due to its tensile ductility.

SHCC has a low coefficient of permeability comparing with normal concrete. It can be observed in 2.3 that even after cracking, SHCC is still more or less the same water permeability ($k = 5 \times 10^{-11}\ m/s$) as uncracked normal concrete.

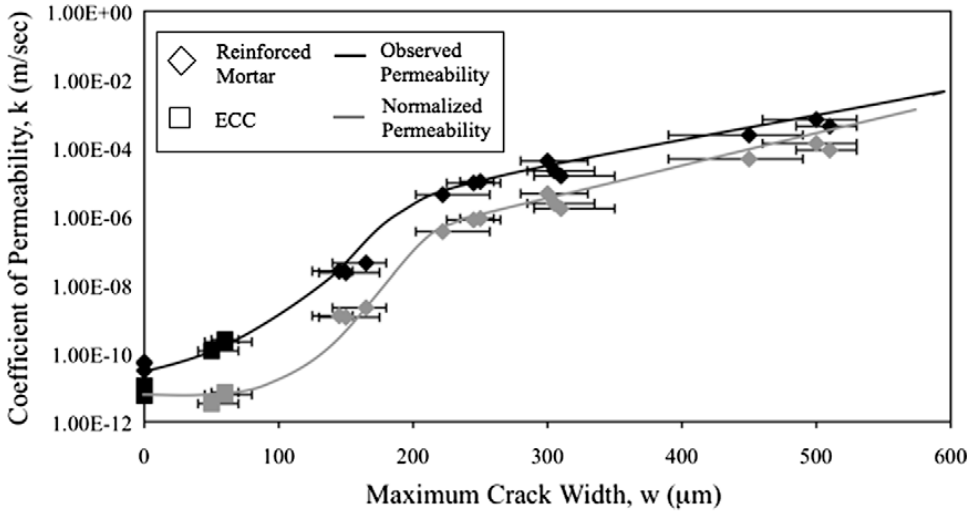

Figure 2.3: Coefficient of Permeability Versus Crack Width for SHCC and Reinforced Mortar series deformed to 1.5% in uniaxial tension [4]

Meanwhile, the sorptivity of SHCC is significantly lower that the value of conventional concrete. Typical sorptivity index of uncracked normal concrete with a water cement ratio of 0.4 is 0.09 $mm/min^{1/2}$ [30]. A enormous difference of the sorptivity index of uncracked SHCC specimens with a water cement ratio of 0.27 (about 0.02~ 0.03 $mm/min^{1/2}$) can be observed (Figure 2.4).

Moreover, SHCC is proved to have lower chloride diffusion coefficient under uncracked condition than normal concrete. Experiments showed that the chloride diffusion coefficient for SHCC is $6.75 \times 10^{-12} m^2/s$. The value of another controlled group of steel reinforced mortar beam was found to be $10.58 \times 10^{-12} m^2/s$ [6]. Research also showed that the chloride diffusion coefficient increases enormously with the increasing of cracks based on test results of specimens subjected up to almost 100000 cycles of flexural loading [31]. Furthermore, it has been discovered that the diffusion coefficient of SHCC has a linear relationship with the number of cracks (with constant crack width despite the increasing of deformation of the experiment specimen, therefore it can be regarded as a linear increased crack

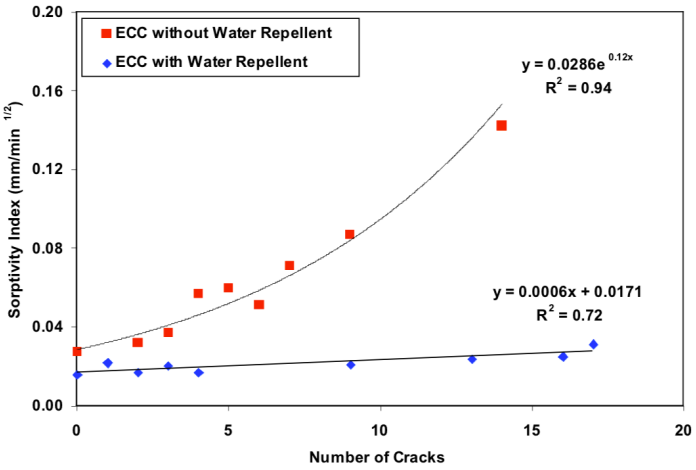

Figure 2.4: Sorptivity Versus Number of Crack for SHCC Mixtures [5]

opening). In contrast, the diffusion coefficient of normal reinforced concrete has a linear relationship with the square of its crack width.

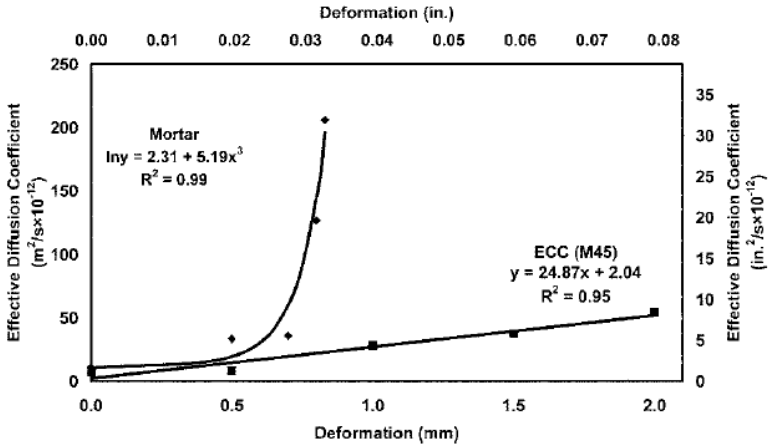

Figure 2.5: Effective Diffusion Coefficient Versus Pre-loading Beam Deformation Level [6]

In conclusion, the ductility, permeability, sorptivity, and chloride diffusion coefficient of SHCC are all improved against normal concrete (especially under cracked condition). Considering that concrete structures are designed to work usually under the cracked condition and these cracks for the most time are the ignition point of corrosion due to the increasing transportation properties, SHCC can be applied as a perfect repairing material (all transport mechanisms are effectively constrained) to improve the durability of existing reinforced concrete structures.

An experiment carried out by Sahmaran (2005) proves the conclusion about SHCC in con-

trolling chloride penetration. Two beams made of SHCC and normal concrete were preloaded first to initialize cracking. The crack width of the SHCC and normal concrete beams are 50 μm and 400 μm respectively. At 29 days of age, a 3% NaCl solution was ponded on the cracked surface of the specimens. The depth of penetration was examined and recorded every 30 days. The chloride penetration depth of SHCC is much lower than that of normal concrete at the same level of immersed time (Figure 2.6).

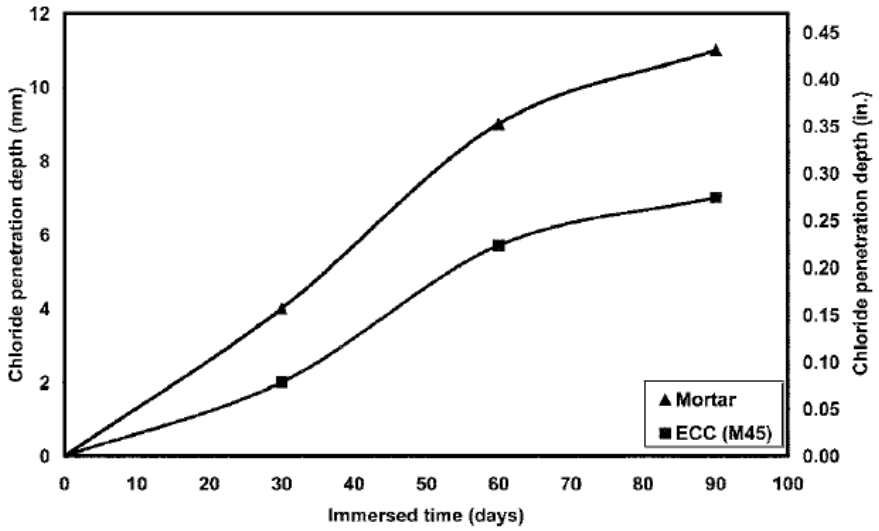

Figure 2.6: Effective Diffusion Coefficient Versus Pre-loading Beam Deformation Level [6]

2.2. LATTICE MODEL

The lattice model is a discrete type of finite element model. The specimen is modelled as a lattice of beam elements (Figure 2.7) [32]. By assigning different properties to those beam elements, these elements can represent different composites in the concrete mix (Figure 2.8). Moreover, the random distribution of lattice beam elements brings the model some degree of randomness which will present the concrete better as a heterogeneous material. Therefore, a lattice model can simulate the cracking behavior of concrete as a brittle material precisely in details [7].

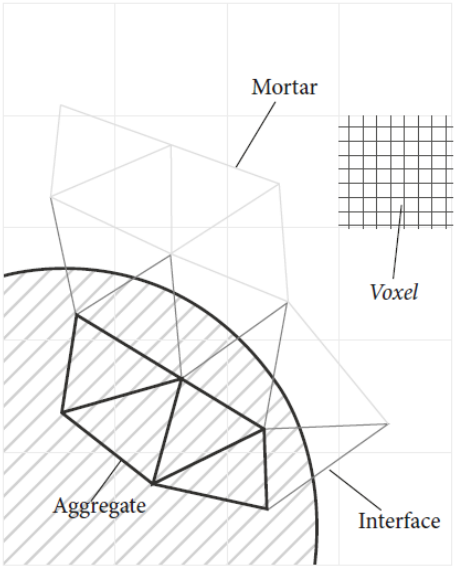

Figure 2.7: Schematic 2D representation of interface zone of mortar-aggregate [7]

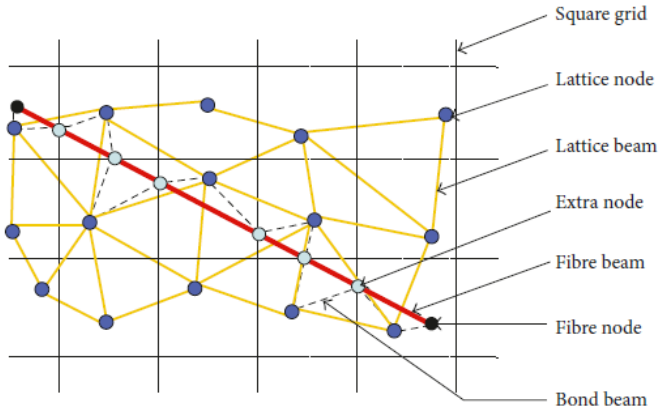

Figure 2.8: Schematic 2D representation of generation of fibre-lattice [8]

In the lattice model, the analysis follows a sequentially linear solution method. Within each analysis step, linear static analysis is performed. The load is scaling in such a way that only one element from the mesh will exceed a certain threshold value (tensile strength or strain energy) [33]. Then that very element will be removed or modified from the mesh. In this way, the stress-strain relation of the material is followed accurately. Thence, the crack pattern can be obtained in a good manner. The solution procedure of lattice model is described as [34]:

- Apply a reference proportional load.
- Calculate the principal stresses through a linear-elastic analysis.
- Determine the critical element (element with the highest value of principal stresses/ strength ratio).
- Determine the scaling factor λ_{crit} of the element (strength/principal stresses).
- Scale the reference load proportionally with λ_{crit} and calculate again.
- Implement the damage in the critical element by reducing the stiffness and strength according to the defined constitutive relation.
- Repeat this process until the scaling factor reaches its limit.

The full detailed lattice model was developed at micro-scale or mesoscale for material study. Therefore, for macro-level experiments, simplification and up-scaling are needed to reduce model complexity and calculation time. In this project, the composite in the concrete mix is not modeled explicitly anymore. Instead of modeling concrete discretely with every composite, lattice model describes the concrete matrix as a homogeneous material with a single type of elements. Figure 2.9 shows the schematic presentation of up-scaled lattice model.

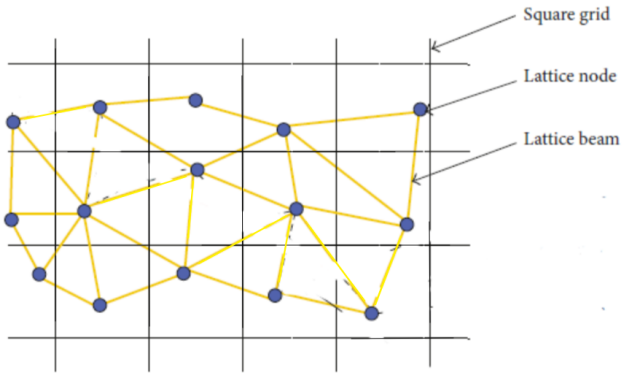

Figure 2.9: Schematic presentation of up-scaled lattice model

Also, the results of the lattice model depend highly on the internal force transformation. Due to the random distribution of lattice beams, the orientation of beam elements can have a significant influence on the load capacity of a model before its failure. This effect gets more apparent when the mesh gets coarser. Therefore, the influence of mesh size in the lattice model is also an interesting aspect to investigate.

2.3. CONTINUUM MODEL

Non-linear finite element analysis is already a widely applied general analyzing technique. In the continuum model, the specimen is represented by continuum elements. Due to nonlinearities from material and geometry, a nonlinear analysis is needed to find the displacement of the model which equilibrates the external and internal forces. The Regular Newton-Raphson method is the solution method applied most in nonlinear analysis. With this incremental solution method, an iterative solving procedure is carried out. Within

every steps, the displacement is calculated through the tangential stiffness for which the internal force equals to external force in an iterative way .The stiffness is calculated every iteration, which means that every prediction is based on the most recent information. Therefore, the convergence speed is pretty fast with this method.

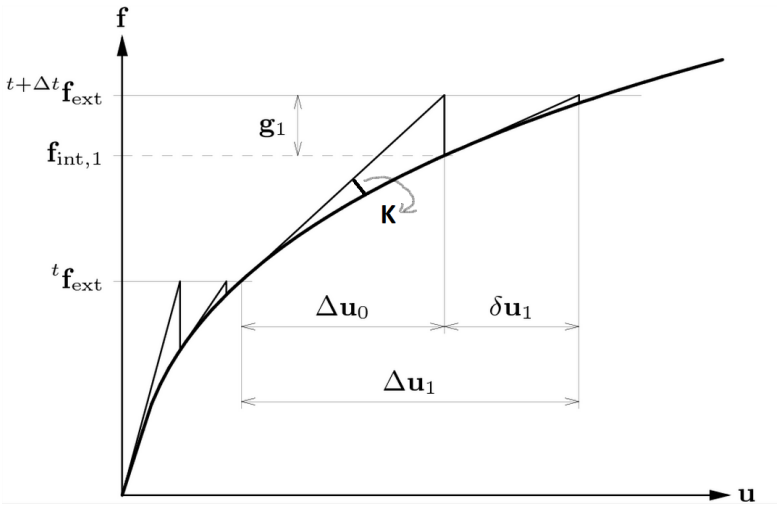

Figure 2.10: Regular Newton-Raphson Method

However, it has some disadvantages when it is applied to simulate crack propagation in brittle materials. After the initiation of cracks, more and more points within the stiffness matrix will get negative or even zero values. This results in difficulties in convergence. Therefore, the accuracy of results come from the non-convergence step are in doubt. However, the cracking path it follows can still be all right. Extra cautions are needed while presenting the crack pattern from non-converged steps.

For normal concrete, the nonlinear strain-softening behavior can be described by the expression proposed by Hordijk et al. [35]. The required input for this expression is only the fracture energy, tensile strength and Young's modulus of the material. Then stress-crack strain relation can be calculated based on those inputs (Figure 2.11).

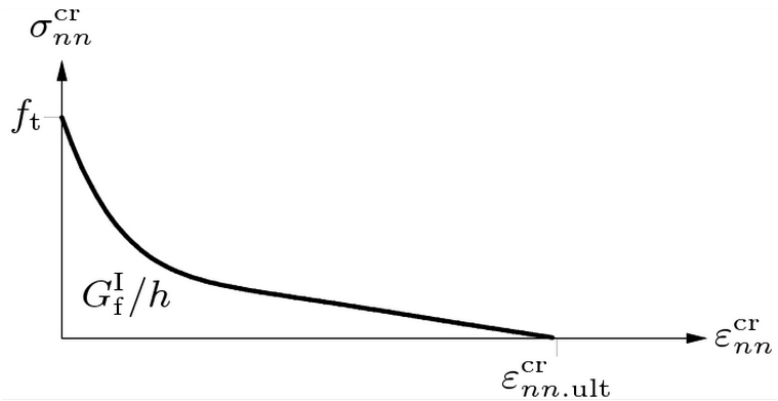

Figure 2.11: Nonlinear Tension Softening (Hordijk et al.) [9]

For fiber reinforced concrete, a unique tensile stress-strain relation curve "FRCCON" is being provided by finite element software package DIANA FEA. It is based on fib model code 2010 for concrete structures [36]. The model can be either specified as function of the total strain (Figure 2.12) or a function of the crack mouth opening displacement (Figure 2.13) [9].

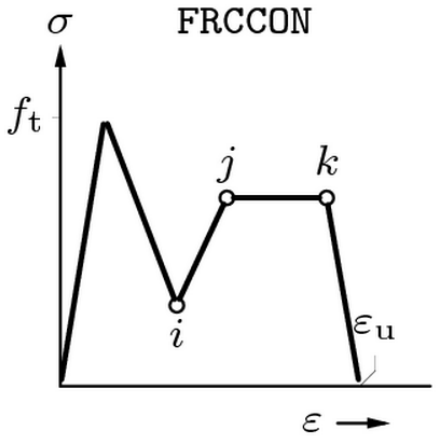

Figure 2.12: FRCCON, Total Stain Based

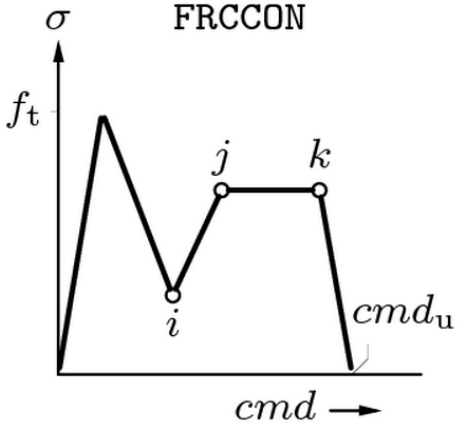

Figure 2.13: FRCCON, Crack Mouth Opening Displacement Based

By using this curve, the cracking of fiber reinforced concrete is initiated at the strain where the tensile strength f_t is reached. Three extra points in the curve are defined with stress state and strain/crack mouth opening to describe the constitutive relation in plastic stage. The stress level of these points can be either higher or lower than the tensile strength f_t. Finally, an extra point is defined to describe ultimate strain/crack mouth opening. Its performance will be tested using SHCC and other fiber reinforced concrete.

2.4. REVIEW ON SIMILAR RESEARCHES

2.4.1. ACCELERATED CORROSION SIMULATION USING THE LATTICE MODEL

A similar accelerated corrosion test has been done with a smaller scale by Luković et al. [7]. Instead of specimens with a size of 400 × 300 × 226 mm, the specimen was designed with a size of 40 × 40 × 40 mm and one rebar with 4mm diameter instead of 36mm. The detail experiment set-up is showed in Figure 2.14.

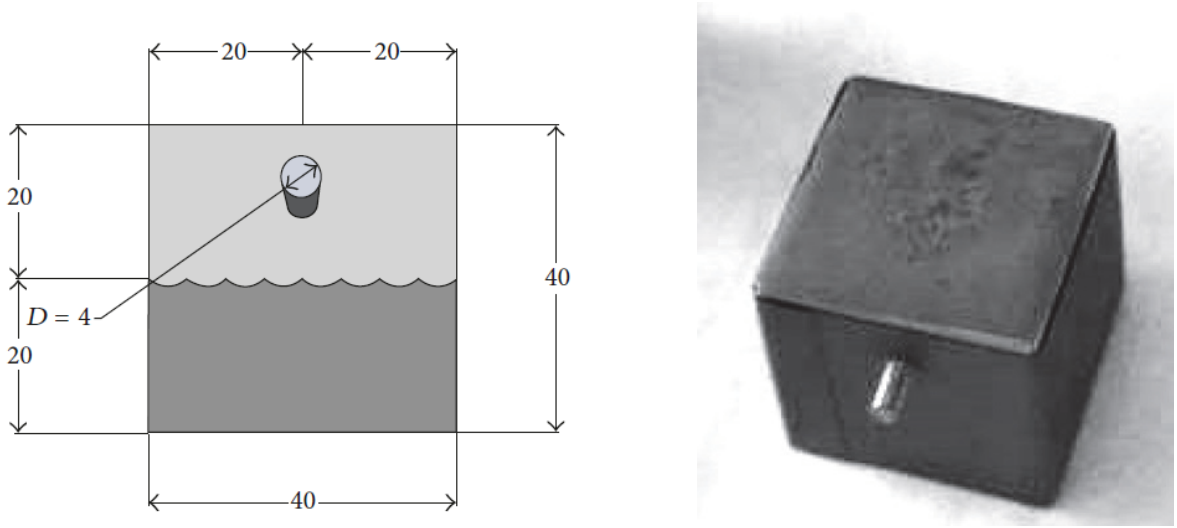

(a) Test Set-up (b) Casting of the Repair Materials

Figure 2.14: Repair System for Accelerated Corrosion Test [7]

Three types of mortar are applied in this experiment, namely SHCC, non-reinforced repair mortar (repair mortar for further reference) and commercial repair material. Comparison of material properties are given in Table 2.2. The commercial repair material (Cuglacrete Hoogoven A middle R3) was chosen because of its similar properties with SHCC. It is a polymer modified blast furnace slag based mortar with polyacrylonitrile fibres (without strain hardening behaviour).

Table 2.2: Comparison of Material Properties [7]

Composite	w/p	Density (kg/m^3)	Young's Modulus (GPa)	f_c (MPa)
Commercial Mortar	0.16	1950	16	45
SHCC	0.26	2025	18	40

Repair mortar was cast over the substrate with two-year-age. After curing of six days, they were left to dry for 72 hours in laboratory conditions (T = 20°C, RH = 50%). Then the specimens were executed for an accelerated corrosion test. After the test, the fluorescent epoxy was applied to all specimens to investigate the crack patterns.

Meanwhile, the lattice models of the specimens have been developed to investigate the cracking behavior of repair mortar loaded by prescribed force to represent the ongoing corrosion [7]. The mortar has been modeled as a heterogeneous material, which means

that all composite of the mixture and their interfaces have been modeled with different elements. The input properties are shown in Table 2.3. The built lattice model is displayed in Figure 2.15.

Table 2.3: Input Values of Lattice Elements [7]

Element	E (GPa)	f_t (MPa)	f_c (MPa)
Matrix (repair mortar, RM)	20	3.5	35
Fibre	40	7380	7380
Interface (RM/fibre)	20	90	900
Substrate	25	4/5	40/50
Aggregate	70	8	80
Interface (aggregate/RM)	15	2.5/3.5	25/35
Interface (substrate/RM)	15	1/3	10/30

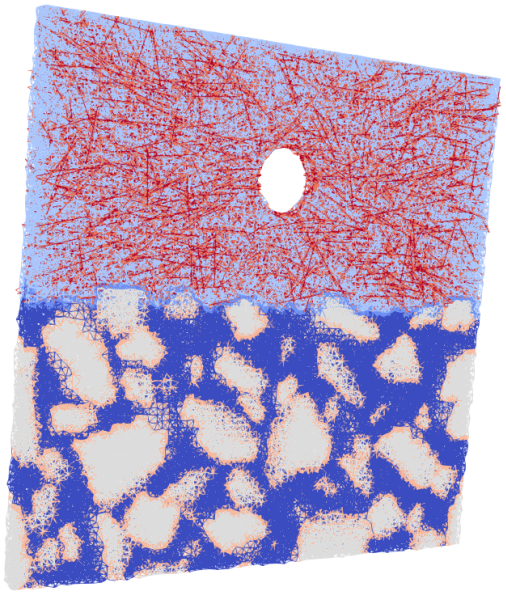

Figure 2.15: Lattice Model with Different Elements

Figure 2.16 shows the damage pattern obtained from experiments. At the same level of loading (corrosion), SHCC can produce cracks with width significantly smaller than repair mortar. Moreover, much more cracks are produced in the SHCC specimen around the rebar than repair mortar.

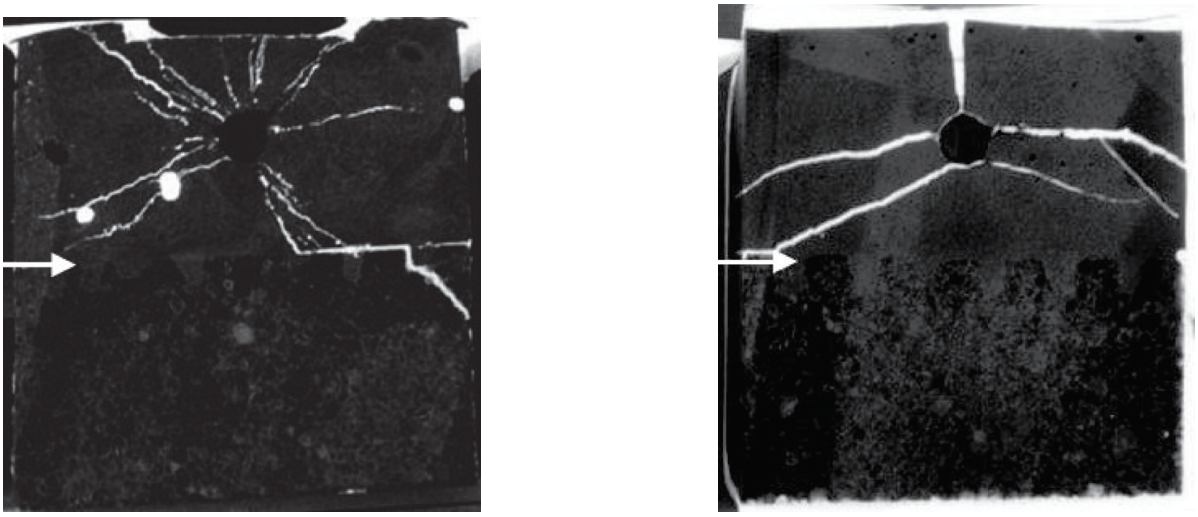

(a) SHCC (b) Commercial Mortar

Figure 2.16: Experimentally Obtained Crack Patterns [7]

Crack patterns of different materials obtained by lattice model are displayed in Figure 2.17. The damage patterns obtained from the lattice model are very similar to experimental results. Numerically, the maximum crack width of SHCC specimen is $66\mu m$, which is only roughly 26.37% of the maximum crack width in the repair mortar model. Moreover, the number of cracks in the SHCC model around the rebar is higher than the other model. Also, the location of the largest crack and crack propagation direction also correspond with experimental results.

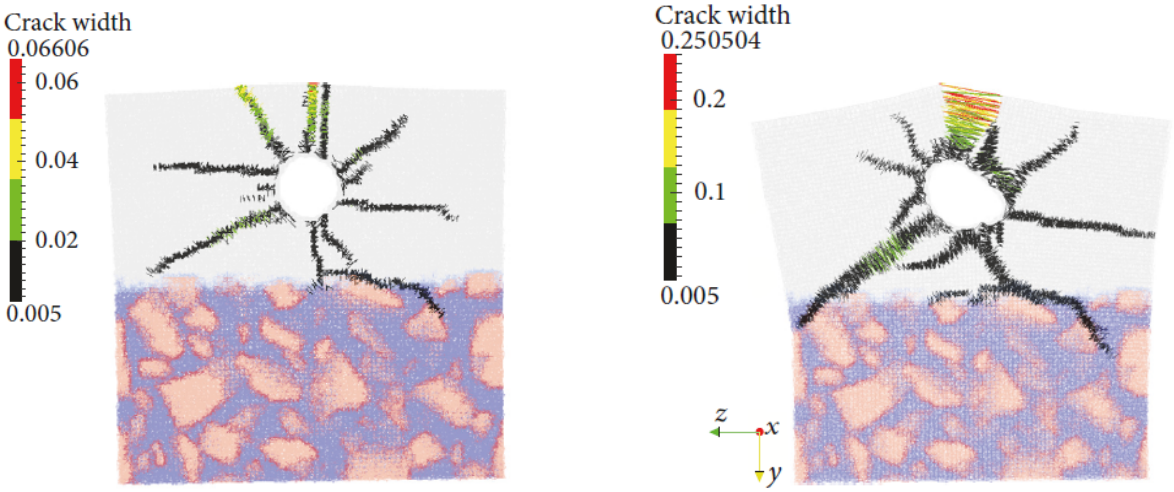

(a) SHCC (b) Commercial Mortar

Figure 2.17: Crack Pattern obtained from Lattice Model, Imposed Pressure $26MPa$ [7]

The influence of the strength of the interface between mortar and substrate was also investigated. Three models were set-up to investigate this factor, respectively smooth surface & $1MPa$ interface strength, rough surface & $1MPa$ interface strength, and rough surface & $3MPa$ interface strength. It can be observed in Figure 2.18 that the bottom crack propagates into substrate instead of interface de-bonding with the stronger interface. The mortar-substrate interface strength has an influence on the crack pattern (on the development of the bottom crack specifically). This result concluded from the lattice model is also observed in the experimental results shown in Figure 2.19.

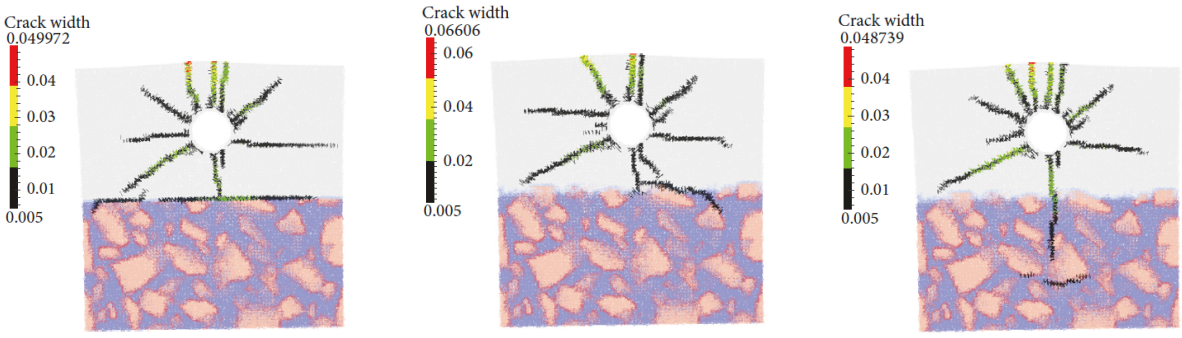

(a) Smooth Surface & $1MPa$ interface strength

(b) Rough Surface & $1MPa$ interface strength

(c) Rough Surface & $1MPa$ interface strength

Figure 2.18: Crack Pattern obtained from Lattice Model, Imposed Pressure $26MPa$ [7]

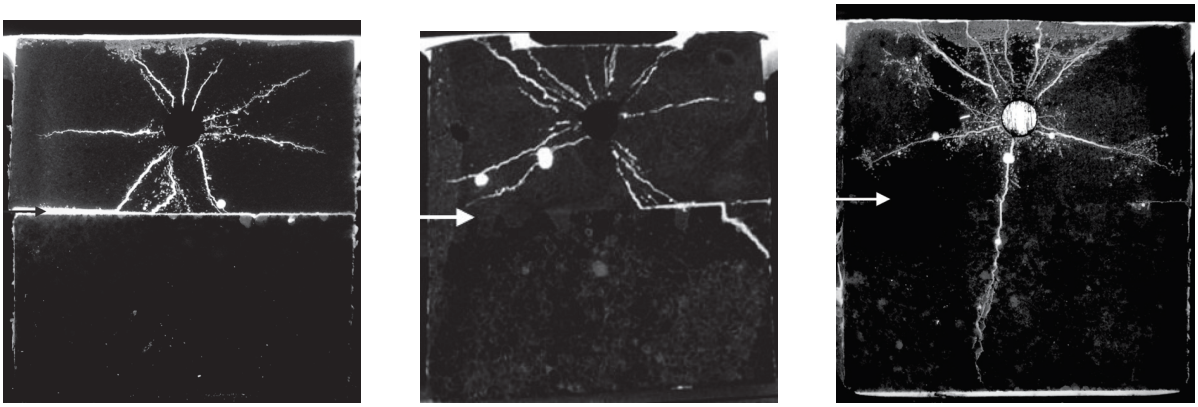

(a) Smooth Surface

(b) Rough Surface, Sample 1

(c) Rough Surface, Sample 2

Figure 2.19: Crack Pattern obtained from Experiments [7]

All of these results show that the results of lattice model are in agreement with the crack pattern of both SHCC and brittle mortar in accelerated corrosion test at micro-scale.

2.4.2. MULTI-SCALE FRAMEWORK FOR MODELING SHCC

A multi-scale framework for modeling SHCC was proposed by Kabele [11]. The main idea of this multi-scale framework is to link the global structural behavior with the micro-mechanical parameters (from micro-scale to mesoscale and finally to macro-scale) (Figure 2.22). It is based on the concept of integrated structures and materials design (ISMD): structures are to be conceptually designed so as to take full advantage of materials' properties, while materials are to be tailored to specific structural needs [37].

The author applied this concept to the scale of structural element [10]. A reinforced SHCC beam loaded in shear was simulated with finite element model (Figure 2.22f). The constitutive relation obtained at mesoscale was assigned to 2-D continuum finite elements. The stress-strain relation was calibrated from the direct tension test (linear interpolation of the upper bond of the experimental curve), which contains tensile strength f_t, ultimate tensile strength $f_{t.ult}$ and strain at peak ε_{mb}. The overall shear behavior considers the shear force carried by single fiber (micro-scale), fiber distribution orientation (mesoscale), components of strain in cracked elements (mesoscale).

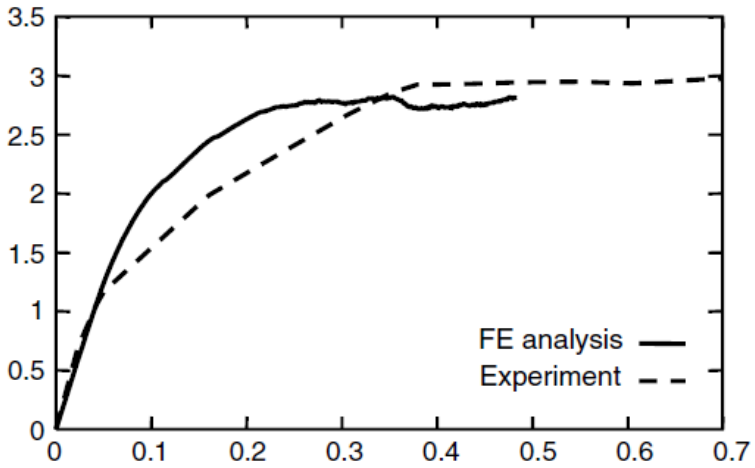

Figure 2.20: Force-Displacement Curve of SHCC Beam in Shear [10]

The model simulated the force-displacement curve of beam in shear in good manner (Figure 2.20). With regards to crack pattern, the model does produce the distributed diagonal cracks as it is in experiment (Figure 2.21 and Figure 2.22a). A conclusion can be drawn that this modelling framework can reproduce cracking behaviour of SHCC, which is very well in

line with experiment results.

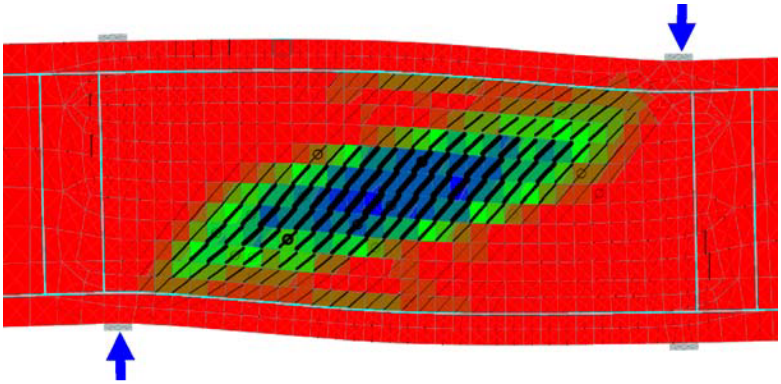

Figure 2.21: FEM Simulated Crack Pattern of SHCC Beam in Shear [10]

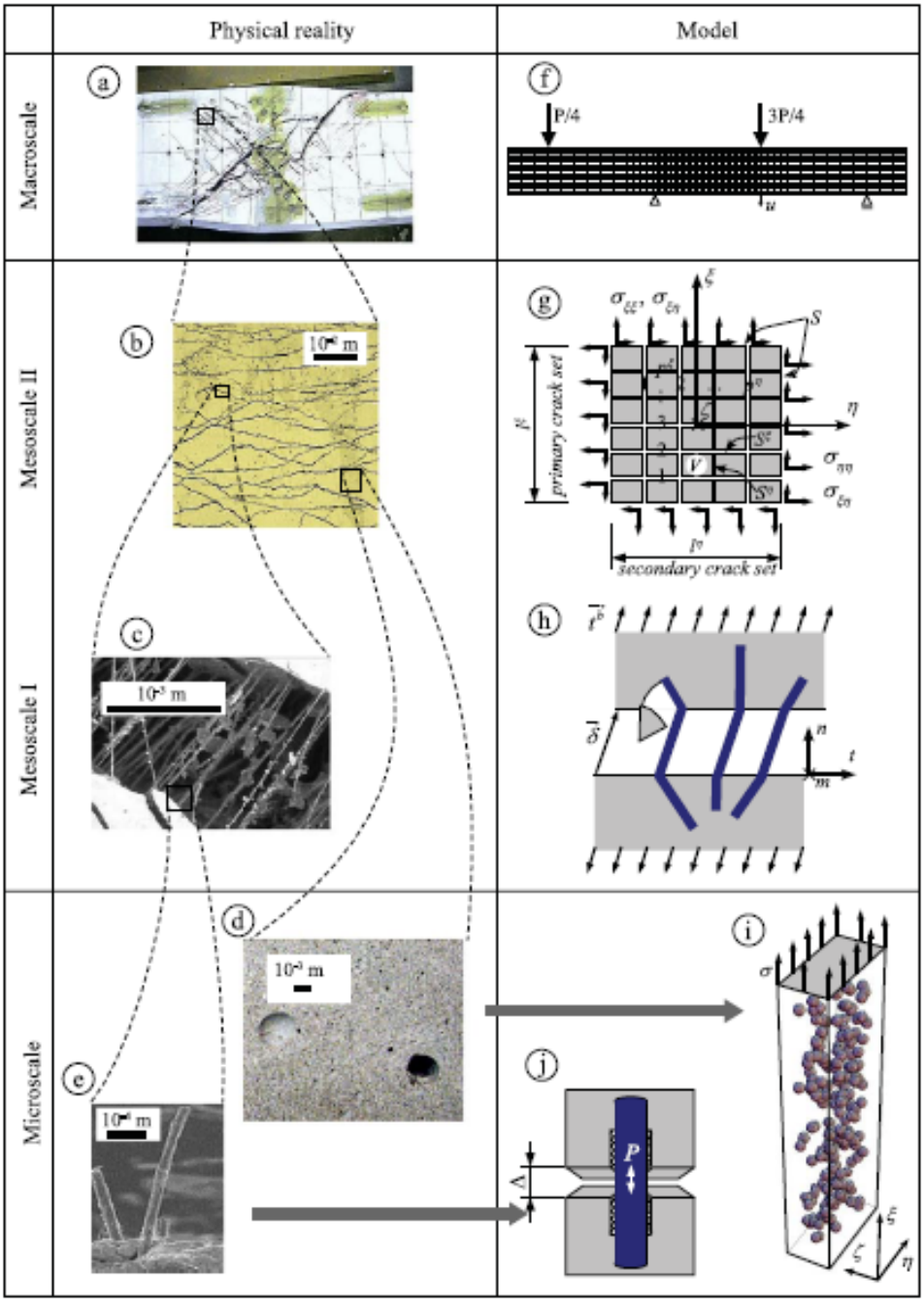

Figure 2.22: Different Scales in Modelling of fracture in SHCC [11]

2.4.3. STOCHASTIC CONTINUUM MODEL

Research done by Kabele indicates that the specimen with material SHCC has a significant size effect. Specimen size especially cross-section area has a big influence on the strain capacity of the specimens [13]. Example (Figure 2.23) shows that large specimens have a strain capacity of over 2%, while small specimens can only have a strain capacity of 0.8%.

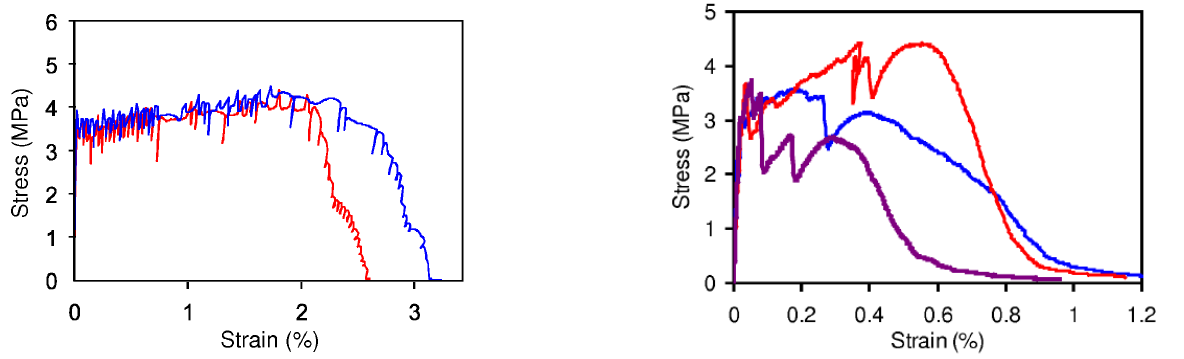

(a) Cast Dumbbell Specimens $100 \times 60 \times 400\ mm$

(b) Cut Coupon Specimens $20 \times 10 \times 200\ mm$

Figure 2.23: Direct Tension Test Results [12]

In previous models (for example in [10]), SHCC materials have been described as a homogeneous material at macro-scale. However, this type of model cannot reproduce the size effect of SHCC specimen and has difficulties in performing the distributed crack pattern. A hypothesis is that the cited phenomena can be attributed to material heterogeneity caused by uneven fiber dispersion or presence of spots with higher matrix porosity. A new stochastic method has been proposed to describe the tensile strength of SHCC [13].

A random field is a spatial variation of the tensile strength and Young's modulus to represent the heterogeneity of SHCC. The set-up process of random field follows these instructions:

- The tensile strength f_t follows the Gauss distribution with parameters given in Table 2.4.
- The spatial variation of tensile strength is described by a squared exponential autocorrelation function proposed in [38].

Table 2.4: Relevant Parameters for Random Field [13]

$f_t\ (MPa)$	COV	$d_x\ (mm)$	$d_y\ (mm)$	$\sigma_{mb}\ (MPa)$	$\sigma_1\ (MPa)$	$E\ (MPa)$
2.9	0.25	10	10	$1.241 f_t$	$0.172 f_t$	f_t/ε_c

An example of the generated random field on tensile strength is shown in Figure 2.24.

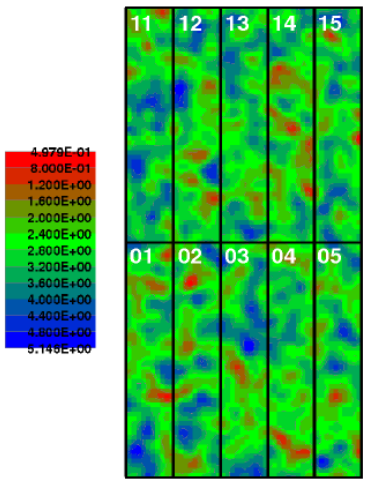

Figure 2.24: Generated Random Field on Tensile Strength [13]

Four different models in direct tension test were set up respectively: two fixed end ($20 \times 200\ mm$ and $100 \times 200\ mm$, the left two models) and two hinged end ($20 \times 200\ mm$ and $100 \times 200\ mm$, the right two models) (Figure 2.25).

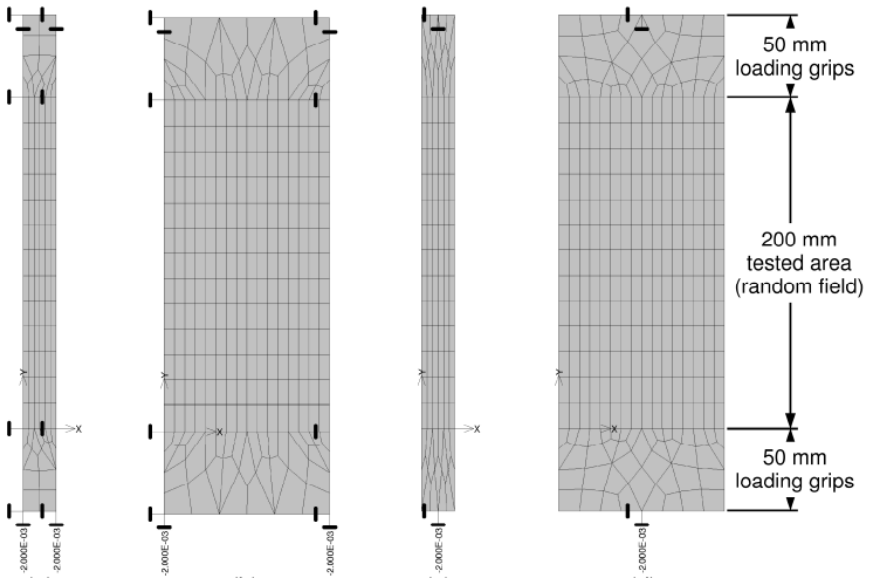

Figure 2.25: Four Models with Different Boundary Condition and Size [13]

It is shown in Figure 2.26 that the specimens with smaller size always show lower mean stress and strain capacity as well as higher variation in results than the large specimens. This size effect is more severe in the strain capacity than in the ultimate tensile strength. Also, the crack pattern generated by the models shows that the random field does have a positive effect in producing the distributed crack pattern of SHCC specimens (Figure 2.27).

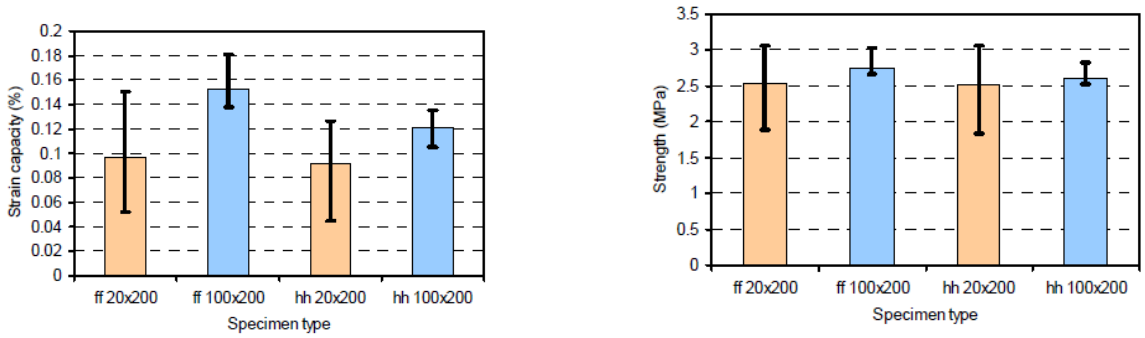

(a) Tensile Strain Capacity

(b) Ultimate Strength

Figure 2.26: Mean Value and Variation of Results from Direct Tension Simulation [12]

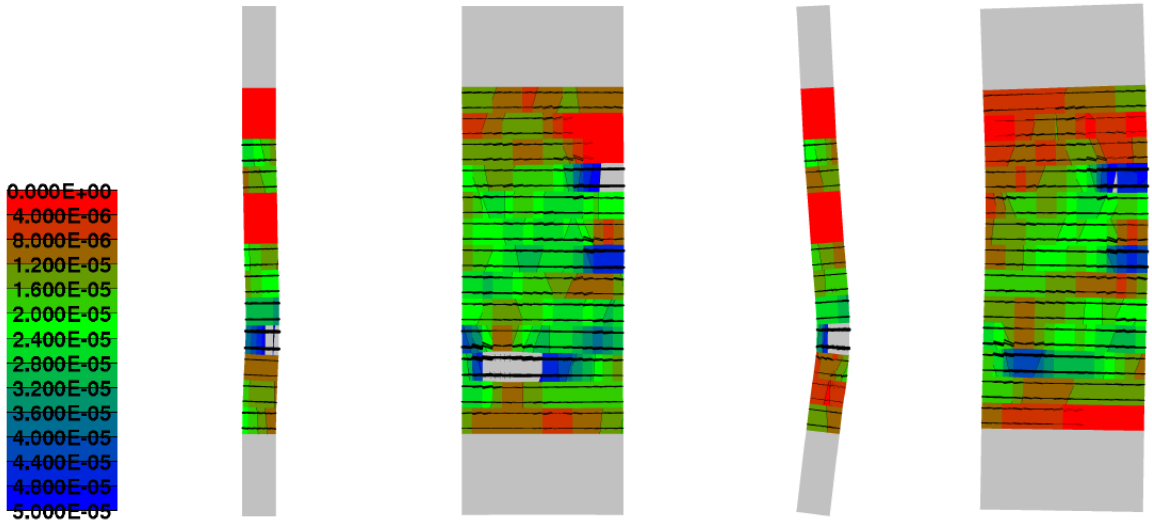

Figure 2.27: Simulated Crack Pattern of SHCC Specimens [13]

In conclusion, the random field on tensile strength can help produce the distributed crack pattern of SHCC in the direct tension test. Also, the size effect of SHCC under direct tension can be simulated using a random field on tensile strength.

3

CONTINUUM MODEL

In this chapter, a series of 2D continuum models with plane stress elements were developed and analyzed to investigate parameters that may influence the accuracy of simulating the cracking behavior of fiber reinforced concrete in accelerated corrosion test. In this chapter, the material with least volume of fibers as repair mortar are investigated first. This material (ON06) has the least fiber volume among the five repair mortars, which can be regarded as normal concrete without fibers.

3.1. PRELIMINARY MODEL

3.1.1. MODEL SET-UP

A preliminary model with material ON06 as repair mortar is developed at the beginning. Symmetry is applied to simplify the model. The width and height of the model is 200 mm and 226 mm. Symmetry is applied in this model to simplify the model. Due to the symmetry applied in this model, a constraint in the x direction is applied along the symmetric axis. Meanwhile, the bottom edge is constrained in the y direction.

In the accelerated corrosion test, the corrosion of the reinforcement is accelerated by the current applied on the rebar. The corrosion product is performed uniformly around the rebar, which results in a uniform expansion of the volume of the reinforcement. This expansion causes stresses on surrounding concrete. In order to simulate this loading condition, three load methods are proposed: prescribed displacement, prescribed strain, and

prescribed force. The prescribed displacement is a displacement control method, by which the uniform expansion of the rebar is simulated. However, after the cracking of surrounding concrete, the corrosion products can penetrate into the cracks, which results in a non-uniform expansion of the reinforcement. Therefore, prescribed strain and prescribed force method are proposed to apply a uniform force instead of displacement around the rebar. The influence of different loading conditions will be discussed later. In this preliminary model, a prescribed displacement is applied as the load.

A semicircular void is made in the model with a radius of 18 mm to represent the steel rod. In order to simulate the uniform expansion caused by the corrosion of the steel rod, a unit prescribed deformation of 1 mm is applied along the radial direction. Quadratic plain stress elements are used. A fine mesh area with 48 mm radius is defined with 0.5 mm mesh size. 2 mm mesh size is applied for the other parts of the model. A schematic view of the model is shown in Figure 3.1.

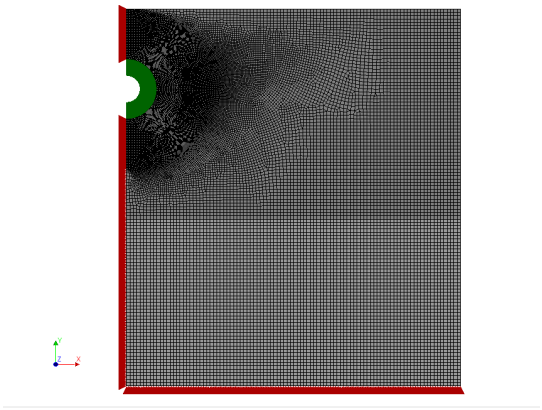

Figure 3.1: Schematic View of Preliminary Model

As explained in the laboratory report, the fibers in material ON06 do not have a significant contribution because of its low volume in the mixture. Therefore, material ON06 can be regarded as normal concrete. The tensile behavior of the material is defined using a tension-softening relation proposed by Hordijk [35]. The substrate is also defined with this relation. The property of C30 concrete adopted from Eurocode 2 is applied as the property of substrate [39]. Whether the strength of the substrate influences the cracking behavior of the model will be examined later. Detailed material properties are shown in Table 3.1. Then, a nonlinear analysis is carried out using the Regular Newton-Raphson method.

Table 3.1: Preliminary Model Material Property

Material	E (GPa)	f_t (MPa)	f_c (MPa)	G_h^I (N/mm)
Substrate	20000	2.4	30	0.12
ON06	37950	2.89	49.1	0.15

3.1.2. CRACK DEVELOPMENT

In the following figures, the development of this model's damage pattern is displayed in crack width. In total, 100 steps with load factor 0.01 per step are simulated. The first crack is localized at the top at step 2. This is due to the thinnest concrete cover at the top. Moreover, due to the thin concrete cover in this area, the concrete is damaged in bending instead of tensile failure. Along this crack, the area close to the top edge is wider than the area close to the rebar. This behavior can also be observed in the experiment. Then, two secondary cracks are developed simultaneously along 1 and 5 o'clock direction (Figure 3.2b and 3.2c). Meanwhile, the top crack is still widening. There is a cone area at the top between the top crack and the secondary crack being pushed out. It is the critical area in this model. Finally, at step 40 the maximum crack width at the top reaches the level of 1 mm, which equals to the maximum crack width observed in the experiment.

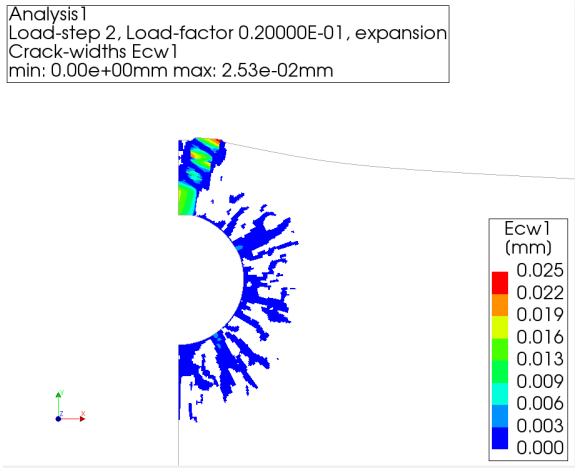

(a) Step 2

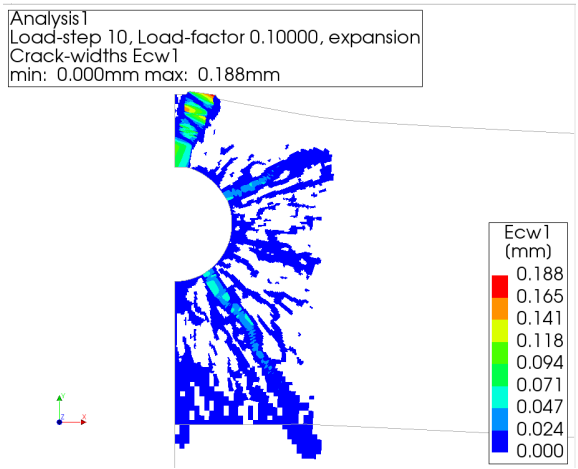

(b) Step 10

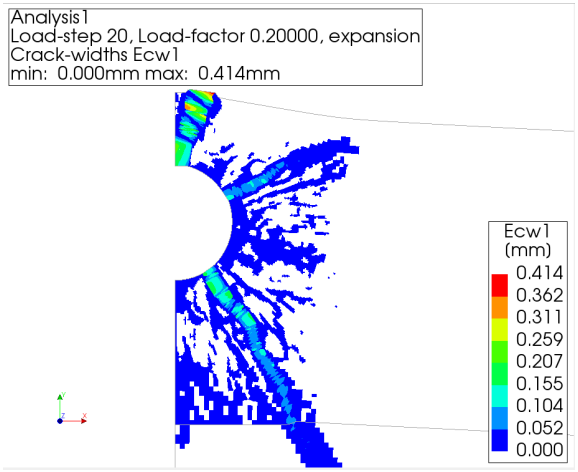

(c) Step 20

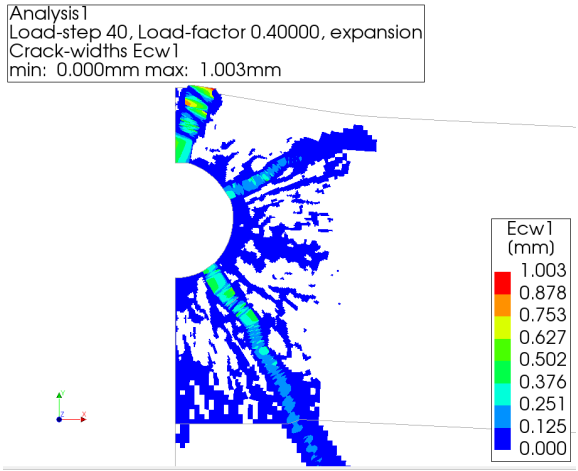

(d) Step 40

Figure 3.2: Crack Width of Preliminary Model

Figure 3.3a and 3.3b show also the crack width at step 40 as Figure 3.2d. The difference is that they are animated to 0.5 mm and 0.3 mm respectively. Figure 3.3c shows the damage pattern obtained by CT scanning of experiment specimen. The substrate of the specimen is cut off after experiment and sent for CT scanning. In general, the result of the continuum model is similar to experimental results. The maximum crack width is located at the top in the continuum model. From Figure 3.3b, a crack along 2 o'clock direction can be observed with a maximum crack width of 0.3 mm and the major part around 0.1 mm. The main difference between the continuum model and experiment happens at the bottom crack. Although the maximum crack width of this crack is at a similar level (0.5 mm), the direction of this bottom crack is more inclined instead of going straight downwards. This is probably due to the boundary condition at the bottom edge. In the experiment, the specimen is soaked into the water out of the current plane. Therefore, with the constraint in the y direction in this model, the stiffness along y direction has been increased. This may result in the inclined bottom crack. Moreover, some elements around the rebar are observed to be damaged tangentially in Figure 3.3b. The reason for this tangential damage will be investigated in later sections.

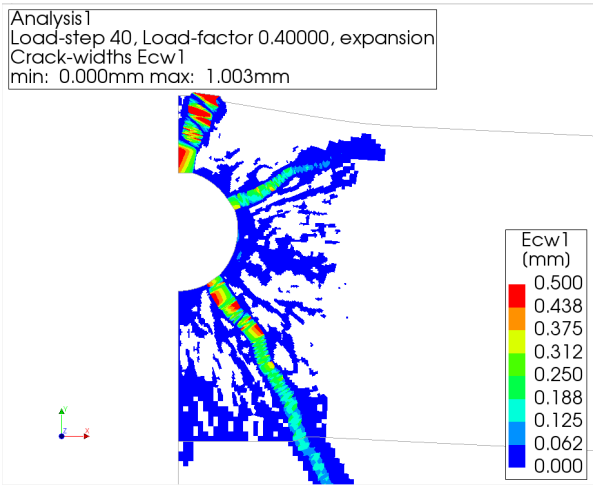

(a) Step 40 animated to 0.5 mm

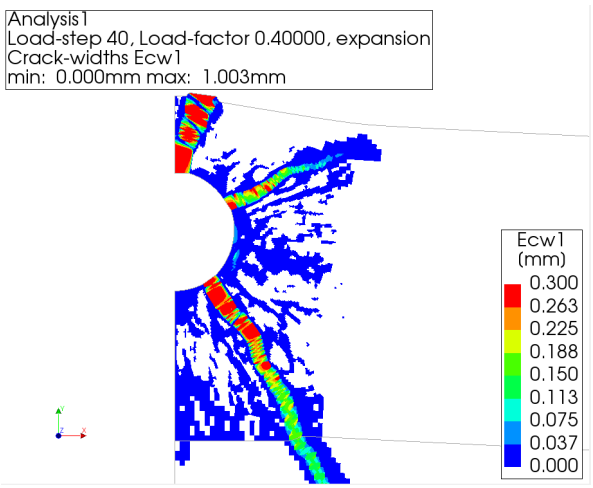

(b) Step 40 animated to 0.3 mm

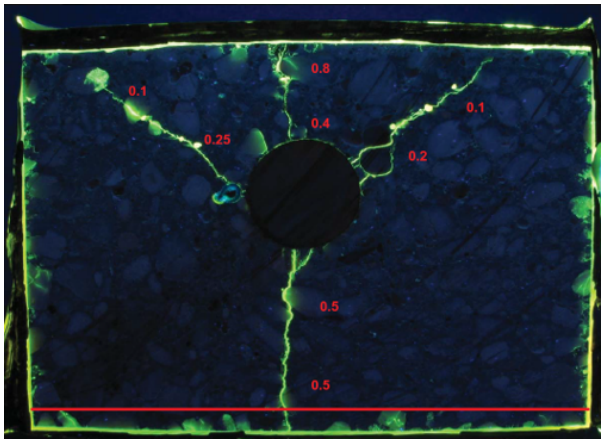

(c) Experiment

Figure 3.3: Comparison of Crack Pattern

3.2. BOTTOM EDGE BOUNDARY CONDITION

3.2.1. FREE BOTTOM EDGE MODEL

In order to investigate the influence of the bottom edge boundary condition on the bottom crack direction, a continuum model is developed with a free bottom edge based on the preliminary model. Except for the boundary conditions, the loading condition, mesh, and material properties are kept identical to the preliminary model. The detailed set-up of the model is shown in Figure 3.4.

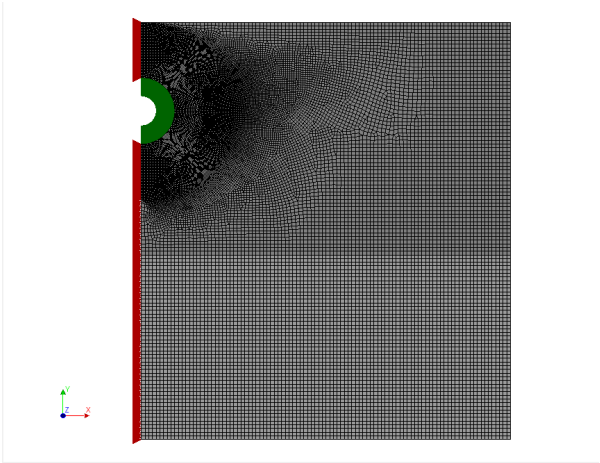

Figure 3.4: Free Bottom Edge Model

3.2.2. CRACK DEVELOPMENT AND COMPARISON

The development of the crack pattern is shown in Figure 3.5 as a contour of the crack width. The development of the cracks in this model is very similar to the preliminary model with a constrained bottom edge. The first crack at the top is localized at step 3. At the 9th step, two secondary cracks are initiated simultaneously. Meanwhile, the top crack is continuously widened with the increase of load. However, the tangential crack is initiated again at step 18. This is neither observed in experiment nor explained by any physical meaning. This crack is probably a result of the loading condition. With prescribed displacement, the rebar is defined to expand uniformly which means that the tangential deformation around the void is constrained. This may be the reason for the tangential crack. Finally, at step 62, the maximum crack width reach 1.005 mm (experiment level).

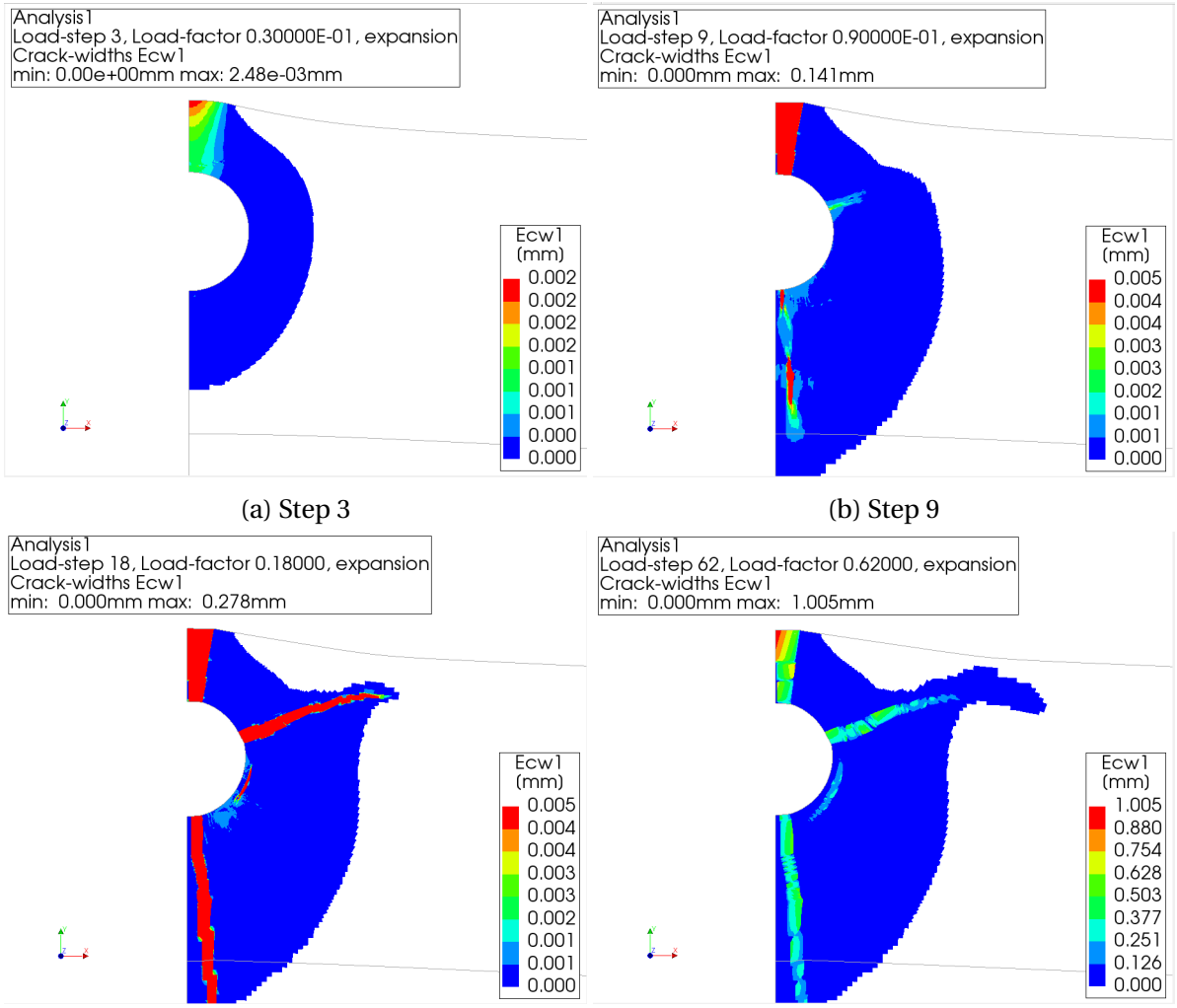

(a) Step 3 (b) Step 9

(c) Step 18 (d) Step 62

Figure 3.5: Crack Width of Free Bottom Edge Model

Figure 3.6 shows a comparison of the free bottom model, constrained bottom model, and experiment. In general, the free bottom model result corresponds to the experimental results better than the constrained bottom model. The top crack in the free bottom model follows the "bending crack" behavior (wide at the edge, thin at rebar). Meanwhile, the secondary cracks are developed following the tension caused by the corrosion of rebar (wide at rebar, thin at the end). However, it can be observed in Figure 3.5d that the maximum crack width of the 2 o'clock crack is at around 0.5 mm, which is twice of the experiment level. This is probably due to the loading condition in this model. With prescribed displacement, the tangential displacement around the void is pre-defined. So the pressure loaded in this secondary crack area cannot be decreased due to the development of other cracks. This results in a wider secondary crack than the experiment. Therefore, the influence of the

loading condition will be investigated in the next section.

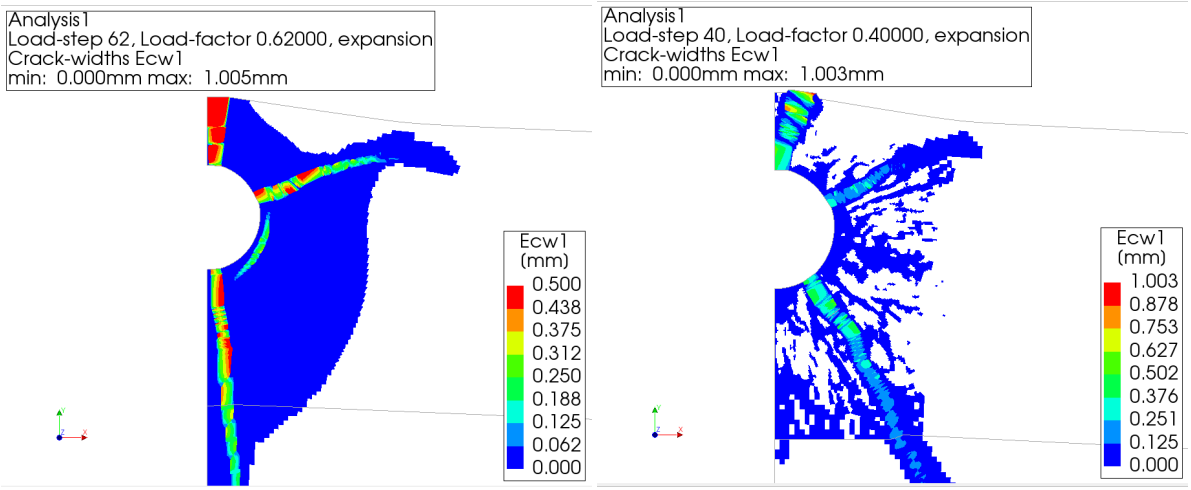

(a) Free Bottom Edge Model, animated to 0.5 mm

(b) Constrained Bottom Edge Model

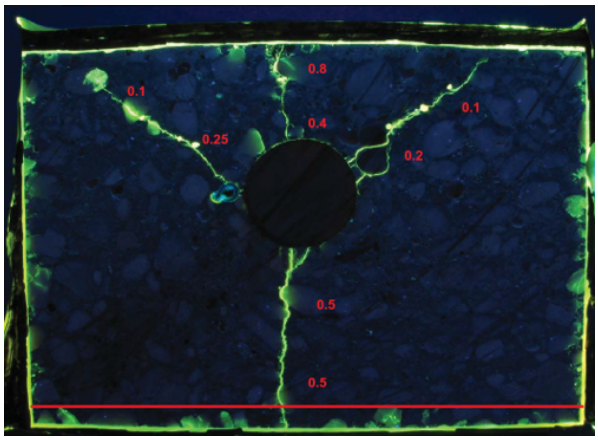

(c) Experiment

Figure 3.6: Comparison of Crack Pattern

Moreover, comparing to the constrained bottom model, the bottom crack develops more straight downwards in the free bottom model. This proves the assumption that the direction of the bottom crack is sensitive to the boundary condition at the bottom edge. Keeping the bottom edge free is a better option to simulate the accelerated corrosion test. However, this sensitiveness of bottom crack direction implies that the boundary settings in the accelerated corrosion experiment may not represent the cracking of the concrete floor due to rebar corrosion in the tunnel correctly. In the floor, the tested area is supported by the surrounding concrete. This means that the crack pattern obtained from the laboratory test may not correspond to the real scenarios in the Maastunnel. Therefore, constrained bottom and side edges are advised for further accelerated corrosion tests to simulate the

cracking behavior of the concrete floor due to ongoing rebar corrosion.

3.3. LOADING CONDITION

In the crack pattern generated by the model loaded with prescribed displacement, a tangential crack has been observed (Figure 3.3b and 3.6b). The crack width of the secondary crack along 2 o'clock direction is overestimated. This might be a result of the loading condition of the free bottom model. With the prescribed displacement load, the displacement field around the void is pre-defined with uniform expansion. However, in this way, the deformation along the tangential direction is constrained. This might be the reason why the model produces a tangential crack which cannot be explained by any physical behavior. This implies that prescribed deformation may not be an accurate way to describe the loading condition in the accelerated corrosion test. In order to verify the assumption and exclude the influence of the loading condition, a sensitive test on loading condition is conducted. In the experiment, although the rod was corroded uniformly, the pressure caused by the rust layer are not identical around the void. This is because of the rust getting into opened cracks as well as different concrete cover depth around the reinforcement. Also, the expansion of the rebar becomes non-uniform after cracking due to the penetration of rust into localized cracks. Based on these, the prescribed displacement load is arguable.

3.3.1. THERMAL LOAD MODEL

Another model loaded with thermal load is developed in this section. With the corrosion of reinforcement, the volume of the reinforcement increases and results in the increase of pressure on the surrounding concrete. Similarly, an increase in temperature can also result in the increase in the volume of the steel rod and then produces pressure on the surrounding concrete. Therefore applying an increasing thermal load over the area of elements with the material property of steel is an indirect way of applying prescribed force load on the structure.

In order to load the model with increasing temperature, the void in the previous model is filled with plain stress elements with 10 mm element size. These elements are assigned

with the material property of steel with a linear elastic relation. In order to let the steel rod expand with increasing temperature, a thermal expansion coefficient (α) of 1 is applied to this material. The properties of the materials in this model are listed in Table 3.2.

Table 3.2: Thermal Load Model Material Property

Material	E (GPa)	f_t (MPa)	f_c (MPa)	G_h^I (N/mm)	α
Substrate	20000	2.89	49.1	0.15	/
ON06	37950	2.4	30	0.15	/
Steel	200000	/	/	/	1

In order to compare with the prescribed displacement load model in Section 3.2, the bottom edge of this model needs to be kept free. However, there will be rotational displacement after cracking, and it will influence the stability of the calculation. Therefore, a constraint in the y direction is applied at the bottom left node for practical use. All the other settings of the model are identical to the prescribed deformation model. A schematic view of this model is shown in Figure 3.7. Meanwhile, ambient time dependency of temperature is applied to the steel rod in order to realize the incremental thermal loading in DIANA, in which temperature increases with time development (Figure 3.8). The load step in this model is defined as time steps. The ambient time dependency of temperature follows a linear relation (Figure 3.8).

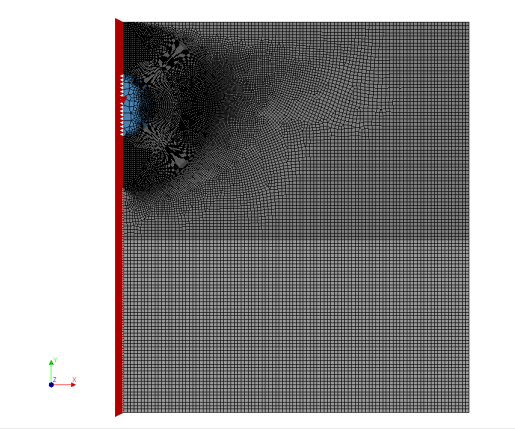

Figure 3.7: Schematic View of Thermal Load Model

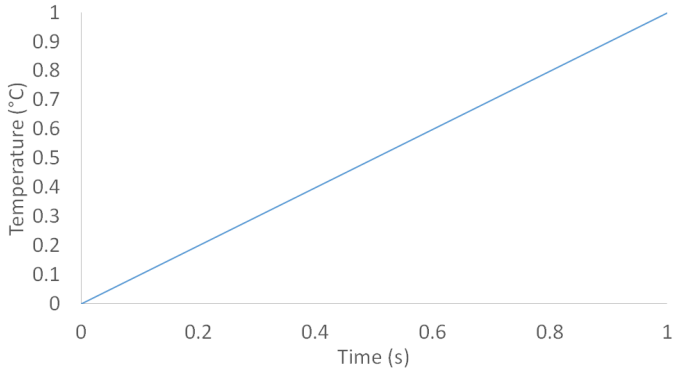

Figure 3.8: Ambient Time Dependency of Temperature

3.3.2. CRACK DEVELOPMENT

This model is loaded with 100 time steps and 0.0002s per step. Figure 3.9 and 3.10 show the development of the crack pattern of the model with thermal load. In general, the crack development of the thermal load model is very similar to the model loaded with prescribed displacement. The first crack is developed and localized at the top at step 16 (Figure 3.9a). At step 20, a secondary crack at bottom is localized (Figure 3.9b). Then at step 22, another secondary crack at 2 o'clock direction is developed (Figure 3.10a. These two cracks are developed more or less simultaneously. The same behavior can also be observed in the prescribed displacement load model.

However, at step 30 two cracks along 4 o'clock direction are developed, and one of them keeps developing in the following steps. As this crack along 4 o'clock gets close to the mortar-substrate interface, there are some elements damaged at the interface and showing de-bonding behavior (Figure 3.10c). This behavior is discovered only in this model. This is probably because of the symmetry condition applied in this model. By releasing the tangential deformation in the model, it is easier to initialize more cracks in this thermal load model (Figure 3.10c). Instead of being further developed, they should show the trend to join those major cracks near them. However, in order to apply symmetry in this model, a fictitious constraint in the x direction is defined along the left edge. This fictitious constraint limits the development of bottom crack and results in the opening of the crack along 4 o'clock direction. After it gets close to the mortar-substrate interface, the stress will be more concentrated at the interface and cause the de-bonding behavior. Finally, at step 75, the maximum crack width reaches the experiment level (0.995 mm).

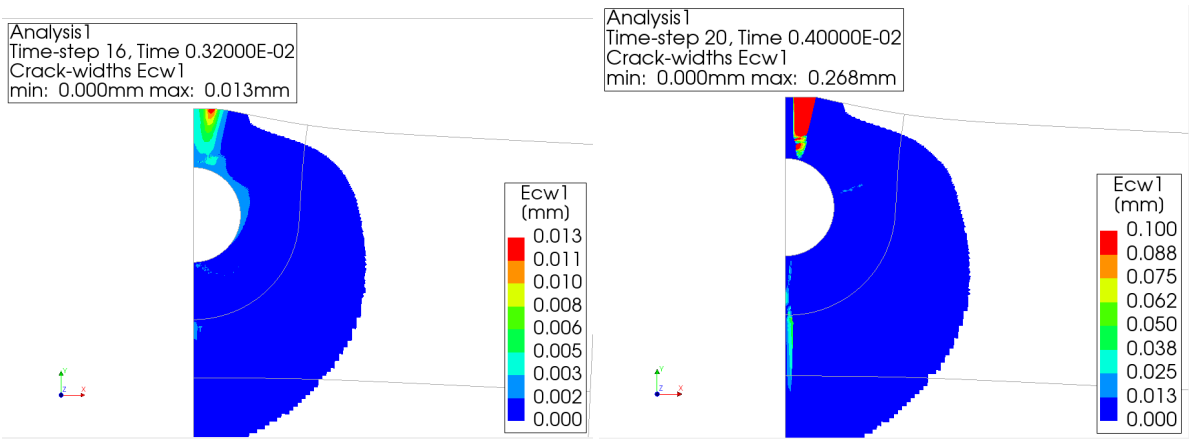

(a) Step 16 (b) Step 20

Figure 3.9: Development of Cracks, Thermal Load Model (1)

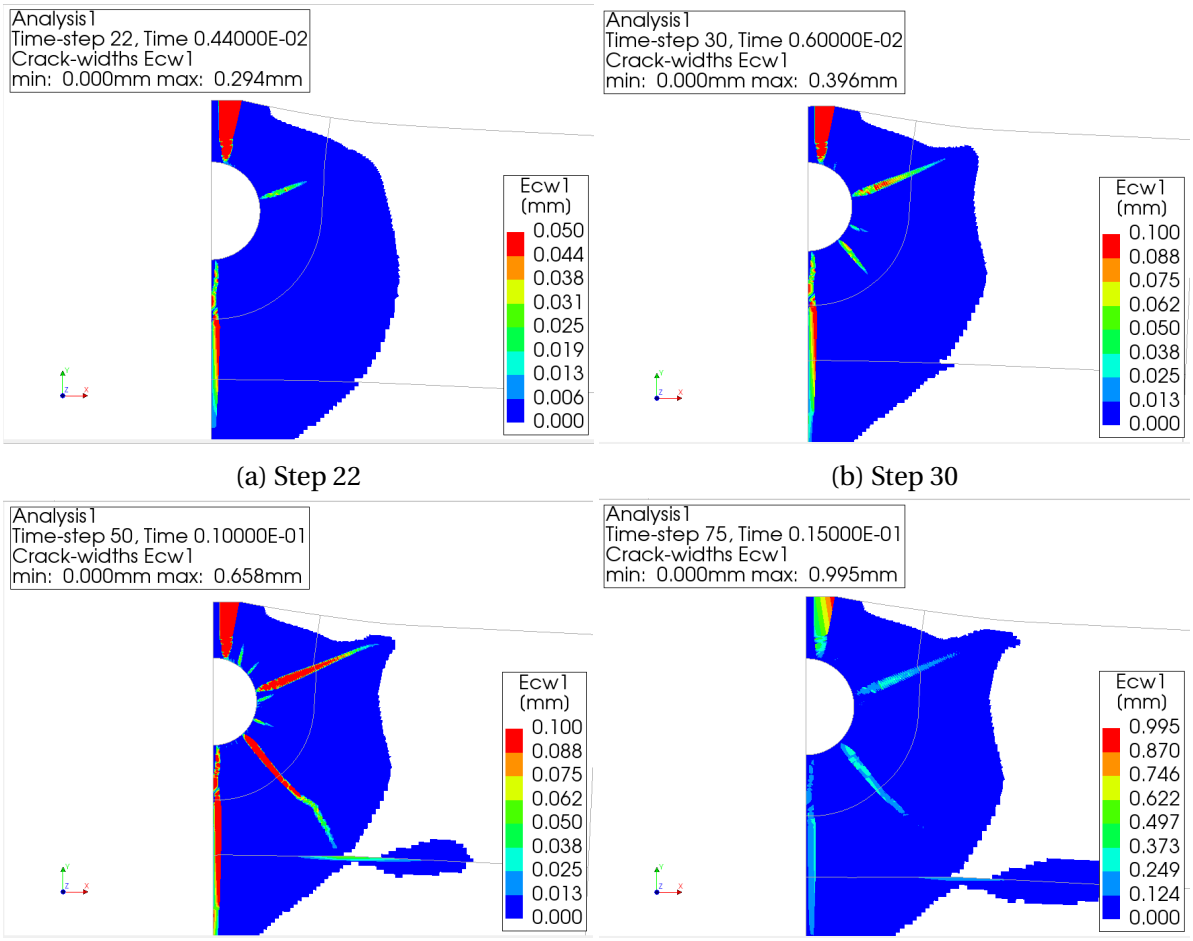

(a) Step 22

(b) Step 30

(c) Step 50

(d) Step 75

Figure 3.10: Development of Cracks, Thermal Load Model (2)

Figure 3.11 shows a comparison of damage pattern between thermal load model and experiment. Figure 3.11a shows the crack width of thermal load at step 75 (same as Figure 3.10d) and they are animated to 0.5 mm and $o.3$ mm respectively. Figure 3.11c shows the damage at step 62 of prescribed deformation model (animated to 0.5 mm). Compared to the displacement control model, this thermal load model has several improvements. The tangential crack in the prescribed displacement model is not presented anymore. This proves the assumption that the presence of this tangential crack is due to the prescribed uniform tangential deformation. By loading the model with thermal expansion, the expansion of the rebar is non-uniform which means that the tangential deformation is released. Moreover, by releasing the tangential constraint, quite some microcracks are developed and joining the major cracks near them. This behavior which is an extra benefit of thermal load can also be observed in the experiment. Meanwhile, the maximum crack width of the secondary

cracks in the thermal load model is at the level of 0.3 mm, which is smaller than that of the prescribed displacement model (0.5 mm). This is due to those micro cracks around the steel rod. Through these cracks, some pressure is released and therefore the crack width of those secondary cracks decrease. In conclusion, this thermal loading condition is more accurate than the prescribed displacement.

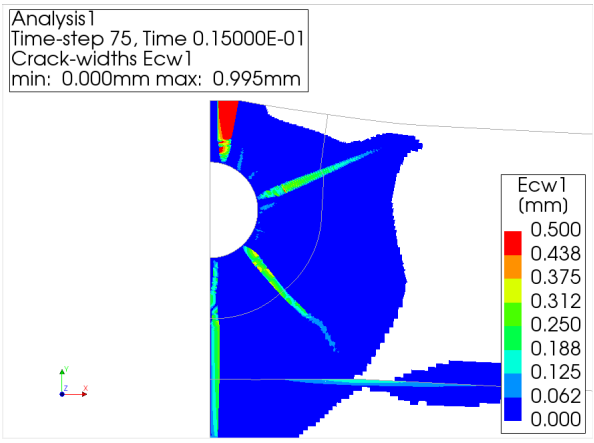

(a) Thermal Load Model, Animated to 0.5 mm

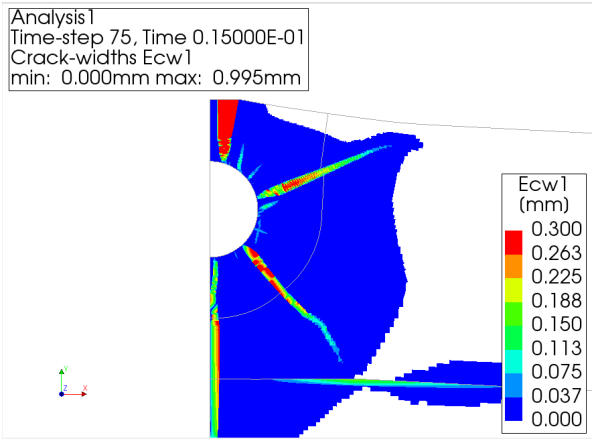

(b) Thermal Load Model, Animated to 0.3 mm

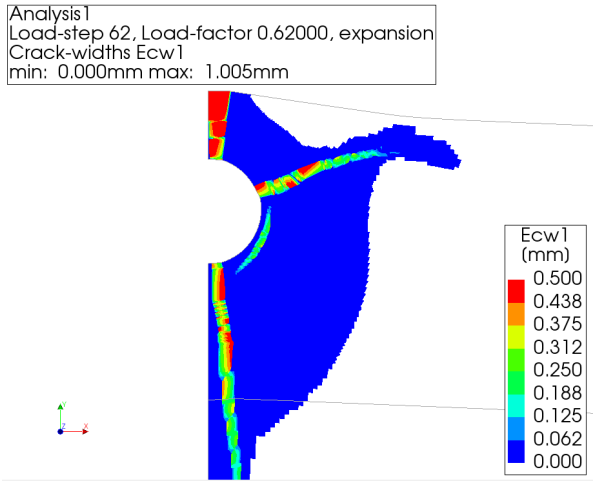

(c) Prescribed Displacement Model, Animated to 0.5 mm

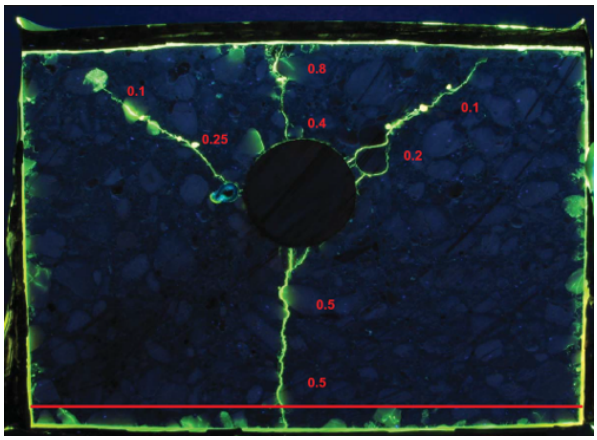

(d) Experiment

Figure 3.11: Comparison of Damage Pattern

However, in this thermal load model, the secondary crack along 4 o'clock shouldn't be developed further and cause the de-bonding problem. Also, its development also limits the widening of the bottom crack. In Figure 3.11b, there are more elements in the inclined crack over the bottom crack reach 0.3 mm crack width. As explained, this is probably due to the symmetry constraint at the left edge. By using the fictitious constraint for symmetry,

the stiffness in this area is higher than the real case which results in the limitation in developing of bottom crack and the development of the inclined crack. Meanwhile, by defining symmetry, a vertical crack along the center line of the model is pre-defined. However, in the real case, the top and bottom cracks are not always developed straight due to the heterogeneity of concrete. Also, the top and bottom cracks in continuum model are not located exactly at the symmetry edge, which indicates that there will be two cracks instead of one localized at the top if a full model is built. Therefore, the influence of symmetry on crack pattern needs to be further investigated. Another possible explanation is still due to the loading condition. Thermal load is an indirect way of loading on the model. A prescribed strain is applied to the steel rod. After the initialization of the inclined bottom crack, this crack will be kept widen due to the prescribed strain. This can be improved by loading the model with the prescribed force (direct force control). However, due to the symmetry of this model, prescribed force load will cause a stress concentration problem at the support. Because the prescribed force cannot be self-balancing in this case. The prescribed force load is possible with the full model. Therefore, this will be examined in the next section also.

3.4. INFLUENCE OF SYMMETRY

In the previous models, Symmetry is implemented to simplify the models. To define symmetry, a fictitious constraint in x direction has to be applied at the left edge. However, an inclined crack at bottom and de-bonding is observed besides the vertical bottom crack in the model in Section 3.3. The fictitious symmetry constraint is a possible reason that causes this behavior. A crack in the middle of the model is also predefined by applying symmetry. Based on the experimental results, this is not always true. Therefore, applying symmetry may not be an accurate method to simulate this test. In order to investigate the assumption, a full model without symmetry is studied in this section.

3.4.1. FULL THERMAL LOAD MODEL

A full model is developed based on the model with symmetry in Section 3.3. In the full model, the width of the model is 400 mm instead of 200 mm. Meanwhile, the constraint

in the x direction at the symmetry line is released. Although the thermal load itself is self-balancing, there will be some rotation after the opening of cracks. Therefore, for the stability of the calculation, the full model should be simply supported at the bottom edge. All other settings (including material property, mesh setting, element type, and load steps) are kept identical to the symmetry model in Section 3.3. A schematic view of the models is shown in Figure 3.12.

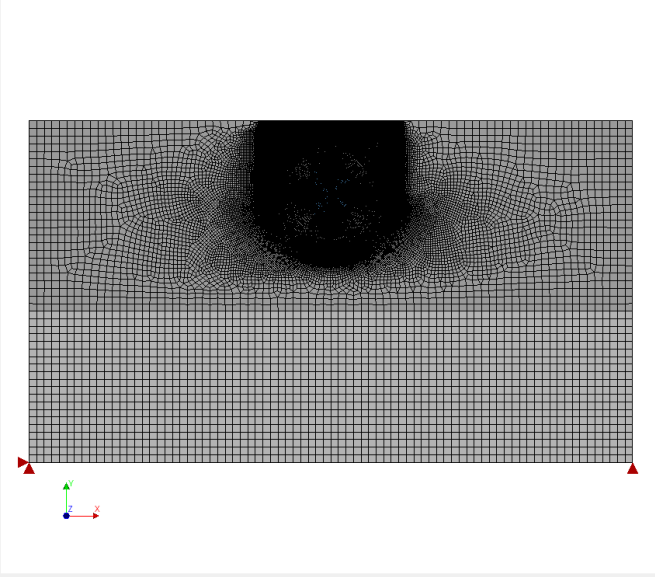

Figure 3.12: Schematic View of Full Thermal Load Model

3.4.2. DEVELOPMENT OF CRACKS

Figure 3.13 shows the comparison of the development of cracking in the full thermal load model and the symmetry model. The damage pattern of the symmetry model is listed on the left, and the full model's results are listed on the right. Both models are developed following a similar trend in general. In the full model, one top crack is localized at step 13. However, this crack is not continuous. Because the crack is localized from both top and bottom and they do not meet each other in the middle. The same behavior can also be discovered in some other experiments. At step 19 (Figure 3.13d), the bottom crack in full model is developed to 0.1 mm. Then at step 22, two more secondary cracks are developed along 10 and 2 o'clock direction (Figure 3.13f).

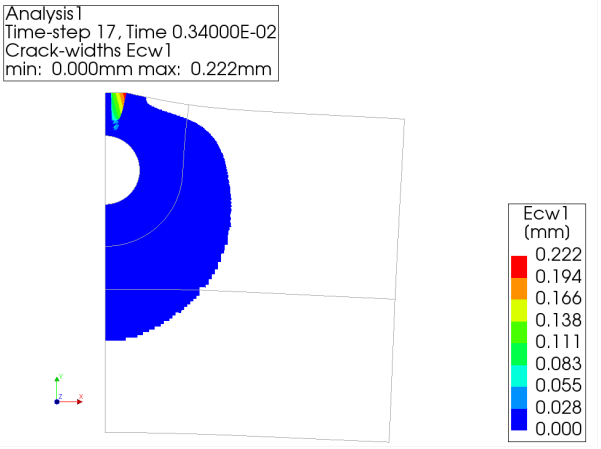

(a) Step 17, Symmetry Model

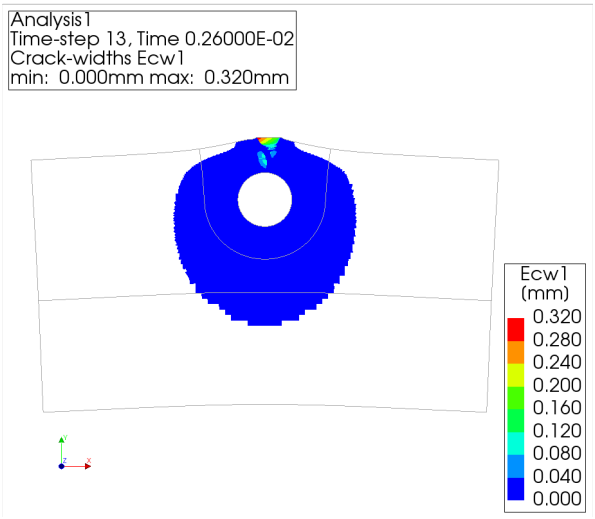

(b) Step 13, Full Model

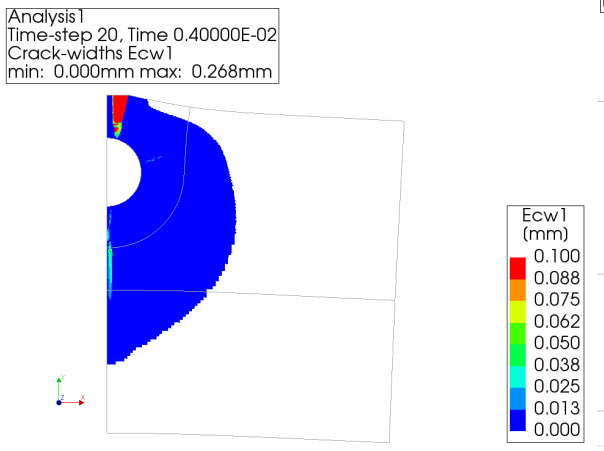

(c) Step 20, Symmetry Model

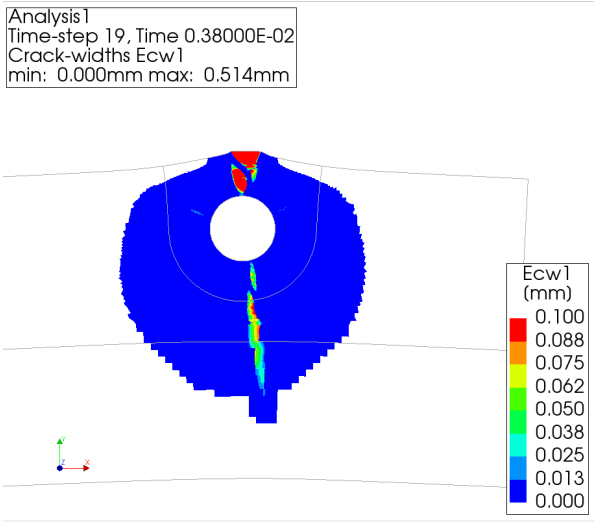

(d) Step 16, Full Model

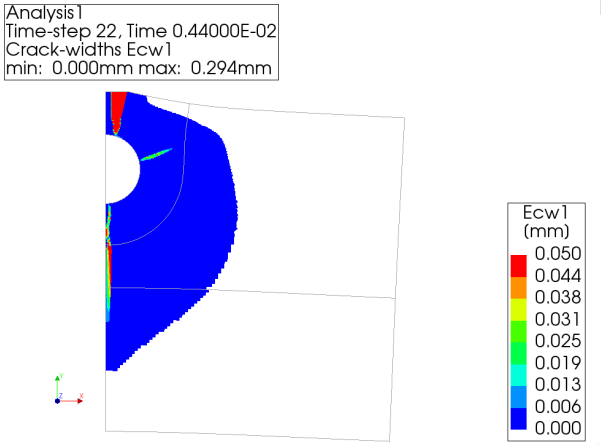

(e) Step 22, Symmetry Model

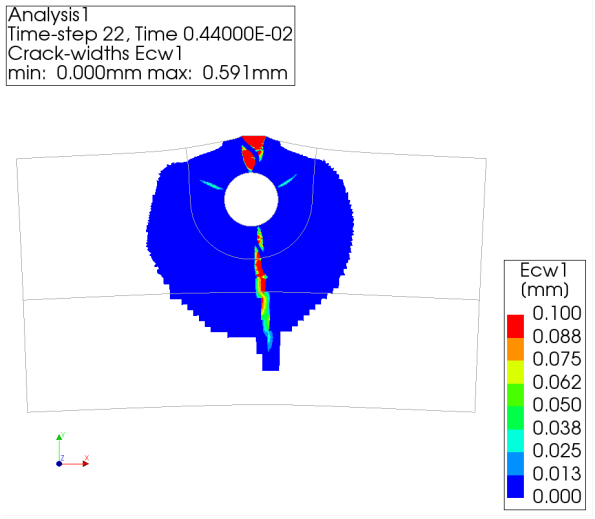

(f) Step 22, Full Model

Figure 3.13: Comparison of Full Model and Symmetry Model

At step 28 of the full model, two inclined top cracks and the bottom crack are developed further. Meanwhile, there are some micro cracks developed around the reinforcement. Especially, the microcrack along 8 o'clock direction has the trend to be developed further(Figure

3.14b), and it can be proved in step 50 that the crack indeed develops further (3.14d). The same behaviour is discovered also in symmetry model (Figure 3.14a and Figure 3.14c). This is probably because of the development of the top inclined cracks. The top cracks along 10 and 2 o'clock direction are developed close to the top edge of the model, which release the stress concentrated in that area. Then, the inclined crack along 4 o'clock is initialized and developed. Another secondary crack at the top in Figure 3.14d is also evidence of this explanation. Therefore, the result after step 30 in the symmetry model and step 28 in the full model are not comparable with experimental results. Because in the experiment, none bottom inclined cracks can be observed (Figure 3.15d). Meanwhile, another possible parameter can influence the developing of this inclined bottom crack is the loading condition. After the initialization of the inclined bottom crack, this crack will be kept widen due to the prescribed strain brought by this thermal load.

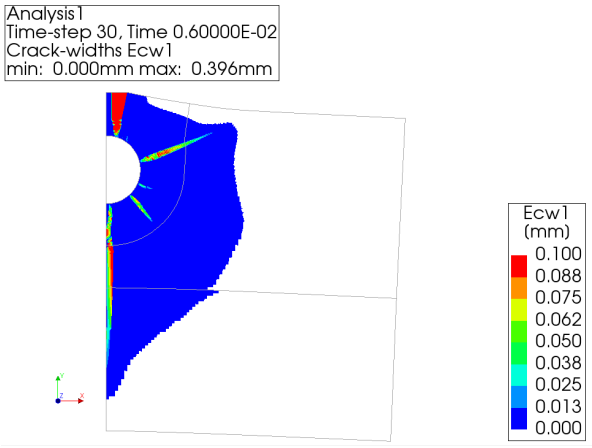

(a) Step 30, Symmetry Model

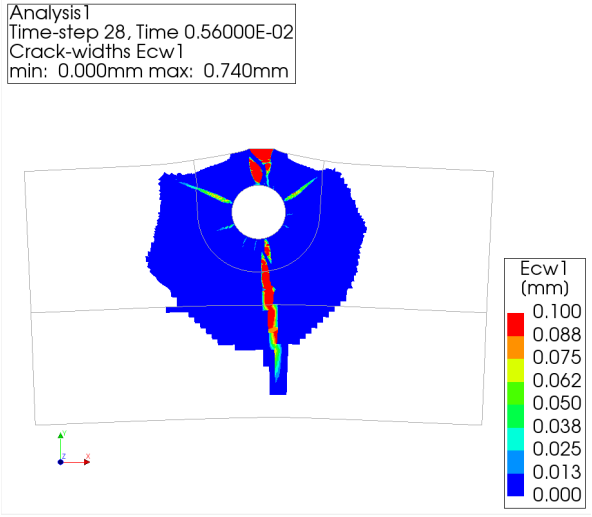

(b) Step 28, Full Model

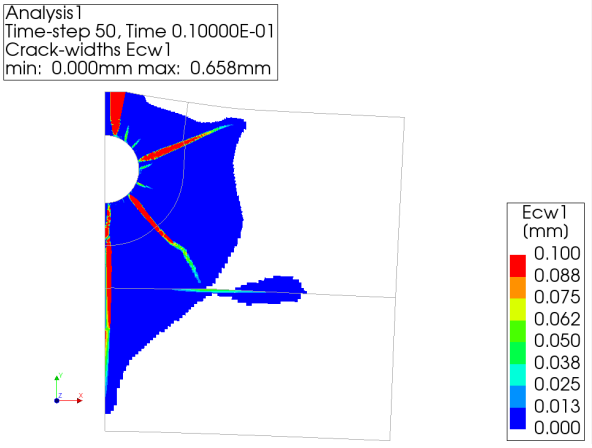

(c) Step 50, Symmetry Model

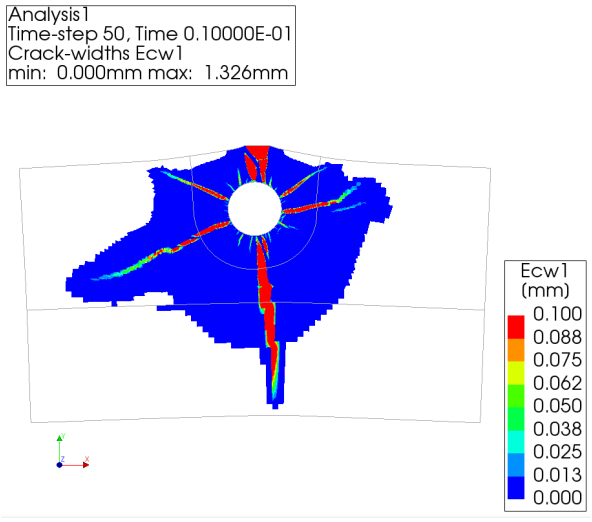

(d) Step 50, Full model

Figure 3.14: Development of Bottom Inclined Crack

In general, the application of symmetry does not influence major crack pattern. However, there are several differences can be observed that brought by symmetry. First, the maximum crack width of the symmetry model is always at around $0.48 - 0.53$ at same step (same load level) of that in the symmetry model. Also, the top crack in the symmetry model is not exactly at the symmetry line. There is another column of undamaged elements between the crack and the symmetry line. Therefore, the top crack is separated in two by defining symmetry. This also explains why the maximum crack width of the symmetry model is only half of the full model. Moreover, after the inclined bottom crack gets close to mortar-substrate interface in the symmetry model, it develops more downwards to the interface. In contrast, this inclined crack in the full model is developed more horizontal when it gets close to the mortar-substrate interface. This verifies the assumption that the cracking in the mortar-substrate interface is due to the inclined crack getting close to the interface. Although the result at this step is not comparable with the experiment, this behavior is another observation of the influence caused by the symmetry condition. Therefore, applying symmetry is not appropriate in simulating this accelerated corrosion test and a full model is advised.

However, even with the full thermal load model, the maximum crack width cannot reach the experiment level. The analysis is not comparable to the experiment after the localization of the inclined second bottom crack. As explained, this is probably connected with the indirect force control loading condition in this model. Therefore, this will be investigated in the next part.

Meanwhile, convergence is always a problem for the continuum model with a nonlinear analysis in simulating strain-softening material. Due to the thermal load (prescribed strain), displacement norm (0.01) in this model is relatively easy to reach. Thermal load is a displacement control method because it can be regarded as a prescribed strain. However, the force norm (0.01) cannot be satisfied since the first step of the analysis. Until step 28, the relative difference in force is lower than 0.1 which still can be regarded as acceptable. The crack pattern at this step (Figure 3.15a still corresponds to the experiment in a proper manner. This implies that the model with thermal load can still provide a good simulation of damage pattern despite the convergence problem. The model loses its convergence due to the localization of the second inclined crack. Thus, step 28 is the final reasonable step of

this model.

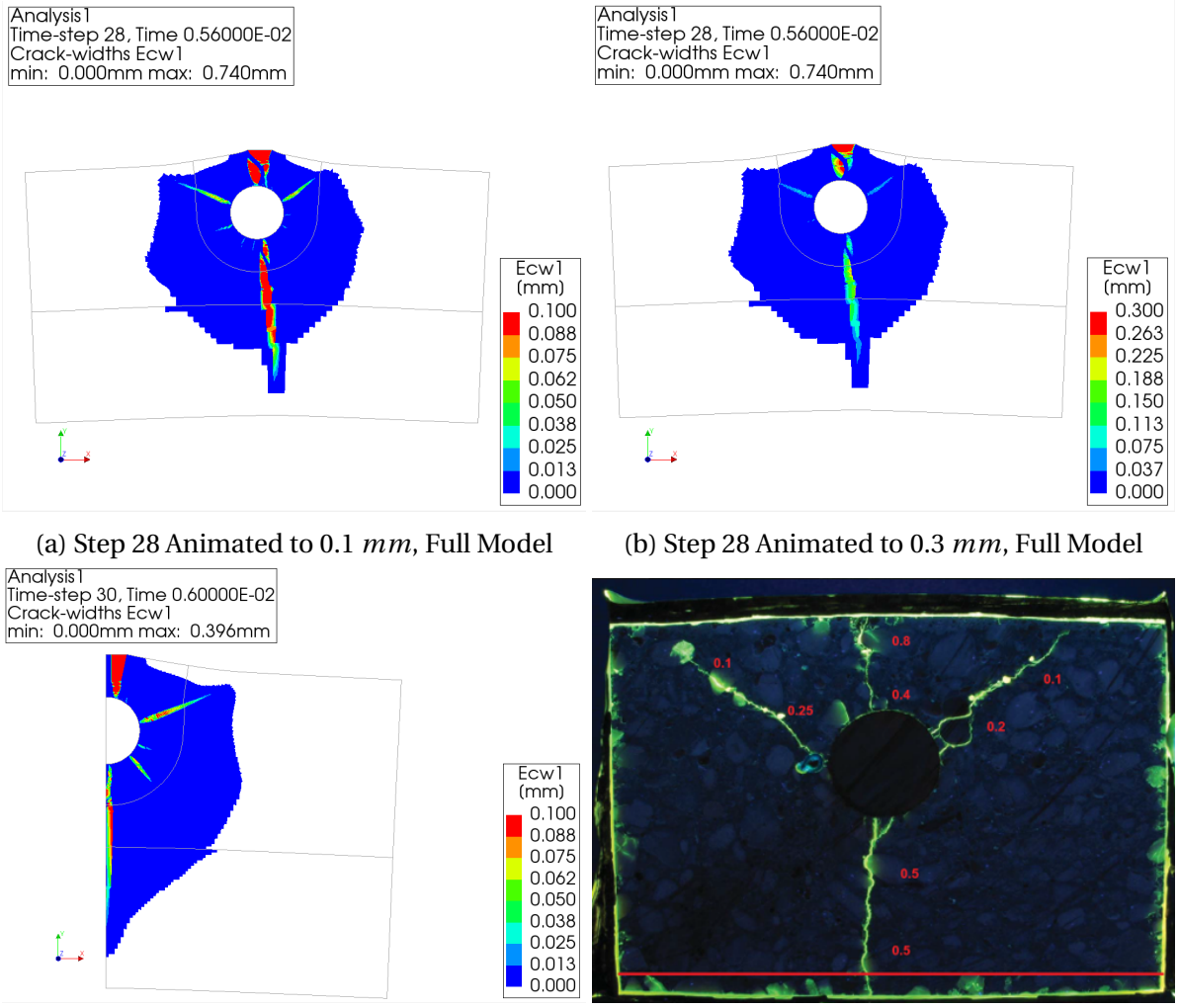

(a) Step 28 Animated to 0.1 mm, Full Model

(b) Step 28 Animated to 0.3 mm, Full Model

(c) Step 30, Symmetry Model

(d) Experiment

Figure 3.15: Comparison of Final Damage Pattern

3.4.3. PRESCRIBED FORCE LOAD MODEL

Due to the development of a second inclined bottom crack, the maximum crack width that the full model with thermal load can reach is 0.740 mm, which is around 70% of the experimental results. An assumption is that a model loaded with a prescribed force can improve this situation. Therefore, in this part, a model loaded with a prescribed force is developed. Figure 3.17 shows a schematic view of this model. In this model, a void with 18 mm radius has been made to represent the reinforcement (similar to the symmetry model).

A distributed force of 3000 N/mm has been applied radically around the void. In order to further improve the stability of the model, the boundary condition at the bottom edge is changed. Instead of simply supported, a vertical constraint is applied at two ends of the edge, and a horizontal constraint is applied in the middle of the edge. Moreover, the whole edge is constrained in the out-of-plane translation. The model is loaded by 200 steps and a load factor of 0.01 each step. All the mesh settings and material properties are identical to the full thermal load model.

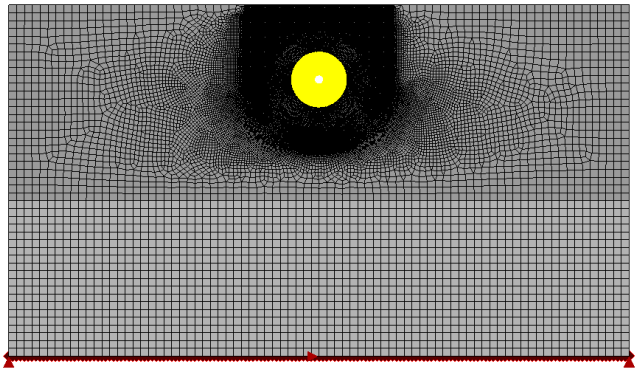

Figure 3.16: Schematic View of Full Prescribed Force Load Model

3.4.4. COMPARISON OF RESULTS

The only difference between these two models is the loading condition. The indirect loading condition is changed into a direct force control load. Therefore, the crack developing process is similar. The key question is whether this can prevent the localization of the inclined bottom crack. Figure 3.18 shows the comparison of the damage pattern of both models with maximum crack width around 1 mm. There are several improvements can be observed. The most important one is that the inclined bottom crack is not developed in the prescribed force model. This verifies the assumption that the localization of this inclined crack is due to the loading condition. By applying a thermal load (prescribed strain), the stress concentration is not released after the localization of major cracks. However, this stress is released by loading the model with a prescribed force. Thus, the inclined bottom crack disappears in the prescribed force model. One another difference can be observed: the maximum crack width of bottom crack in prescribed force model is in the range 0.5 mm − 0.6 mm and that of thermal load model are 0.3 mm − 0.4 mm. The crack width of bottom crack in the prescribed force model corresponds more with the experimental result. Because the fracture energy released through the second bottom crack in the thermal load model is now held by the bottom crack in the prescribed force model. Therefore, the

prescribed force model predicts the crack width of the bottom crack more accurately.

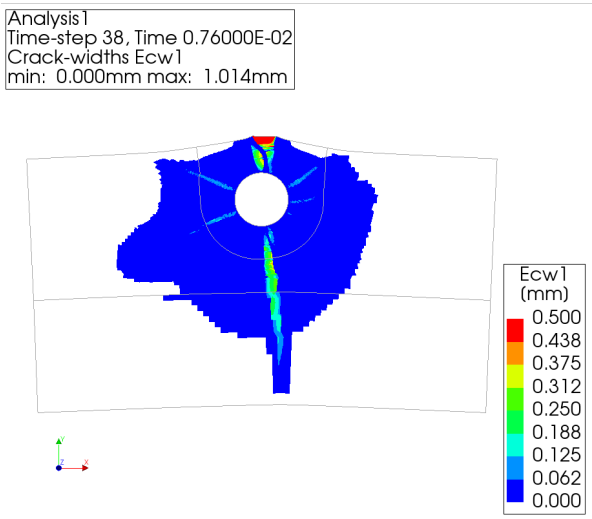

(a) Step 38, Animated to 0.5 mm, Thermal Load Model

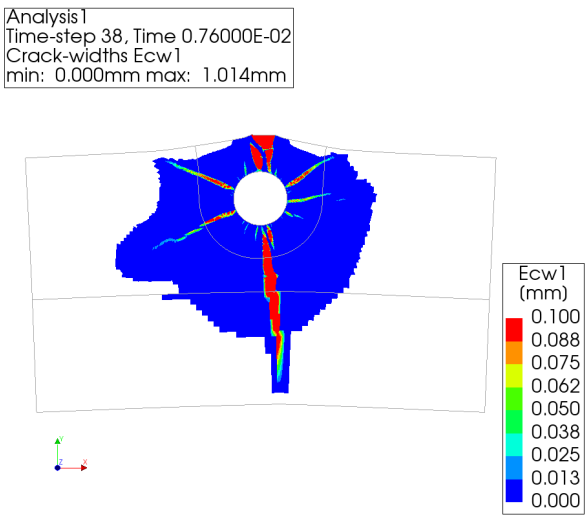

(b) Step 38, Animated to 0.1 mm, Thermal Load Model

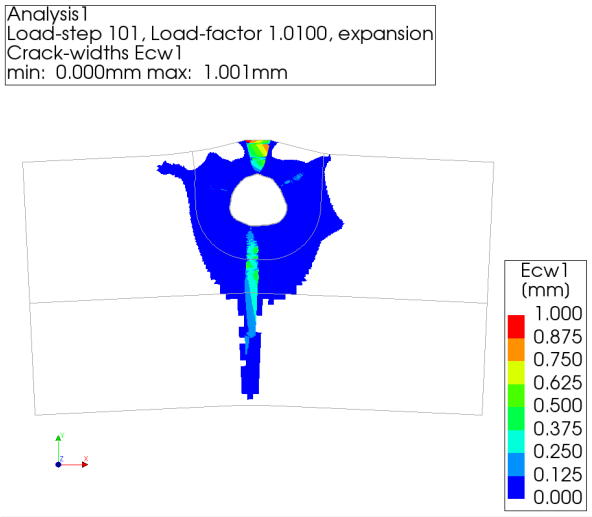

(c) Step 101 Animated to 1.0 mm, Prescribed Force Model

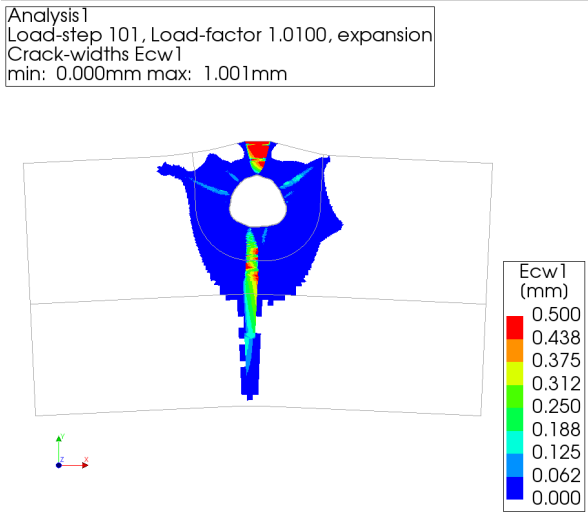

(d) Step 101 Animated to 0.5 mm, Prescribed Force Model

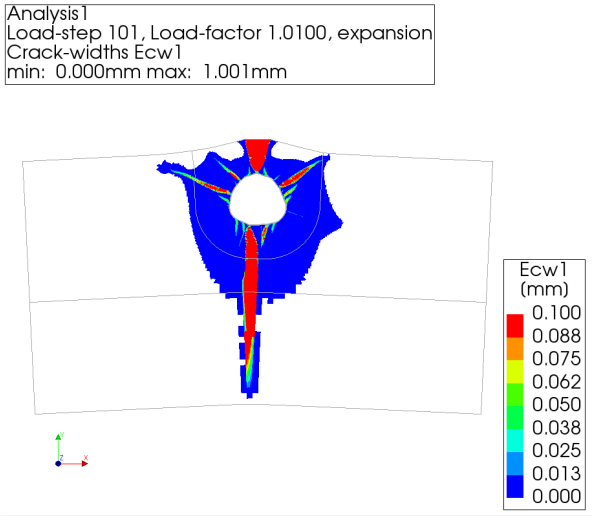

(e) Step 101, Animated to 0.1 mm, Prescribed Force Model

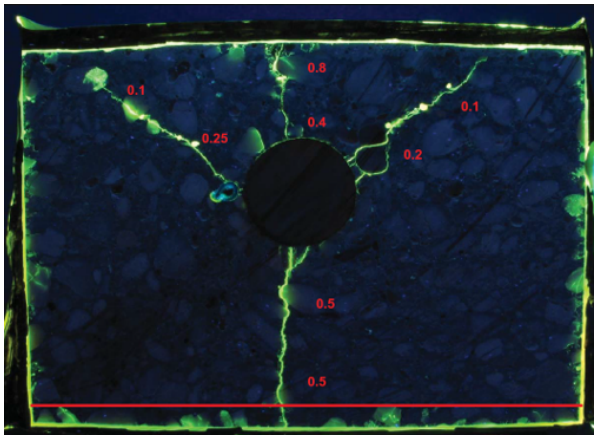

(f) Experiment

Figure 3.17: Comparison of Damage Pattern

Meanwhile, another interesting point is the failure mechanism of the model. It is also not reasonable if the model can be unlimited loaded. At step 130, the damage shows the trend of a different failure mechanism (Figure 3.18). In the red circled area, two surrounding cracks are developing in both sides. One side is joining the major cracks nearby (2, 10, 6 o'clock), the other side is developing to connect another surrounding crack. These surrounding cracks are showing the trend to join and perform a tangential crack around the reinforcement. This behavior will finally result in the stripping out of reinforcement upwards from repair mortar. Therefore, the damage after step 130 is not reasonable anymore. In general, the continuum model can simulate this strain-softening fiber reinforced concrete very well with regards to damage pattern and predicting crack width.

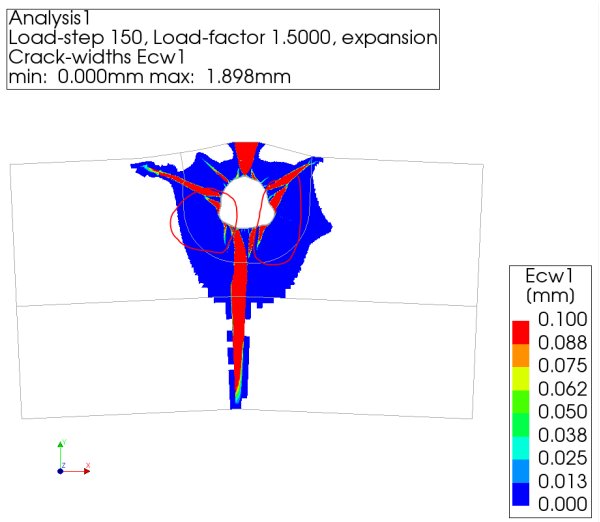

Figure 3.18: Failure Mechanism of Prescribed Force Load Model

However, this prescribed force loading condition has its limitation. This model has terrible performance in convergence. Figure 3.19 shows a scatter with average pressure added around the void versus the maximum crack width at the same step in the model. The average pressure can be simply calculated by dividing the applied distributed force with the depth of the model ($d_g = 300\ mm$) (Eq. 3.1).

$$\sigma_r = \frac{\alpha_l \cdot F_r}{d_g} \tag{3.1}$$

in which, F_r stands for the distributed force applied (N/mm) and α_l stands for the load factor.

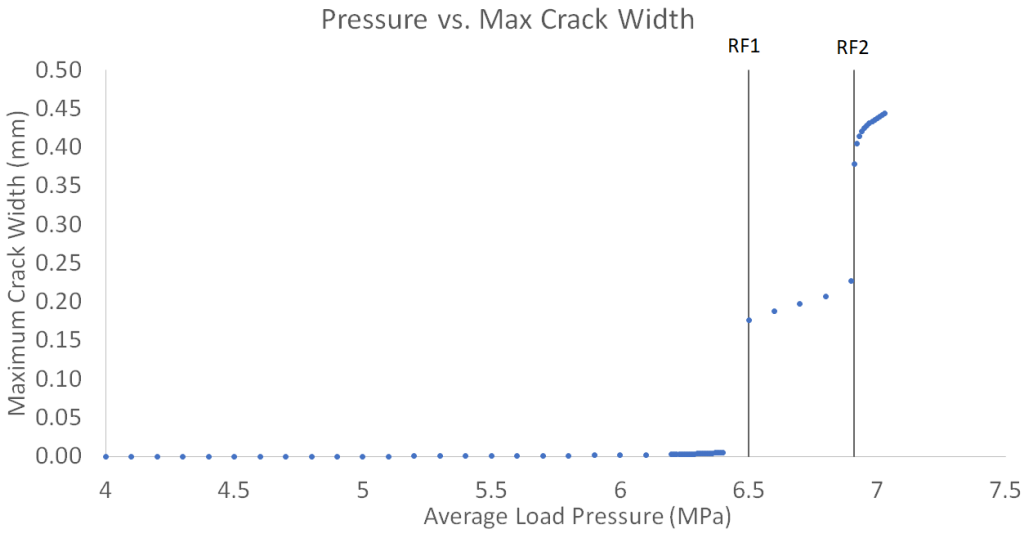

Figure 3.19: Pressure vs. Maximum Crack Width

There are two instant increases in maximum crack width at reference 1 (RF1) and 2 (RF2) in the figure. At these two steps, the model indicates convergence problems. The desired tolerance of convergence norm for force and deformation is 0.01. However, the displacement norm is not fulfilled at reference 1 (between 0.1 and 0.01). The force and displacement norm are both in the range 0.1 and 0.01 at reference 2. Therefore, the accuracy of the result after these steps are in doubt. However, the variance of the convergence norms is still acceptable. The damage pattern at both reference locations is shown in Figure 3.20 and 3.21. At these steps, the top and bottom cracks are localized respectively. This localization of a through crack causes the convergence problem in the model. It is always a problem for continuum models with incremental solution method to converge after the opening of concrete. The convergence problem is due to the solving method of nonlinear analysis itself. With an incremental method, multiple integration points are pushed to damage within a step which means their stiffness is negative in the stiffness matrix.

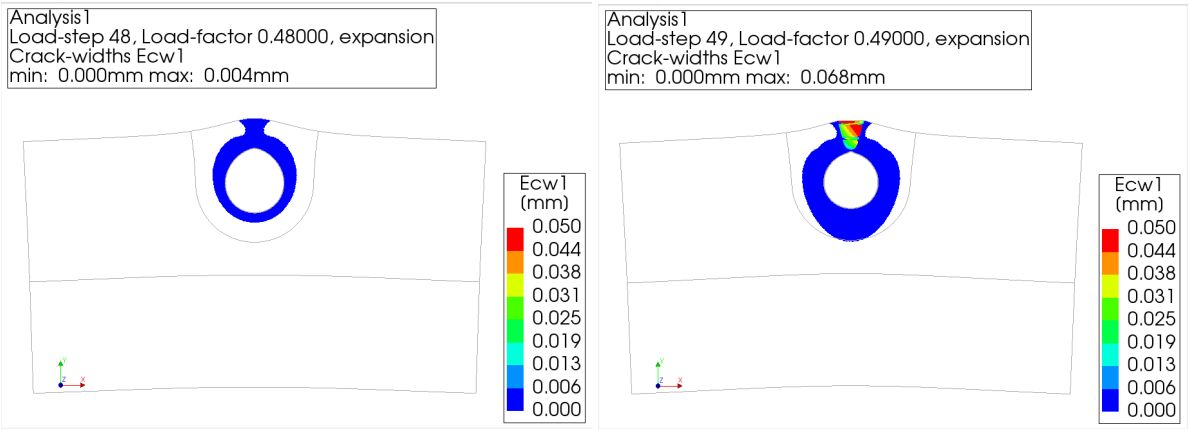

(a) Before Reference 1 (b) After Reference 1

Figure 3.20: Crack Localization at RF1

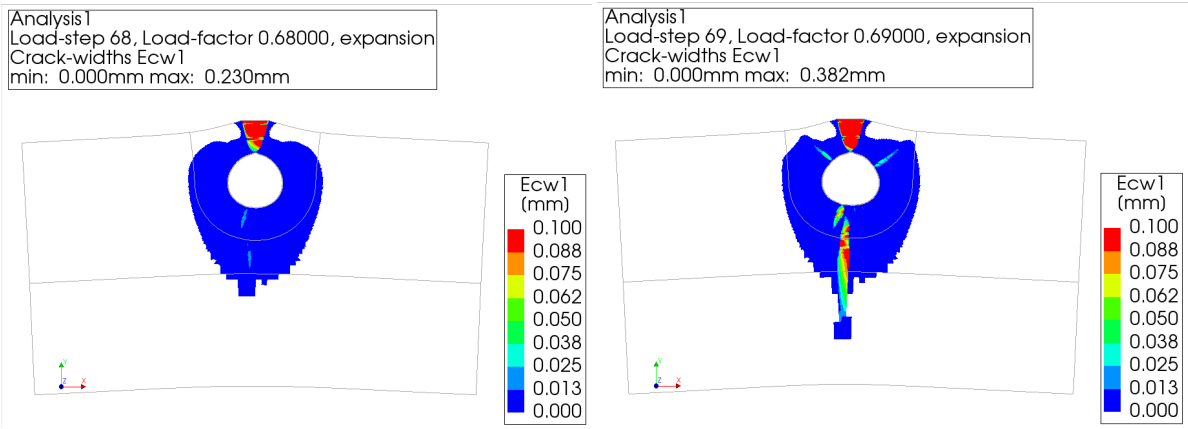

(a) Before Reference 2 (b) After Reference 2

Figure 3.21: Crack Localization at RF2

At load factor 0.703, the relative difference in force reaches higher than 0.1. The results after this step are not reasonable anymore. Therefore, Step 100 (load factor 0.703, Pressure 7.03 MPa) is the final acceptable step in this model. The damage pattern is compared with the experiment in Figure 3.22. The damage pattern is still very similar to the experiment which means that this model can still give a good prediction in damage pattern.

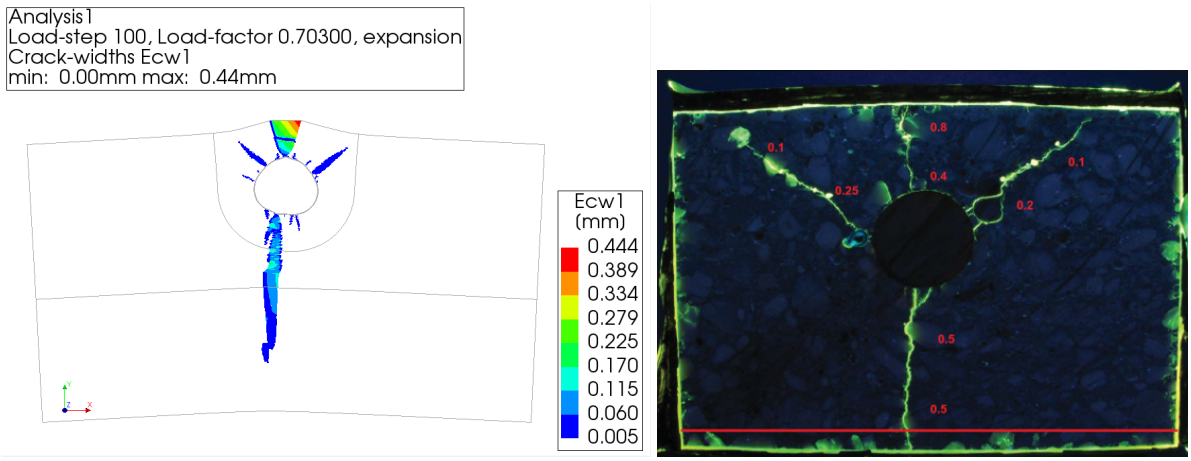

(a) Continuum Model (b) Experiment

Figure 3.22: Comparison of Crack Pattern between Prescribed Force Model and Experiment

4

LATTICE MODEL

In this chapter, a series of lattice model is developed to investigate the performance of the lattice model in simulating the cracking behavior of fiber reinforced concrete in accelerated corrosion test at the macro level. The material used is identical to that of continuum models: ON06 (strain-softening behavior, similar to normal concrete).

4.1. PRELIMINARY MODEL WITH BRITTLE MATERIAL

In this section, a preliminary model with brittle material property is developed. The goal of this section is to set up a preliminary model to be the foundation for models with the experimental material property.

The procedure to generate the lattice system can be described as [40]:

- A square grid is chosen.
- A location with certain randomness for a lattice node is selected in each cell of the square. The nodes are randomly positioned inside a sub-cell with a size of s in a regular grid with size A. In this way certain randomness with a ratio s/A is defined, and it is set to be 0.5 in this case. Some stochastic is built in the lattice system.
- A node tag is assigned to each node based on its coordinates to represent the material it belongs to, respectively mortar, substrate and steel rod.
- Each node is connected to four closest nodes with lattice elements. Delaunay triangulation algorithm is applied to realize this.

- All elements are assigned with an element tag to represent its material property based on the node tag of the nodes connected.
- Material property and failure modes are assigned to all elements based on its element tag. For the fracture criterion, only axial forces are taken into account to determine the stress in the beams.

In this preliminary model, all the materials are modeled as the brittle material. Two types of materials are used in this model, respectively substrate and repair mortar:

Table 4.1: Brittle Material Property

Material	Number of Segment	E (GPa)	G (GPa)	f_t (MPa)	f_c (MPa)
Substrate	1	20	8.33	2	-30
Repair Mortar	1	30.32	12.63	2.317	-25.5

4.1.1. DIRECT TENSION TEST

For the lattice model, an important parameter is the radius of lattice beams. Therefore, calibration is needed to get the correct lattice radius. The radius should be calibrated in such a way that under direct tension test, the global structural stiffness should be identical to the local material input. In practical, an iterative process to calibrate the lattice radius is developed. From the first step of analysis, displacement d_x and reaction force F_R can be recorded. The global structural stiffness E_g can be calculated as:

$$E_g = \frac{F_R / l_y / d_m}{d_x / l_x} \tag{4.1}$$

in which, l_x and l_y stand for the length and height of the specimen and d_m stands for mesh size. Based on the result from equation 4.1, the calibrated lattice beam radius r_c can be calculated as:

$$r_c = r_i \cdot \sqrt{\frac{E_l}{E_g}} \tag{4.2}$$

in which, r_i is the input lattice beam radius and E_l is the local material Young's modulus. Then the calibrated radius is used as input and the procedure is repeated until the difference between global and local stiffness is smaller than desired tolerance (0.0001%).

In this section, two models are set up with different mesh size for direct tension test, namely $2mm$ and $5mm$ mesh size. The length and height of the specimen are $400mm$ and $226mm$. All elements in both models are assigned to material repair mortar. Both models are constrained in the x direction along the short edge. Meanwhile, a prescribed displacement is applied on the right edge of the model. The calibrated lattice beam radius (based on the explained procedure) are $1.004844mm$ and $2.502264mm$ respectively. The distribution of lattice beams in both models is shown in Figure 4.1.

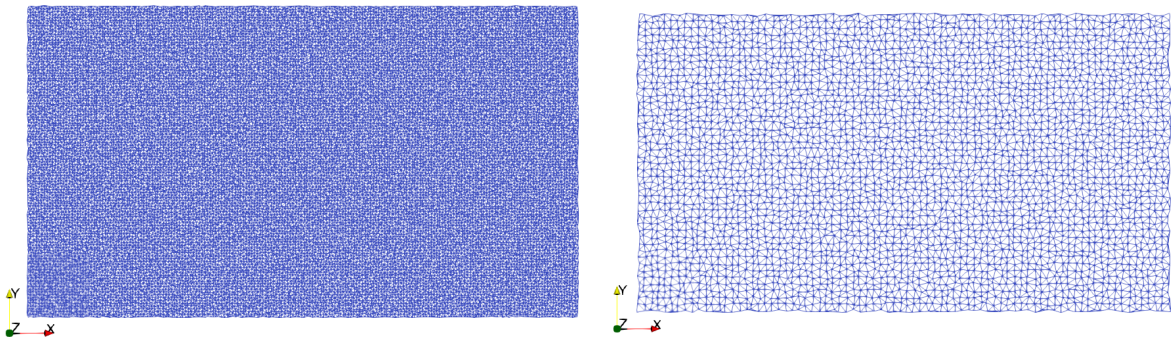

(a) $2mmModel$ (b) $5mmModel$

Figure 4.1: Distribution of Lattice Beams

Then, the model runs until its failure to check whether the global structural behavior is identical to the material input. The Stress-Strain relation calculated from direct tension test is shown in Figure 4.2. In general, both models show brittle behavior under direct tension. However, there are some influences of mesh size in the fracture behavior after the elastic stage. The 5 mm model shows more fracture energy than the $2mm$ model. Thus, the behavior of the 2 mm model is more brittle than the 5 mm model. The difference in the number of elements can explain this. With more than twice the number of lattice beams, the 2 mm model can describe the cracking of the model better than $5mm$ model. Because of the finer mesh, the 2 mm model can reduce the uncertainty caused by the orientation of lattice beams and follow the constitutive law (brittle) better. This also reminds that the $5mm$ mesh may be too coarse for the specimen of structural size.

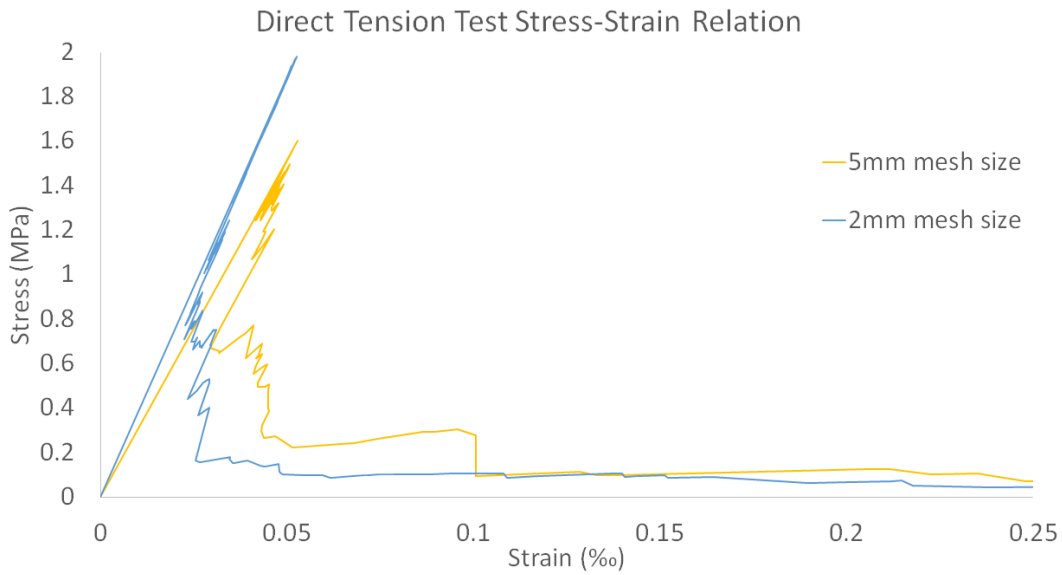

Figure 4.2: Direct Tension Test Stress-Strain Relation

The damage pattern of both models is shown in Figure 4.3. Elements in blue are damaged, and elements in red are undamaged. Because of the randomness of lattice beams, the crack is not located perfectly in the center of the specimen. However, the cracks are also not along the edge or inclined. This shows that the calibration and direct tension results are acceptable. Meanwhile, the crack in the 5 mm model is slightly inclined, which might be the result of the influence caused by the orientation of lattice beams.

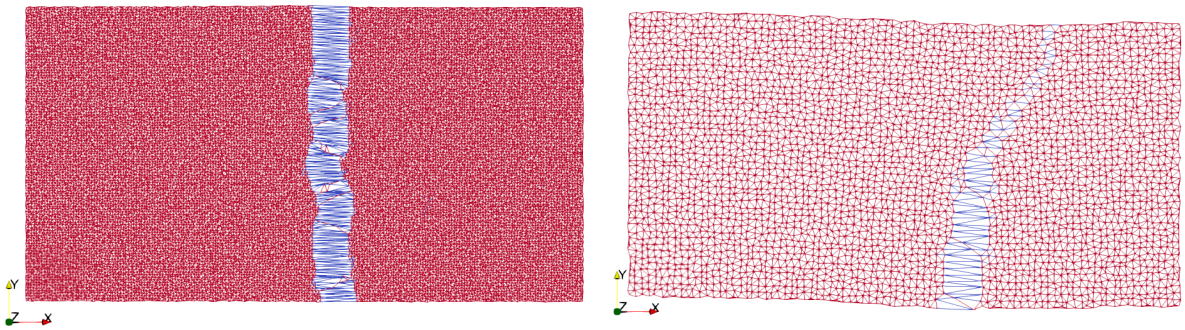

(a) $2mm$ *Model*, Step 400 (b) $5mm$ *Model*, Step 130

Figure 4.3: Damage Patter of Direct Tension Test

4.1.2. ACCELERATED CORROSION MODEL

Based on the calibration results from the direct tension test, an accelerated corrosion model with $2mm$ mesh size has been set up. The nodes distribution and beam connection are im-

ported. Then the model is built through the following steps:

- Nodes with y coordinates smaller than 100 are tagged as 1 (substrate). For nodes with y coordinates larger than 100, those with their distance with point (200, 178) smaller than 18 are tagged as 3 (rebar), and the others are tagged as 2 (repair mortar).

- Remove two type of elements: elements connected by tag 3 node, elements connected by one tag 2 and one tag 3 node. Meanwhile, if an element is connected by one tag 2 and one tag 3 node, tag the tag 2 node as 4 (load point) instead.

- Elements connected by tag 1 node are defined as substrate elements (tag 1). Elements connected by tag 2 node are defined as substrate elements (tag 2). Elements connected by one tag 1 and one tag 2 node are defined as interface elements (tag 3). Elements connected by one tag 2 and one tag 4 node are defined as load elements (tag 4).

- All elements are assigned with a radius of $1.004844mm$ based on calibration. Tag 1 elements are assigned to the material substrate, and tag 2, 3, 4 elements are defined as repair mortar material.

- Tag 1, 2, 3 elements are allowed to fail in tension. Tag 4 elements are defined as unbreakable.

- A reference prescribed force F_r is applied to tag 4 nodes along the radial direction. All nodes with y coordinates smaller than $2mm$ are constrained in all 6 degrees of freedom.

A schematic view of the model is shown in Figure 4.4.

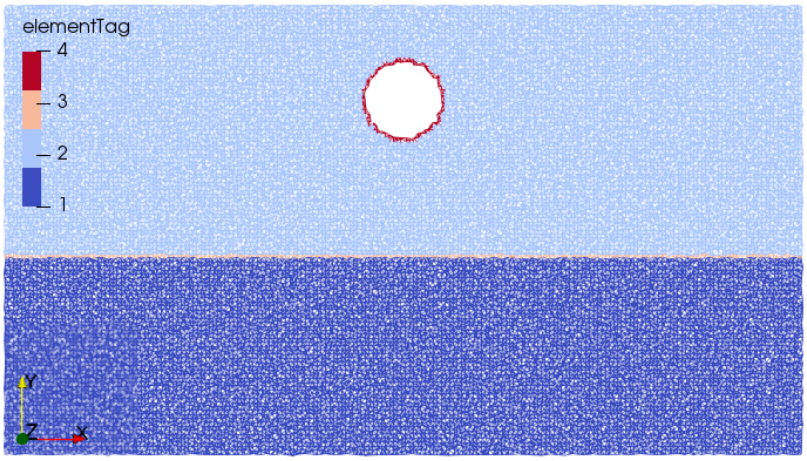

Figure 4.4: Schematic View of the Accelerated Corrosion Model

From the analysis results, the load factor of each step can be recorded. Based on this, the average pressure on rebar σ_r can be calculated as the total load over the loading area:

$$\sigma_r = \frac{\alpha \cdot F_r \cdot n_{lp} \cdot 1000}{d_m \cdot \pi \cdot d_R} \tag{4.3}$$

in which, n_{lp} stands for the number of load points and d_R is the diameter of steel rod. Figure 4.5 shows the rebar pressure with analysis steps in orange. Due to the solution method of lattice model, some zig-zags can be observed in this curve. However, only the steps with increasing pressure are meaningful to be studied. Therefore, the curve is smoothed by presenting only increasing pressures.

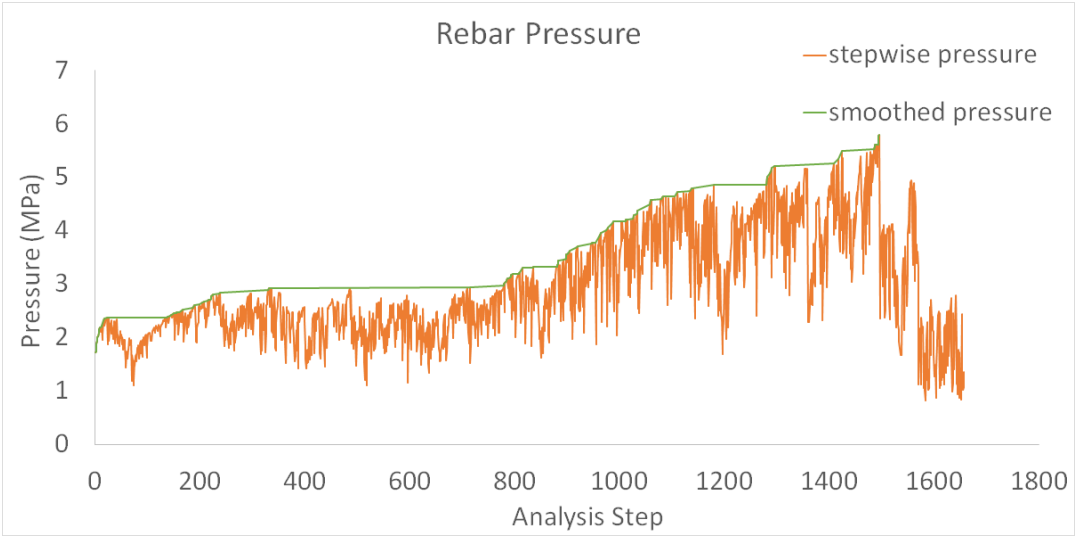

Figure 4.5: Average Load Pressure by Analysis Steps

In this section, the detailed formation and propagation of cracks (based on the curve shown in Figure 4.5) in the accelerated corrosion model are explained. There is a drop in rebar pressure between step 69 and 70. Figure 4.6a shows the damage pattern (in black colour) at step 69. There is a through crack developed at the top of steel rod. Even though there are some other elements damaged around the void, this is the only crack till this step. Because the concrete cover is thinnest at the top, which is the weakest spot of the specimen. Therefore, the damage at this step is in line with its mechanical behavior. As the analysis goes on, another peak in pressure at step 239 can be found. At this step, the major crack at the top kept going wider. Besides, multiple cracks are initialized around the steel rod. This is a result of the advantage brought by the built-in randomness of the lattice model. However, not all these microcracks can be further developed.

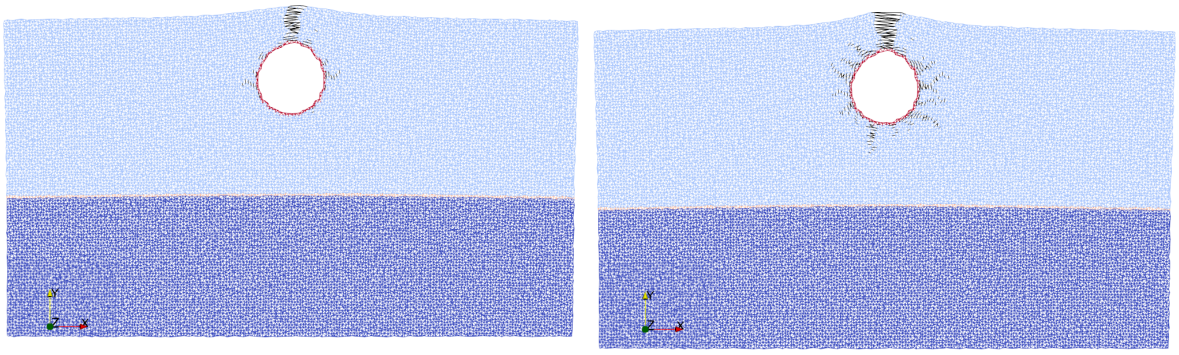

(a) Step 69 (b) Step 239

Figure 4.6: Damage Pattern of Accelerated Corrosion Model at Step 69 and 239

Step 488 is also another peak in rebar pressure before a drop in pressure. Figure 4.7a shows that two other secondary cracks are developed along 2 and 8 o'clock direction. Meanwhile, the other microcracks are still at a preliminary level. In step 598, there are two other cracks localized along 1 and 4 o'clock direction. Physically, the cone area between 11 and 1 o'clock at the top is the most critical area and controls the capacity of the specimen. There are two possible explanations of the 1 o'clock crack. It can be that the crack width of this crack is still much smaller than the crack along 2 o'clock. It also can be that the crack along 2 o'clock is going more horizontal instead of upwards. These assumptions will be verified in the following parts.

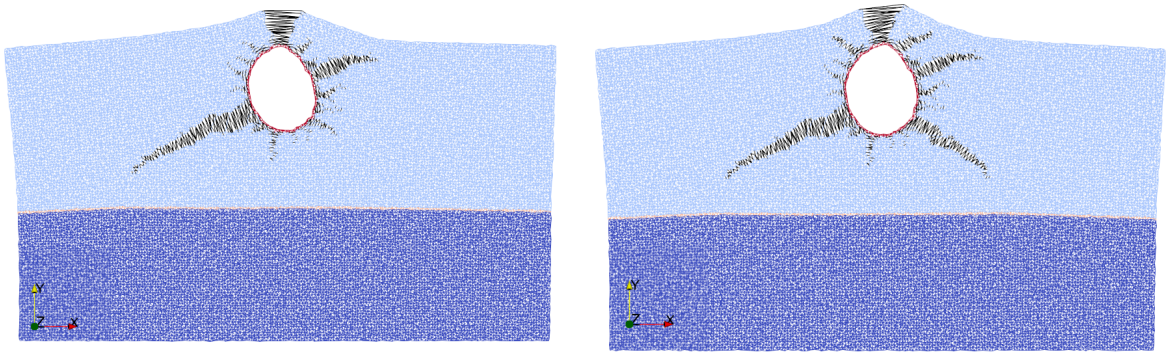

(a) Step 488 (b) Step 598

Figure 4.7: Damage Patter of Accelerated Corrosion Model at Step 488 and 598

Figure 4.8a indicates that another crack along 11 o'clock direction is developed symmetrically at step 715. This supports the assumption that the crack along 2 o'clock is going more horizontal instead of upwards and this results in another crack along 1 o'clock. Moreover, the crack along 4 o'clock reaches the interface between substrate and repair mortar. At step 835, all the performed cracks are almost fully developed. However, some elements around the rebar start being randomly broken without any localization. This means that this model has reached its end. Considering the crack pattern in the experiment that only cracks in repair mortar are examined (Figure 3.3c), the results after step 715 is not comparable.

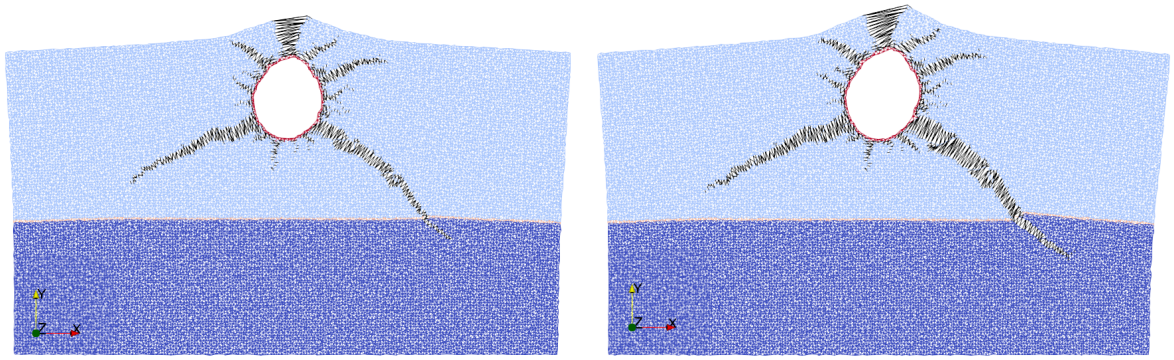

(a) Step 715 (b) Step 835

Figure 4.8: Damage Patter of Accelerated Corrosion Model at Step 715 and 835

The crack width at step 715 is displayed and compared with the experiment in Figure 4.9. The crack width is defined as the difference between the deformed beam length and the original beam length. The crack at the top shows the largest crack width, which is wide at the top and thin at the bottom. This is due to the local bending failure and can also be

observed in the experiment. The crack width of two bottom cracks is more or less twice the width of other secondary cracks. Moreover, the cracks at 1 and 2 o'clock are at the same level. This verifies the assumption that the crack along 2 o'clock is going more horizontal instead of upwards and this results in another crack along 1 o'clock. However, all the crack widths are one order of magnitude lower that experiment. This may be the result of low fracture energy in this model. This can be improved if we add some softening in the material property. We will investigate this later in the following sections. Moreover, the direction of the bottom cracks is inclined and develops towards the side edges. However, the bottom crack in experiment goes straight downward. This behavior can also be observed in the continuum models. This implies that the constrained bottom boundary may have a too strong influence on the structure also in the lattice model, which is also an interesting parameter to investigate.

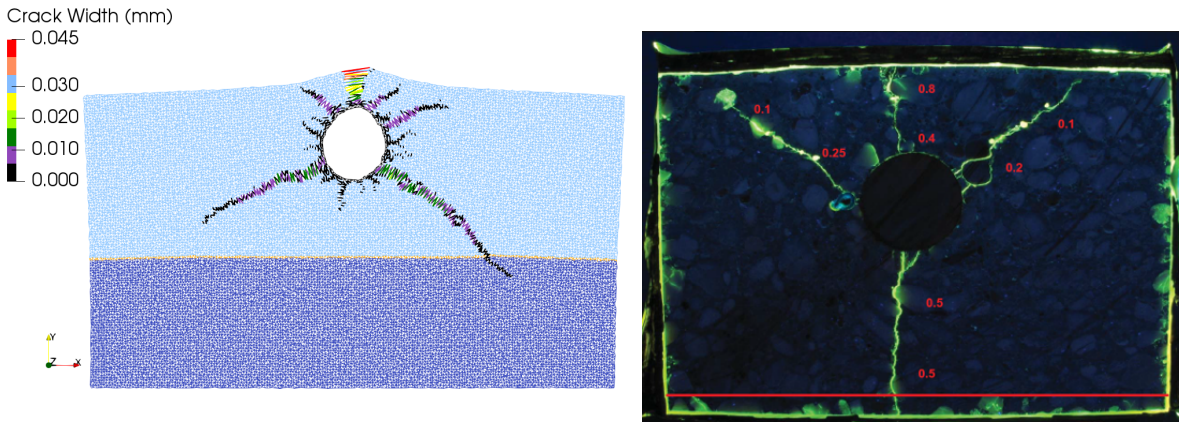

(a) Step 715, Lattice Model (b) Experiment

Figure 4.9: Comparison of Damage Pattern

4.2. INFLUENCE OF BOUNDARY CONDITION

4.2.1. SIMPLY SUPPORTED BOTTOM EDGE

In this section, the influence of different boundary conditions on the crack pattern will be investigated. The conclusion drawn from the continuum model is to keep the bottom edge as free as possible. However, for the stability of the system, at least one constraint is needed in the model. Moreover, due to the built-in randomness of lattice model, the

lattice distribution is not perfect symmetry and the load applied is not exact self-balancing. After the formation of a crack, there will be some rotation applied to the model (worse than in continuum model). Therefore, at least one edge has to be constrained to counter this rotational deformation. As the boundary condition applied in the continuum model (Section 3.3), the simply supported boundary condition is applied along the bottom edge. The bottom left node is constrained in both x and y direction, and the bottom right node is only constrained in the y direction. This model is adopted from the model with 2 mm mesh size in the previous section (using the same lattice beam distribution). Therefore, the radius of the lattice beam does not need to be calibrated. The brittle material law is still applied in this model as it is shown in Table 4.1. A unit radial load of 1 N is applied around the void. Figure 4.10 shows the applied boundary condition in this model.

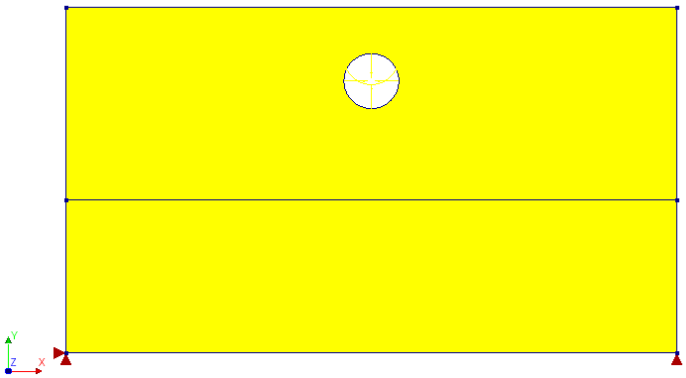

Figure 4.10: Simply Supported Model

Figure 4.11 shows the damage pattern and crack width of this model at step 570. Several cracks have been developed at this step. However, the left edge starts being damaged after this step (circled area, elements in grey color). Due to the crack formation around the void, rotational deformation is accumulated. At step 570, the model reaches the point that bottom left support cannot hold this stress anymore and starts damaging. However, the bottom crack has just passed the mortar-substrate interface. The crack pattern might be influenced by the support damage. Moreover, even before the step where support fails, the stress distribution has already been influenced by the stress concentration at left bottom support. Thus, the damage pattern of this model may have been influenced already. One improvement that can already be observed at this step is the direction of the bottom crack. Instead of inclined and heading towards the bottom right corner, the bottom crack follows

roughly 6 o'clock direction which corresponds with the experiment. This verifies the assumption that the development of bottom crack is very sensitive to boundary condition at the bottom edge. The bottom edge needs to be kept as free as possible to ensure accurate simulation of the crack pattern.

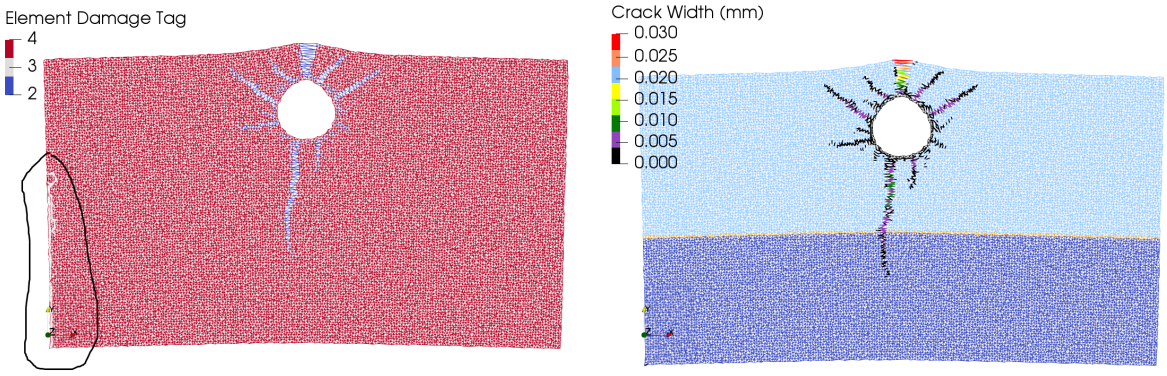

(a) Damage Pattern (b) Crack Width

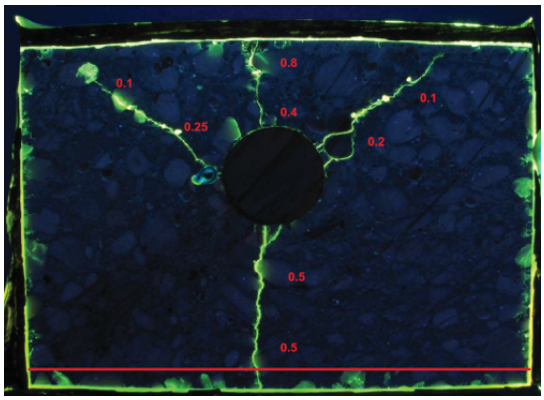

(c) Experiment

Figure 4.11: Step 570, Simply Supported Model

4.2.2. LINEAR ELASTIC BOTTOM EDGE

In order to solve the stress concentration problem, another model is developed. All the elements along the bottom edge are defined as linear elastic. In this way, the supports in this model cannot be damaged, which is an improvement in the stability of the system and reduces the rotational deformation after cracking. All the other settings are kept identical to the model in the previous section. Local failure permission mode of this model is shown in Figure 4.12a. Besides the elements around the void, the elements at bottom edge are marked as red (ideal elastic). However, the stress concentration problem happens again

at step 863 of this model (circled area in Figure 4.12b). As the bottom crack gets close to the bottom edge, the bottom left support is damaged. This can be a result of the elastic bottom edge. As the bottom crack gets close the bottom edge, some bottom edge elements reach the elastic strain capacity. However, they cannot be broken in tension. Therefore, the stress is passed over to the left bottom support and the elements around the support start damaging. Although this model can damage 293 more elements with the help of the unbreakable bottom edge, the stress concentration problem is improved but not solved.

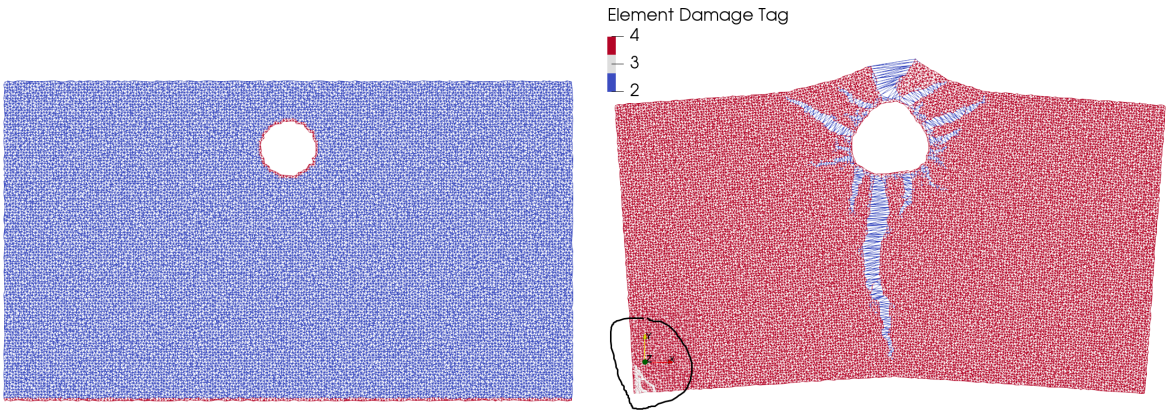

(a) Local Failure Permission Mode

(b) Damage Pattern

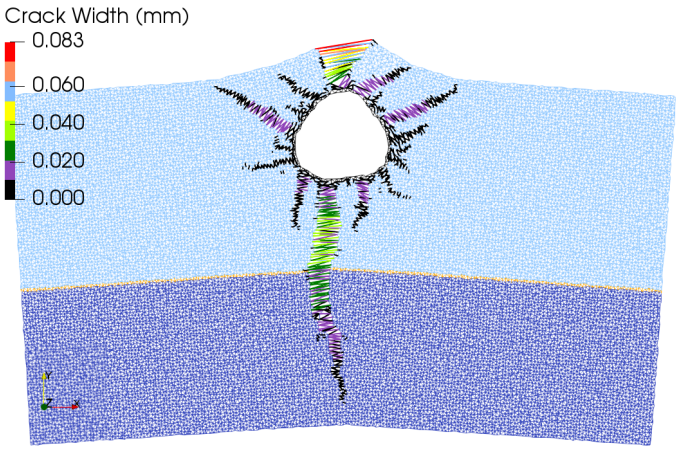

(c) Crack Width

Figure 4.12: Step 863, Simply Supported Model with Elastic Bottom Edge

4.2.3. THREE NODES SIMPLY SUPPORTED BOTTOM EDGE

Another bottom boundary condition is proposed to solve the stress concentration problem further. Besides unbreakable bottom edge, the simply supported boundary is separated

into three nodes instead of two. The bottom left and right corner are constrained in the y direction, and the node in the middle of the bottom edge is constrained in the x direction. By doing this, both left and right bottom corner are allowed to move in x direction which means the stress on support caused by rotational deformation is distributed to three supported nodes. This can help delay the appearance of stress concentration at support. The boundary condition and local failure permission mode are shown in Figure 4.13.

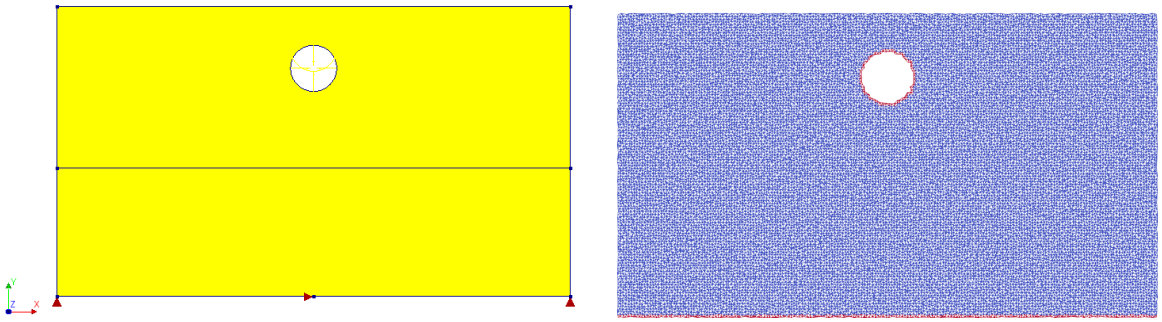

(a) Boundary Condition (b) Local Failure Permission Mode

Figure 4.13: Three Nodes Simply Supported Model with Elastic Bottom Edge

Figure 4.14 shows the development of cracking in this model. At step 776 (Figure 4.14a), the bottom crack propagates through interface and gets close to bottom edge. After this step, the bottom edge starts producing an influence on the stress distribution in the model. Another inclined bottom crack is initialized and developed (Figure 4.14b). Another crack can be developed in this model instead of support failure. This proves the assumption that the support failure in the simply supported model with an unbreakable bottom edge is due to the unlimited elastic behavior at the bottom edge. As the development of the analysis, a tangential crack is developed at the left of the void. This crack is meaningless which indicates that the results are not reasonable after this step. However, the present of the second inclined bottom crack is due to the unbreakable bottom edge. This is a fictitious setting for the stability of the model. Therefore, as soon as it shows influence on the damage pattern, the results should not be trusted anymore. Therefore, step 776 is the last reasonable step of this model.

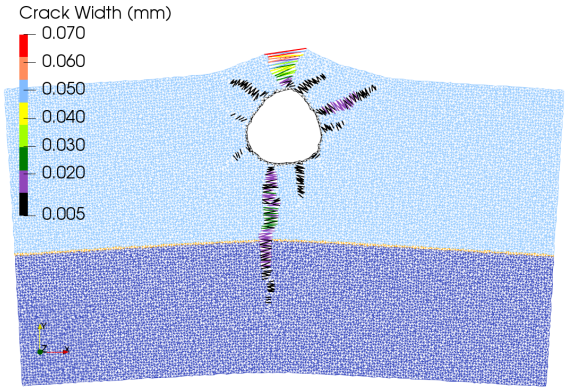

(a) Step 776

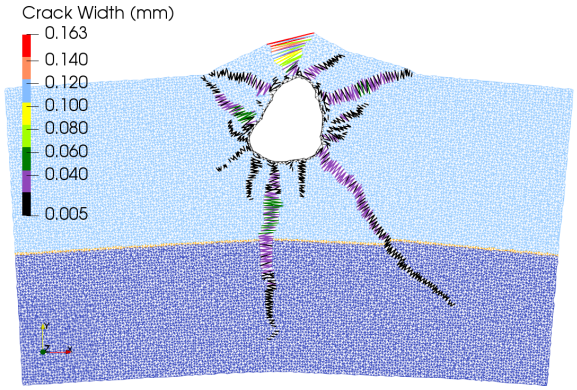

(b) Step 1335

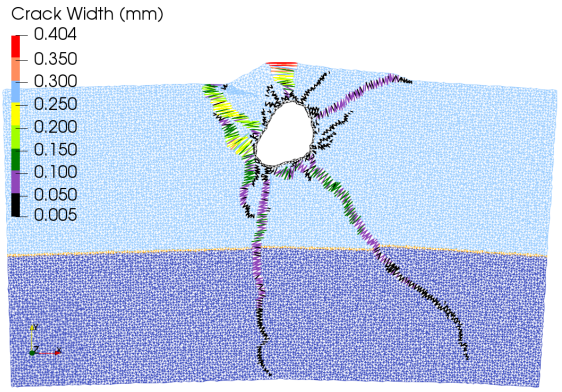

(c) Step 1568

Figure 4.14: Crack Development

Comparison of the final damage pattern between fixed and simply supported bottom model is displayed in Figure 4.15. A clear improvement can be observed by modifying the boundary condition from the comparison. The bottom crack direction is along 6 o'clock direction instead of inclined, which is more correspond to experimental results. This verifies the observation with the continuum model that the bottom crack direction is very sensitive to bottom edge boundary direction. Besides, at similar analysis step, the maximum crack width of three nodes simply supported model is 35.71% higher than the fixed bottom model with similar top cracks in the crack pattern. Also, the averaged pressure applied in the simply supported model is 18.72% lower (3.82 MPa and 4.70 MPa). This implies that the fixed boundary results in an increase of capacity and limits the widening of cracks. Therefore, to perform accurate simulation, the three nodes simply supported and the unbreakable bottom edge will be applied for further models. Moreover, the maximum crack width which lattice model can reach is roughly one magnitude lower than the experimental

results. This is probably due to the brittle material law implemented into this model. The cracking behavior of material with softening will be studied in the next section.

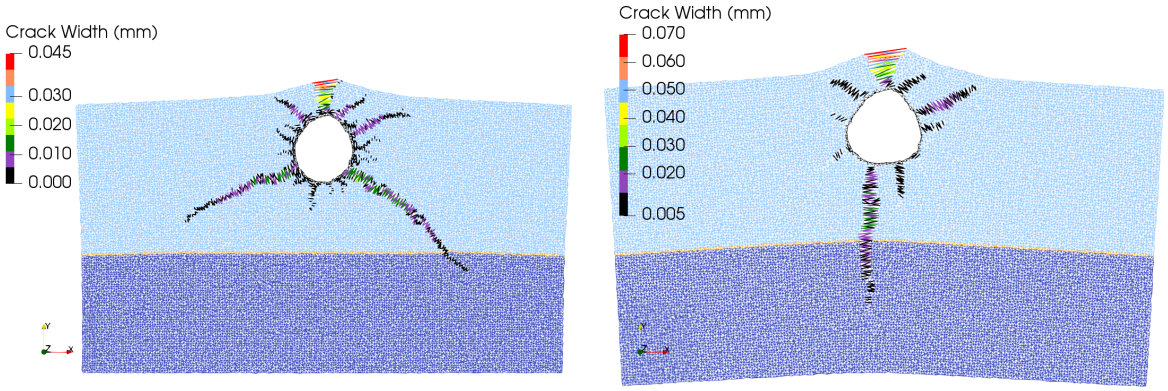

(a) Step 715,Fixed Bottom

(b) Step 776, Three Nodes Simply Supported Model

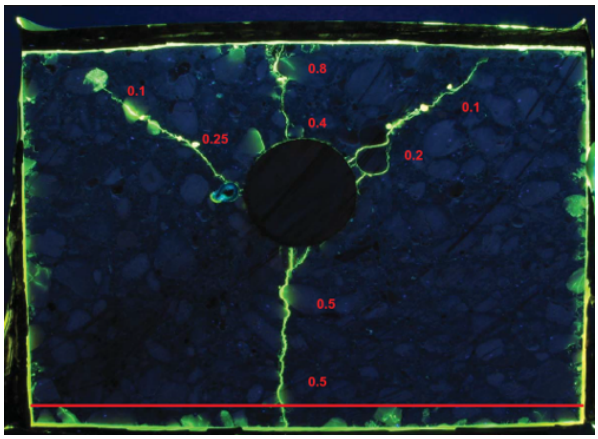

(c) Experiment

Figure 4.15: Comparison of Crack Pattern

4.3. STRAIN SOFTENING IN LATTICE MODEL

4.3.1. MATERIAL INPUT

In this section, repair mortar with strain-softening behaviour is implemented instead of brittle material. Hordijk et al. proposed an expression to describe the softening behavior of

plain concrete [35]. The expression can be described as a function of crack strain:

$$\frac{\sigma^{cr}_{nn}(\epsilon^{cr}_{nn})}{f_t} = \begin{cases} (1+(c_1\frac{\epsilon^{cr}_{nn}}{\epsilon^{cr}_{nn.ult}})^3)exp(-c_2\frac{\epsilon^{cr}_{nn}}{\epsilon^{cr}_{nn.ult}}) - \frac{\epsilon^{cr}_{nn}}{\epsilon^{cr}_{nn.ult}}(1+c_3^3)exp(-c_2) & 0<\epsilon^{cr}_{nn}<\epsilon^{cr}_{nn.ult} \\ 0 & \epsilon^{cr}_{nn}>\epsilon^{cr}_{nn.ult} \end{cases} \tag{4.4}$$

with the parameters $c_1 = 3$ and $c_2 = 6.93$. The ultimate crack strain can be calculated as :

$$\epsilon^{cr}_{nn.ult} = 5.136\frac{G^I_f}{hf_t} \tag{4.5}$$

In the experiment, the fibers in ON06 does not help too much in strain capacity of this material. Therefore, it can be regarded as plain concrete. Based on engineering experience, a fracture energy of 0.15 N/mm is given. Also, the crack band width h in this lattice model is defined as the measuring distance of the model, which is 226 mm. Therefore, the ultimate crack strain is calculated as:

$$\epsilon^{cr}_{nn.ult} = 5.136\frac{G^I_f}{hf_t} = 5.136\times\frac{0.15}{226\times 2.89} = 1.18\times 10^{-3} \tag{4.6}$$

This calculated ultimate crack strain is in line with the engineering value of normal concrete (around 0.01%). Based on the ultimate crack strain, ten points with identical spacing are chosen to represent the softening curve. Based on Eq. 4.4, the tensile stress of these points are calculated. Also, the strain is calculated based on the tensile stress, E modulus and crack strain:

$$\epsilon_{nn} = \epsilon^{cr}_{nn} + \frac{\sigma^{cr}_{nn}}{E} \tag{4.7}$$

The calculated stress-strain relation is displayed in Figure 4.16. However, at strain level 0.0484% (the fifth point), the residual tensile stress is only 0.461 MPa which is 15.96% of the tensile strength of this material. After this point, the residual tensile stress is relatively low which means that not too much fracture energy is represented after that point. Therefore, that part of the curve will not influence the cracking behavior of the model too much. Due to the limitation of computing power, only the first five nodes are selected for material input. In total, five softening segments are applied in the lattice model. Their material properties are listed in Table 4.2.

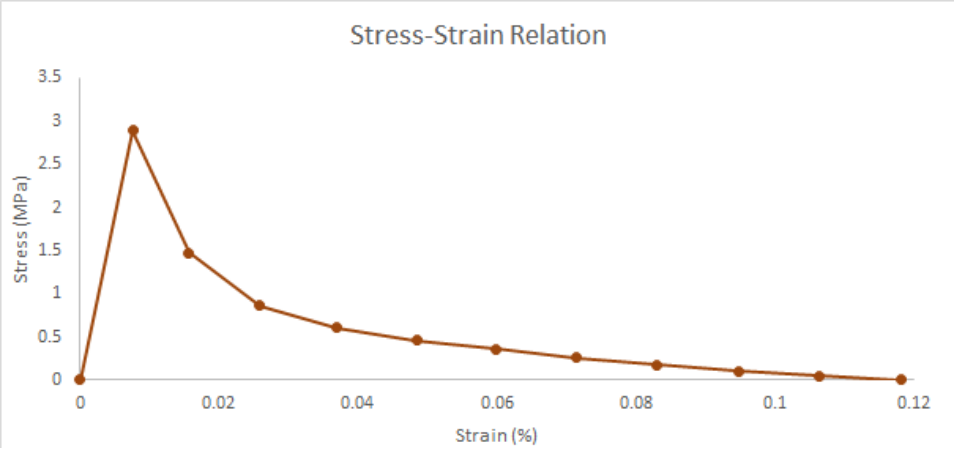

Figure 4.16: Calculated Hordijk Softening Stress-Strain Curve

Table 4.2: Hordijk Softening Material Property

Number of Segment	E (GPa)	G (GPa)	f_t (MPa)	f_c (MPa)
1	37.95	15.8125	2.89	-25.5
2	9.4120	3.9217	1.4763	-12.7709
3	3.3366	1.3902	0.8630	-7.4653
4	1.6260	0.6775	0.6011	-5.2001
5	0.9533	0.3972	0.4614	-3.9912

This material with tension-softening property is only applied to the repair mortar. After one element with softening reaches its tensile strength, its property will move to the following segment instead of being completely removed from the stiffness matrix. In this way, the softening behavior of this material is simulated. The material of the substrate is defined as it showed in Table 4.1. An unbreakable bottom edge with simply supported in three nodes is applied. A radial unit load is applied inside the void to represent the expansion caused by corrosion.

4.3.2. DEVELOPMENT OF CRACKS

Figure 4.17 shows a plot of the maximum crack width with the increase of average pressure loaded on both softening mortar model and brittle mortar model. Several reference locations (RF) are marked to indicate important load steps.

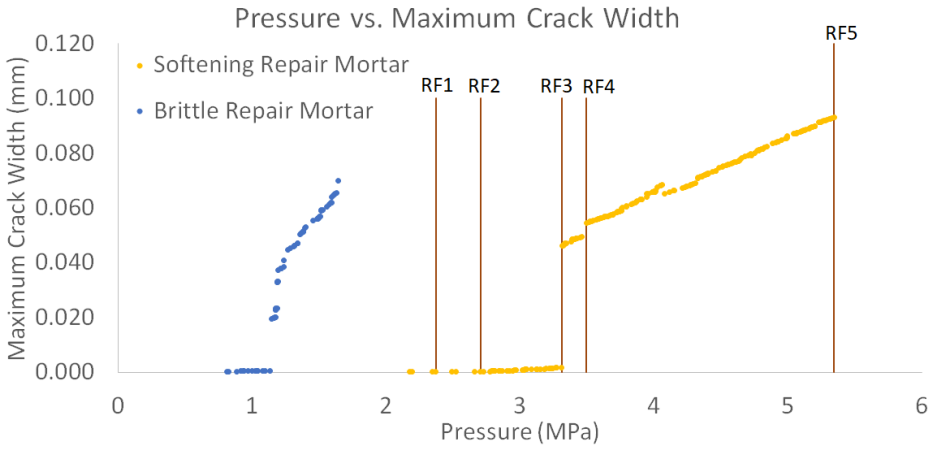

Figure 4.17: Load Pressure - Maximum Crack Width Curve

At step 800 (reference location 1, RF1), the top crack is localized. After a through crack is developed at the top, one bottom crack is performed along 6 o'clock direction at step 1200 (RF2).

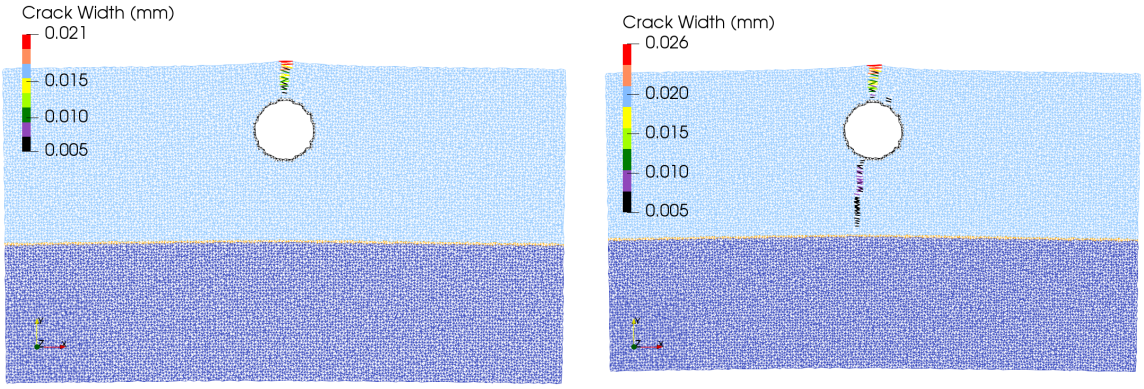

(a) Step 800, RF1 (b) Step 1200, RF2

Figure 4.18: Crack Plots at Starting Phase

Then a secondary crack is developed along 1 o'clock direction at step 1792 (RF3), and another secondary crack is developed along 11 o'clock direction at step 1833 (RF4). At these two steps, a jump in maximum crack width can be observed in Figure 4.17. This is because of the location of these two cracks. The cone area circled by these two cracks is the critical area of this model. The top crack of this model is caused by the bending behavior of the concrete cover. Therefore, after push-out behavior caused by the formation of these two secondary cracks, the normal compressive stress on both sides of the top crack is released. Then a major increase in maximum crack width is performed.

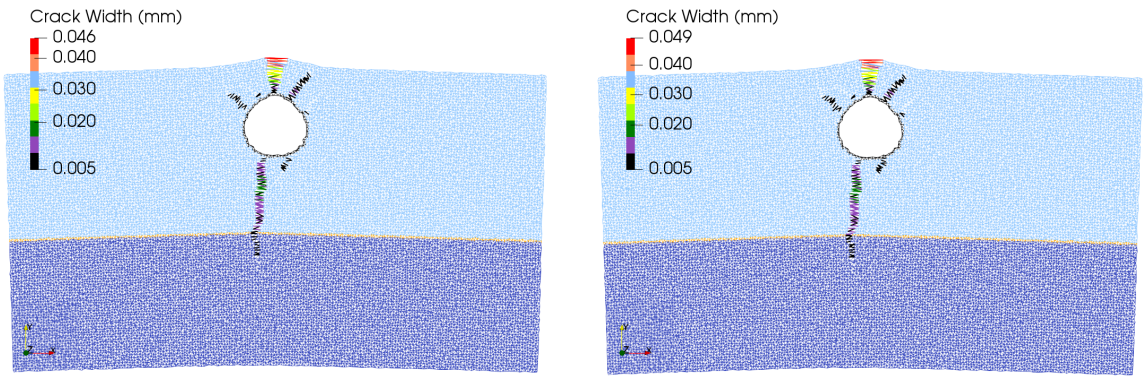

(a) Step 1792, RF3 (b) Step 1833, RF4

Figure 4.19: Crack Plots at Jump in Max Crack Width

Until step 3520 (RF5), there are two more secondary cracks performed at 1 and 2 o'clock direction. This is due to the tension-softening behavior implemented in the repair mortar. With after-peak fracture energy, a performed crack has higher strain capacity before full damage. It allows more cracks to be developed near the existing cracks. Moreover, due to the randomness of the model itself, those cracks are only performed at the right side of the model. Actually, some elements are damaged on the left side, but they are not further developed. However, at step 3520, the bottom crack has already been developed close to the bottom edge. Therefore, the unbreakable bottom edge starts showing its influence after this step. At step 4146 (Figure 4.20b), the second inclined crack at the bottom has been developed towards the mortar-substrate interface. The formation of this crack is due to the stress redistribution caused by the bottom edge. This behavior is not in line with real case anymore. Therefore, step 3520 will be the last step with a reasonable crack pattern.

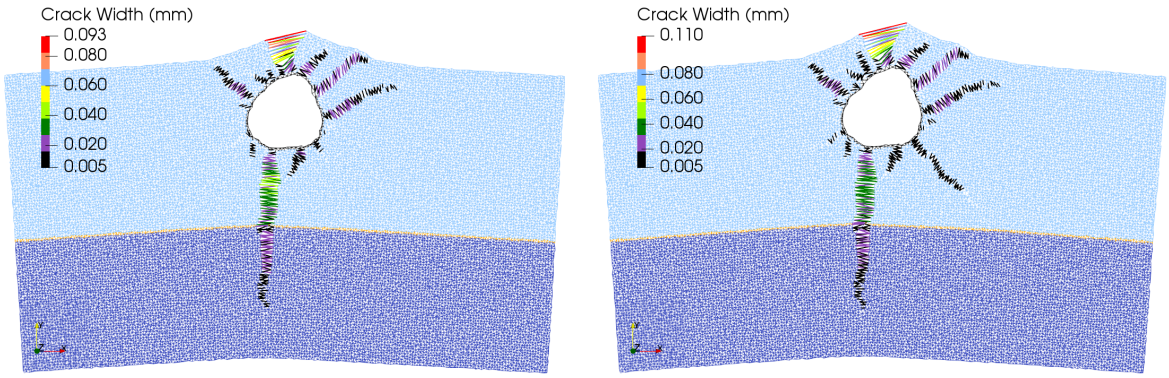

(a) Step 3520, RF5 (b) Step 4146

Figure 4.20: Crack Pattern Influenced by Bottom Boundary

A comparison of damage pattern at the last reasonable step with lattice model (brittle and softening mortar) and experiment is shown in Figure 4.21. With softening property in re-

pair mortar, the model produces more secondary cracks in 2 o'clock direction than the brittle model. This verifies the conclusion that the increase in strain capacity can result in more separated secondary cracks. At the final reasonable step, the maximum crack width of softening model (0.093 mm) is 24.73% higher than the brittle model (0.070 mm). This is also brought by the after-peak softening in the softening model. With higher strain capacity, the model can hold more pressure before failure. This results in the higher maximum crack width in softening model. Another proof is that in the maximum crack width - pressure curve (Figure 4.17), the first major jump in maximum crack width is at higher pressure in softening model than the brittle model. Moreover, the curve (Figure 4.17) shows that the increase in maximum crack width of the brittle model is steeper than that of softening model after the jump in maximum crack width. Therefore, the implementation of tension-softening helps to increase the load capacity and maximum crack width that this model can reach.

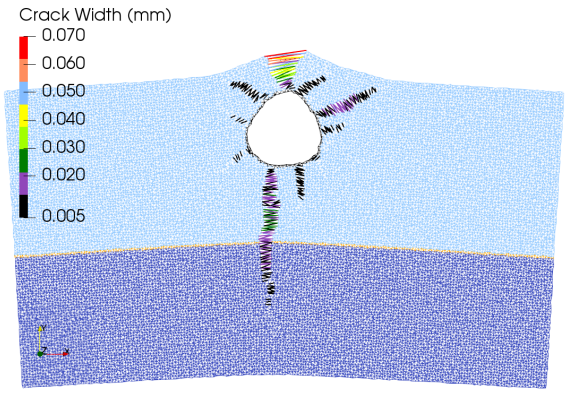

(a) Step 776, Brittle Mortar

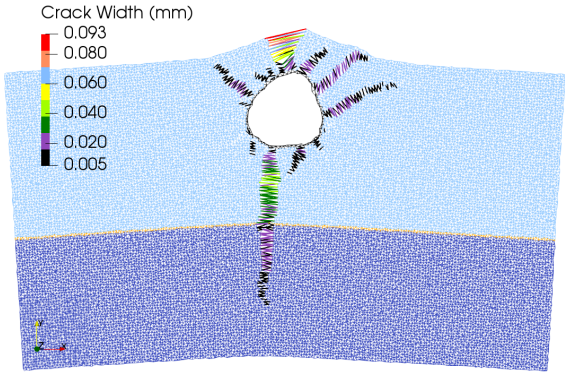

(b) Step 3520, Strain-Softening Mortar

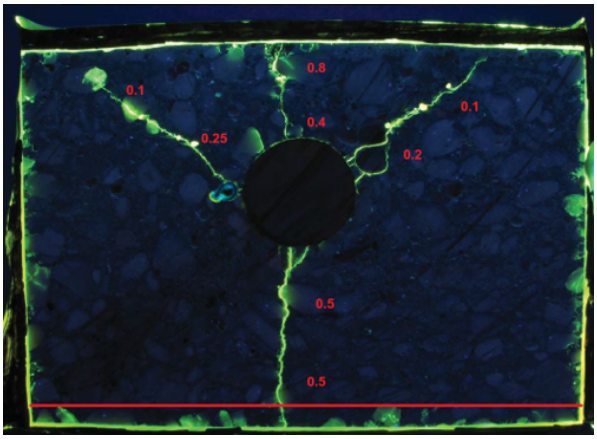

(c) Experiment

Figure 4.21: Comparison of Damage Pattern

Comparing the damage pattern of lattice models and experimental results, the damage is very similar. One major crack at the top is developed because of bending in that area (wide at the top and thin at the bottom). The second widest crack is developed at the bottom. Some other cracks are developed in 11 and 1 o'clock direction. This crack pattern corresponds with experimental results well. The ratio of the maximum crack width of bottom crack and top inclined crack over the major top crack in lattice models and experiment are shown in Table 4.3. The ratio from lattice models has less than 5% difference with experiment. Therefore, a conclusion can be drawn that the lattice model can describe the cracking behavior of normal concrete in accelerated corrosion test. This is due to one main advantage of the lattice model: the solution method. In the lattice model, a sequentially linear analysis method is applied which damages only one element (integration point) in one step and avoid convergence problem. Thus, the model can follow the input constitutive relation precisely, which produces a good prediction of the crack pattern.

Also, all the cracks in the lattice model are performed one by one, which shows a good process in the crack development and avoids bifurcation problem. Moreover, some microcracks are developed and joining the nearby major cracks. This behavior can also be observed in experimental results. This is due to another advantage of the lattice model: built-in randomness. With this imperfection, some microcracks can be localized around the void instead of distributing the stress over a smeared area. With the help of this randomness, the study of really local cracking behavior is possible, which allows describing the cracking behavior even better.

Table 4.3: Crack Width Ratio

Model	Bottom Crack / Major Top Crack	Inclined Top Crack / Major Top Crack
Brittle Mortar Model	43.01%	26.88%
Softening Mortar Model	42.86%	28.57%
Experiment	46.97%	26.85%

Although the maximum crack width of the softening mortar model increases 32.85% compared with the brittle mortar model, it is still one order of magnitude lower than the experiment. Therefore, the lack of after peak fracture energy is not the main reason for the difference in maximum crack width. This is probably because of the characteristics of the

lattice model itself. By using a lattice beam to represent the connection of two square plain stress elements, the number of degree of freedom is reduced from 16 (quadratic elements) to 6 (2D). Therefore, the lattice model is more brittle and cannot hold higher pressure. Another reason is that the lattice model has to damage one element at one step. Thus, after specific steps, the analysis is forced to stop because of the influence of boundary conditions. However, the experiment can continue after a through crack is developed. Moreover, the crack width in the lattice model is calculated as the difference in the length of the deformed and the original lattice beam. This calculation is inferior to the crack band width theory and rotating crack theory applied in the continuum model. This could also be the reason for the difference in crack width.

In conclusion, the lattice model performs well in simulating the crack pattern of normal concrete in accelerated corrosion test. However, the crack width in the lattice model is underestimated. Therefore, the lattice model is a useful tool to predict the cracking behavior of normal concrete at structural level qualitatively instead of quantitatively.

5

IMPLEMENT OF STRAIN HARDENING CEMENTITIOUS COMPOSITE

Strain Hardening Cementitious Composite (SHCC) is the material with the most fracture energy and strain capacity used in the accelerated corrosion test. Due to the strain-hardening behavior of SHCC, its cracking behavior is completely different with material ON06 (can be regarded as normal concrete). Instead of concentrated cracks, a distributed crack pattern with smaller crack width is performed. In this chapter, the performance of the lattice model and continuum model in simulating this unique cracking behavior will be investigated.

5.1. MATERIAL PROPERTY

In the lab test done by SGS Intron, a three-point bending test was done with SHCC instead of direct tension test. Therefore, a reverse engineering process needs to be applied to get the stress-strain relation under direct tension. However, this experiment is using the same composite with Luković's research in the performance of concrete repairs with SHCC [14]. In her work, the stress-strain relation of SHCC under direct tension is studied and can be directly adopted:

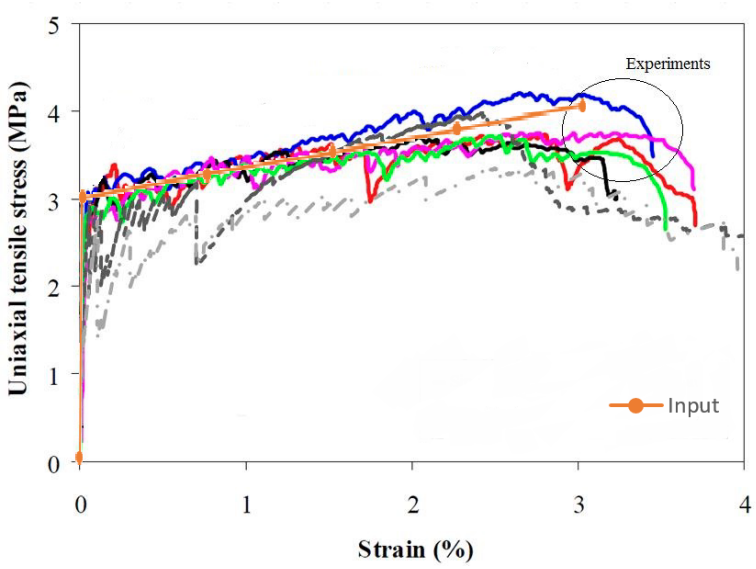

Figure 5.1: Tensile Stress-Strain Curve of SHCC [14]

The five colored curves in Figure 5.1 are the test results from a direct tension test. For all five tests, the tensile strength is around 3.1 MPa. Meanwhile, the ultimate hardening strain and ultimate tensile strain are around 3.02% and 3.43% respectively. A multi-linear interpolation of constitutive relation for material input can be calculated and displayed in Figure 5.1. Based on this, the material input for repair mortar in the lattice model is still defined by five segments.

Table 5.1: SHCC Material Property Input

Number of Segment	E (GPa)	G (GPa)	f_t (MPa)	f_c (MPa)
1	18.725	7.8021	3.1	-48.9
2	0.4398	0.1832	3.375	-48.9
3	0.2404	0.1002	3.65	-48.9
4	0.1730	0.0721	3.925	-48.9
5	0.1391	0.0579	4.2	-48.9

In continuum model, tensile curve FRCCON (fib fibre reinforced concrete, total strain based) (Figure 2.12) is chosen to describe the tensile behaviour of SHCC. The input value in continuum model is showed in Table 5.2.

Table 5.2: DIANA SHCC Input

E (MPa)	f_t (MPa)	f_{Ri} (MPa)	ϵ_i	f_{Rj} (MPa)	ϵ_j	f_{Rk} (MPa)	ϵ_k	ϵ_u
18725	3.1	3.4667	0.010177	3.8333	0.020189	4.2	0.0302	0.0343

In order to verify this material input adopted from the direct tension test, a three-point bending test has been performed with the continuum model. A 2D model with plain stress elements is developed. The size of the beam is $390mm \times 75mm \times 100mm$ in length, width, and height. A notch is designed in the middle with $5mm$ width and $20mm$ height. All these dimensions are kept identical to the experiment. SHCC is applied to all elements of this model. A schematic view of this three-point bending model is shown in Figure 5.2.

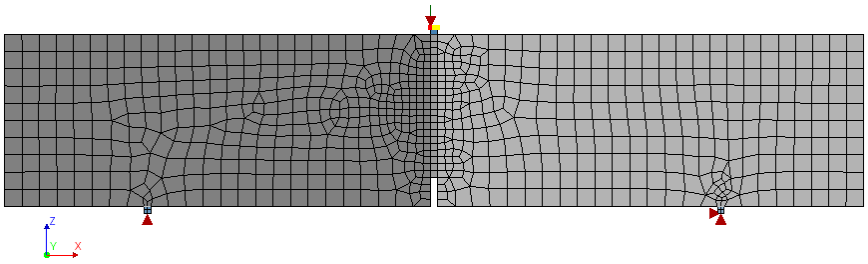

Figure 5.2: Three Point Bending Model

Figure 5.3 shows the comparison of stress - crack mouth opening distance (CMOD) curve between simulation and tests. In the elastic stage, the stiffness shows good correspondence with experimental results. The tensile stress is always within the range of experiment until 200 microns. There is a drop in stress after the localization of the first crack which cannot be observed in the simulation. This drop is because of the stress redistribution after the first crack. However, this does not influence the overall correspondence of the simulation. Therefore, the material input is verified and can be further applied in accelerated corrosion simulations.

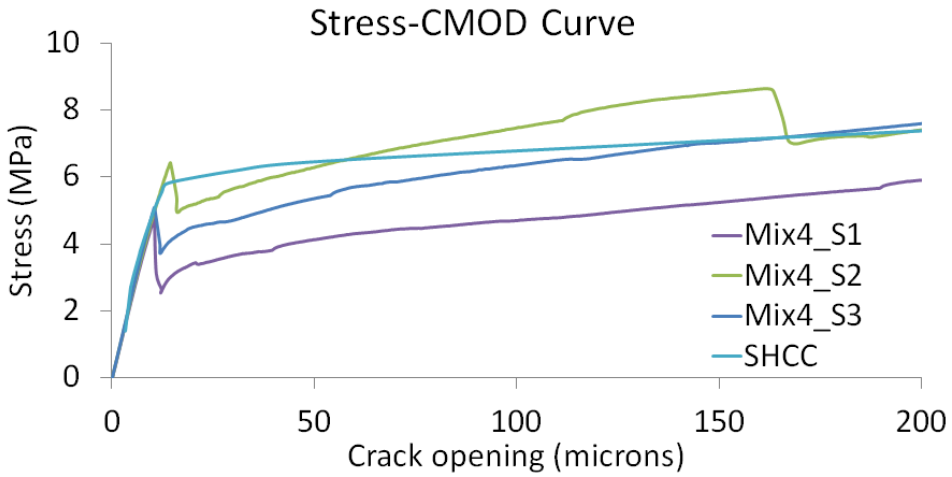

Figure 5.3: Stress-CMOD Curve in Three Point Bending

Except for the material property of repair mortar, all the other aspects of lattice model: substrate property, loading condition, and boundary condition are kept identical to the model

with softening mortar in Section 4.3. Meanwhile, the continuum model is completely identical to the model loaded by prescribed deformation in Section 3.4 except tensile behavior of repair mortar. The schematic view of both models is shown in Figure 5.4.

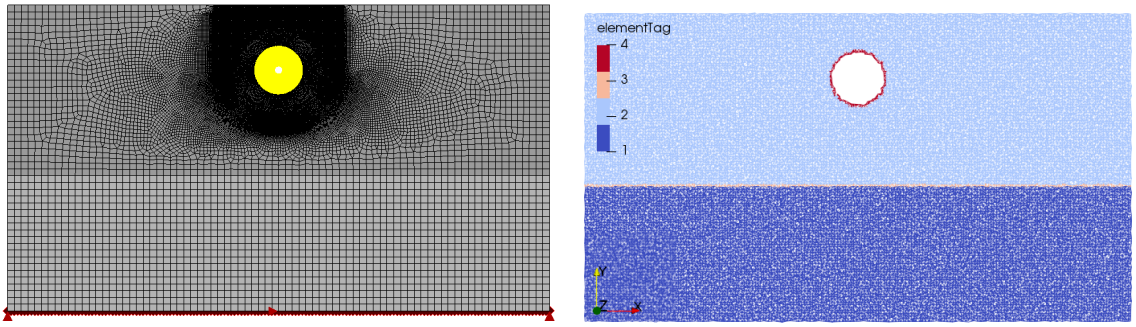

(a) Continuum Model (b) Lattice Model

Figure 5.4: Crack Localization at Non-converged Steps

5.2. COMPARISON OF CRACK DEVELOPMENT

Figure 5.5 shows a comparison of the maximum crack width by average load pressure between the continuum model and lattice model. The two models are showing different behavior in this curve. The maximum crack width of the lattice model always stays lower than 0.05 mm. After a small jump at the beginning, the maximum crack width increases relatively slow. However, the maximum crack width in continuum increases very slow at the beginning. After load pressure 9.9 MPa, the maximum crack width starts increasing sharply until 0.254 mm. Meanwhile, the maximum crack width in the repair mortar part of the continuum model remains at a relatively low level. The cracking development will be examined in detail to investigate the reason for this difference in maximum crack width development.

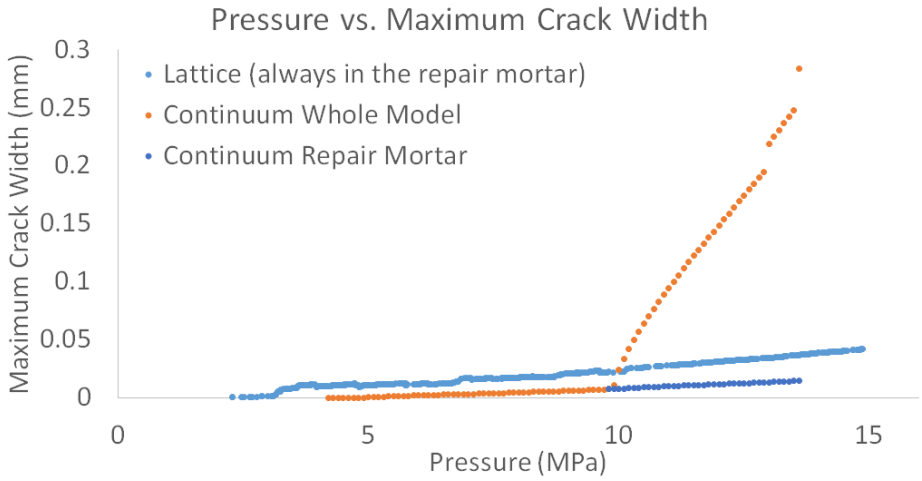

Figure 5.5: Maximum Crack Width - Pressure Curve

In order to illustrate the behavior of the lattice model more clearly, Figure 5.6 shows the pressure - maximum crack width curve of lattice model only. Several reference location (RF) is marked in the curve to represent the critical steps during the analysis.

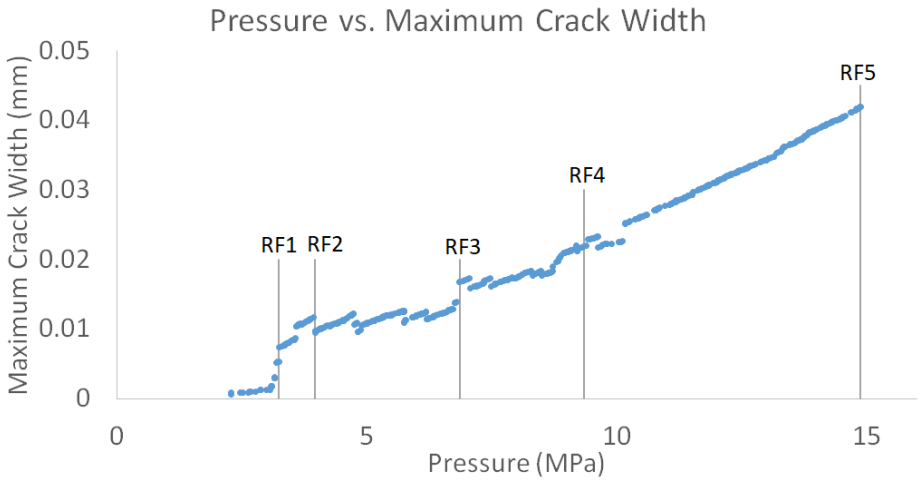

Figure 5.6: Maximum Crack Width - Pressure Curve Lattice Model

At step 101 (RF1), one top crack is localized (Figure 5.7a). The localization of this top crack causes the jump in maximum crack width. Meanwhile, some other microcracks are initialized around the void. At step 258 (RF2), a slight drop in maximum crack width is observed (Figure 5.7b). At this step, a second top crack is localized. The formation of this crack closes the first top crack slightly which results in the drop in maximum crack width. Some more drop can also be observed in later steps. All of these behaviors are due to the formation of more top cracks next to the first top crack.

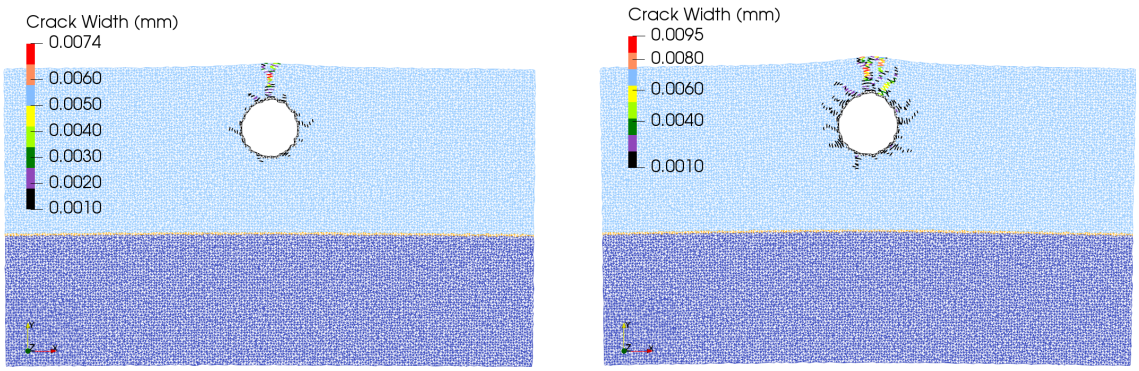

(a) Step 101 (b) Step 258

Figure 5.7: Crack Pattern at RF1 and RF2

Figure 5.8 shows the damage pattern at step 1101 (RF3) and step 2081 (RF4). At these two steps, a slight jump in maximum crack width can be observed in Figure 5.6. At these two steps, two bottom cracks propagate through the mortar-substrate interface. The strain capacity of the substrate (brittle, 0.01%) is significantly lower than repair mortar (302 times lower). When the bottom cracks reach the interface, the strain level is much higher than the elastic strain of the substrate. Thus, the cracks in the substrate are suddenly widened. Therefore, the cracks in the substrate are wider than in SHCC. This difference is crack width in SHCC and normal concrete can also be observed in Luković's work about SHCC repair system in a beam under bending [14]. This is a good proof that the lattice model can simulate the cracking behavior of SHCC precisely. Moreover, the microcracks around the void at RF2 is further developed into distributed cracks. In the top "cone" critical area defined in softening mortar model, more top cracks are developed next to each other, which turns this area into a "smeared" cracking area. The concentrated cracks at the top cannot be produced anymore.

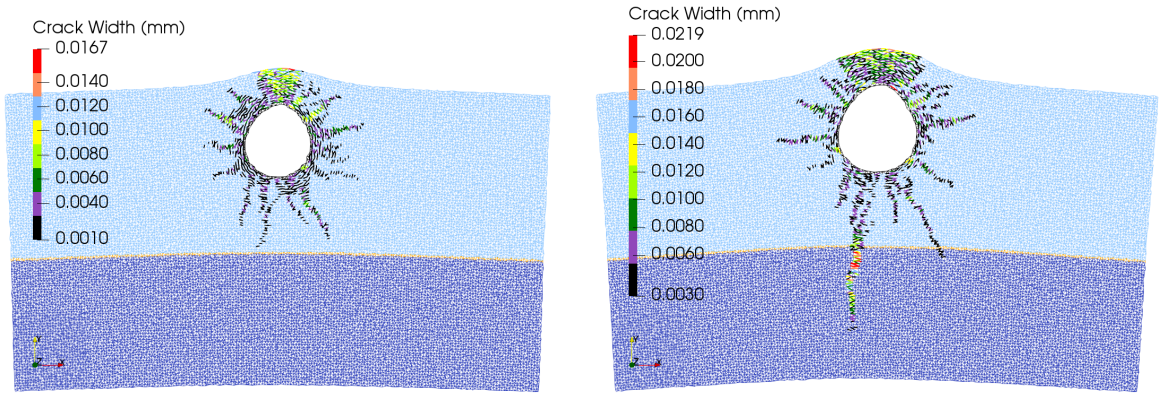

(a) Step 1101 (b) Step 2081

Figure 5.8: Crack Pattern at RF3 and RF4

At step 3775 (RF5), more secondary cracks are developed further. Two other bottom cracks reach the mortar-substrate interface. This distributed crack pattern is more and more clear in this model. However, at this step, the inclined bottom crack shows the trend to develop horizontally. Because this crack gets too close to the bottom edge that the unbreakable bottom edge starts showing influence on the stress distribution within the model. Therefore, the results after this step are not reasonable anymore (Figure 5.9b).

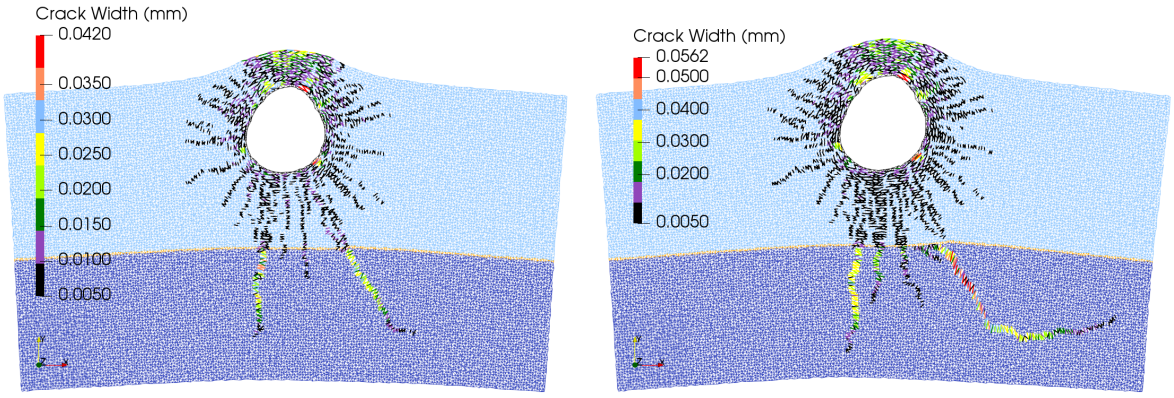

(a) Step 3775 (b) Step 4684

Figure 5.9: Crack Pattern at RF5 and Failure Step

Figure 5.10 shows a comparison of crack pattern between the lattice model and experiment. In general, the lattice model can simulate the distributed crack pattern of SHCC repair system. This behavior comes from the strain-hardening behavior after elastic tensile failure. With hardening after tensile failure, a developed crack can hold even more stress after crack initialization which allows some other cracks developed next to it. The fracture energy is released through more cracks which results in the decrease in average crack width. Moreover, the sequentially linear solution method is also a considerable advantage. Because it is a series of linear analysis. Lattice model can successfully avoid the convergence problem. Also, this method only damages one element (integration point) each step. This allows lattice model follows the constitutive relation more precisely than incremental solution method and avoids bifurcation problem. Meanwhile, the built-in randomness of lattice model helps also in the initialization of the microcracks around the reinforcement at an early stage. These two main advantages help lattice model produce an accurate crack pattern of SHCC repair system in accelerated corrosion test.

However, in the top cracking area, a smeared cracking zone is developed instead of separated discrete cracks. This area is the most critical area of the model because of its thinnest concrete cover. Therefore, the strain level in this area is the highest. Thus, there are so many cracks developed in this area that the randomness is not high enough to perform discrete cracks. Meanwhile, the maximum crack width that lattice model can reach is still much lower than the experimental level. As explained in Section 4.3, this is due to the characteristic of the lattice model. By using a lattice beam to represent the connection of one

square plain stress element, the degrees of freedom per element is reduced from 16 to 6. Therefore, the lattice model is more brittle and cannot hold higher pressure as high as experimental level. Another reason is that the lattice model has to damage one element at one step. Thus, after certain steps, the analysis is forced to stop because of the influence of boundary conditions. Moreover, the crack width in the lattice model is calculated in a relatively inferior way (does not consider crack rotation). This could also be the reason for the difference in crack width.

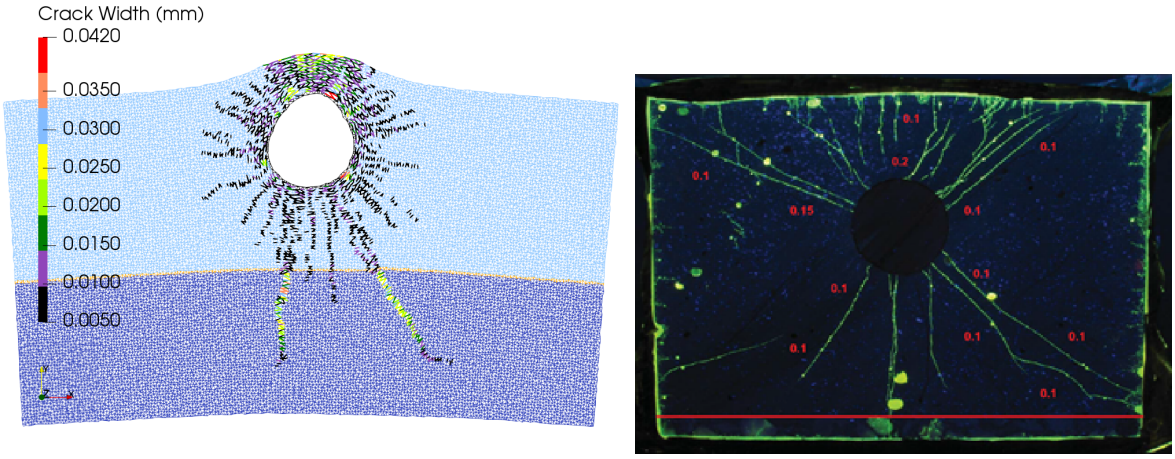

(a) Lattice Model (b) Experiment

Figure 5.10: Comparison of Crack Pattern, Lattice Model vs. Experiment with SHCC mortar

However, the cracking behavior in the continuum model is entirely different. Before the sharp increase in maximum crack width (pressure 9.8 MPa in Figure 5.5), there is no crack localized actually. Figure 5.11a shows the principle stress S1 at this step. A huge area around the reinforcement has stress higher than 3.1 MPa. Due to the strain-hardening behavior of SHCC, an element can hold higher stress after its tensile failure. Therefore, more stress can be transferred to the surrounding elements. Because of the homogeneity of all the elements, it is complicated for the model to find a discrete path to crack. Thus, the smeared cracking area is performed around the reinforcement. Due to the thinnest concrete cover, the top area has the highest strain level. This corresponds to the conclusion from the lattice model. Three other smeared cracking areas are located at 10, 2 and 6 o'clock direction, which are also the areas where distributed cracks are performed in the experiment.

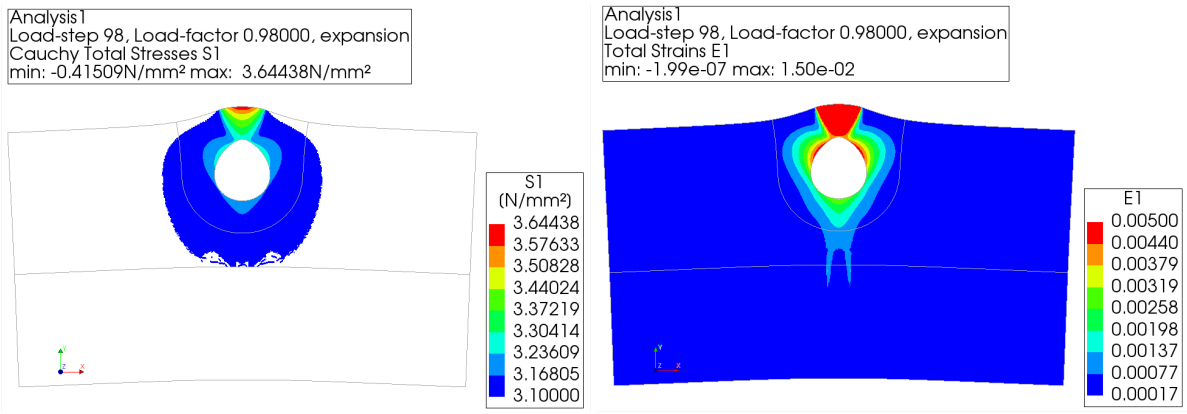

(a) Principle Stress S1 (b) Principle Strain E1

Figure 5.11: Strain and Stress Plot at Pressure 9.8 MPa

After this step, the stress propagates into the substrate. Some elements in the substrate reach their tensile strength. The substrate is modeled as normal plain concrete which means that the fracture energy of the substrate is significantly lower than SHCC. Therefore, the stress is more concentrated instead of smeared over an area. Thus it is easier for the model to localize a crack as in softening mortar model. Figure 5.12 shows the crack width of continuum model at pressure 13.6 MPa. A discrete bottom crack can be observed in the substrate. This verifies the assumption that the strain-hardening behavior influences the localization of cracks. However, with the lattice model, a discrete crack pattern can be produced from SHCC mortar (Figure 5.10a). The advantage of the lattice model comes from its built-in randomness. By the random distribution of lattice beams, an imperfection is applied in lattice model which can help concentrate stress along certain path instead of spreading over an area. Therefore, this localization of cracks in the continuum model with SHCC can be improved by implementing certain randomness into the model.

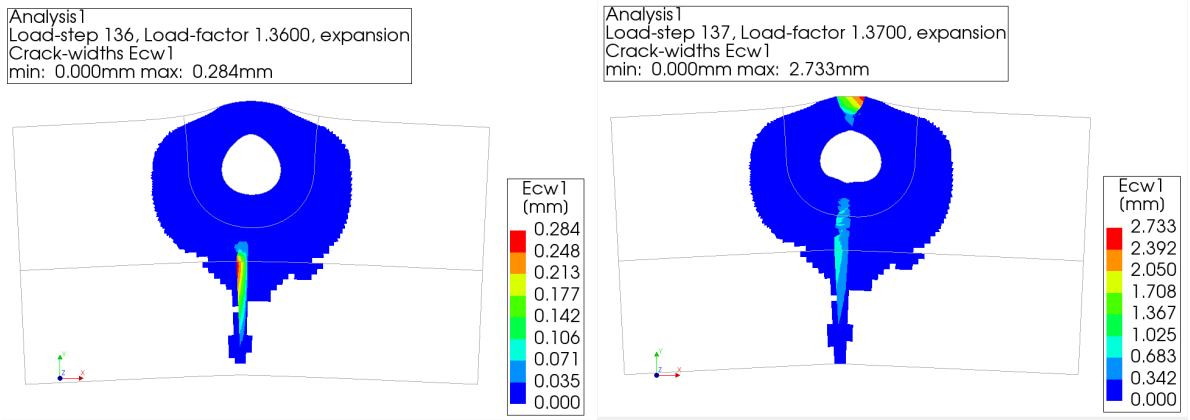

(a) Pressure 13.6 MPa (b) Pressure 13.7 MPa

Figure 5.12: Crack Plot at the Final Step

Two localized cracks are observed in the analysis after step pressure 13.6 MPa (Figure 5.12b. This is because of the convergence problem in this model. The convergence norms applied in this model are the force and displacement norm with a tolerance of 0.01. However, the relative differences of the norms at this step are 0.5709 and 0.6199 which are more than 50 times higher then criteria. Thus, the results from this step are not accurate enough anymore. At this step (pressure 13.7 MPa), too many integration points have principle tensile strain larger than the ultimate tensile strain. The stiffness of these points is zero in the stiffness matrix, which makes the stiffness matrix not positive definite anymore. Thus, the stiffness matrix is hard to be inverted under this situation and the convergence norms cannot be satisfied anymore. Even when decreases the step size 100 times lower, it is still not possible to overcome the convergence problem. By decreasing step size, the occurrence of the convergence problem is only delayed instead of solved. However, at this pressure level, the stiffness matrix is just in too ill-conditioned to let the analysis go further. Therefore, this convergence problem cannot be avoided.

5.3. RANDOM FIELD ON TENSILE STRENGTH

5.3.1. RANDOM FIELD GENERATION

In Section 5.2, the lattice model with built-in randomness can perform the distributed crack behavior in SHCC instead of the smeared cracking area in the continuum model. Therefore, the performance of the continuum model can be improved by implementing certain randomness into the model. SHCC (and concrete) is never a homogeneous material. Therefore, the randomness in the lattice model is representing the heterogeneity of the material. A random field over the tensile strength in the continuum model should have a similar effect. The random field also can be attributed to material heterogeneity, which always occurs on macro-scale structural elements. Moreover, the mixing and compacting process can also result in material anisotropy, which is another theoretical basis for applying this random field while simulating the cracking behavior of SHCC.

A random field $\boldsymbol{z}_c(x)$ is a continuous function in space, consisting of infinite small parts which are associated with a random variable [41]. A Covariance Matrix Decomposition

method (CMD) is chosen in this case to generate a set of correlated random variables (tensile strength in this case):

$$\boldsymbol{z}_c(x) = \boldsymbol{L}\chi \tag{5.1}$$

in which $\boldsymbol{z}_c(x)$ is the vector containing spatially correlated random variables, χ is the vector of independent zero mean, unit variance and normally distributed random variables and $\boldsymbol{L}$ represents for the decomposed correlation matrix. For n random variables collected in vector y, the correlation matrix is defined as:

$$\boldsymbol{R}_{ij} = \frac{Cov(y_i, y_j)}{\sqrt{Var(y_i)Var(y_j)}} = \begin{bmatrix} 1 & \rho(y_1, y_2) & \cdots & \rho(y_1, y_n) \\ & 1 & \cdots & \rho(y_2, y_n) \\ & & \ddots & \vdots \\ & & & 1 \end{bmatrix} \tag{5.2}$$

This matrix has to be decomposed in such a way that the vector $\boldsymbol{z}_c$ has to be normally distributed random variables having zero mean, a unit variance and a specific correlation. Cholesky decomposition method is applied at this step to decompose matrix into a upper triangular and a lower triangular matrix [42]:

$$\boldsymbol{R} = Cov[\boldsymbol{z}_c, \boldsymbol{z}_c] = E[\boldsymbol{z}_c \boldsymbol{z}_c^T] - E[\boldsymbol{z}_c]E[\boldsymbol{z}_c^T] = \boldsymbol{L}\boldsymbol{L}^T \tag{5.3}$$

A correlation function is applied to calibrate the values in the correlation matrix $\boldsymbol{R}$. An exponential correlation function (EXP) was used as function of leg distance (Δ_x):

$$\rho(\Delta_x) = \rho + (1-\rho)\exp(\frac{\Delta_x}{d_c}) \tag{5.4}$$

in which, ρ is the threshold value for minimum correlation. In the probabilistic model code, Joint Commission of Structural Safety (JCSS) suggests a value of 0.5 for this threshold value [43]. d_c represents the correlation length which is an important parameter in random field. It indicates the variability in the random field which in practical defines a certain area that the parameter with randomness is kept identical with this area. The correlation length is

defined in Vanmarcke's work as [44]:

$$d_c = \lim_{D\to\infty} D\gamma(D) \tag{5.5}$$

in which, D is the averaged random field domain and γ is the variance function. However, it is very difficult to determine the correlation length in practice. The value of the correlation length of concrete specimen depends on multiple factors: specimen size, specimen shape, aggregate size etc. In Kabele's study, a fictitious value is given without any explanation [13]. However, in van der Have's research, he did a sensitive test of correlation length with a concrete floor under pressure. With decreasing correlation length, the crack band gets smaller [41]. Considering SHCC is a very fine material (without aggregate), a relatively small correlation length is needed. Following the same correlation length / specimen size in van der Have's paper, the correlation length is defined with a value of $1mm$ in this model.

For the distribution type of variable, a log-normal distribution is implemented in this model. If a variable Y has to be normal distributed, it has a logarithm relation with variable X: $Y = ln(X)$. This ensures that variable X is always greater than zero. Variable X follows the following transformation:

$$X = exp(\mu_Y + \sigma_Y Y) \tag{5.6}$$

in which, μ is the mean value and σ is the standard deviation. The components in Eq. 5.6 can be calculated as:

$$\sigma_Y^2 = ln(1+\frac{\sigma_x^2}{\mu_x^2}) \qquad \mu_Y = ln(\mu_X) - \frac{1}{2}\sigma_Y^2 \tag{5.7}$$

From Petr and Viktor's research [12] the standard deviation of tensile strength for SHCC under monotonic load is 0.3 by average. However, for SHCC (using tensile curve FRCCON) directly applying random field over its tensile strength is not accurate. Due to its strain-hardening behavior, it is more precise to scale the whole tensile stress curve instead of changing tensile strength only. There is a "Stress Factor Fibre Reinforced Concrete model" (FRCFAC) available representing the scaling factor of tensile stress. Thus, a transformation is needed to convert the standard deviation of tensile strength into the standard deviation of FRCFAC:

$$\sigma_{FRCFAC} = \sigma_{f_t} \cdot \frac{FRCFAC}{f_t} = 0.0968 \tag{5.8}$$

After a random field domain D is generated, it is imprinted on nodes in the mesh of the continuum model. An example of the generated random field is shown in Figure 5.13. This random field is only applied over the repair mortar. Thus, the substrate is in white.

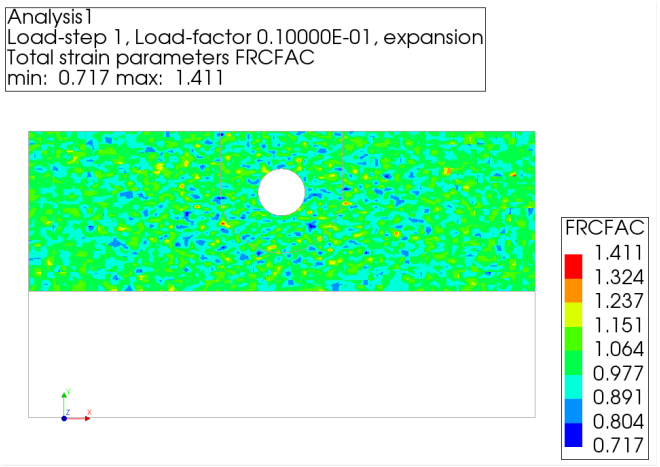

Figure 5.13: Generated Random Field

5.3.2. RESULT COMPARISON

The Load Pressure - maximum crack width curve for all three models with SHCC are displayed in Figure 5.14. The continuum model with random field follows a similar behavior in maximum crack width to the homogeneous continuum model. The sharp increase in maximum crack width indicates that a crack in the substrate is localized after the stress propagates through the mortar-substrate interface. However, the sharp increase in maximum crack width (pressure 9 MPa) happens slightly earlier than the homogeneous continuum model (9.8 MPa). This implies that stresses are more concentrated before the localization of the substrate crack. The detailed comparison in crack pattern between the two models will be explained.

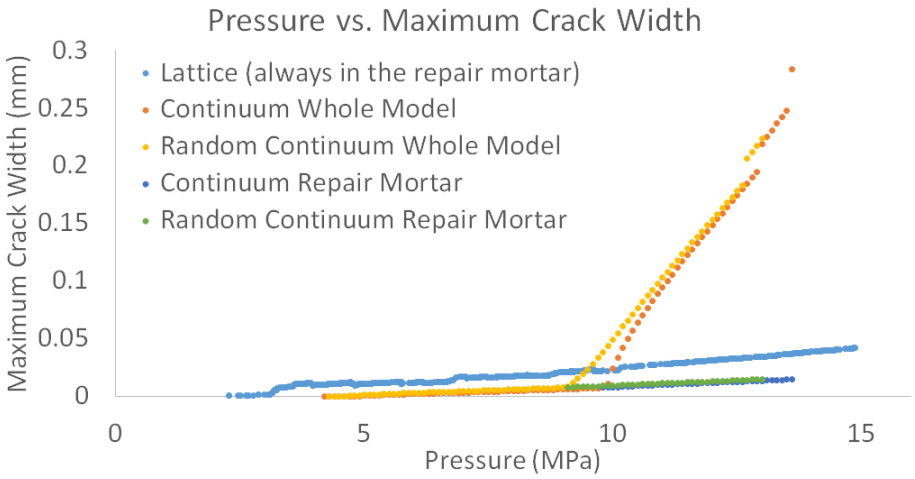

Figure 5.14: Pressure-Maximum Crack Width Curve of SHCC Models

With the help of the random field, this continuum model is now capable of performing a different stress distribution than the homogeneous model. Figure 5.15 shows the crack width Ecw1 distribution of both models. In the random field model, the distribution of damaged elements (colored, have crack strain) is relatively discrete instead of the smeared distribution around the reinforcement in the homogeneous model. Also, elements with crack width higher than 0.001 mm (in red) can display discrete cracks around the steel rod. Therefore, the random field in the continuum model indeed can help in the localization of cracks. Because of SHCC's strain-hardening behavior, it is hard for homogeneous continuum model to initialize cracks. However, with the help of the random field, stress distribution is more discrete in this model, which helps a lot in producing distributed cracks.

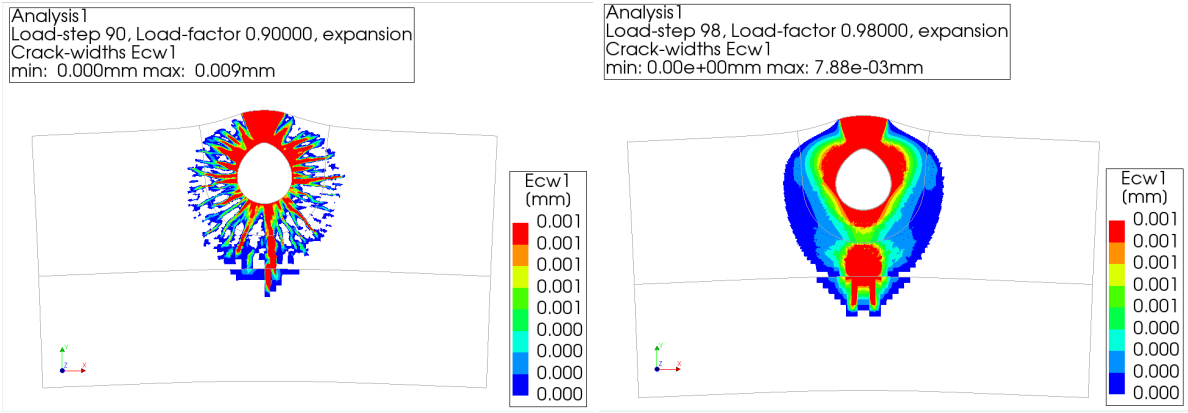

(a) Pressure 9.0 MPa, Random Model (b) Pressure 9.8 MPa, Homogeneous Model

Figure 5.15: Comparison of Crack Width Distribution

With the development of the analysis, one of the bottom cracks in reaches the mortar-substrate interface. Then a bottom crack in substrate is localized (Figure 5.16a). This localization happens earlier in the random model than the homogeneous model. As the stress distribution now is more discrete instead of smeared over an area, the released fracture energy at same pressure level is transferred by fewer elements in the random model. Thus, the stress is transferred to the substrate at a lower load level which results in an earlier crack localization in the substrate. Also, the random model has a convergence problem with load pressure higher than 13.0 MPa as in the homogeneous model (Figure 5.16b). After this step, too many integration points in the top cone area have reached their ultimate tensile strain. Thus the stiffness of these nodes is zero in the stiffness matrix which results in an ill-conditioned stiffness matrix. Then, the analysis cannot find convergence after this step.

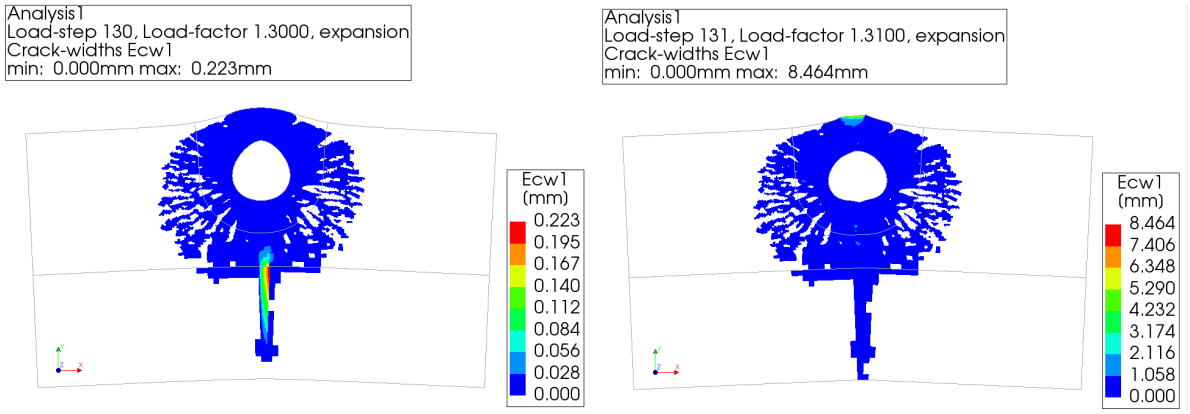

(a) Pressure 13.0 MPa (b) No Convergence Step

Figure 5.16: Crack Pattern by the End of the Analysis

Figure 5.17 shows a comparison of crack pattern among the lattice model, random continuum model, and experiment. It has been proved that the random field on tensile strength in the continuum model has a similar effect as the built-in randomness in the lattice model in producing distributed cracks. However, in both continuum and lattice model, the cracks in the top cone area are smeared instead of discrete. This area is the most critical area in this specimen with highest strain level and densest crack distribution. Thus the randomness in both models is not strong enough to distribute the stress into a discrete way. In Luković's work, a lattice model was developed with also fibers and interface elements which means an extra degree of randomness in that model [7]. With that model, the distributed cracks at the top can be successfully produced. However, the size of that specimen is one order of magnitude lower. Thus it is not practical to model fibers discretely in this model. In general, both random continuum model and lattice model can describe the crack pattern of SHCC in accelerated corrosion test in a reasonable manner. It is necessary to implement a random field in the continuum model to simulate the distributed crack pattern of SHCC.

However, there is a difference between the lattice model and continuum model on the crack width of the bottom crack in the substrate. The crack width of bottom crack in the lattice model is roughly at the same size level with the top cracks. However, in the continuum model, this ratio is around 20. In the experiment, the substrate is cut off. Thus the crack width of this crack cannot be compared to experimental results. However, a two-layered (one SHCC, one normal concrete) beam in three-point bending is studied by Luković [45]. A larger crack width in normal concrete can be observed as it is in the continuum model. This

is another proof that the lattice model underestimates the crack width of normal concrete as discovered in Section 4.3.

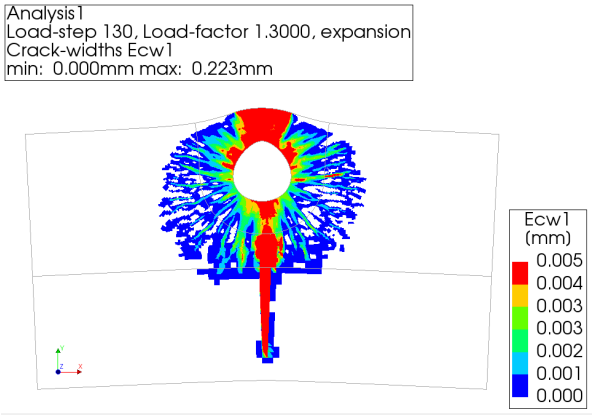

(a) Pressure 13.0 MPa, Random Continuum Model

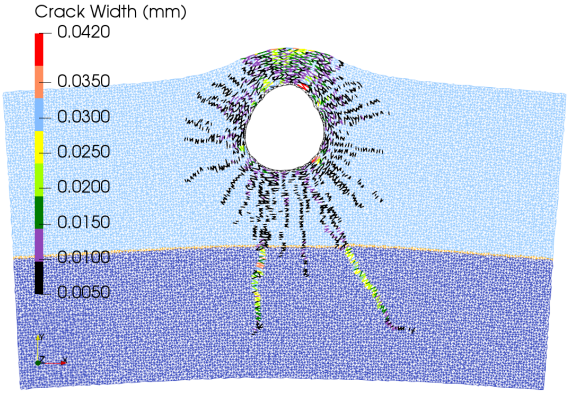

(b) Pressure 14.86 MPa, Lattice Model

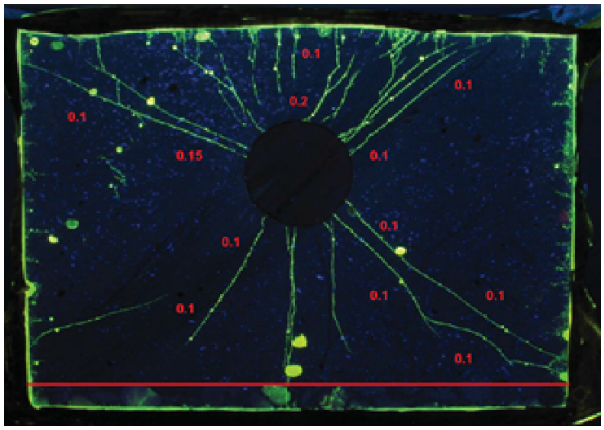

(c) Experiment

Figure 5.17: Crack Pattern by the End of the Analysis

In conclusion, both models have their advantages in simulating the cracking behavior of SHCC. Due to the sequentially linear solution method, the lattice model can follow the stress-strain input precisely and avoid bifurcation problem. Moreover, with the built-in randomness, lattice model can produce the distributed crack pattern of SHCC. Meanwhile, the continuum model can also simulate the distributed crack pattern of SHCC with the help of a random field. Also, due to higher degrees of freedom and the advanced crack width theory, the continuum model shows a higher crack width in the strain-softening mortar. However, convergence is always a problem for the continuum model because of its incremental solution method. This becomes even worse while simulating strain-softening material.

5.4. INFLUENCE OF CORRELATION LENGTH

In Section 5.3, a random field on tensile strength is applied in the continuum model to simulate the cracking behavior of SHCC in accelerated corrosion test. The result proves that the random field has a positive effect in concentrating stress and producing discrete cracks in a model with SHCC mortar. Correlation length d_c is a critical parameter in generating a random field, which indicates the variability in the random field. Thus, correlation length will influence significantly on the distribution of stress. Van der Have found out that the decreasing correlation length results in a decreasing crack band [41]. Meanwhile, correlation length is tough to be determined in practice. Multiple factors including specimen shape, specimen size, and aggregate size can influence the correlation length. Therefore, it is important to investigate the influence of correlation on damage pattern. In this section, three other models with different correlation length are developed:

Table 5.3: Different Correlation Length Models

Model Name	AC_SHCC_0.45	AC_SHCC_1	AC_SHCC_4.5	AC_SHCC_45
Correlation Length (mm)	18.725	7.8021	3.1	-48.9

The influence of correlation length in the generated random field over FRCFAC is displayed in Figure 5.18 and 5.19. The variation in FRCFAC is increasing with the decreasing correlation length. The influence of this variation will be investigated further.

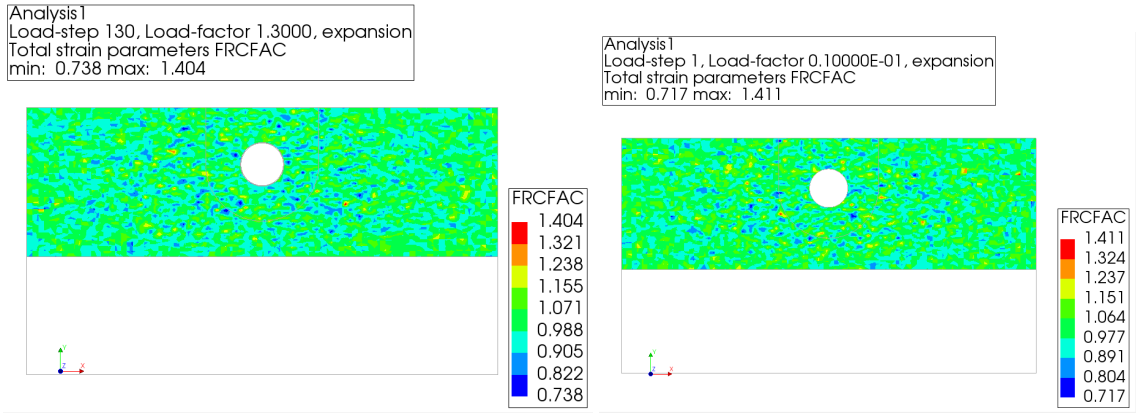

(a) AC_SHCC_0.495 (b) AC_SHCC_1

Figure 5.18: Random Field on FRCRAC with Various Correlation Length (1)

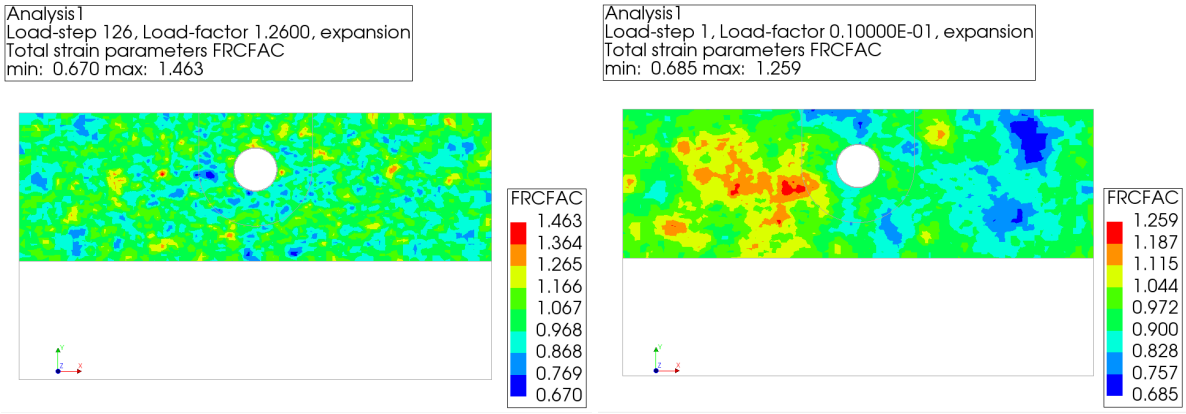

(a) AC_SHCC_4.5 (b) AC_SHCC_45

Figure 5.19: Random Field on FRCRAC with Various Correlation Length (2)

The load pressure - maximum crack width curve of these four models are visualized in Figure 5.20. These four curves follow a similar trend in developing. This indicates that the difference in the random field cannot influence the global crack width development in the continuum model. Moreover, with decreasing correlation length, the load pressure where the bottom crack in the substrate is localized is lower. This verifies the conclusion in Section 5.3 that due to the implementation of the random field, the stress distribution is more concentrated. Therefore, the localization of the bottom substrate crack happens at lower load level. This behavior can also be observed with increasing of variation in the field due to decreasing correlation length. Moreover, at the final steps before the convergence problem (connected by the red line), the convergence problem happens earlier in the model with smaller correlation length.

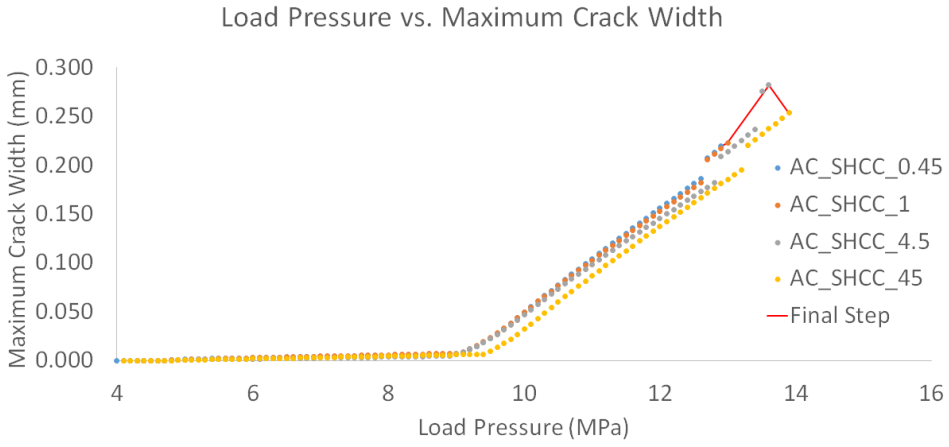

Figure 5.20: Pressure-Maximum Crack Width (Whole Model) Curve of Various Correlation Length Models

Figure 5.21 shows the damage pattern of four models at the last step before the convergence problem. An obvious difference can be observed within these four models. In general, the difficulty to localize cracks increases with the increasing correlation length. Model

AC_SHCC_45 behaves very similar to homogeneous model (Figure 5.21a). No crack can be localized basically in this model which implies that the randomness with correlation length 45 mm is not strong enough to localize tensile stresses. As for model AC_SHCC_4.5, the situation is improved (Figure 5.21b) where some cracks can be localized to the left and right of the steel rod. However, compared to model AC_SHCC_1 (Figure 5.21c, the crack band is wider in this model and none localized cracks are performed in 2 and 10 o'clock direction. Model AC_SHCC_0.45 (Figure 5.21d)behaves very similar to Model AC_SHCC_1. None improvement can be observed in this model. Correlation length of 0.45 mm is an extreme case. Due to the 2 mm mesh size in the continuum model, every node is assigned to a value which is uncorrelated with other values. However, this increase in variation cannot have any effect due to the limitation of the mesh size. Another evidence of this is the development of maximum crack width. In the model with correlation length 0.45 mm and 1 mm, the convergence problem happens at similar steps and the maximum crack width is very close to each other, which indicates that the stress distribution and development in both models are very similar. Therefore, the lower bond of correlation length can be concluded as twice of the mesh size.

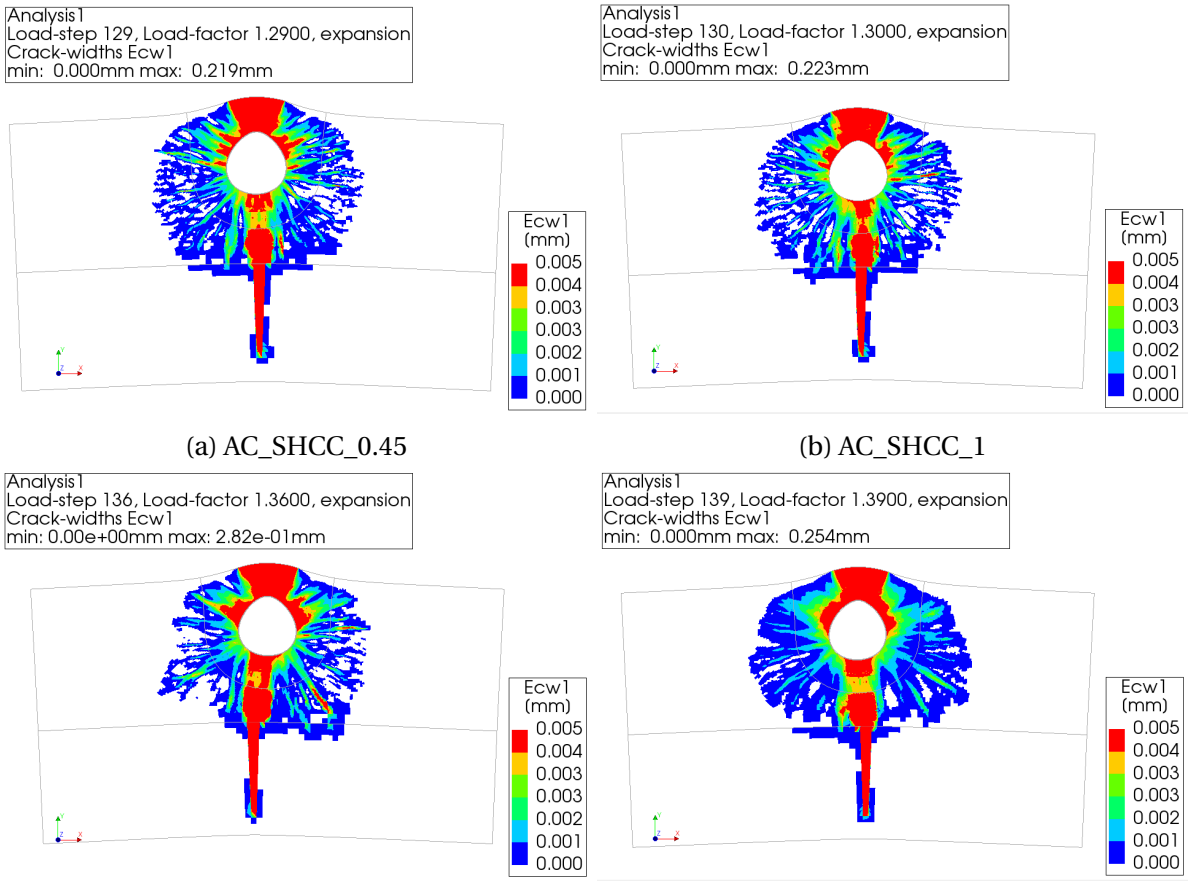

(a) AC_SHCC_0.45

(b) AC_SHCC_1

(c) AC_SHCC_4.5

(d) AC_SHCC_45

Figure 5.21: Crack Pattern of Models with Various Correlation Length

In conclusion, the decreasing in correlation length can indeed improve the performance of the localization of cracks due to the increase in variation in tensile strength. Nevertheless, a lower bond of twice of the mesh size of correlation length is observed. This is due to the limitation of node spacing based on the mesh size. However, all these correlation lengths applied in this section are artificial values. These values are not proved by experiment study. More works need to be done in material aspects to investigate the relation between correlation length and material property. Moreover, the convergence problem is always a problem that continuum model with nonlinear analysis cannot avoid. After enough integration points reach their ultimate tensile strain, it is impossible for the model to find convergence.

6

PARAMETRIC STUDY

In the previous chapters, the performance and critical parameters of the lattice model and continuum model in simulating accelerated corrosion test have been investigated. In those models, two extreme types of materials namely ON06 and SHCC are studied as the repair mortar. ON06 is the fiber reinforced concrete with the least volume of fibers and fracture energy, which can be regarded as normal concrete. SHCC is a fiber reinforced mortar with strain-hardening behavior after tensile failure which has most fracture energy and a strain capacity of 3.43%. Thus, it is interesting to investigate the performance of both models with material between these two extreme cases. Moreover, how the interface tensile strength will influence the damage pattern in the model is another interesting point to be discussed. Therefore, two series of parametric study are conducted in this chapter.

6.1. FRACTURE ENERGY

In this section, materials with different tensile behavior as repair mortar are simulated by lattice and continuum model. The crack development of these materials from both models are studied and compared in detail. The performances of both models on the different materials are evaluated. In the final part of this section, recommendations for modeling is given for further simulations.

6.1.1. MATERIAL SELECTION

In order to study the performance of both models with different repair material, two other types of stress-strain relation are defined to represent two other materials. One is FRC_0% with strain-softening behavior after tensile failure. The other is FRC_50% with half strain-softening behavior. The stress-strain relations of all selected materials are shown in Figure 6.1. Material FRC_0% and FRC_50% have the same strain capacity with SHCC. These three materials follow linear interpolation after the elastic stage. However, FRC_0% and FRC_50% only have 0% and 50% of the ultimate tensile strength of SHCC.

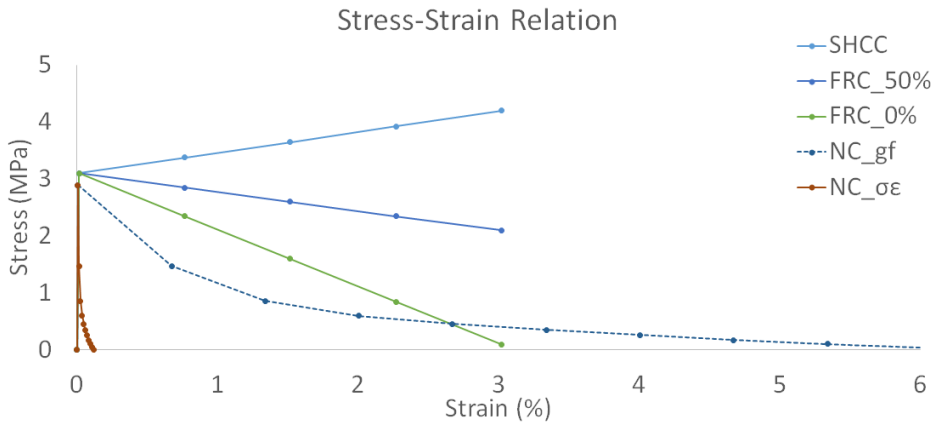

Figure 6.1: Input Stress-Strain Relation

In order to verify the material input, a three-point bending test is done with all the materials in the continuum model. The size of the beam is $390mm \times 100mm$ in length and height. A notch is designed in the middle with $5mm$ width and $20mm$ height. All these dimensions are kept identical to the test done in 5.1. The stress-CMOD curve from the bending test is visualized in Figure 6.2.

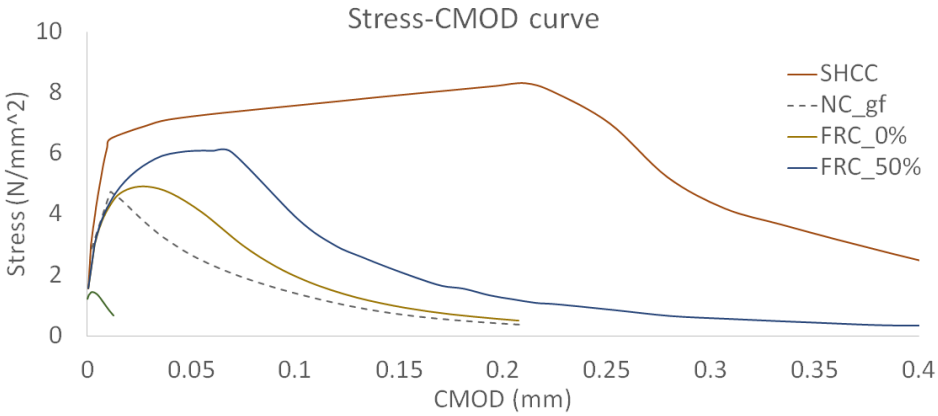

Figure 6.2: Three Point Bending Stress-CMOD Curve

A problem can be discovered in Figure 6.2. The results show that material NC_gf has similar fracture energy as FRC_0%, which is not reasonable. NC_gf represents for material ON06 which is very brittle compared with FRC_0%. This is a problem of mesh objectivity. In DIANA, a "hordijk softening curve" is used to implement material NC_gf. The required parameter is fracture energy G_f^I and tensile stress f_t. Thus the ultimate tensile strain can be calculated as:

$$\epsilon_{nn.ult}^{cr} = 5.136\frac{G_f^I}{hf_t} \tag{6.1}$$

in which, h represents crack band width in the continuum model. The crack band width in this case (quadratic elements) is equal to mesh size 5 mm. Thus, the ultimate tensile strain $\epsilon_{nn.ult}^{cr}$ is 6.01% based on Eq. 6.1, which is even higher than the value of three other materials. Following Eq. 4.4, the actual stress-strain input is NC_gf (dotted line)in Figure 6.1. This is much more ductile than the desired input ($NC\_\sigma\epsilon$, solid line). The fracture energy of NC_gf is comparable with FRC_0%. Therefore, their stress-CMOD relation is similar in the bending test. To make the material input in the continuum model comparable to the lattice model, a multi-linear softening curve is chosen for the continuum model instead of "hordijk softening curve". The tensile behavior is directly implemented as a stress-strain relation in this curve ($NC\_\sigma\epsilon$), which can avoid the mesh objective problem.

As it shows in Figure 6.2, material $NC\_\sigma\epsilon$ behaves very brittle in the bending test which corresponds with the behavior of normal concrete. With increasing fracture energy in the material input, FRC_0% can bear higher pressure than $NC\_\sigma\epsilon$. However, it still shows deflection-softening behavior after tensile failure. Meanwhile, FRC_50% is able to show a deflection-hardening behavior after elastic failure in three-point bending test with half strain-softening input. SHCC shows a strong strain-hardening behavior up to 0.21 mm. These four materials are applied in the accelerated corrosion models to investigate their cracking behavior.

6.1.2. LATTICE MODEL

All the lattice models developed in this section is identical to the softening lattice model in Section 4.3 in geometry settings. Material $NC\_\sigma\epsilon$ and SHCC are the same as the softening material in Section 4.3 and SHCC in Section 5.1. Two new materials are applied as repair

mortar with 5 segments in lattice model. The detailed material input are listed in Table 6.1.

Table 6.1: Material Input of FRC_50% and FRC_0%

Material	Number of Segment	E (GPa)	G (GPa)	f_t (MPa)	f_c (MPa)
FRC_50%	1	18.725	7.8021	3.10	-48.9
	2	0.3714	0.1547	2.85	-48.9
	3	0.1712	0.0714	2.60	-48.9
	4	0.1036	0.0432	2.35	-48.9
	5	0.0695	0.0290	2.10	-48.9
FRC_0%	1	18.725	7.8021	3.10	-48.9
	2	0.3062	0.1276	2.35	-48.9
	3	0.1054	0.0439	1.60	-48.9
	4	0.0375	0.0156	0.85	-48.9
	5	0.0033	0.0014	0.10	-48.9

The preliminary model with brittle repair mortar (NC_brittle) in Section 4.1 is also taken into comparison. The maximum crack width-pressure curves of all models are displayed in Figure 6.3. This figure shows a clear difference in cracking behavior among five materials. The models with repair mortar $NC\_brittle$ and $NC\_\sigma\epsilon$ have a jump in maximum crack width which is due to the localization of major cracks. This behavior can also be observed in the model with repair mortar FRC_0%, which is probably because of the same reason. The shape of the curve of models with material FRC_50% and SHCC is very similar. Therefore, the cracking behavior in these two models probably corresponds to each other.

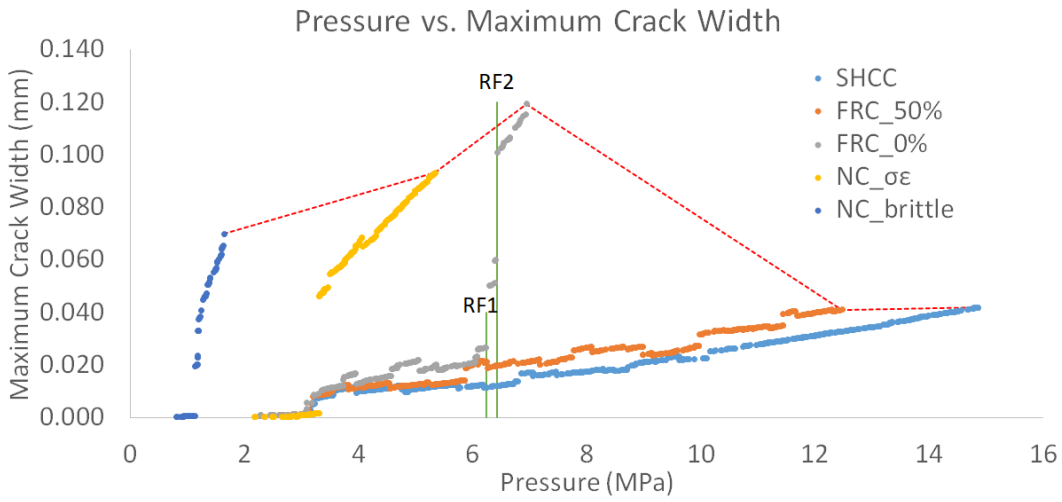

Figure 6.3: Pressure-Maximum Crack Width of Lattice Models

With increasing fracture energy in repair mortar, the model can bear a higher pressure. The maximum crack width in the material with higher fracture energy is lower at similar pressure level. However, the maximum crack width which model $NC\_brittle$, $NC\_\sigma\epsilon$ and $FRC\_0\%$ can reach increases with the increase of fracture energy (connected by the red dotted line). This is due to the limitation of the load level. The repair mortar with less fracture energy can carry less load in the analysis. Therefore, the model fails completely before it can reach a higher crack width. The increase in crack width after the jump is more sharp in the model with less fracture energy.

Figure 6.4 shows the damage pattern of $FRC\_0\%$ Model at step 868 (RF1) and 1208 (RF2). At step 868, multiple cracks are developed in the top area. However, at step 1208, one crack at the top is localized and widened at this step which results in the jump in maximum in crack width. This behavior can also be observed in Model $NC\_brittle$ and $NC\_\sigma\epsilon$. Nevertheless, this jump in maximum crack width cannot be observed in model $FRC\_50\%$ and $SHCC$, which implies that $FRC\_0\%$ is probably the threshold value for lattice model can produce discrete crack at the top.

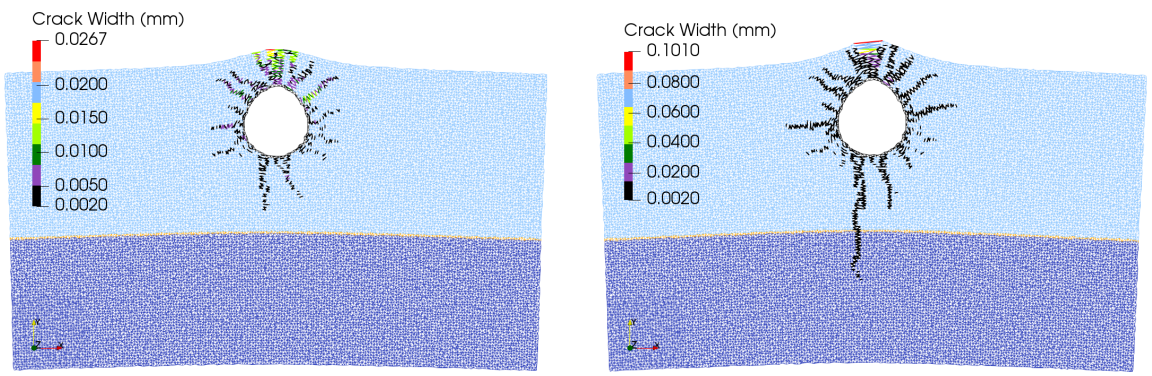

(a) Step 868 (RF1)

(b) Step 1208 (RF2)

Figure 6.4: Top Crack Localization in Model $FRC\_0\%$

At step 1399, model $FRC\_0\%$ reaches its limit. After step 1399, the top localized crack is suddenly widened and the secondary cracks next to this crack are closed. Moreover, the cracks around the reinforcement are not developed further, which means that the stress is only concentrated in the top crack after step 1399. Therefore, the result after this step is not reasonable anymore. The crack pattern around this step is displayed in Figure 6.5.

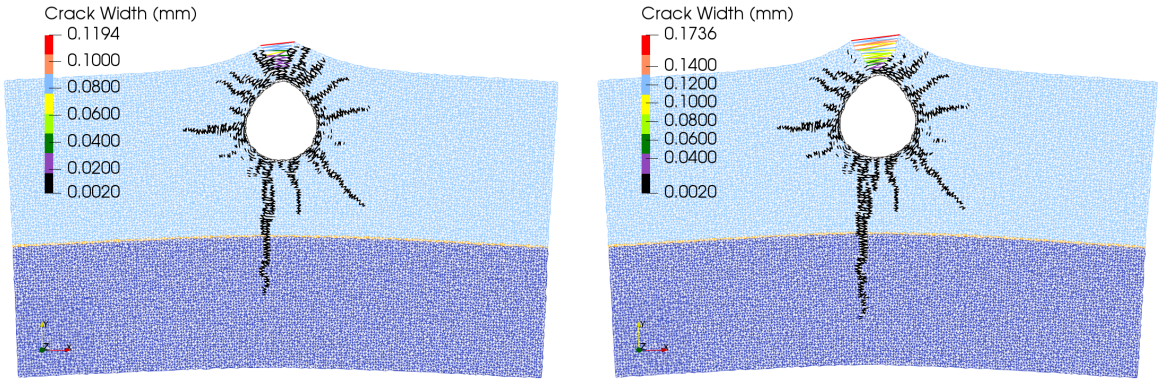

(a) Step 1399 (b) Step 1567

Figure 6.5: Final Reasonable Step in Model *FRC*_0%

The crack pattern of all five models at their final reasonable step is compared in Figure 6.6 and 6.7. A clear difference can be observed in cracking behavior among models with different repair mortar. As it is in the assumption, model *FRC*_50% (Figure 6.6b) behaves very similar to model *SHCC* (Figure 6.6a): a smeared cracking area at top, distributed cracks around reinforcement and two discrete bottom cracks developed into substrate with higher crack width in their part in substrate. The failure mechanism of Model *FRC*_50% is the inclined bottom crack gets too close to the bottom boundary and starts developing horizontally, which is identical to model *SHCC*. This is due the influence of unbreakable bottom edge on stress distribution explained in Section 5.2. Thus, a conclusion can be drawn that these two materials behave similarly due to the deflection-hardening behavior that material *FRC*_50% shows in structural analysis (three-point bending test). This cracking behavior in accelerated corrosion test verifies the observation in the previous section.

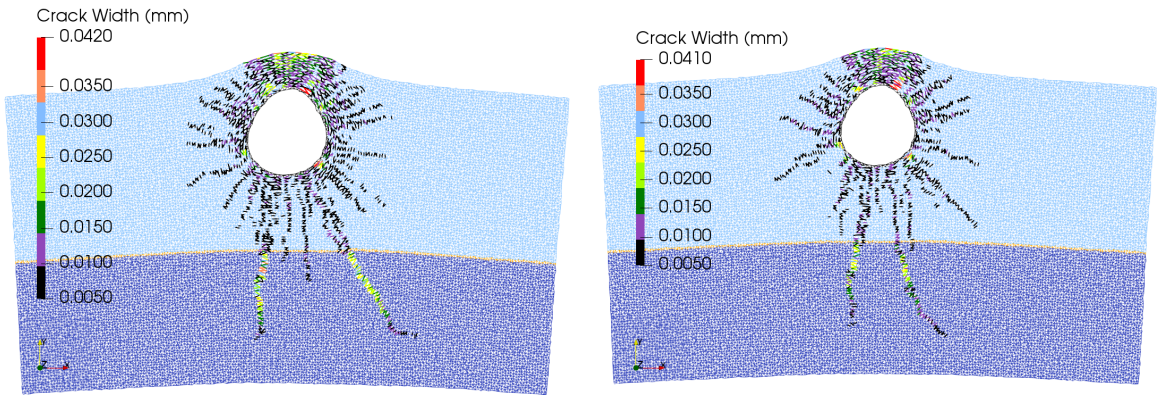

(a) Step 3775, Model *SHCC* (b) Step 3076, Model *FRC*_50%

Figure 6.6: Comparison of Crack Pattern of Lattice Model with Different Repair Mortar (1)

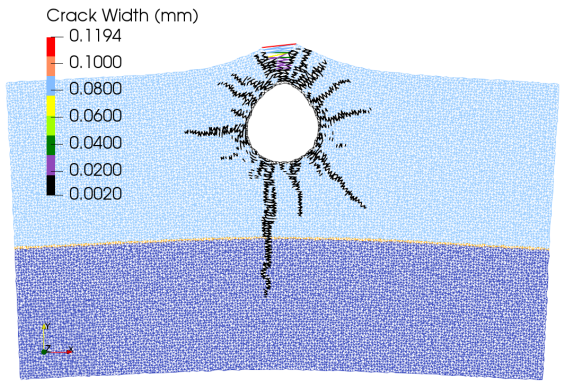

(a) Step 1399, Model $FRC\_0\%$

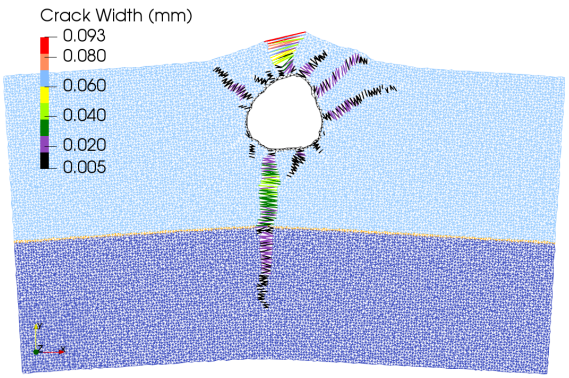

(b) Step 3520, Model $NC\_\sigma\epsilon$

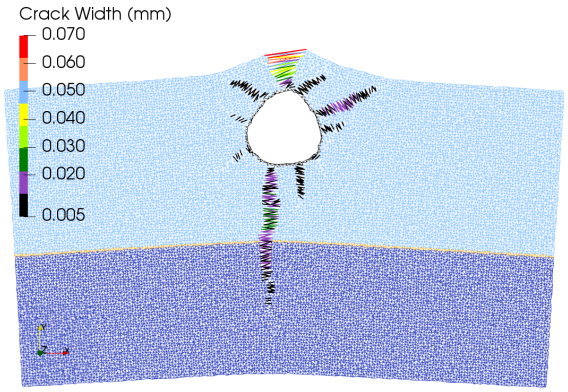

(c) Step 776, Model $NC\_brittle$

Figure 6.7: Comparison of Crack Pattern of Lattice Model with Different Repair Mortar (2)

The same behavior has been observed in an experiment done by di Prisco [15]. As it is shown in Figure 6.8, strain-hardening material under uniaxial tension can always show deflection-hardening under bending. Meanwhile, the strain-softening material under uniaxial tension can have either deflection hardening or softening behavior under bending. The material with deflection-hardening in bending can perform more separated cracks in structural analysis (floor in punching).

As for model $FRC\_0\%$ (Figure 6.7a), it behaves more brittle than model $FRC\_50\%$ and $SHCC$. A discretely localized crack can be performed at the top. Although the distributed cracks around the steel rod can still be developed, the number of the distributed cracks becomes less. Meanwhile, distributed cracks cannot be performed anymore in model $NC\_brittle$ (Figure 6.7b) and $NC\_\sigma\epsilon$ (Figure 6.7c). Two major cracks at top and bottom are localized instead. Therefore, the material with less fracture energy than $FRC\_0\%$ will reduce the num-

ber of distributed cracks around the reinforcement until the cracking behavior of $NC\_\sigma\epsilon$. However, model $NC\_\sigma\epsilon$ can perform two more secondary cracks along 2 o'clock direction than model $NC\_brittle$, which is benefit from the softening branch after tensile failure.

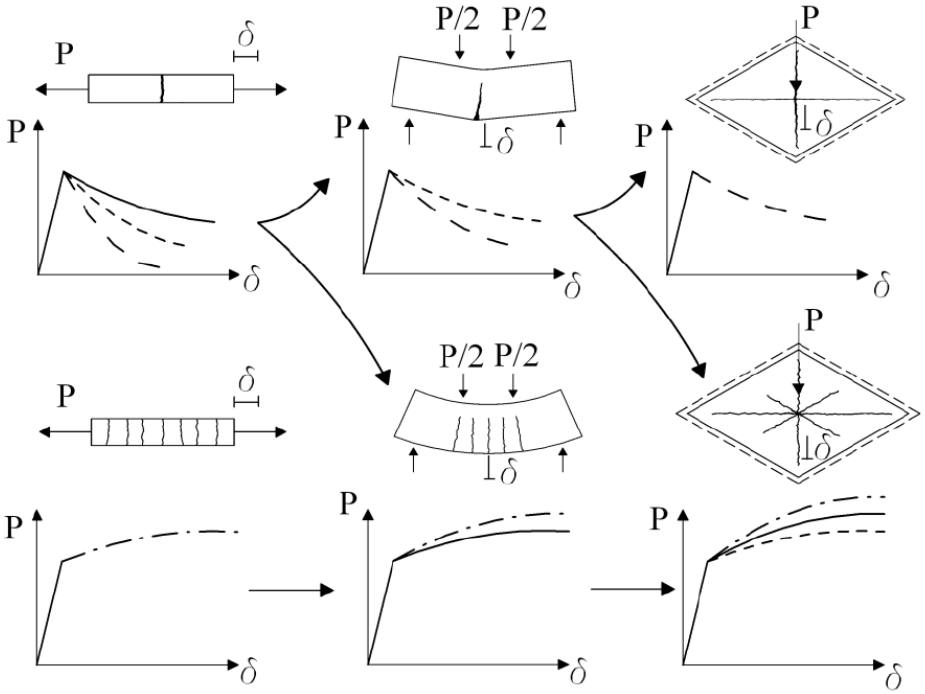

Figure 6.8: Different Response of Structures Made of FRC [15]

In conclusion, the model can carry higher load pressure with more fracture energy and strain capacity in repair mortar. Meanwhile, the maximum crack width decreases with the increasing fracture energy. The maximum crack width in model $NC\_brittle$, $NC\_\sigma\epsilon$ and $FRC\_0\%$ is 170.41% (166.61%), 227.02% (221.95%) and 290.82% (284.34%) of that model $FRC\_50\%$ ($SHCC$) respectively. Besides, the number of cracks performed also has a positive correlation with fracture energy. Moreover, material $FRC\_0\%$ is the threshold value of producing on discrete crack at the top cracking area instead of smeared cracking area. Meanwhile, half strain-softening material $FRC\_50\%$ indicates deflection-hardening behavior in the structural analysis as $SHCC$. By this deflection-hardening behavior, these two types of material can reduce their maximum crack width by performing the distributed crack pattern. In general, the lattice model can successfully display the different cracking behavior due to different fracture energy in repair mortar. This is because of the sequentially linear solution method which allows the lattice model following the stress-strain relation accurately and avoiding the convergence problem.

6.1.3. CONTINUUM MODEL

In continuum model, material $NC\_\sigma\epsilon$, FRC_0%, FRC_50% and $SHCC$ are applied as repair mortar for comparison. All the other aspects of the models in this section are kept identical to the continuum model in Section 5.2. The random field developed in Section 5.3 is only applied to model with repair mortar $SHCC$. The load pressure-maximum crack width curves are visualized in Figure 6.9.

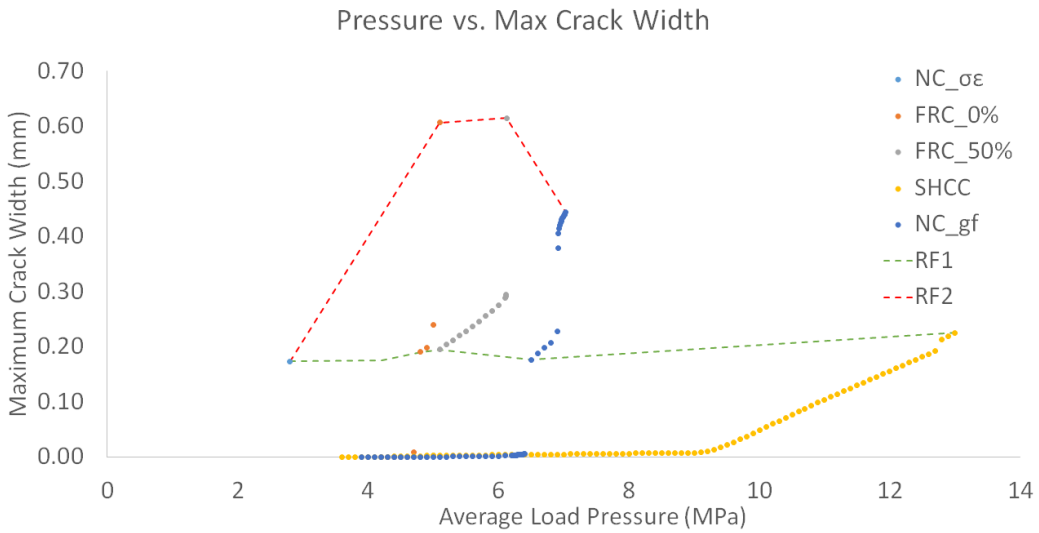

Figure 6.9: Load Pressure-Maximum Crack Width (Repair Mortar) Curves of Continuum Model

Convergence problem happens in all of these models. The convergence norms used in the nonlinear analysis are both force norm and displacement norm. The tolerance of both norms is set to be 0.01. At the first step without convergence (connected by the green line, RF1), at least one norm has reached tolerance with a value in the range 0.01 and 0.1. As the development of analysis, at the secondary reference step (connected by the red line, RF2), the models fail to meet both force and displacement norms. The variance of both norms is within the range 0.01 and 0.1 now.

The convergence problem is because of the incremental solution method applied in the nonlinear analysis. With the Regular Newton-Raphson method, the stiffness of each integration point is calculated as its tangential stiffness. When this integration point is in the softening stage of its constitutive relation, the stiffness of this point in the stiffness matrix

will be negative. Then the stiffness matrix $\boldsymbol{K}$ is not a positive definite matrix anymore. As the analysis goes on, more and more integration points have a negative stiffness which makes the stiffness matrix very ill-conditioned. This becomes even worse when some of the integration points are completely damaged which means the stiffness of these points in the matrix is zero. In this case, many eigenvalues of the stiffness matrix will be negative or even zero. By doing finite element analysis, an equation is solved in every iteration to find the displacement:

$$\boldsymbol{u} = \boldsymbol{K}^{-1}\boldsymbol{f} \tag{6.2}$$

in which, $\boldsymbol{u}$ and $\boldsymbol{f}$ are displacement and force vector. The stiffness matrix $\boldsymbol{K}$ has to be inverted to solve Eq. 6.2. Therefore, it is impossible to solve the equation in a good manner by using a stiffness matrix with many zero and negative eigenvalues. Thus, the convergence problem happens earlier in the model with a brittle material.

A delay in convergence problem with increasing fracture energy in repair mortar can be observed. Model $NC\_\sigma\epsilon$ suffers the convergence problem earliest and most severe. Figure 6.10 shows the damage pattern of model $NC\_\sigma\epsilon$ at its first non-converged step (RF1). Due to the small strain capacity of repair mortar, this mode behaves very brittle. The relative differences of convergence norms are 0.3022 and 0.1897 in displacement and force, which is even higher than the standard for RF2. This implies that the results at this step are not acceptable anymore. However, it can still indicate a possible crack pattern of this model. A symmetric crack pattern is developed at this step. Compared with experimental results, the generated crack pattern has two bottom cracks localized instead of one.

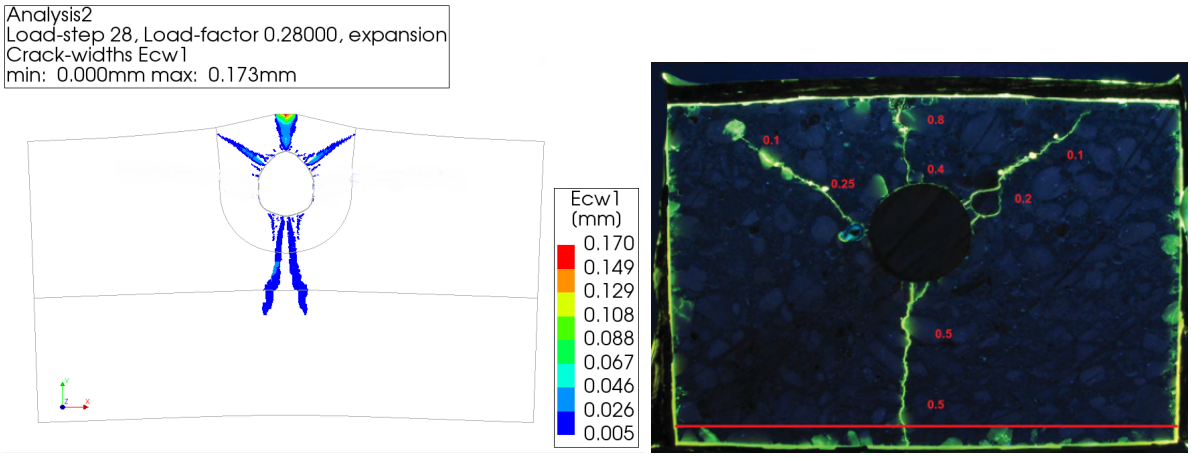

(a) Model $NC\_\sigma\epsilon$ (b) Experiment

Figure 6.10: Crack Pattern at RF1, Model $NC\_\sigma\epsilon$

In model $FRC\_0\%$ and $FRC\_50\%$, the relative difference at RF1 and RF2 are higher than the tolerance which means that the result is not accurate enough. However, the value of this variance is not too far from the tolerances. This means that the results at these steps are still acceptable. Although not accurate enough, the crack pattern at these steps can still be regarded as a good indication of cracking behavior of $FRC\_0\%$ and $FRC\_50\%$. In model $FRC\_0\%$ and $FRC\_50\%$, the top crack is localized at RF1 and the bottom crack is localized at RF2 (Figure 6.11 and 6.12). This proves the assumption about the reason for the convergence problem. At crack localization, too many integration points within this step are pushed to damage which results in an ill-conditioned stiffness matrix. The step size is decreased even to a factor of 0.0001 which is 100 times smaller than the normal step size in order to push the analysis going further. However, it is not possible. This trick can only delay slightly in the occurrence of a non-converged step. The analysis cannot go further than the original non-converged load level. Because at that step, the number of integration points with tensile failure reaches a critical value that the convergence cannot be reached anymore.

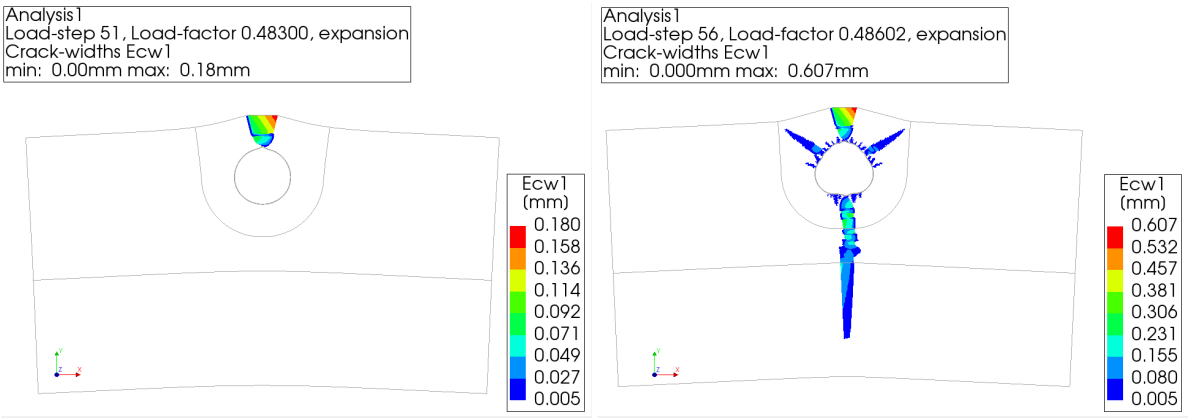

(a) RF1 (b) RF2

Figure 6.11: Crack Pattern of Model $FRC\_0\%$

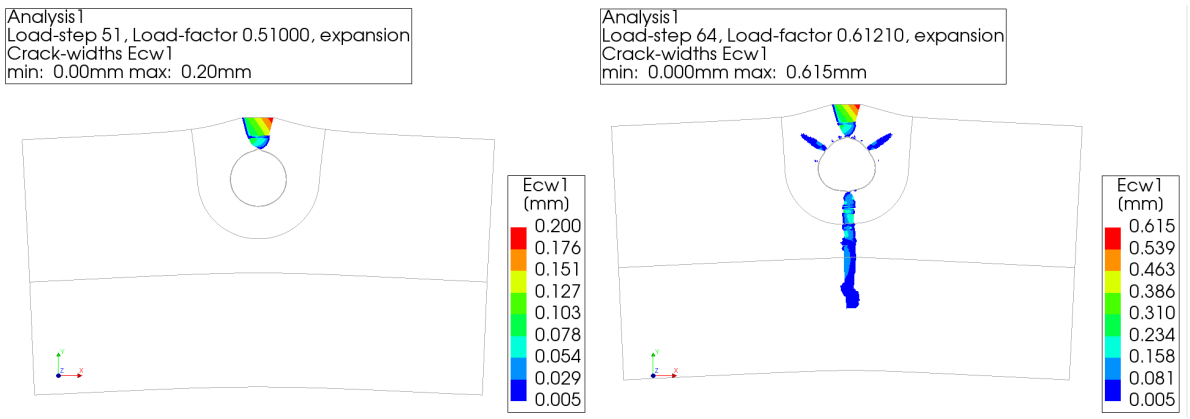

(a) RF1 (b) RF2

Figure 6.12: Crack Pattern of Model $FRC\_50\%$

The damage pattern of all models at the final step (RF2) is displayed in Figure 6.13. With the help of the random field, model $SHCC$ can produce distributed crack pattern in repair mortar. Due to the strain-hardening behavior of $SHCC$, the stiffness of an integration point can always be positive until its complete failure. Therefore, model $SHCC$ can still run stably until load pressure 13.0 MPa after the localization of multiple cracks. Meanwhile, a delay in the localization of cracks can be observed in Figure 6.9. This corresponds with the discovery in the lattice model that material with more fracture energy can improve the load capacity of the model.

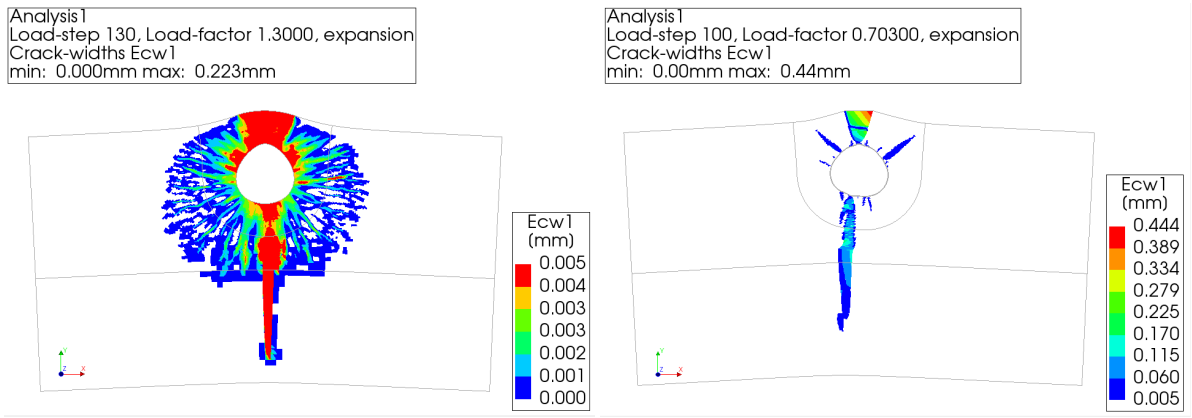

(a) Model $SHCC$

(b) Model NC_gf

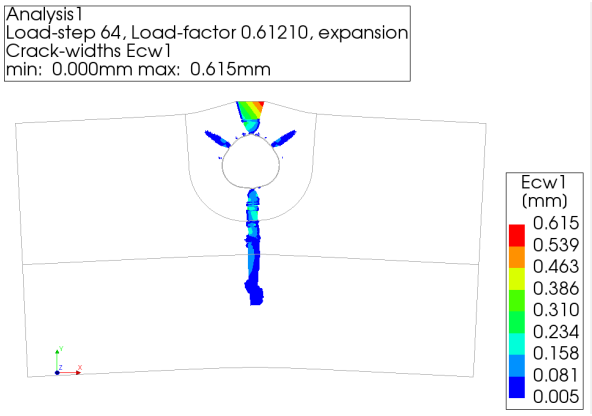

(c) Model $FRC\_50\%$

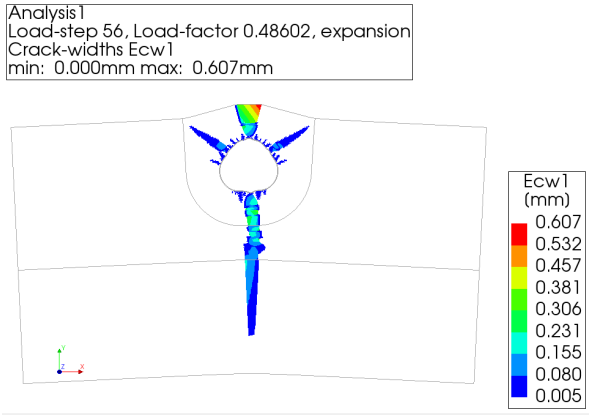

(d) Model $FRC\_0\%$

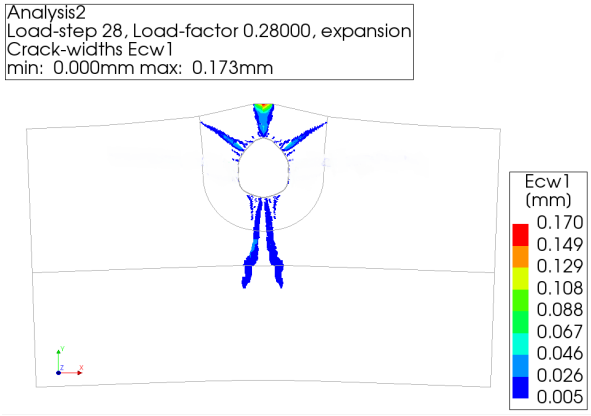

(e) Model $NC\_\sigma\epsilon$

Figure 6.13: Crack Pattern of Continuum Model with Different Repair Mortar

However, except model *SHCC*, cracks are localized similarly in four other models. The increase in the number of cracks localized with increasing fracture energy cannot be produced in the continuum model as in lattice model. This is probably due to the bifurcation problem caused by the incremental solution method of the continuum model. In one step of the nonlinear analysis, multiple integration points are pushed to failure. Multiple equilibrium paths are available within the model. The model will localize specific crack which is regarded as the "weakest" path. Therefore, no apparent difference in the crack pattern can be performed within these four models.

6.1.4. EVALUATION

In this section, four types of materials as repair mortar in accelerated corrosion test are simulated by continuum model and lattice model. Lattice model can successfully display the different cracking behavior due to different fracture energy in repair mortar. However, the continuum model has a stability problem in simulating the cracking behavior of the strain-softening material. This is because of the sequentially linear solution method which allows the lattice model following the stress-strain relation accurately and avoiding the convergence problem.

Figure 6.14 shows the comparison between the two solution methods. Tangential stiffness is used in nonlinear incremental solution method (NLFEA). In contrast, secant stiffness is used in sequentially linear solution method (SLA). As the development of analysis, the stiffness matrix of NLFEM will become more and more ill-conditioned. More integration points get into softening stage which produces negative stiffness in the stiffness matrix. Then, it is hard to solve the system equation. However, SLA does not have to consider this problem until the complete damage of one point. Evidence of this is that the continuum model can simulate the cracking behavior of SHCC properly. However, convergence problems happen to the continuum model at crack localization steps with the strain-softening material. An assumption can be made that an ideal-plastic FRC will behave as brittle as normal plain concrete in the continuum model with nonlinear analysis. Nevertheless, the model has to develop into the highly nonlinear zone in the softening part In order to get a properly developed crack pattern. The nonlinear analysis will become more and more unstable with

the analysis.

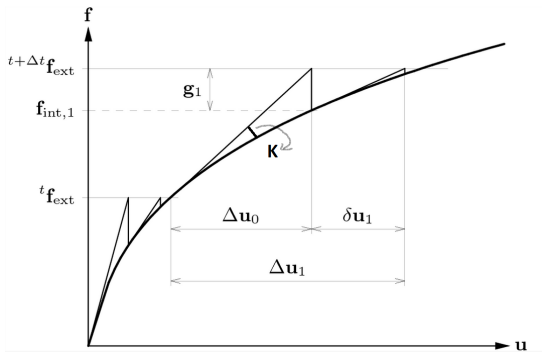

(a) Nonlinear Incremental Solution Method

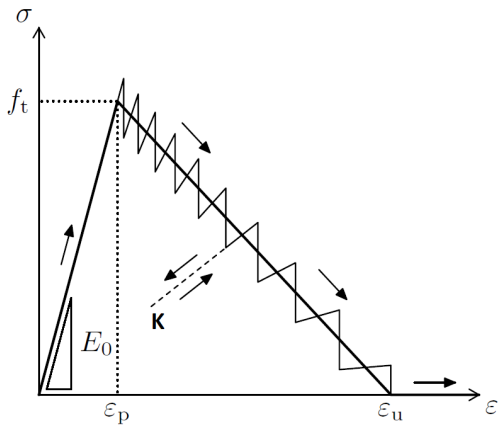

(b) Sequentially Linear Solution Method

Figure 6.14: Comparison of Solution Method

There is a method called "arc length control" to help go through the non-converged points [9]. However, this is a complex model with cracks developed in multiple directions. A "global snap back" behavior can occur under this situation. The model will be unloaded completely instead of a bit to find the equilibrium [46]. A modified Crack Mouth Opening Displacement (CMOD) method is advised to avoid this problem. Within this method, the nodes from both sides of the crack and their displacement direction need to be defined. This is very difficult in accelerated corrosion simulation cause it is hard to define the exact location of the cracks in this model.

One extra advantage of SLA is that only one integration point is damaged within one step. However, multiple integration points are damaged in a step of NLFEA. Thus, the model can follow all the equilibrium path to avoid bifurcation problem. Thence, more distributed cracks can be performed in the lattice model instead of the concentrated cracks in the continuum model. However, only one of the equilibrium paths is followed in NLFEA. Thus, only the weakest crack in the continuum model with the strain-softening material can be localized. In general, the continuum model is not suitable to simulate the crack pattern of strain-softening material.

Nevertheless, the lattice model has its limitation in predicting crack width. The crack width in the lattice model is calculated as the difference between the length of the deformed beam

and original beam which is relatively simple. The total strain based crack width theory in the continuum model considers more aspects such as crack band width and crack rotation. Moreover, the degrees of freedom decrease from 16 to 6 by simplifying two plane stress elements into a lattice beam. Then the crack width in the lattice model may be influenced. Also, one element has to be damaged in each step of analysis in the lattice model. After certain steps, the model has to step due to the influence of boundary conditions before the desired crack width level.

Built-in randomness has been proved to be necessary to simulate the cracking behavior of SHCC. The random field in the continuum model is a better option than the built-in randomness of the lattice model. The built-in randomness of the lattice model comes from the random orientation of lattice beams. This randomness is an artificial parameter that has no physical relation with material property. However, the random field on tensile strength in the continuum model is correlated with the material property through some parameters like standard deviation and correlation length. The random field has a physical basis and can be adjusted with different material. Therefore, the random field in the continuum model is a better option to represent the heterogeneity of concrete.

Both types of models show their advantages in different aspects. Lattice model can successfully simulate the different cracking behavior of material with different fracture energy. However, the lattice model shows its problem in predicting crack width. Meanwhile, the continuum model always suffers from the stability of the analysis due to the convergence problem. Thus, a combination of these two models is proposed for future investigation. Based on the continuum model, random field on tensile strength can have a similar effect as the randomness in the lattice model. Also, the solution method is adopted from the lattice model as Sequentially Linear Analysis (SLA) by Rots [47]. The random field can accurately represent the heterogeneity of concrete. The advanced cracking theory in the continuum model can help in predicting crack width. Meanwhile, the SLA method can help the continuum model avoid convergence and bifurcation problem in simulating softening material.

In material aspects, the model with more fracture energy in repair mortar has a higher capacity. Meanwhile, the maximum crack width decreases with the increasing fracture en-

ergy. Also, the number of cracks performed also has a positive correlation with fracture energy. The material with deflection-hardening behavior can produce the distributed crack pattern. A strain-softening material (FRC_50%) can also perform deflection-hardening material as strain-hardening material ($SHCC$). The top crack will first be localized while the cracks in other directions remain distributed with decreasing fracture energy (FRC_0%). As the fracture energy decreases further, a concentrated crack pattern will finally present.

6.2. INTERFACE TENSILE STRENGTH

Interface tensile strength, which represents the quality of the bond between repair mortar and substrate in reality is also an important parameter in concrete repair system. With different tensile strength and interface roughness, the cracking behavior of the repair system under ongoing corrosion should be different (specifically the development of bottom cracks). Luković verifies this assumption through a series of accelerated corrosion test with three different interface settings: smooth surface of 1 MPa, rough interface of 1 MPa and rough interface of 3 MPa [7]. Besides, different repair mortar with same interface setting can produce different bottom crack development due to different strain capacity. Also, the discrete crack pattern lattice model developed can simulate these behaviors in a good manner.

Figure 6.15 shows an experiment done by Luković at macro level ($40 \times 40 \times 40\ mm^3$). SHCC with the same composite is applied in the specimens as the repair mortar. Normal concrete is applied as the substrate. Three different types of interface settings are implemented: smooth surface with 1 MPa strength, rough surface with 1 MPa strength and rough surface with 3 MPa interface. Figure 6.16 shows the pressure-maximum crack width curve obtained by the lattice simulation. Figure 6.17 shows the crack pattern obtained from the lattice model in Luković's simulation with different interface strength. It can be observed in both the experiment and the simulation that different crack patterns are performed in the specimens with different interface strength. The crack patterns obtained by the lattice models correspond well with the experimental results.

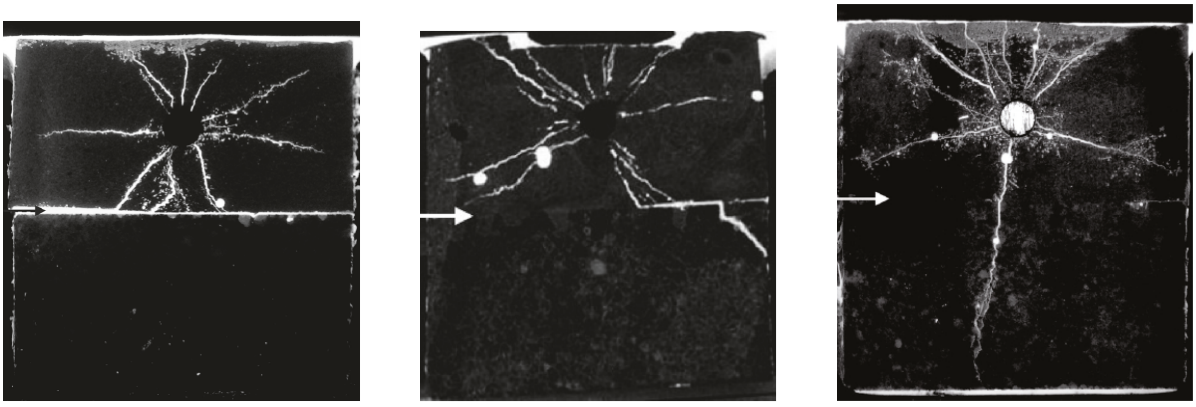

(a) Smooth Surface. Complete De-lamination (Interface Failure)

(b) Grooved Surface. Sample 1 (Groove Interlocking the Crack to the Substrate)

(c) Grooved Surface. Sample 2 (Groove Interlocking the Crack to the Substrate)

Figure 6.15: Experimental Crack Pattern in *SHCC* Repair System with Different Interface Settings [7]

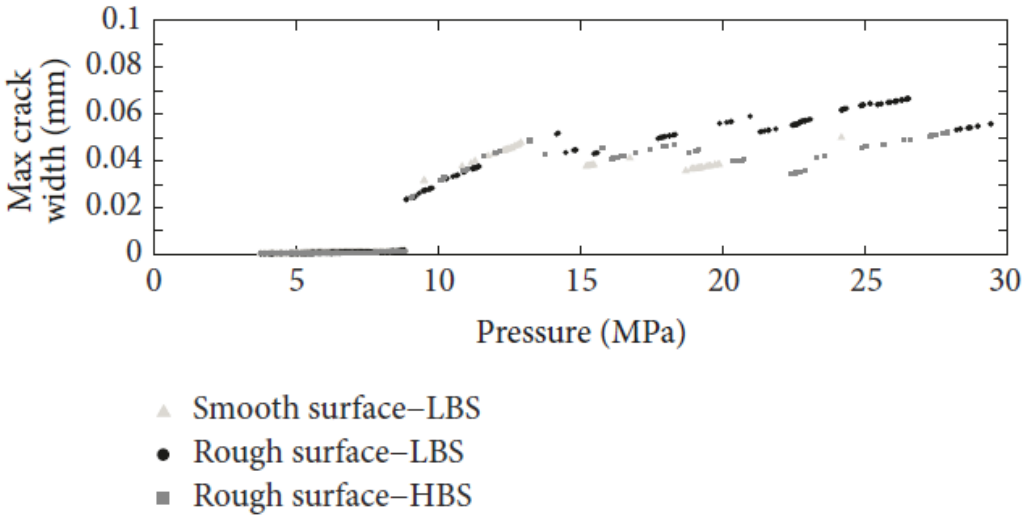

Figure 6.16: Load Pressure-Maximum Crack Width Curves of Model with Different Interface Strength(LBS corresponds to interface strength 1 MPa and HBS to interface strength of 3 MPa) [7]

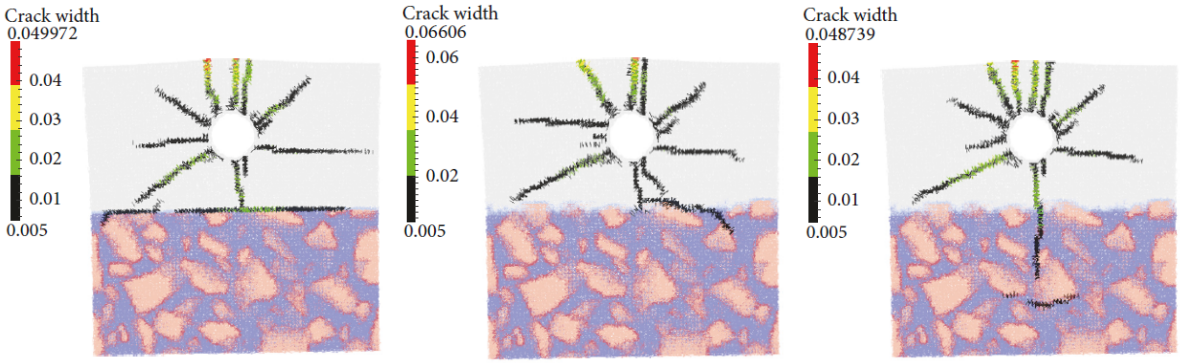

(a) Smooth Surface. Interface Strength of 1 MPa. Imposed Pressure of 24 MPa

(b) Rough Surface. Interface Strength of 1 MPa. Imposed Pressure of 26 MPa

(c) Rough Surface. Interface Strength of 3 MPa. Imposed Pressure of 26 MPa

Figure 6.17: Numerical Obtained Crack Pattern in *SHCC* Repair System with Different Interface Settings [7]

However, the dimension of the specimens in Luković's experiment is one order of magnitude lower than the experiment done by SGS INTRON. During the up-scaling in the lattice model, the concrete is modeled as an isotropic material and aggregates, fibers and their interfaces with cement matrix are ignored. Therefore, it is also interesting to investigate the performance of up-scaled lattice model with different interface settings at the structural level. However, the brittle interface input can make the convergence problem even worse in the continuum model. Moreover, the unsymmetrical cracking behavior of interface is difficult to be developed in the continuum model due to the bifurcation problem. The interface elements in the continuum model might be damaged completely after their first cracking. The parametric study of interface strength is conducted in both models to test their performance.

6.2.1. INTERFACE SETTINGS

In this section, two extreme materials are selected as repair mortar: $NC\_\sigma\epsilon$ (FRC with least fiber volume, can be regarded as normal concrete) and $SHCC$ (strain-hardening material). Four types of interface tensile strength are defined for investigation, ranging from 10% to 100% of the tensile strength of repair mortar. The interface property of all models are listed in Table 6.2.

Table 6.2: Interface Material Input

Repair Mortar	Model Name	E (GPa)	f_t (MPa)
$SHCC$	$SHCC$_100%	18.725	3.10
	$SHCC$_50%	9.3625	1.55
	$SHCC$_30%	5.6175	0.93
	$SHCC$_10%	1.8725	0.31
$NC\_\sigma\epsilon$	$NC_\sigma\epsilon$_100%	37.95	2.89
	$NC_\sigma\epsilon$_50%	18.975	1.445
	$NC_\sigma\epsilon$_30%	11.385	0.867
	$NC_\sigma\epsilon$_10%	3.795	0.289

All the interface elements follow the brittle material law and have only one segment in the material input. Interface elements are tagged as 3 in the lattice model. Figure 6.18 indicates the element tag in the lattice model. All other aspects of these models are identical to the lattice models in Section 6.1.

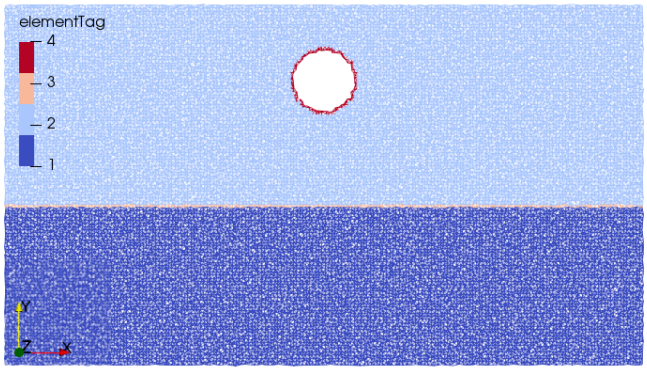

Figure 6.18: Element Tag Distribution of Lattice Model

6.2.2. MODEL WITH REPAIR MORTAR SHCC

Figure 6.19 shows the pressure-maximum crack width curve of all the four models with repair mortar *SHCC*. All the models behave similarly at the beginning phase of the analysis. However, the models with weaker interface strength end earlier and show higher maximum crack width at their end. This is probably because of the de-bonding behavior at the mortar-substrate interface. Several reference points are marked in Figure 6.19 in order to investigate the cracking behavior in detail.

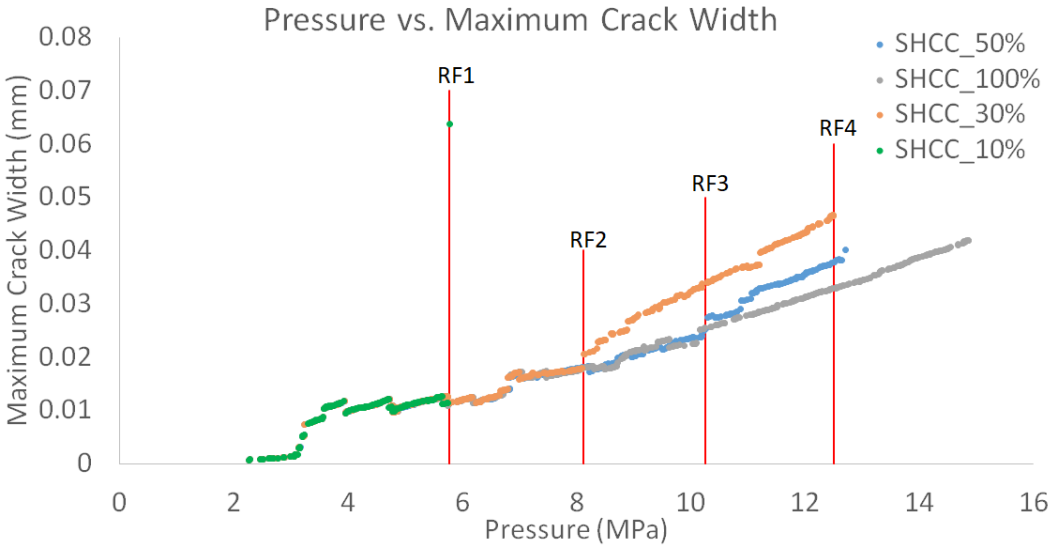

Figure 6.19: Pressure-Maximum Crack Width Curves of Models with *SHCC* mortar

All the four models follow the cracking behavior of the lattice model with *SHCC* repair mortar until pressure 5.755 *MPa* (RF1). At this step, a huge jump in maximum crack width

in the model *SHCC*_10% can be observed. Figure 6.20 shows the damage pattern before and after this location. The mortar-substrate interface is observed to be completely damaged at this step. This de-lamination behavior even happens before any bottom crack reaches the mortar-substrate interface, which implies that the interface tensile strength in this model is (10% of repair mortar) too weak.

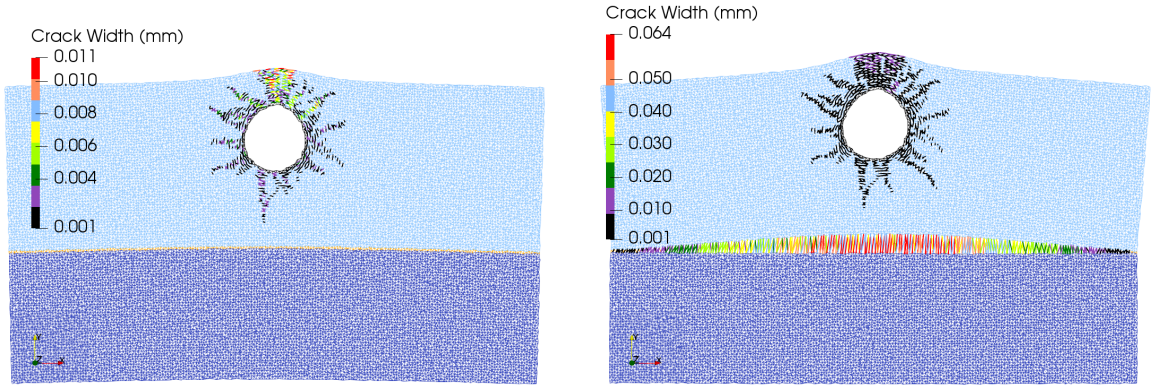

(a) Step 728, Before RF1 (b) Step 1325, After RF1

Figure 6.20: De-bonding Behaviour of Model *SHCC*_10%

At RF2, model *SHCC*_30% shows a jump in maximum crack width and shows divergence in development of the curve with two other models. The crack pattern of the steps around this location is displayed in Figure 6.21. This model behaves differently with model *SHCC*_10%. With the increase in interface tensile strength, a bottom crack propagates through the interface into the substrate (Figure 6.21a). Then the damage is performed horizontally to the right of the bottom crack at the interface. This is the reason for the jump crack width and the divergence in the pressure-maximum crack width curve.

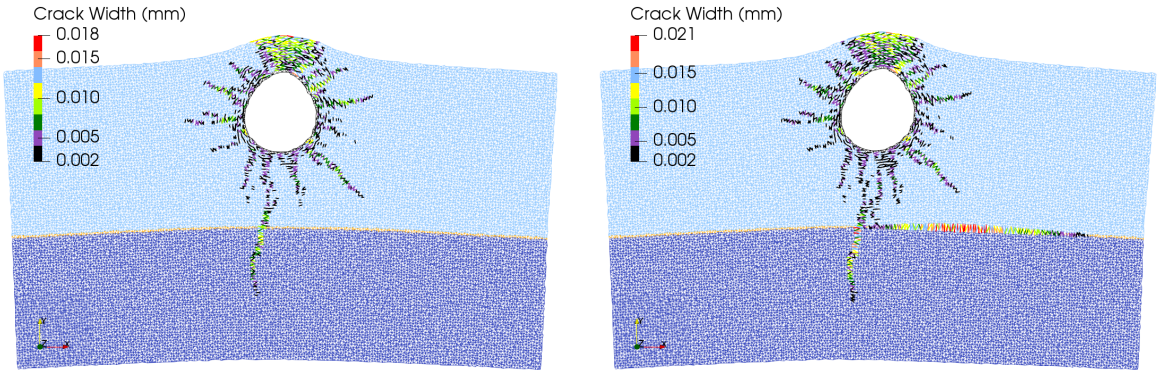

(a) Step 1601, Before RF2 (b) Step 1931, After RF2

Figure 6.21: Damage of Interface in Model *SHCC*_30%

However, this damage in the interface does not result in a complete failure in the interface after RF2. The maximum crack width after RF2 also does not jump incredibly like at RF1 in model *SHCC*_10%. Instead, there are more distributed cracks developed around the reinforcement until pressure level 12.499 *MPa* (Step 3091, Figure 6.22a). After this step, the interface is damaged completely (Figure 6.22b). This implies that with a stronger interface, the complete failure of the mortar-substrate interface can be delayed which allows some bottom cracks propagates into the substrate.

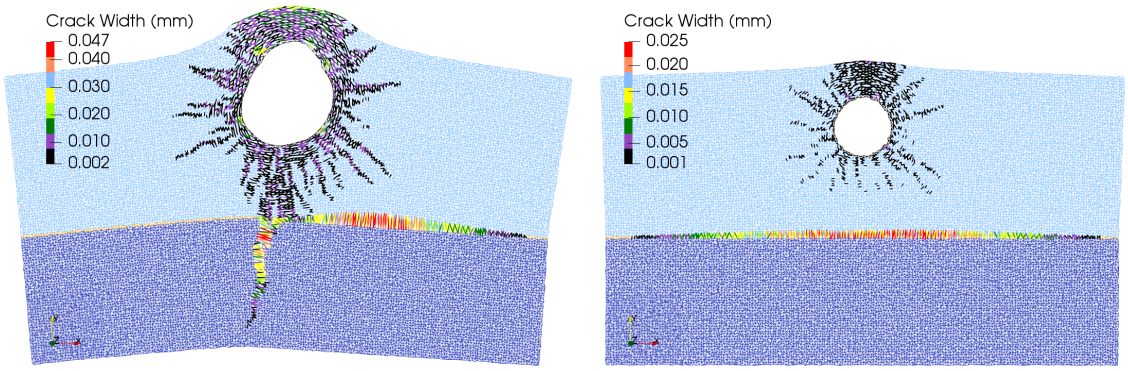

(a) Step 3091, Before RF3

(b) Step 3300, After RF3

Figure 6.22: Complete Failure of Interface in Model *SHCC*_30%

Model *SHCC*_50% follows the cracking behavior of model *SHCC*_100% until RF4 where the second bottom reaches the mortar-substrate interface. Instead of propagates deeper into substrate (like model *SHCC*_100%, Figure 6.23a), several interface elements are damaged at first. Then this second bottom crack propagates into the substrate, but it develops more horizontally towards the right edge of the model (Figure 6.23b).

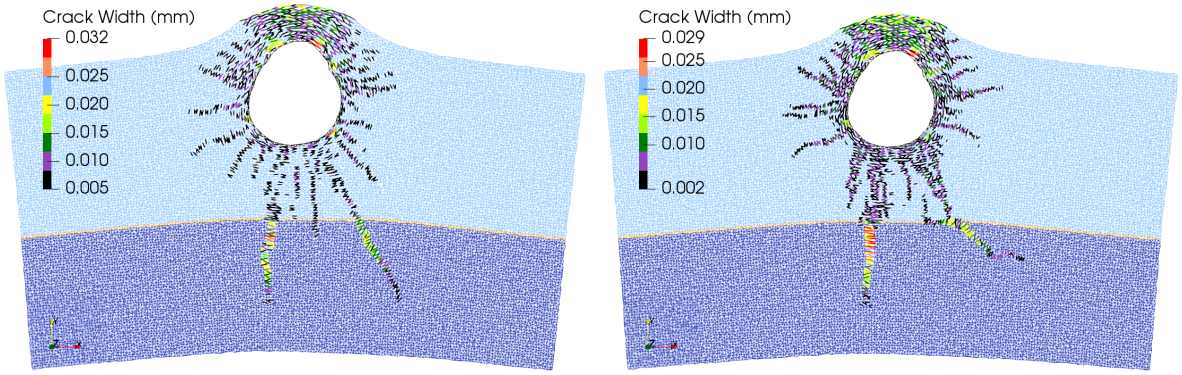

(a) Step 3017 in Model *SHCC*_100%, Pressure 12.357 *MPa*

(b) Step 2613 in Model *SHCC*_50%, After RF4, Pressure 10.262 *MPa*

Figure 6.23: Second Bottom Crack Development Direction

Figure 6.24 shows the comparison of damage pattern in all four models. In general, the weaker in tension the interface is, the more severe de-bonding behavior will be. In model *SHCC*_10%, the interface is completely damaged before any bottom crack reaches the interface. Meanwhile, one bottom crack can develop into the substrate and only half of the interface is damaged in the model *SHCC*_30%. However, only a few interface elements are damaged in the model *SHCC*_50% and the second bottom crack propagates more horizontally in the substrate. Finally, no de-bonding behavior can be observed in model *SHCC*_100%. Moreover, there is no major difference in the crack pattern in the repair mortar area by changing interface strength except model *SHCC*_10%, in which the interface is completely damaged before bottom crack reaches interface. However, interface strength indeed has an influence on crack development in the substrate. Also, the model can bear higher load pressure with increasing interface strength.

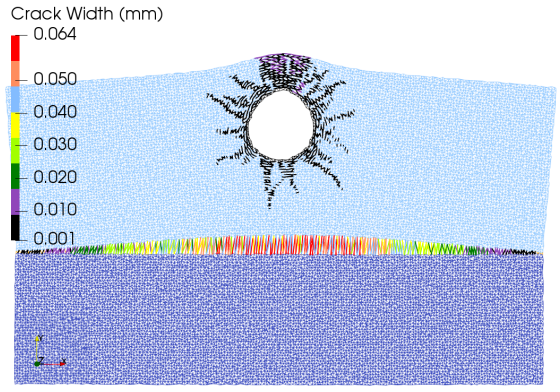

(a) Model *SHCC*_10%, Pressure 5.777 *MPa*

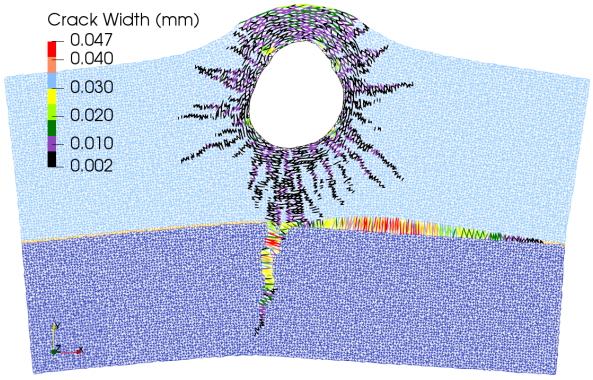

(b) Model *SHCC*_30%, Pressure 12.499 *MPa*

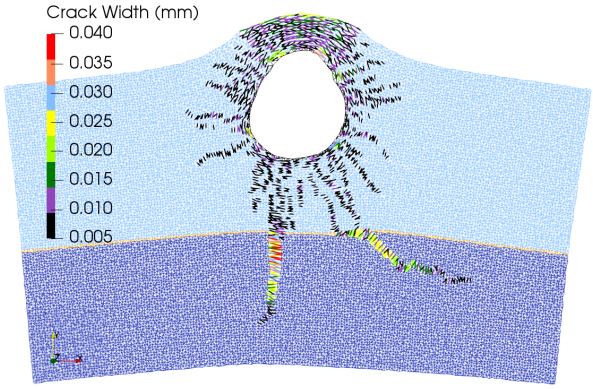

(c) Model *SHCC*_50%, Pressure 12.703 *MPa*

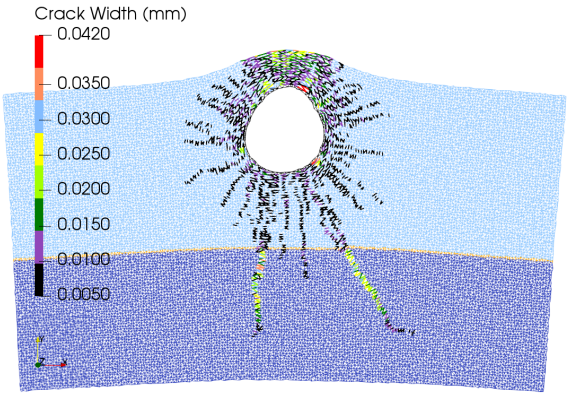

(d) Model *SHCC*_100%, Pressure 14.864 *MPa*

Figure 6.24: Crack Pattern of SHCC Repair Mortar Model with Different Interface Strength

6.2.3. MODEL WITH REPAIR MORTAR $NC\_\sigma\epsilon$

As the models with repair mortar SHCC, the pressure-maximum crack width curve of models with repair mortar $NC\_\sigma\epsilon$ is shown in Figure 6.25. A jump in maximum crack width can be observed in all four models at same pressure level. This is due to the localization of top crack in the models. However, except model $NC_\sigma\epsilon$_10%, all other models behave similarly after the localization of top crack. Nevertheless, model $NC_\sigma\epsilon$_30% reaches its limit very early after the jump. Model $NC_\sigma\epsilon$_50% and$NC_\sigma\epsilon$_100% can carry higher load pressure in contrast.

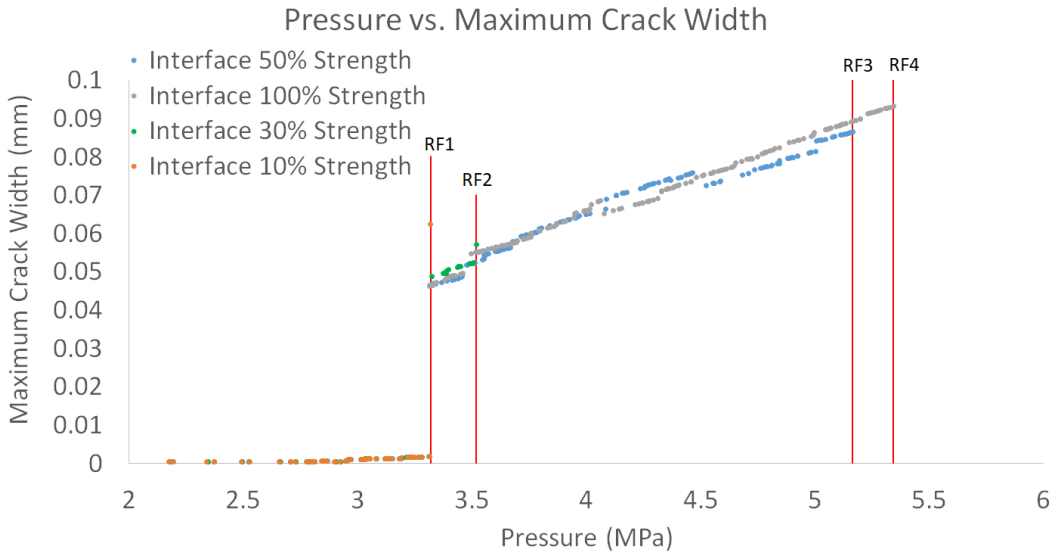

Figure 6.25: Pressure-Maximum Crack Width Curve for $NC\_\sigma\epsilon$ Model

$NC_\sigma\epsilon$_10% is the most brittle model due to the weakest interface tensile strength. Within RF1, a complete failure in the mortar-substrate interface is produced. Then the analysis is not reasonable anymore. Due to the de-bonding, the other localized cracks in repair mortar are slightly closed.

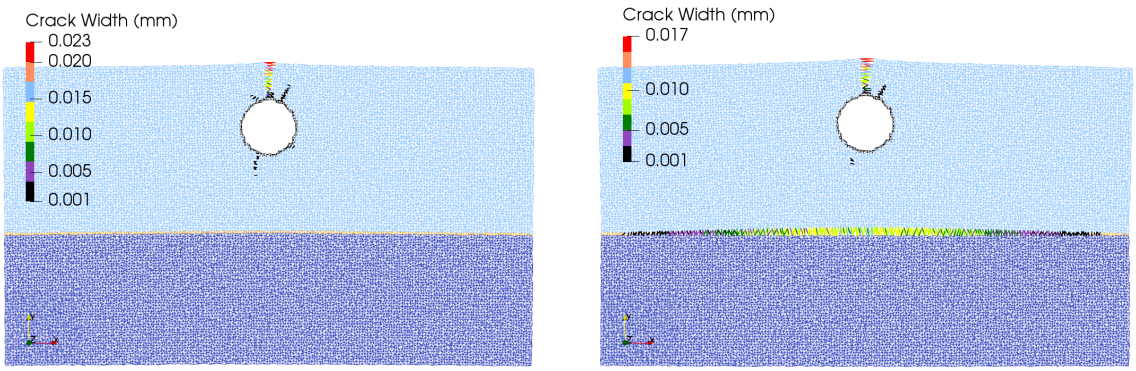

(a) Step 768, Before RF1

(b) Step 1144, After RF1

Figure 6.26: Complete Failure in Interface, Model $NC_\sigma\epsilon$_10%

However, in model $NC\_\sigma\epsilon\_30\%$, the cracking behavior is changed. After the bottom crack reaches the mortar-substrate interface, some interface elements start being damaged at step 1137 (Figure 6.27a). Nevertheless, these damaged elements do not cause de-bonding in the interface. The bottom crack propagates deeper into substrate instead (Figure 6.27b). However, the relatively weak interface influences the load capacity of model $NC\_\sigma\epsilon\_30\%$. Therefore, the bottom crack gets close to the bottom edge at a lower pressure (RF2) than model $NC\_\sigma\epsilon\_50\%$ and $NC\_\sigma\epsilon\_100\%$. Thence, model $NC\_\sigma\epsilon\_30\%$ shows lower load capacity. However, the failure mechanism of model $NC\_\sigma\epsilon\_30\%$ is localization of a second bottom crack (Figure 6.27c), which is the same as model $NC\_\sigma\epsilon\_50\%$ and $NC\_\sigma\epsilon\_100\%$. This verifies the conclusion that these three models behave similarly.

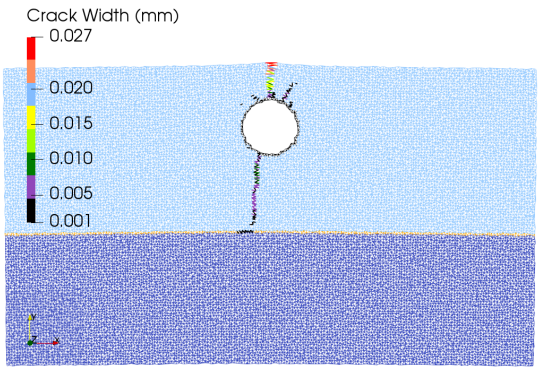

(a) Step 1137

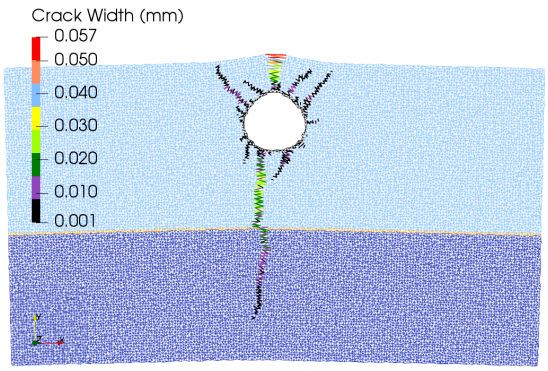

(b) Step 2283, RF2

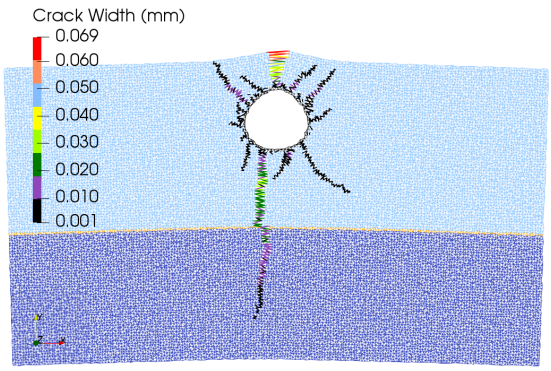

(c) Step 3000

Figure 6.27: Crack Pattern of Model $NC\_\sigma\epsilon\_30\%$

With the model $NC\_\sigma\epsilon\_50\%$, the analysis can run until the same level of model $NC\_\sigma\epsilon\_100\%$. The tensile strength of the interface in this model is strong enough that no de-bonding or damage in interface elements is performed (Figure 6.28a). Therefore, the crack pattern this model corresponds very much to model $NC\_\sigma\epsilon\_100\%$. Another proof is that this model also fails due to the localization of the second bottom crack (Figure 6.28b).

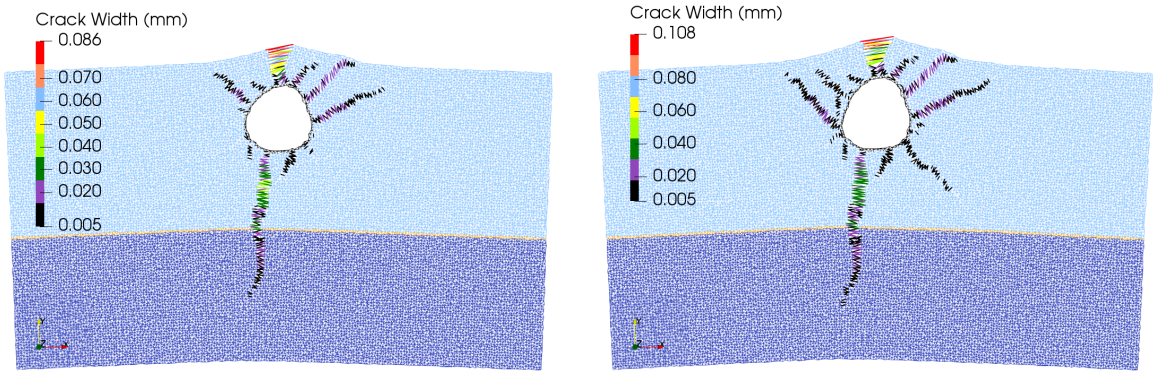

(a) Step 3518, RF3 (b) Step 4415

Figure 6.28: Crack Pattern of Model $NC_\sigma\epsilon$_50%

Figure 6.29 and 6.30 compare the final crack pattern of all models. 10% of repair mortar tensile strength is still too weak for interface strength. Therefore, a complete failure in the mortar-substrate interface is produced before bottom cracks reach the interface. However, the three other models with stronger interface strength behave very similarly. Model $NC_\sigma\epsilon$_30% is relatively brittle among these three models, the cracks developed in 2 o'clock direction is one less than the two other models. Because 30% of repair mortar tensile strength is still relatively weak. The bottom crack gets close to the bottom edge and is influenced by unbreakable bottom edge before the localization of the third crack. Meanwhile, the interface of model $NC_\sigma\epsilon$_50% is strong enough that its crack pattern is basically the same as model $NC_\sigma\epsilon$_100%.

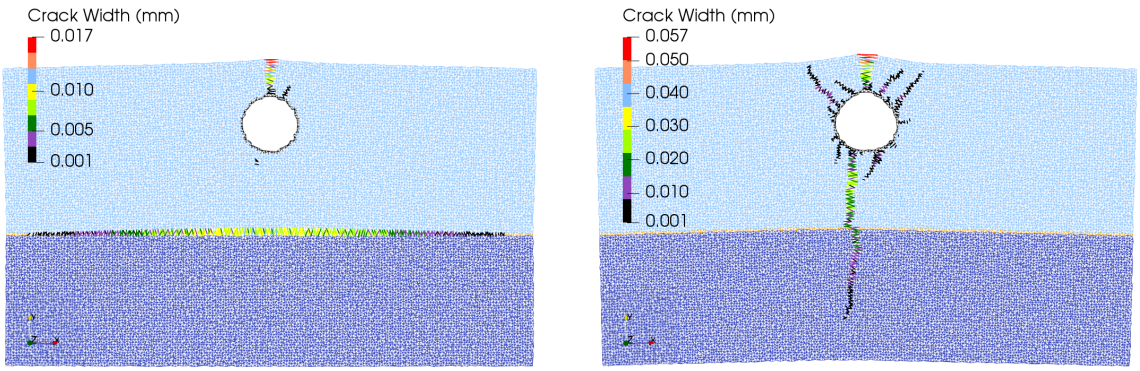

(a) Model $NC_\sigma\epsilon$_10%, RF1 (b) Model $NC_\sigma\epsilon$_30%, RF2

Figure 6.29: Crack Pattern of $NC\_\sigma\epsilon$ Repair Mortar Model with Different Interface Strength (1)

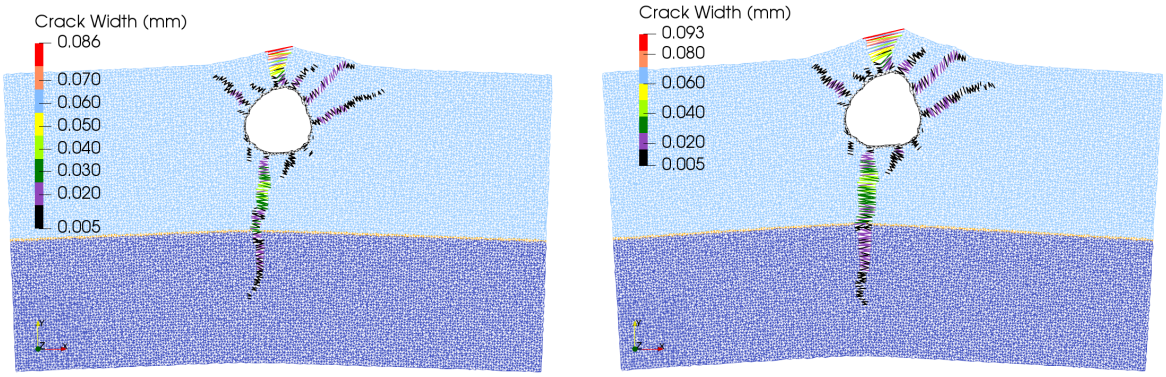

(a) Model $NC_\sigma\epsilon$_50%, RF3 (b) Model $NC_\sigma\epsilon$_100%, RF4

Figure 6.30: Crack Pattern of $NC\_\sigma\epsilon$ Repair Mortar Model with Different Interface Strength (2)

6.2.4. CONTINUUM MODEL RESULTS

In order to verify the assumption that the continuum model cannot perform the unsymmetrical damage in the interface with different tensile strength, two continuum models with interface elements between repair mortar and substrate are developed. 50% of the tensile strength of the repair mortar are applied as the tensile strength of the interface. As in the lattice model, the interface elements follow a brittle material law in tension. Figure 6.31 and Figure 6.32 show the crack pattern of the models with repair mortar $SHCC$ and NC_gf.

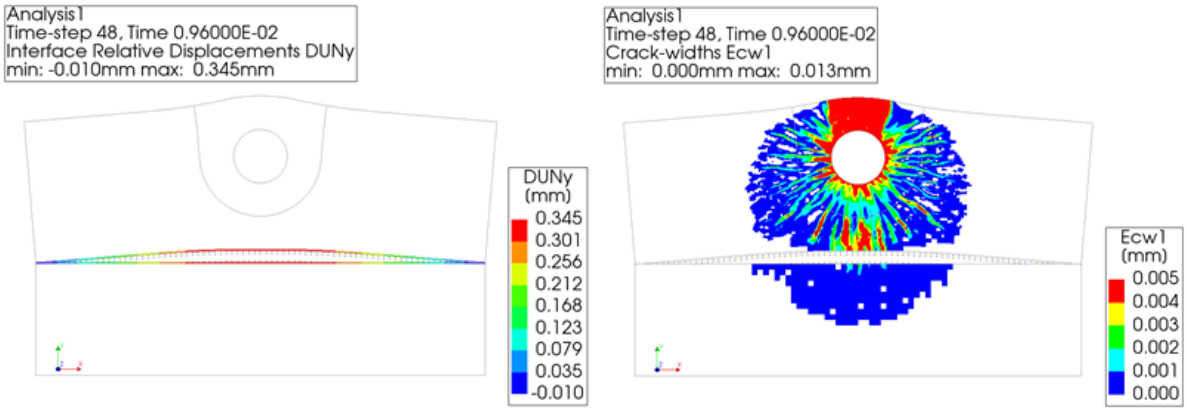

(a) interface traction (b) crack width

Figure 6.31: Crack Pattern of NC_gf Repair Mortar Model with 50% Interface Strength

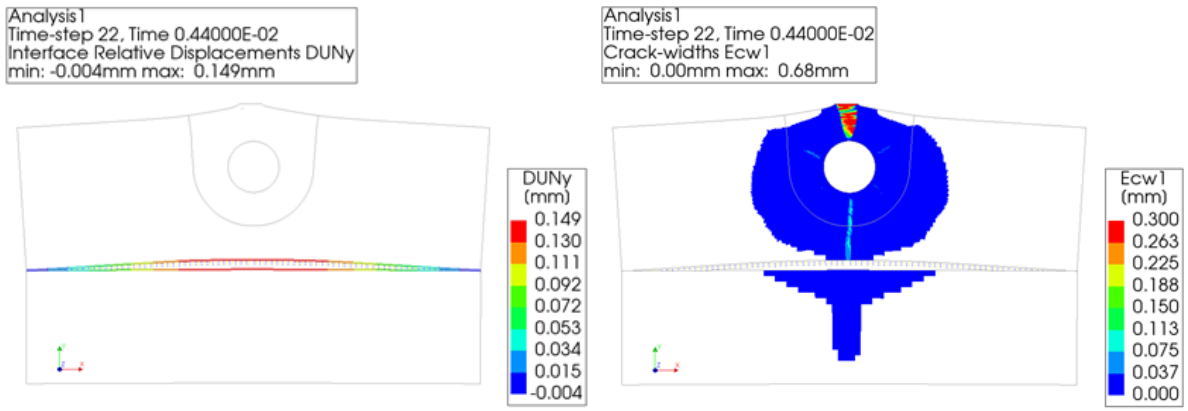

(a) interface traction (b) crack width

Figure 6.32: Crack Pattern of *SHCC* Repair Mortar Model with 50% Interface Strength

In both models, none bottom cracks can propagate into the substrate. Whenever a bottom crack reaches the interface, the interface is damaged completely within the next step. Due to the incremental solution method in the continuum model, the unsymmetrical damage pattern cannot be produced. When one element of the interface has enough stress to be damaged, the program will decide that the easiest equilibrium path is to damage all the interface elements. Therefore, no influence of interface tensile strength on the crack pattern can be observed in the continuum model.

6.2.5. EVALUATION

In general, the lattice model can successfully simulate the different cracking behavior caused by the different interface tensile strength. Especially some unsymmetrical damage in the mortar-substrate interface can be observed in the model with repair mortar SHCC. This is due to the sequentially linear solution method. By applying sequentially linear solution method, only one integration point (beam element in the lattice model) is damaged within one step. Therefore, the lattice model can follow every equilibrium paths and avoid bifurcation problem.

In contrast, the continuum model cannot show the different cracking behavior caused by the different interface tensile strength due to the bifurcation problem caused by its solution method. A complete damaged interface is produced whenever a bottom crack reaches the mortar substrate interface. Therefore, the continuum model is not a proper tool to study

the influence of interface strength on the cracking behavior.

In the models with both type of repair mortar, 10% of repair mortar tensile strength is too low for the interface tensile strength. A complete failure in the interface can be observed with both materials before any bottom crack reaches the interface. However, SHCC as repair mortar is more sensitive to interface strength than $NC\_\sigma\epsilon$. With model $NC_\sigma\epsilon$_30%, a crack pattern without de-bonding behavior can be produced similarly to that of the model $NC_\sigma\epsilon$_100%. Nevertheless, even with 50% of repair mortar strength in the interface, an evident influence on the crack pattern can still be observed in the SHCC model. There are two possible explanations. It is probably due to the cracking behavior of SHCC. The major straight bottom crack does not result in any de-bonding behavior in SHCC models. The orientation of this crack is relatively straight. Therefore, not too much vertical stress vector can be derived from this crack. The de-bonding effect can be initiated only when a second bottom crack reaches interface. Multiple cracks can be localized at the bottom in SHCC models because of its distributed cracking behavior. Meanwhile, $NC\_\sigma\epsilon$ models cannot localize a second bottom crack. Moreover, the strain capacity of SHCC is much higher than $NC\_\sigma\epsilon$. Therefore, when the bottom crack reaches interface, a much higher strain level is applied to the interface elements in the SHCC models. Therefore, a relatively strong bond is advised for applying SHCC in repairing system.

Interface strength has been proved to have a significant influence on the crack pattern and load capacity of a model. In order to simulate the cracking behavior of a concrete repair system accurately, the interface strength should be decided carefully in future analysis. This parameter should also be taken into consideration while designing a repair system.

6.3. SUBSTRATE TENSILE STRENGTH

In the previous models, concrete C30 is applied as the substrate. However, the concrete used in the tunnel can be much stronger in reality. The substrate strength can be regarded as a "boundary condition" of the repaired area in a broad sense. Whether the difference in the substrate strength will result in different crack pattern needs to be investigated. In this section, the lattice model is used to investigate the influence of substrate strength on the

cracking behavior of the specimen.

6.3.1. MATERIAL INPUT

In this section, the influence of the substrate strength is studied with two extreme material as repair mortar: $SHCC$ and $NC\_\sigma\epsilon$. The material input of $SHCC$ and $NC\_\sigma\epsilon$ are kept identical to the applied input in Section 6.1. Two different types of concrete are applied as the substrate: C30 and C60. The properties of these materials are adopted from the Eurocode 2 [39]. They are modeled as a brittle material with one segment representing their elastic stage. Their material inputs are listed in Table 6.3. All the other aspects of the model are kept identical to the settings in Section 6.1.

Table 6.3: Material Input of the Substrate

Model	Substrate	Number of Segment	E (GPa)	G (GPa)	f_t (MPa)	f_c (MPa)
$SHCC\_C60$	C60	1	39.1	16.29	4.35	-60
$SHCC\_C30$	C30	1	20	12.63	2.317	-25.5
$NC\_\sigma\epsilon\_C60$	C60	1	39.1	16.29	4.35	-60
$NC\_\sigma\epsilon\_C30$	C30	1	20	12.63	2.317	-25.5

6.3.2. RESULTS

The pressure-maximum crack width curves are displayed and compared in Figure 6.33 and 6.34. In the models with material $NC\_\sigma\epsilon$, the development of the maximum crack width is similar. Due to higher strength in the substrate, the maximum crack width that model $NC\_\sigma\epsilon\_C60$ can reach is 30.99% lower than the model $NC\_\sigma\epsilon\_C30$. A lower crack width can also be observed in the model $NC\_\sigma\epsilon\_C60$ during the whole analysis. In the models with material $SHCC$, the development of the maximum crack width is very similar to each other at the same crack width level.

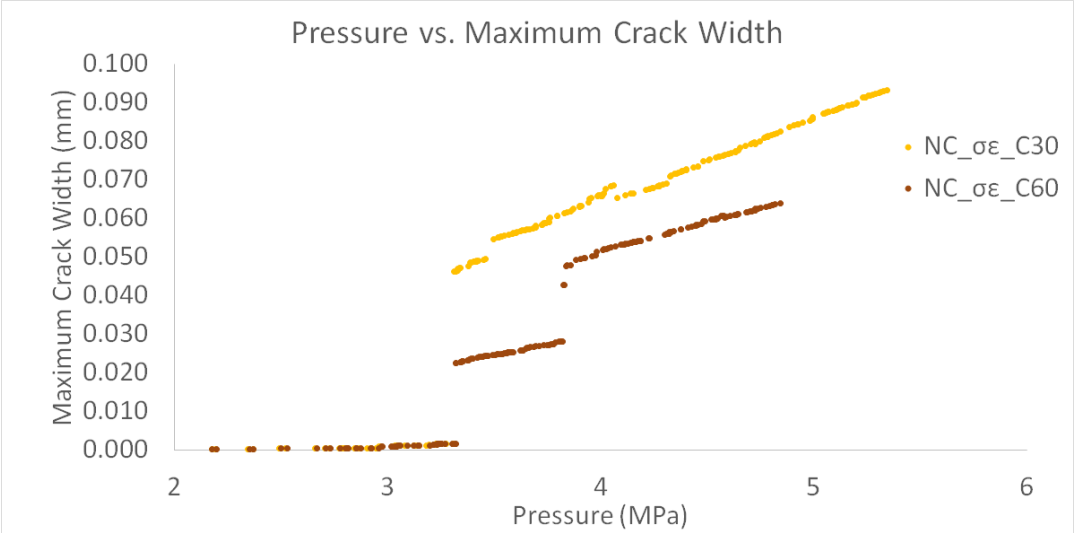

Figure 6.33: Pressure-Maximum Crack Width (Repair Mortar) Curve for $NC\_\sigma\epsilon$ Model with Different Substrate strength

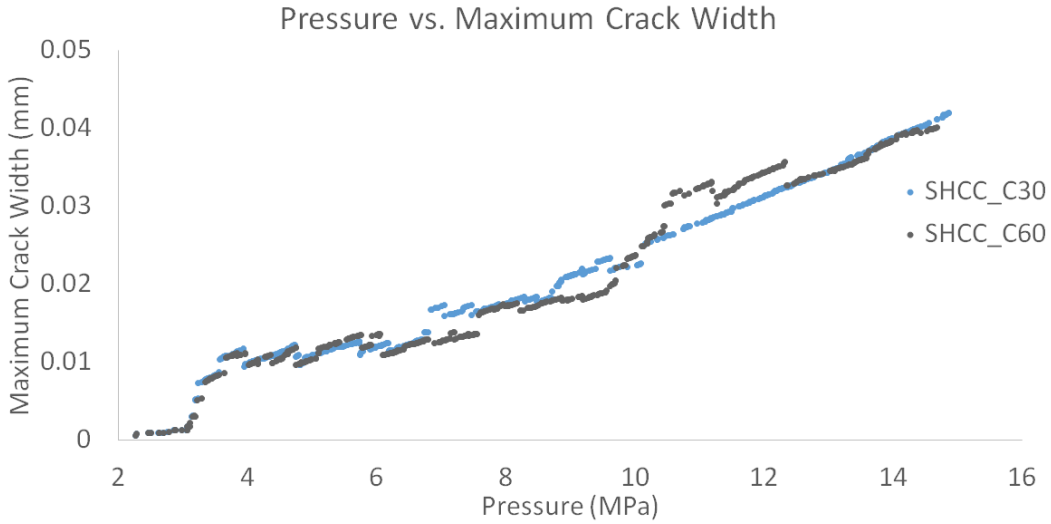

Figure 6.34: Pressure-Maximum Crack Width Curve (Repair Mortar) for $SHCC$ Models with Different Substrate Strength

The detailed crack pattern of all the four models at their final reasonable steps are compared in Figure 6.35 and 6.36. No difference in the crack pattern can be observed in the models with $NC\_\sigma\epsilon$ as repair mortar. However, the models with $SHCC$ as repair mortar produce a slightly different crack pattern at the bottom due to different substrate strength. A slightly inclined bottom crack is localized instead of a straight one in the model $SHCC\_C60$.

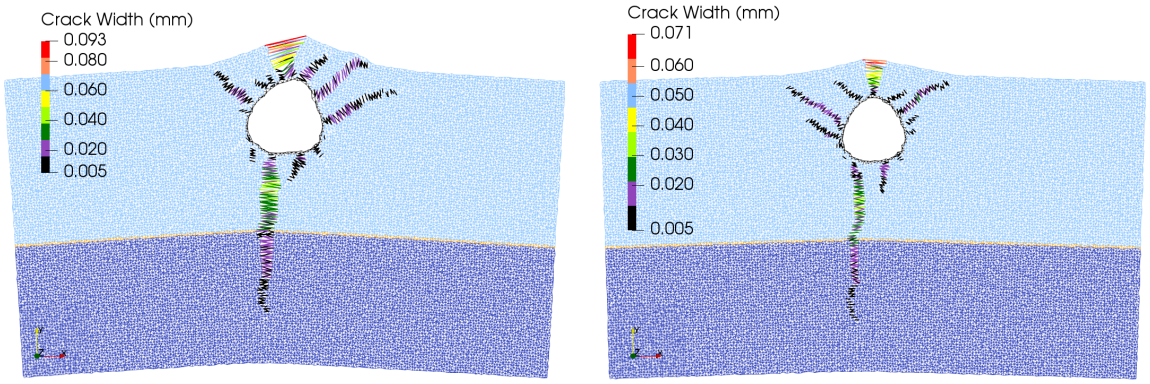

(a) C30 Substrate (b) C60 Substrate

Figure 6.35: Crack Pattern of $NC\_\sigma\epsilon$ Models with Different Substrate Strength

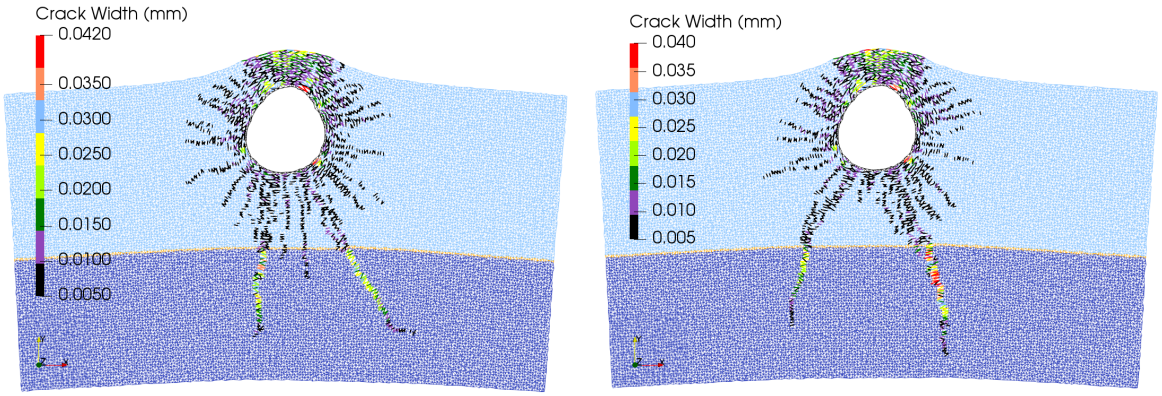

(a) C30 Substrate (b) C60 Substrate

Figure 6.36: Crack Pattern of $SHCC$ Models with Different Substrate Strength

These differences are probably due to the difference in the ultimate tensile strain of the repair mortar and the substrate. With material $NC\_\sigma\epsilon$, the stain capacity difference between the repair mortar and the substrate is pretty small. Therefore, no difference in the crack pattern can be observed. However, the maximum crack width is reduced due to higher substrate strength. In contrast, the strain capacity of $SHCC$ is significantly higher than concrete C60 and C30 (both more than 300 times). Thence, no difference can be observed in the maximum crack width. However, the bottom crack direction is slightly influenced by the substrate strength at the high tensile strain level.

7

DISCUSSIONS AND RECOMMENDATIONS

7.1. COMPARISON OF MATERIALS WITH DIFFERENT FRACTURE ENERGY

Both types of models are tested with five materials with different fracture energy. Their performances in simulating the cracking behavior of accelerated corrosion test are compared in Table 7.1.

Table 7.1: Comparison of Performance in Simulating Accelerated Corrosion Test

Model	Repair Mortar	Cracks Pattern	Number of Cracks	Maximum Crack Width (mm)
Continuum	$SHCC$	Distributed	19	0.015
	NC_gf	Concentrated	4	0.44
	FRC_50%	Concentrated	4	0.615
	FRC_0%	Concentrated	4	0.607
	$NC\_\sigma\epsilon$	Concentrated	5	0.173
Lattice	$SHCC$	Distributed	18	0.042
	FRC_50%	Distributed	15	0.041
	FRC_0%	Mixed	11	0.119
	$NC\_\sigma\epsilon$	Concentrated	6	0.093
	$NC\_brittle$	Concentrated	5	0.070

Both models can perform the distributed crack pattern of SHCC with the help of the randomness in the model. However, no significant difference in the crack pattern can be observed in the continuum model with strain-softening material due to bifurcation problem caused by the incremental solution method. Moreover, the convergence problem always happens due to the tangential stiffness used in this method. In contrast, the different crack

pattern with different repair mortar can be observed without any convergence problems in the lattice model because of its sequentially linear solution method. Therefore, the lattice model has better performance in the prediction of crack pattern in accelerated corrosion test simulation than the continuum model.

However, the lattice model shows the behavior of underestimating the crack width of the strain-softening materials. There are several possible explanations:

- After the localization of a complete damaged crack in the experiment, the specimen can still be further loaded and the cracks can still be widened. However, the analysis has to end because of the stability of the numerical analysis in the lattice model.

- By setting up a lattice model, the degrees of freedom per element is reduced from 16 (two quadratic plain stress elements) to 6 which results in a more brittle model than the continuum model with same mesh size.

- The crack width in the lattice model is calculated as the difference in the length between the deformed lattice beam and the original lattice beam. The cracking theory applied in the continuum model is more advanced (considering crack rotation, crack band width, etc.).

The crack width calculated by the lattice model is not comparable with the experiment. In the continuum model, a good prediction of crack width can be observed. Due to the convergence problem, it is not accurate enough. However, it is still a good indication of the development of the crack width.

Both types of models show their pros and cons. A combined model is proposed for further research to take advantage of both models. The combined model can be developed based on the continuum model. A random field on tensile strength can be applied to represent the heterogeneity of concrete. The sequentially linear analysis (SLA) solution method can be adopted from the lattice model. This combined model may have good performance in predicting both the crack width and the crack pattern. At the same time, the convergence problem will no longer trouble this combined model.

From the material point of view, with increasing fracture energy and strain capacity, more but thinner cracks can be performed in the accelerated corrosion test. SHCC material can perform the distributed crack pattern with a maximum crack width roughly one order of magnitude smaller than normal concrete. This behavior of SHCC is very suitable for being applied to a concrete repair system. The distributed cracks with smaller crack width can effectively limit the possibility of further corrosion. It is observed that the materials with deflection-hardening behavior in the bending test can produce this distributed crack pattern. Besides SHCC, some strain-softening (under direct tension) materials can also show the deflection-hardening behavior in the bending test and produce the distributed crack pattern. SHCC and fiber reinforced concrete with deflection-hardening behavior in the bending test are advised to be used in the concrete repair system further.

7.2. COMPARISON OF MORTAR-SUBSTRATE INTERFACE WITH DIFFERENT STRENGTH

The mortar-substrate interface tensile strength shows a good indication of the bond between repair mortar and substrate, which is very important for a concrete repair system. Both the lattice and the continuum model are used to simulate the accelerated corrosion test with four different tensile strength. Their results are summarized in Table 7.2.

Table 7.2: Comparison of Performance in Models with Different Interface Strength

Model	Repair Mortar	Interface Tensile Strength (as ratio of the repair mortar)	Interface Damage
Lattice	$SHCC$	100%	no damage
		50%	small part damaged
		30%	right half damaged
		10%	completely damaged
	$NC\_\sigma\epsilon$	100%	no damage
		50%	no damage
		30%	no damage
		10%	completely damaged
Continuum	$SHCC$	50%	completely damaged
	NC_gf	50%	completely damaged

The lattice model can perform the different damage in the interface brought by the differ-

ent interface tensile strength. However, the continuum model cannot show any difference in the cracking of the interface. This is another observation that shows the advantage of sequentially linear analysis in avoiding bifurcation problem. Thus, the lattice model is a better tool in simulating the detailed multiple crack pattern.

Models with material $SHCC$ is more sensitive to the strength of the interface tensile strength than models with material $NC\_\sigma\epsilon$. This is due to the significantly higher strain capacity of $SHCC$ than $NC\_\sigma\epsilon$ (around 300 times). When the bottom crack reaches the interface, the strain level in the models with $SHCC$ is much more higher than the models with $NC\_\sigma\epsilon$, which results in the failure of the interface at a lower strength. This indicates that extra caution is needed on the bond between the mortar and the substrate when applying SHCC in a concrete repair system.

7.3. INFLUENCE OF BOUNDARY CONDITIONS

It has been found in Section 3.1 and Section 4.2 that the boundary condition at the bottom edge has an influence on the direction of the bottom crack. The bottom cracks in the models with a constrained bottom edge are inclined towards 4 and 8 o'clock direction. In contrast, the bottom cracks in free bottom edge models are performed straight downwards towards the bottom edge. In the experiment, all the edges of the specimen are kept free. However, can this specimen simulate the cracking behavior of the floor in the Maastunnel is in doubt. In the real scenarios, the repaired area is constrained by the surrounding concrete. Based on the observation from numerical simulation, this constraint will have an influence on the crack pattern of the repair system. Therefore, the constrained edges are suggested for further experiments to corresponds better to the reality.

The substrate tensile strength can also be regarded as a "boundary condition" of the repair mortar in a broad sense. As observed in Section 6.3, the strength of the substrate does not show obvious influence on the crack pattern in the model with normal concrete as repair mortar. However, the maximum crack width in the model with C60 substrate is lower than the model with C30 substrate. The crack pattern of the models with SHCC as repair mortar shows a slight difference with different substrate strength. This indicates that the

different substrate strength can influence the crack pattern of material with high strain capacity slightly. However, the influence caused by the substrate strength is not significant. In the aspect of numerical simulation, this is negligible. In the decided repair strategy of the Maastunnel, a hydro-jetting is applied to clean the concrete. This can reduce the strength of the concrete significantly. The strength of the substrate should also be investigated theoretically. However, it is not necessary due to its minor influence in the numerical simulation.

8

CONCLUSIONS

The aims of this research are to test and compare the performance of lattice model and continuum model in simulating the cracking behavior of an accelerated corrosion test with different repair mortars and whether the different cracking behavior affected by mortar-substrate interface strength can be simulated. Main conclusions from the research are summarized.

- The continuum model suffers severe convergence problem in simulating the cracking behavior strain-softening material. Moreover, due to the bifurcation problem, the continuum model cannot produce the multiple crack pattern for strain-softening material. But the continuum model can produce the distributed crack pattern of SHCC.

- Symmetry shows influences on the crack pattern and crack width in a model. Therefore, a full model is suggested in simulating the crack pattern of accelerated corrosion test.

- The lattice model can simulate the different cracking behavior of mortar with different fracture energy in accelerated corrosion test. More distributed crack pattern, smaller crack width, and higher load pressure are simulated with increasing fracture energy in repair mortar.

- The Lattice model shows the behavior of underestimating the maximum crack width of the strain-softening material. The crack width value in the lattice model is not comparable with the experiments.

- The direction of bottom crack is found to be sensitive to the boundary conditions at the bottom edge. This indicates that the experiment done might not show the correct crack pattern of the reality in the tunnel. Constrained edges (by molds) are needed for simulating the cracking behavior caused by rebar corrosion in a floor in the future.

- Certain randomness is necessary for simulating the cracking behavior of SHCC the continuum model. The continuum model can realize the randomness by applying a random field over the tensile strength of repair mortar. The lattice model can produce the distributed crack pattern of SHCC with the help of its inherent randomness from the distribution of lattice beams. However, the discrete cracks cannot be produced in the top cracking area. Too many elements are damaged in that area that even random field cannot compensate the stresses.

- Correlation length which represents for the variation in a random field can significantly influence the damage pattern in a simulation with the continuum model. An artificial value is used as input considering the composite of SHCC. More researches are needed in the future in material aspects to investigate a proper correlation length for SHCC and other mortars.

- Interface tensile strength is found to influence the development of the cracks in the substrate in the numerical simulations. Therefore, the interface strength needs to be investigated in order to verify the numerical simulations of the crack pattern in the concrete repair system. Moreover, the de-bonding behavior at mortar-substrate interface happens at lower interface strength in a mortar with higher strain capacity. SHCC concrete repair system is more sensitive to the bond properties than fiber reinforced concrete.

- The lattice model can simulate the different crack pattern brought by the different interface tensile strength. However, the interface in the continuum model is always damaged completely irrespectively of its strength.

- The substrate strength shows only a slight influence on the crack pattern with material SHCC on the bottom crack direction. It is relatively less important for the numerical simulation.

- No only SHCC, but also some strain-softening FRC with deflection-hardening behavior in bending test can produce the distributed crack pattern. The distributed cracks can restrain the widening of the cracks and limit the possibility of the future corrosion of the repair system. Materials with the distributed cracking behavior are recommended for future implementation in the concrete repair system as the repair mortar.

BIBLIOGRAPHY

[1] C. K. Blom, M. M. Lukovic, and E. E. Taffijn, *Repair strategy of the deteriorated immersed maastunnel dr. ir. cbm (kees) blom1, 2, dr. ir. m.(mladena) lukovic2, ir. e.(erik) taffijn1, ir. dc (diederik) van zanten1, ir. wa (alex) gellweiler1 1municipality of rotterdam, engineering department. po box 6575, 3002 an rotterdam, the netherlands,* .

[2] V. C. Li, *Engineered cementitious composites (ecc) material, structural, and durability performance,* (2008).

[3] V. C. Li, *On engineered cementitious composites (ecc),* Journal of advanced concrete technology **1**, 215 (2003).

[4] M. D. Lepech and V. C. Li, *Water permeability of engineered cementitious composites,* Cement and Concrete Composites **31**, 744 (2009).

[5] M. Şahmaran and V. C. Li, *Influence of microcracking on water absorption and sorptivity of ecc,* Materials and structures **42**, 593 (2009).

[6] M. Sahmaran, M. Li, and V. C. Li, *Transport properties of engineered cementitious composites under chloride exposure,* Materials Journal **104**, 604 (2007).

[7] M. Luković, B. Šavija, G. Ye, E. Schlangen, and K. van Breugel, *Failure modes in concrete repair systems due to ongoing corrosion,* Advances in Materials Science and Engineering **2017** (2017).

[8] K. Kobayashi, S. C. Paul, and G. P. van Zijl, *Reinforcing bar corrosion,* in *A Framework for Durability Design with Strain-Hardening Cement-Based Composites (SHCC)* (Springer, 2017) pp. 147–170.

[9] J. Manie, *Diana user's manual, release 10.2,* (2017).

[10] P. Kabele, *Fracture behavior of shear-critical reinforced hfrcc members,* in *Proc. on the 49th Int. RILEM Workshop on HPFRCC in Structural Applications, USA* (2006) pp. 383–392.

[11] P. Kabele, *Multiscale framework for modeling of fracture in high performance fiber reinforced cementitious composites,* Engineering Fracture Mechanics **74**, 194 (2007).

[12] P. Jun and V. Mechtcherine, *Behaviour of strain-hardening cement-based composites (shcc) under monotonic and cyclic tensile loading: part 1–experimental investigations,* Cement and Concrete Composites **32**, 801 (2010).

[13] P. Kabele, *Stochastic finite element modeling of multiple cracking in fiber reinforced cementitious composites,* Fracture and damage of advanced fibre-reinforced cement-based materials , 155 (2010).

[14] M. Lukovic, *Influence of interface and SHCC material properties on the performance of the repair system*, Ph.D. thesis, PhD thesis, Delft University of Technology, in preparation (2015).

[15] M. Di Prisco, G. Plizzari, and L. Vandewalle, *Fiber reinforced concrete in the new fib model code,* in *4th International Conference on Construction Materials: Performance, Innovations and Structural Implications*, Vol. 1 (2009).

[16] M. Lukovic, W. Gellweiler, M. Sierra Beltran, C. Blom, B. Savija, D. van Zanten, E. Schlangen, G. Ye, and E. Taffijn, *In situ and laboratory testing of different repair materials,* in *Concrete Institute of Australia Conference, 27th, 2015, Melbourne, Victoria, Australia* (2015).

[17] V. C. Li, H. Horii, P. Kabele, T. Kanda, and Y. Lim, *Repair and retrofit with engineered cementitious composites,* Engineering Fracture Mechanics **65**, 317 (2000).

[18] C. E. C. for Standardization), *Test method for metallic fiber concrete—measuring the flexural tensile strength (limit of proportionality (lop), residual),* (2007).

[19] H. J. Herrmann, *Introduction to modern ideas on tracture patterns,* in *Random Fluctuations and Pattern Growth: Experiments and Models* (Springer, 1988) pp. 149–160.

[20] O. Çopuroğlu and E. Schlangen, *Modeling of frost salt scaling,* Cement and Concrete Research **38**, 27 (2008).

[21] L. Sluys and R. de Borst, *Computational methods in non-linear solid mechanics,* TU Delft **21**, 76 (2001).

[22] J. Zhou, *Performance of engineered cementitious composites for concrete repairs,* (2011).

[23] M. Luković, B. Šavija, H. Dong, E. Schlangen, and G. Ye, *Micromechanical study of the interface properties in concrete repair systems,* Journal of Advanced Concrete Technology **12**, 320 (2014).

[24] M. G. Sierra-Beltran, H. Jonkers, and E. Schlangen, *Characterization of sustainable bio-based mortar for concrete repair,* Construction and Building materials **67**, 344 (2014).

[25] B. Šavija, *Experimental and numerical investigation of chloride ingress in cracked concrete*, Ph.D. thesis, TU Delft, Delft University of Technology (2014).

[26] J. Pacheco, *Corrosion of steel in cracked concrete*, Ph.D. thesis, Thesis (PhD). Delft University of Technology (2015).

[27] B. Šavija, M. Luković, J. Pacheco, and E. Schlangen, *Cracking of the concrete cover due to reinforcement corrosion: a two-dimensional lattice model study,* Construction and Building Materials **44**, 626 (2013).

[28] F. Wittmann, P. Wang, P. Zhang, T. Zhao, and F. Beltzung, *Capillary absorption and chloride penetration into neat and water repellent shcc under imposed strain,* in *2nd International RILEM Conference on Strain Hardening Cementitious Composites (SHCC2-Rio)* (RILEM Publications SARL Rio de Janeiro, 2011) pp. 165–172.

[29] G. P. van Zijl, F. H. Wittmann, B. H. Oh, P. Kabele, R. D. Toledo Filho, E. M. Fairbairn, V. Slowik, A. Ogawa, H. Hoshiro, V. Mechtcherine, *et al.*, *Durability of strain-hardening cement-based composites (shcc),* Materials and structures **45**, 1447 (2012).

[30] A. M. Neville, *Properties of concrete*, Vol. 4 (Longman London, 1995).

[31] B. H. Oh and K. J. Shin, *Cracking, ductility and durability characteristics of hpfrcc with various mixture proportions and fibers,* in *Intl. workshop on HPFRCC in structural application, Hawaii, USA* (Citeseer, 2005) pp. 1–9.

[32] E. Schlangen and J. Van Mier, *Experimental and numerical analysis of micromechanisms of fracture of cement-based composites,* Cement and concrete composites **14**, 105 (1992).

[33] E. Schlangen and E. Garboczi, *Fracture simulations of concrete using lattice models: computational aspects,* Engineering fracture mechanics **57**, 319 (1997).

[34] A. Slobbe, M. Hendriks, and J. Rots, *Sequentially linear analysis of shear critical reinforced concrete beams without shear reinforcement,* Finite Elements in Analysis and Design **50**, 108 (2012).

[35] D. Hordijk, *Local approach to fatigue of concrete,* Doctoral Thesis, Delft University (1991).

[36] P. Beverly, *fib model code for concrete structures 2010* (Ernst & Sohn, 2013).

[37] V. C. Li and G. Fischer, *Reinforced ecc-an evolution from materials to structures,* (2002).

[38] M. Vořechovskỳ, *Interplay of size effects in concrete specimens under tension studied via computational stochastic fracture mechanics,* International Journal of Solids and Structures **44**, 2715 (2007).

[39] E. C. for Standardization, *Eurocode 2: Design of concrete structures* (Central Secretariat, CEN, 1994).

[40] M. Luković, H. Dong, B. Šavija, E. Schlangen, G. Ye, and K. van Breugel, *Tailoring strain-hardening cementitious composite repair systems through numerical experimentation,* Cement and Concrete Composites **53**, 200 (2014).

[41] R. Van der Have, *Random fields for non-linear finite element analysis of reinforced concrete,* (2015).

[42] Wikipedia contributors, *Cholesky decomposition — Wikipedia, the free encyclopedia,* https://en.wikipedia.org/w/index.php?title=Cholesky_decomposition&oldid=847586360 (2018), [Online; accessed 6-July-2018].

[43] J. JCSS, *Probabilistic model code,* Joint Committee on Structural Safety (2001).

[44] E. Vanmarcke, *Random fields: analysis and synthesis* (World Scientific, 2010).

[45] M. Lukovic, *Influence of interface and strain hardening cementitious composite (SHCC) properties on the performance of concrete repairs*, Ph.D. thesis, TU Delft, Delft University of Technology (2016).

[46] M.-b. Geers, *Enhanced solution control for physically and geometrically non-linear problems. part ii—comparative performance analysis,* International Journal for Numerical Methods in Engineering **46**, 205 (1999).

[47] J. Rots, *Sequentially linear continuum model for concrete fracture,* Fracture mechanics of concrete structures **2**, 831 (2001).

A

THREE-POINT AND FOUR-POINT BENDING TEST RESULTS

The size of the tested beam is $100 \times 100 \times 500\ mm^3$ with a notch of $5 \times 17\ mm^2$. The clear span of the beam is $334\ mm$. The results of the three-point bending rest results of OG26 with $26 kg/m^3$ $Kurary^{TM}$ PVA-micro fibers are displayed.

Table A.1: Three-point Bending Test Results of OG26

Deflection	Test 1	Test 2
LOP (N/mm^2)	6.4	6.3
f_{R1} $(\delta_1 = 0.47\ mm)$ (N/mm^2)	7.8	9.7
f_{R2} $(\delta_2 = 1.32\ mm)$ (N/mm^2)	4.2	8.7
f_{R3} $(\delta_3 = 2.17\ mm)$ (N/mm^2)	2.2	5.9
f_{R4} $(\delta_4 = 3.02\ mm)$ (N/mm^2)	1.6	3.7

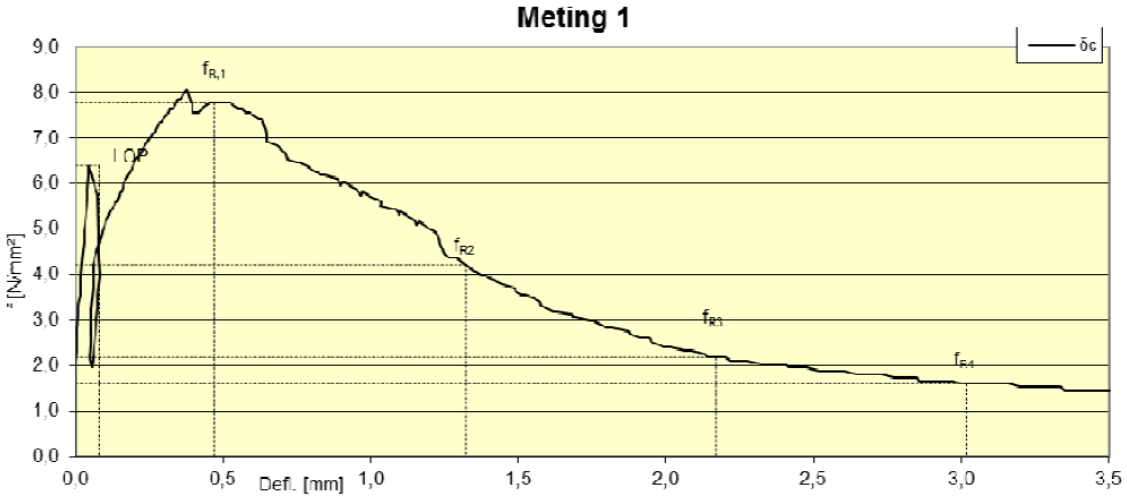

Figure A.1: Deflection-Stress Curve of OG26 in Three-poing Bending, Test 1

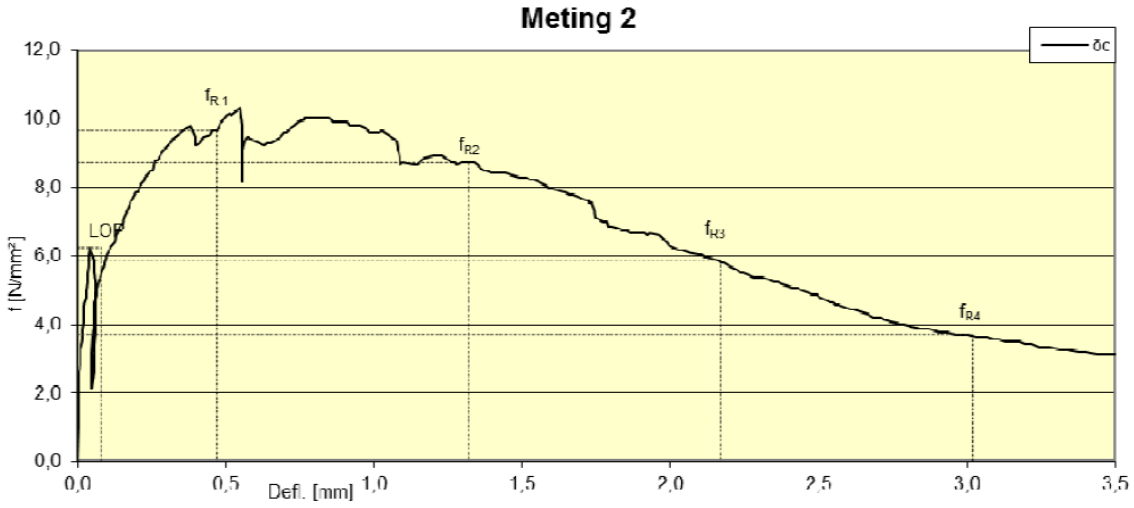

Figure A.2: Deflection-Stress Curve of OG26 in Three-poing Bending, Test 2

The results of the three-point bending test of material ON25 with $25kg/m^3$ $Istrice^{TM}$ macro fibers were lost due to the ICT issues. The results of the three-point bending test of material OG15 with $15kg/m^3$ $Kurary^{TM}$ PVA-micro fibers were partly lost. Its result is displayed.

Table A.2: Three-point Bending Test Results of OG15

Deflection	Test 1	Test 2
LOP (N/mm^2)	/	5.7
f_{R1} ($\delta_1 = 0.47\ mm$) (N/mm^2)	/	4.4
f_{R2} ($\delta_2 = 1.32\ mm$) (N/mm^2)	/	1.5
f_{R3} ($\delta_3 = 2.17\ mm$) (N/mm^2)	/	0.7
f_{R4} ($\delta_4 = 3.02\ mm$) (N/mm^2)	/	0.4

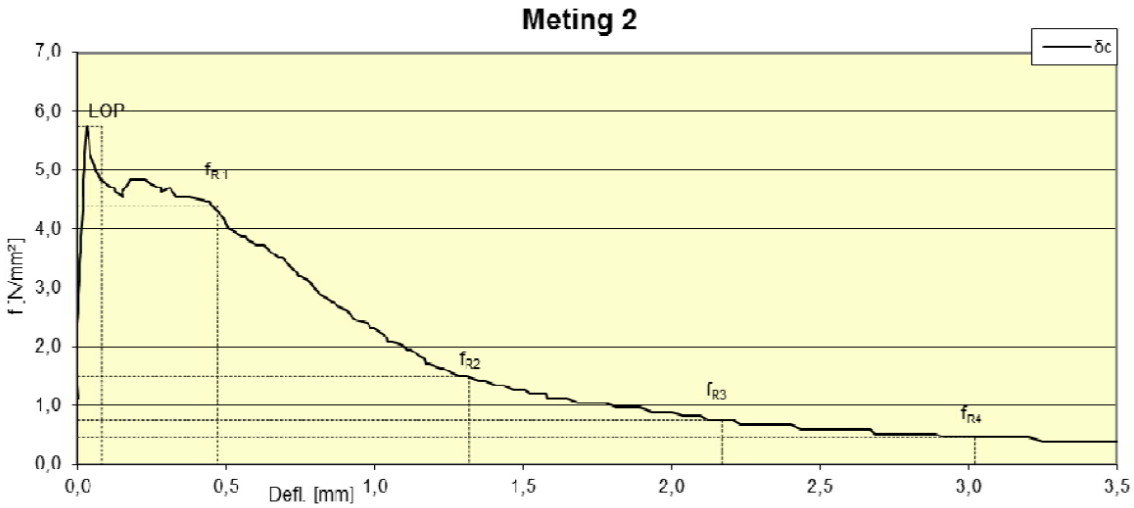

Figure A.3: Deflection-Stress Curve of OG15 in Three-poing Bending, Test 2

The results of the four-point bending test of material OG15 with $15 kg/m^3$ $Kurary^{TM}$ PVA-micro fibers are displayed.

Table A.3: Four-point Bending Test Results of OG26

Deflection	Test 1	Test 2
LOP (N/mm^2)	6.0	6.5
f_{R1} ($\delta_1 = 0.47\ mm$) (N/mm^2)	2.8	1.8
f_{R2} ($\delta_2 = 1.32\ mm$) (N/mm^2)	0.8	0.4
f_{R3} ($\delta_3 = 2.17\ mm$) (N/mm^2)	0.3	0.2
f_{R4} ($\delta_4 = 3.02\ mm$) (N/mm^2)	0.2	0.1

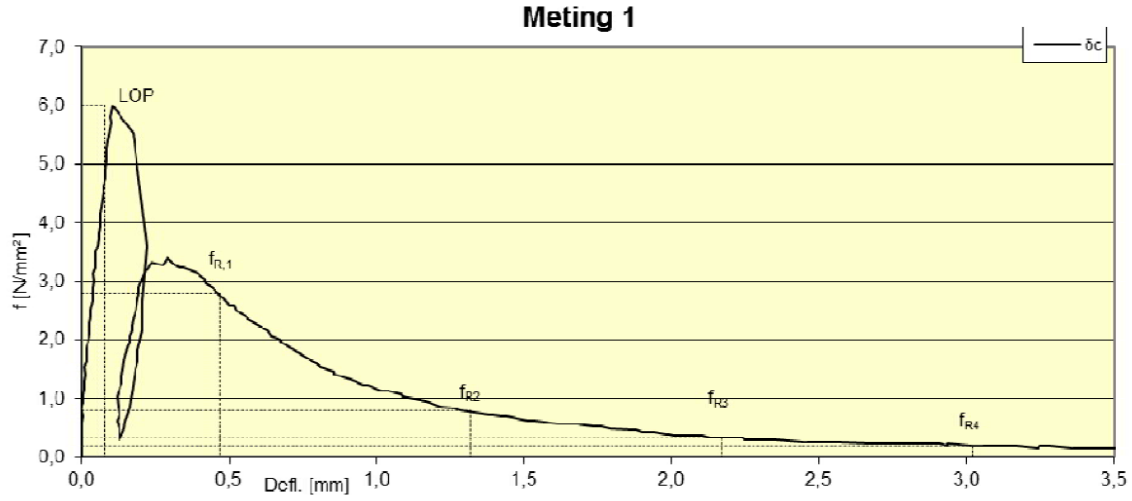

Figure A.4: Deflection-Stress Curve of OG15 in Four-poing Bending, Test 1

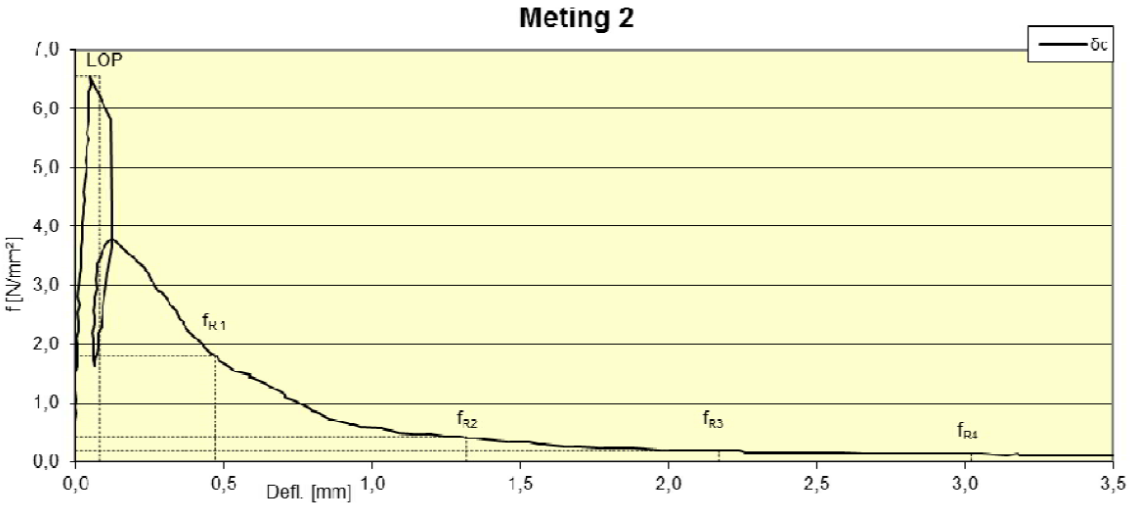

Figure A.5: Deflection-Stress Curve of OG15 in Four-poing Bending, Test 2

B

Crack Pattern of the Accelerated Corrosion Test

In the experiment, five types of mixtures are applied as the repair mortar. The composite of all materials are listed in Table B.1.

Table B.1: Recipes for test mixtures

Name Code	OG26 M1	ON01 M2	ON06 M3	ON25 M4	OG15 M5
Cement (kg/m^3)	790	420	420	440	730
Limestone flour (kg/m^3)	790		65	65	
PPr-macrofibres "Istrice - iShots®29mm" (kg/m^3)			6	25	
PPr-microfibres "Bonar - Confiber 23" (kg/m^3)		1.35	0.90		
PVA-microfibres "Kuraray - RECS 15/8" (kg/m^3)	26				15
Sand 0/4 (kg/m^3)		753	727	895	456
Gravel 3/5 (kg/m^3)		160	154	281	97
Gravel 5/8 (kg/m^3)		240	231	422	145
Gravel 8/16 (kg/m^3)		599	578		363
Mixing Water (kg/m^3)	411	177	177	182	328
Cugla Cretoplast (kg/m^3)		1.26	1.26	1.45	
Cugla LR-9400 (kg/m^3)	2.40	1.04	1.04	1.36	1.10

The test is conducted in phases. Different current level is applied at each phase (Table B.2).

Table B.2: Accelerated Corrosion Test Phase

Phase	Current ($\mu A/cm_s^2$)	Current (mA)	Lasted Time (d)	Measurement Stage
1	50	15.8	7	
2	75	23.7	7	1
3A	100	31.6	7	
3B	100	31.6	7	
4A	175	55.2	7	
4B	175	55.2	7	
4C	175	55.2	7	
5A	300	94.7	7	
5B	300	94.7	7	2

The damage recorded by the end of phase 3A is displayed in Figure B.1 and Figure B.2.

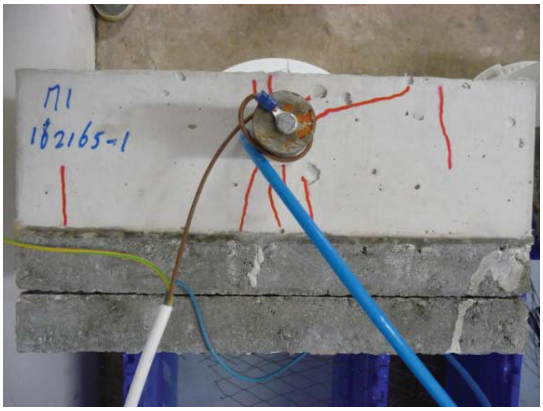

(a) M1

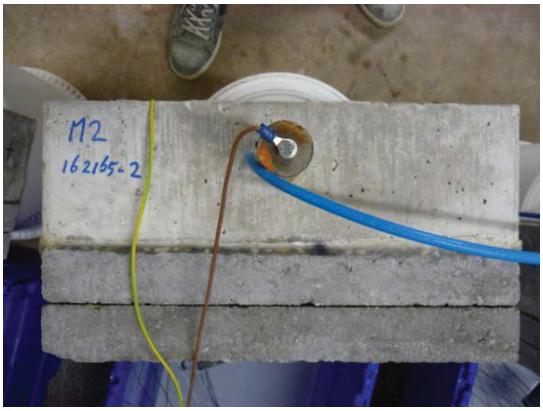

(b) M2

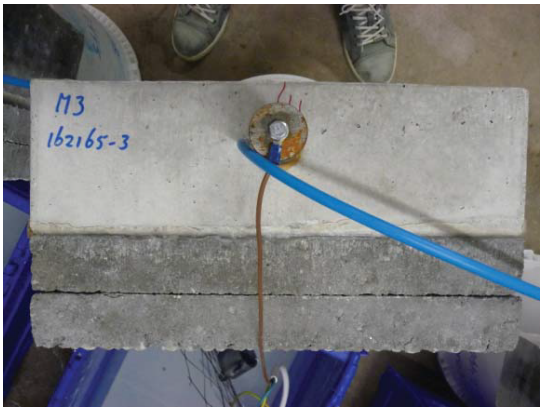

(c) M3

Figure B.1: Damage by the end of Phase 3A (1)

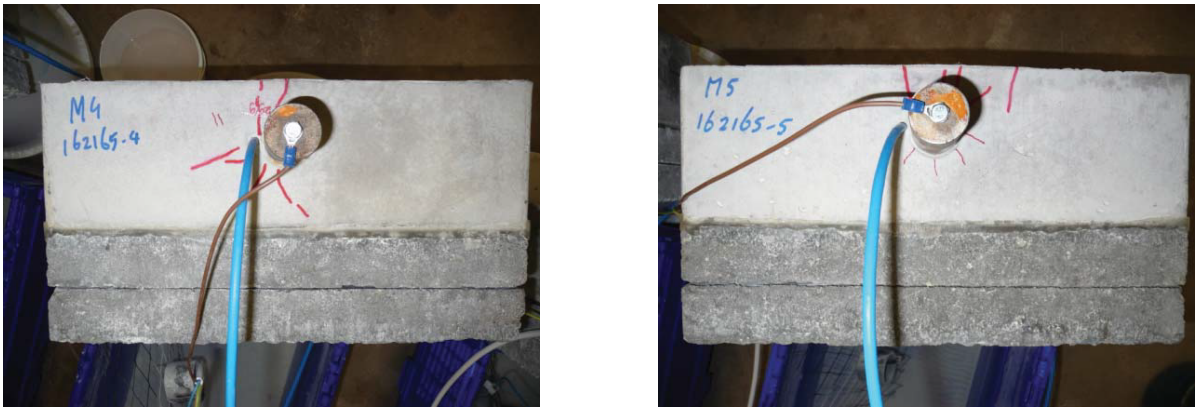

(a) M3 (b) M4

Figure B.2: Damage by the end of Phase 3A (2)

The damage recorded by the end of phase 3B is displayed in Figure B.3.

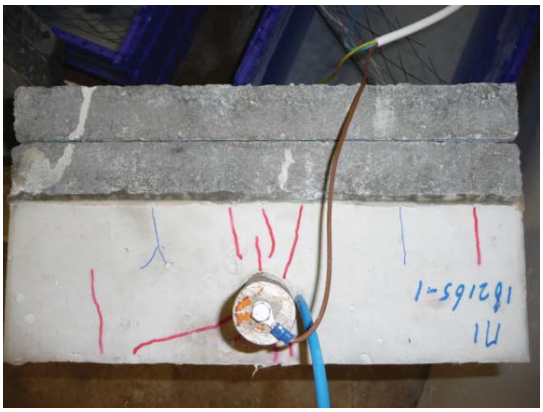

(a) M1

(b) M2

(c) M3

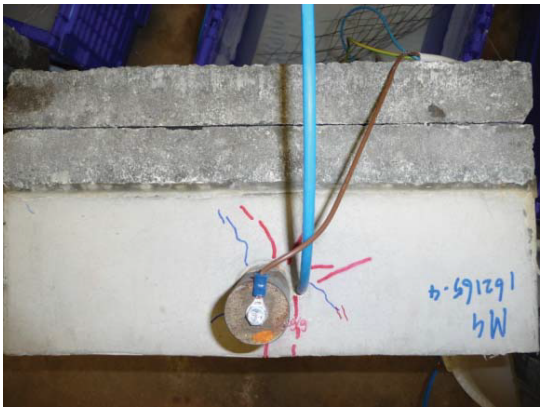

(d) M4

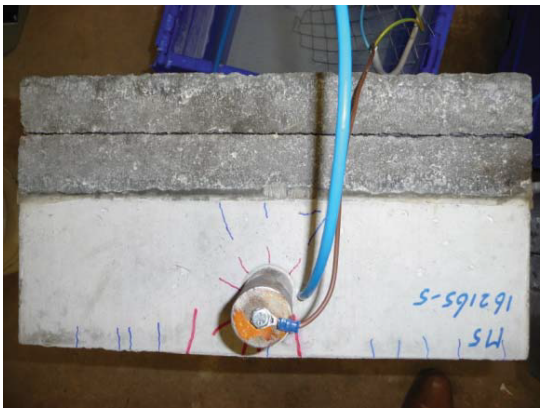

(e) M5

Figure B.3: Damage by the end of Phase 3B

The damage recorded by the end of phase 4A is displayed in Figure B.4.

(a) M1

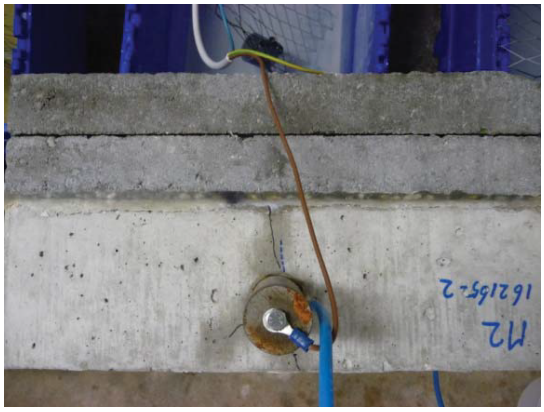

(b) M2

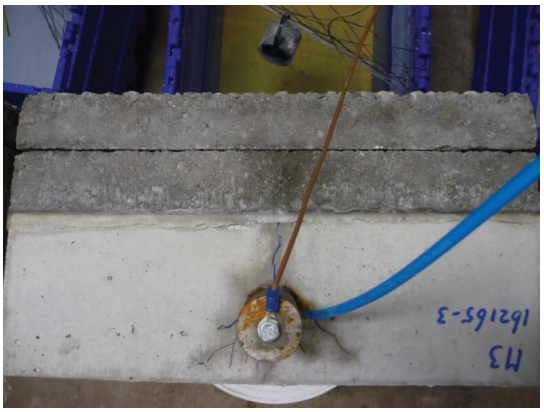

(c) M3

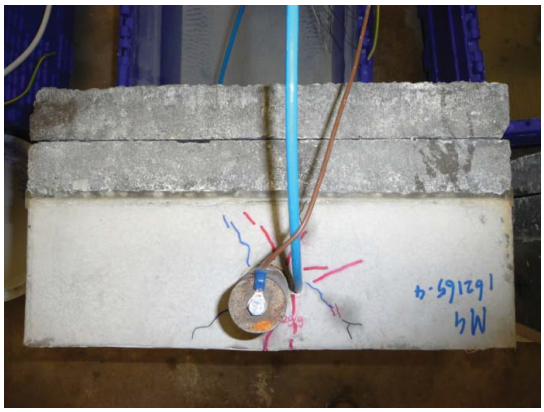

(d) M4

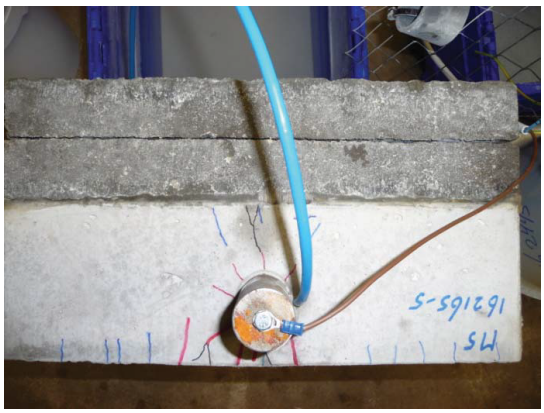

(e) M5

Figure B.4: Damage by the end of Phase 4A

The damage recorded by the end of phase 4B is displayed in Figure B.5.

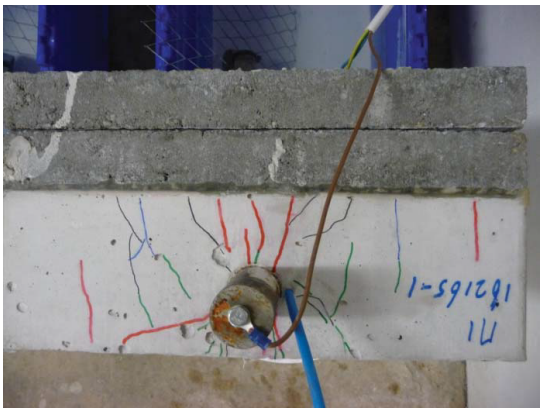

(a) M1

(b) M2

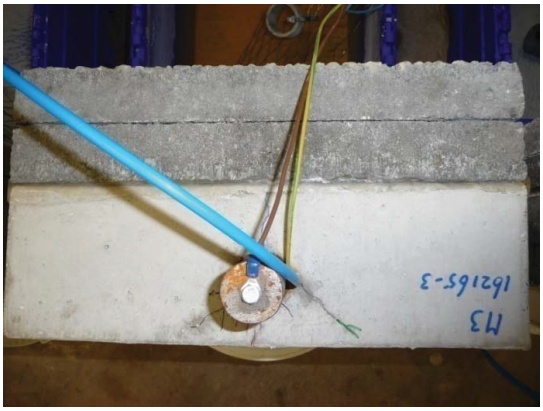

(c) M3

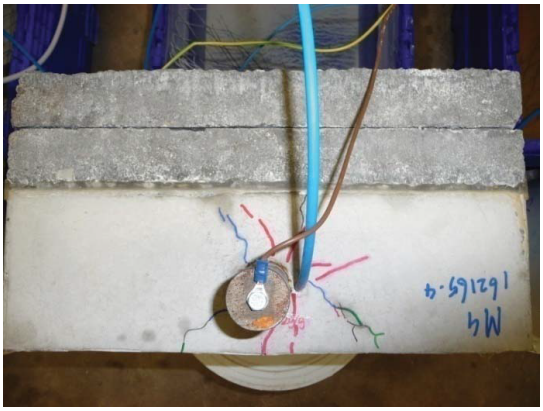

(d) M4

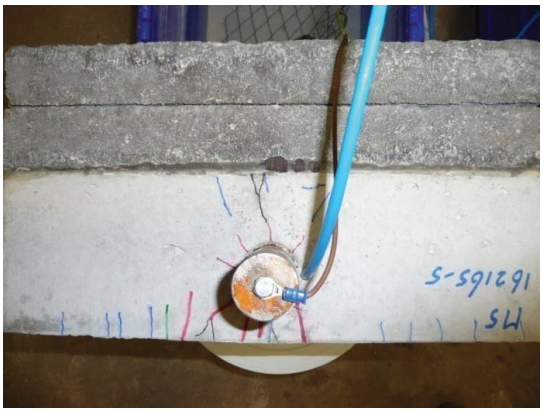

(e) M5

Figure B.5: Damage by the end of Phase 4B

The damage recorded by the end of phase 4C is displayed in Figure B.6.

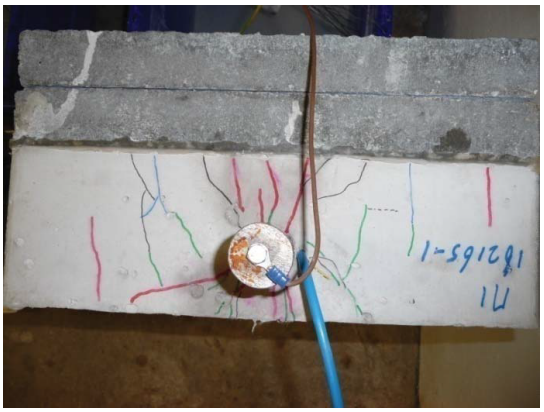

(a) M1

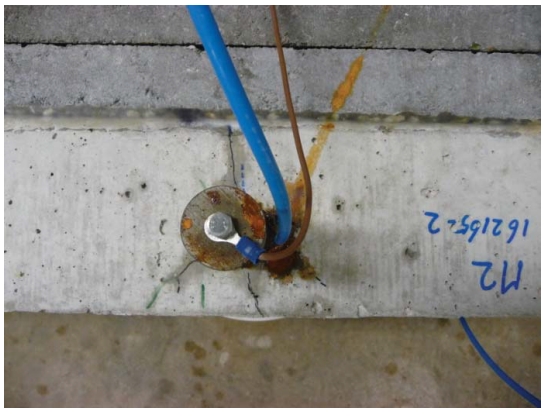

(b) M2

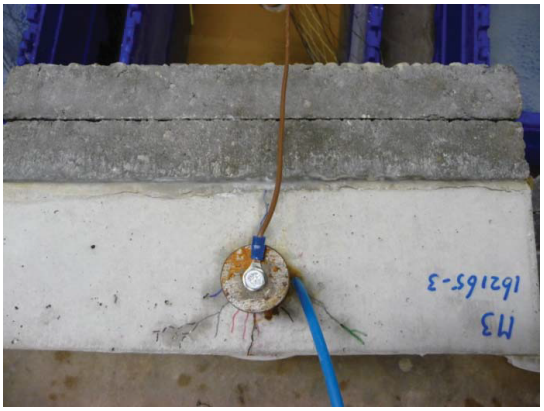

(c) M3

(d) M4

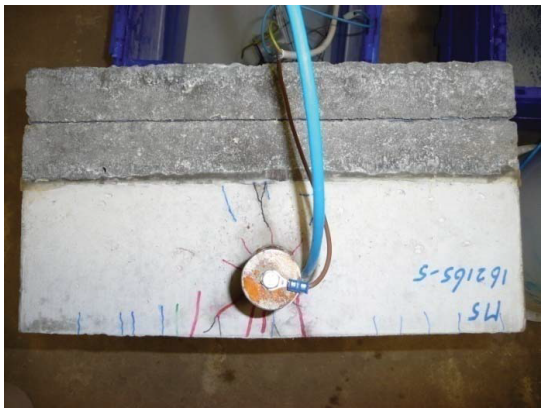

(e) M5

Figure B.6: Damage by the end of Phase 4C

The damage recorded by the end of phase 5A is displayed in Figure B.7.

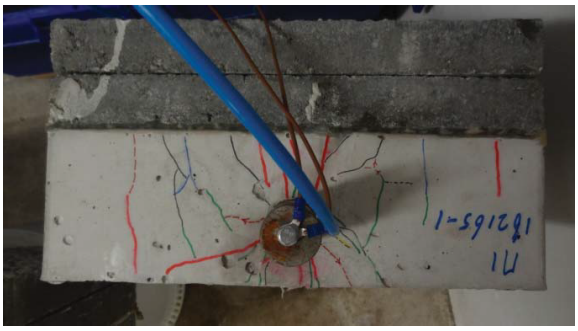

(a) M1

(b) M2

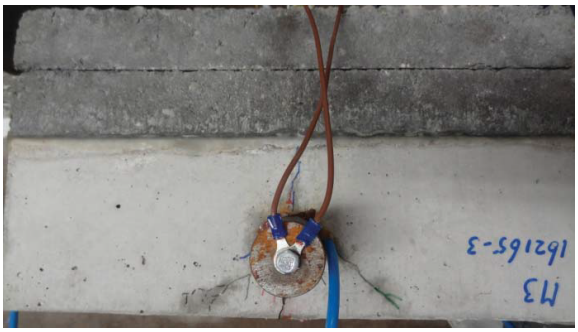

(c) M3

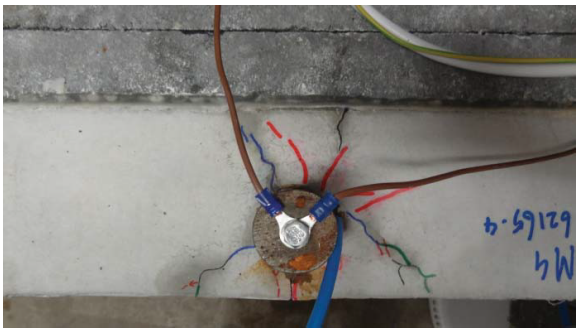

(d) M4

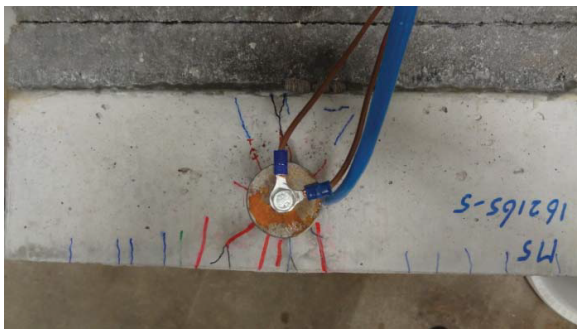

(e) M5

Figure B.7: Damage by the end of Phase 5A

The damage recorded by the end of phase 5B is displayed in Figure B.8.

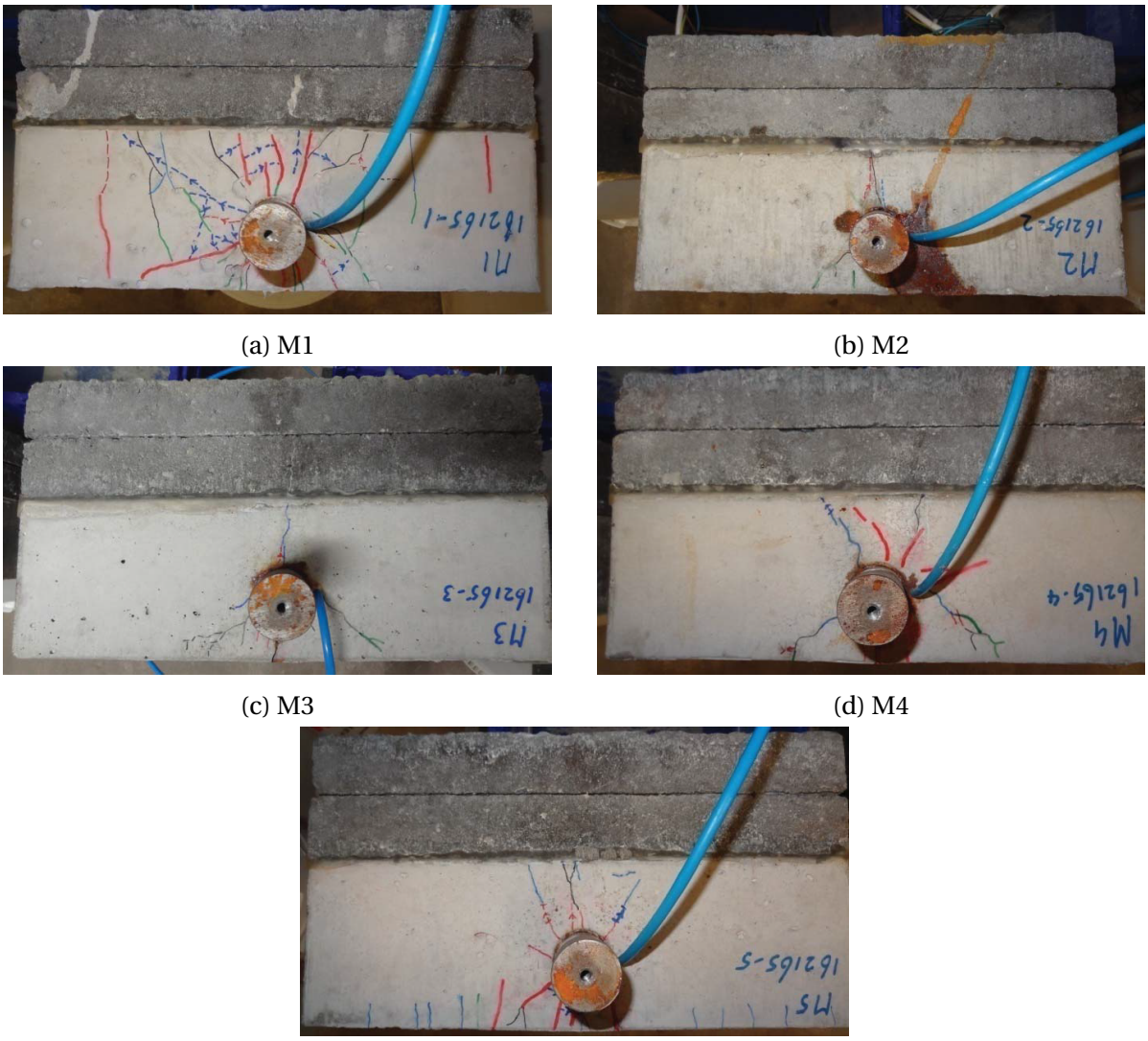

(a) M1

(b) M2

(c) M3

(d) M4

(e) M5

Figure B.8: Damage by the end of Phase 5B

The test specimens are also impregnated with fluorescent resin and examined under UV light. Before the vacuum impregnation, the outer 100 mm on both sides of the specimen and around 95 mm of the substrate are removed using a water-cooled saw. The test specimens are cut and examined at three depths: 30 mm, 50 mm, and 100 mm (Figure 1.12). The crack patterns are shown in both natural and UV light.

The crack pattern of material M1 is shown in Figure B.9.

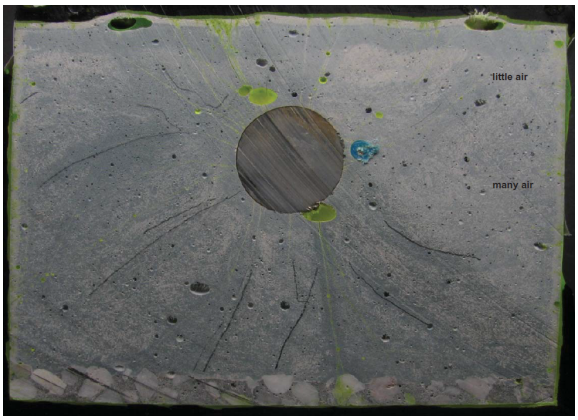

(a) 30 mm depth, normal light

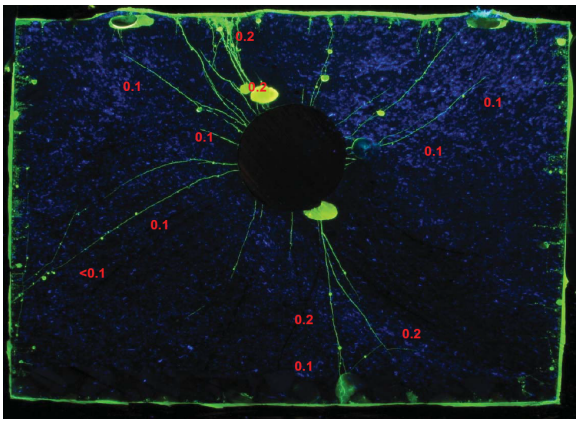

(b) 30 mm depth, UV light

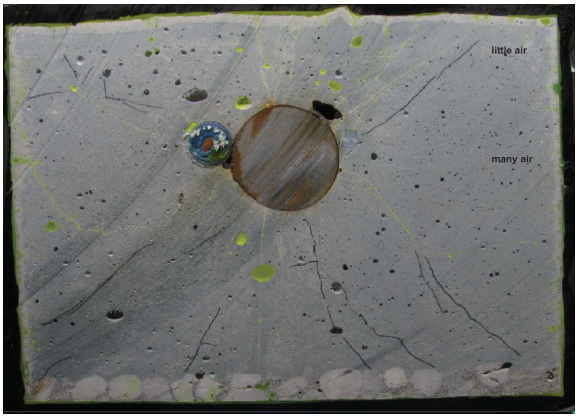

(c) 100 mm depth, normal light

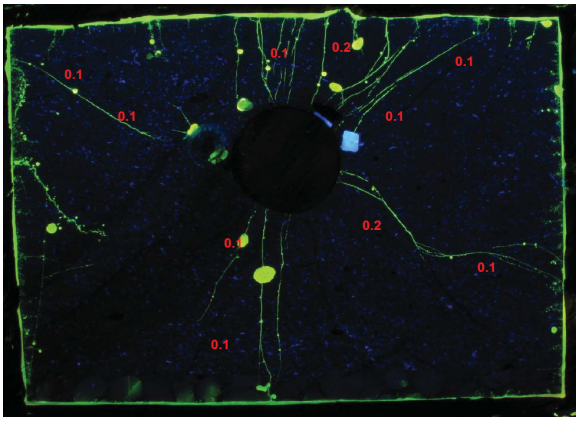

(d) 100 mm depth, UV light

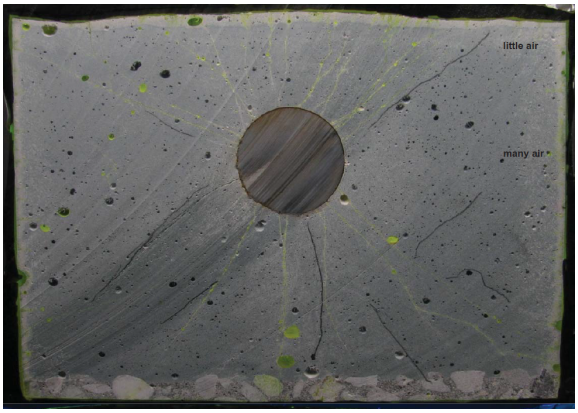

(e) 200 mm depth, normal light

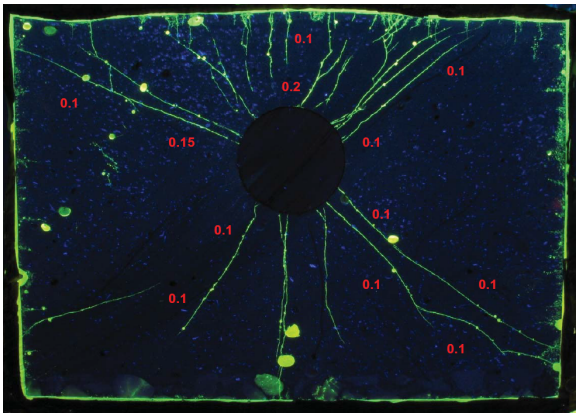

(f) 200 mm depth, UV light

Figure B.9: Crack Pattern of Material M1

The crack pattern of material M2 is shown in Figure B.10.

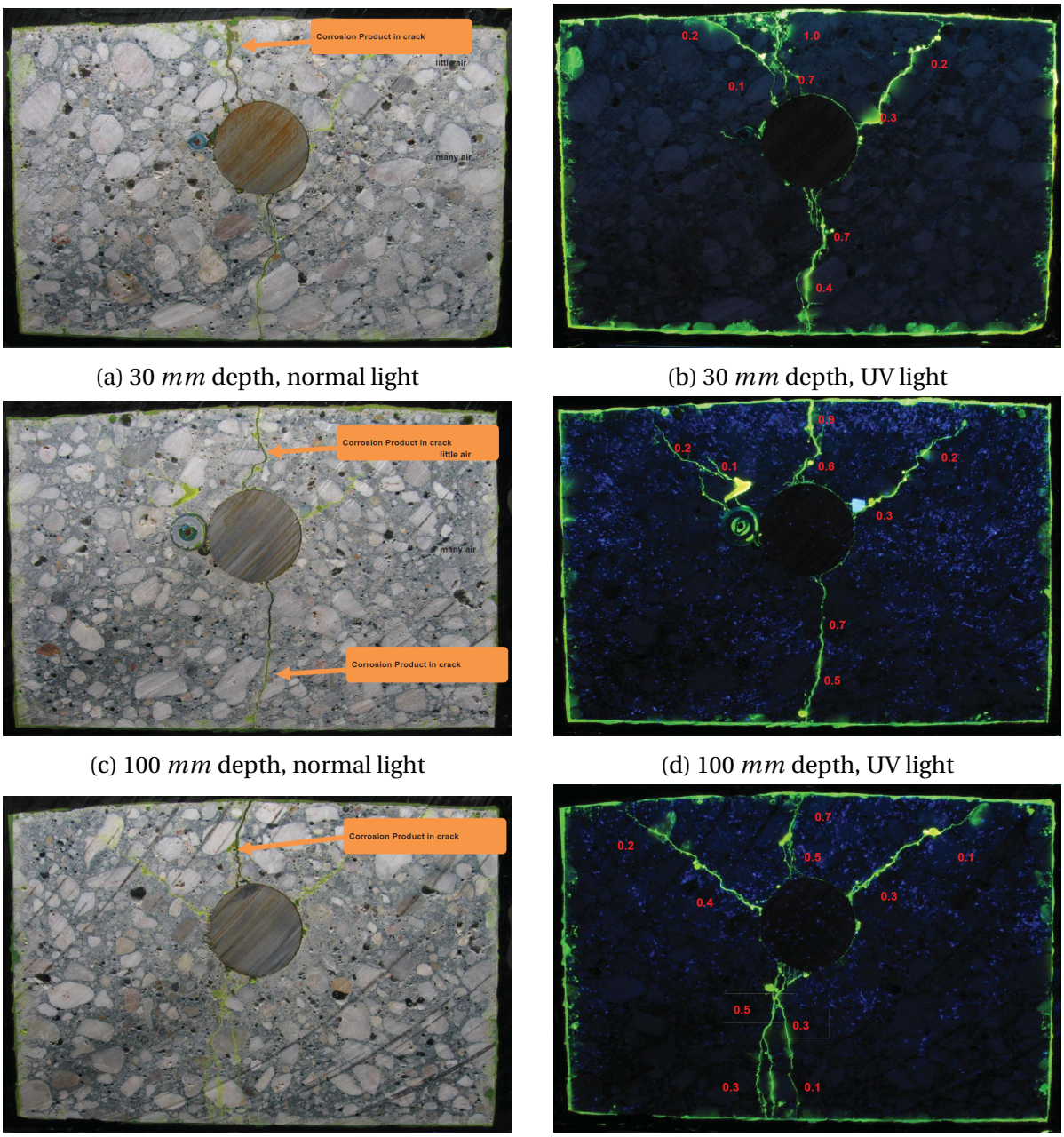

(a) 30 mm depth, normal light

(b) 30 mm depth, UV light

(c) 100 mm depth, normal light

(d) 100 mm depth, UV light

(e) 200 mm depth, normal light

(f) 200 mm depth, UV light

Figure B.10: Crack Pattern of Material M2

The crack pattern of material M3 is shown in Figure B.11.

(a) 30 mm depth, normal light

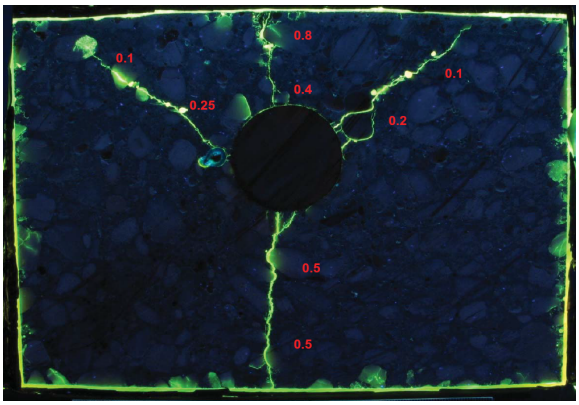

(b) 30 mm depth, UV light

(c) 100 mm depth, normal light

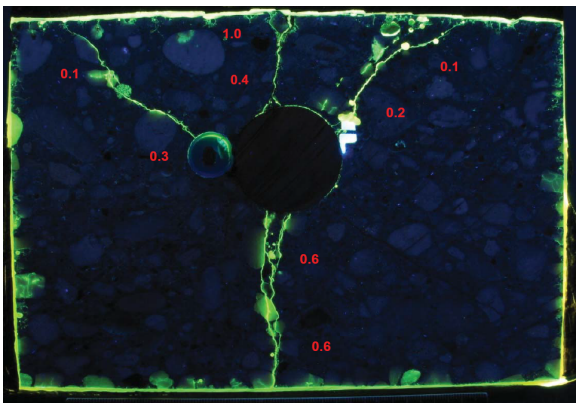

(d) 100 mm depth, UV light

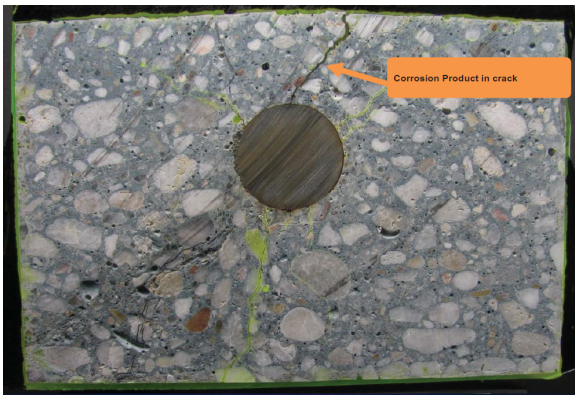

(e) 200 mm depth, normal light

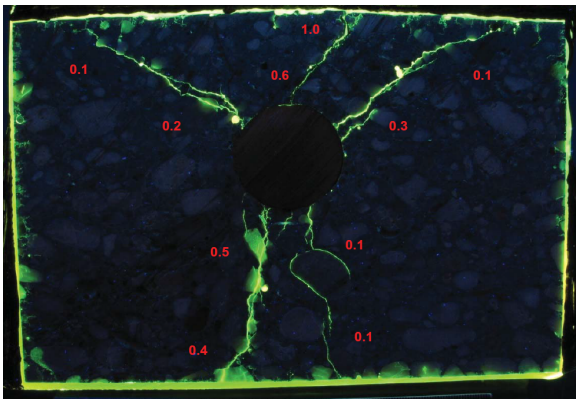

(f) 200 mm depth, UV light

Figure B.11: Crack Pattern of Material M3

The crack pattern of material M4 is shown in Figure B.12.

(a) 30 mm depth, normal light

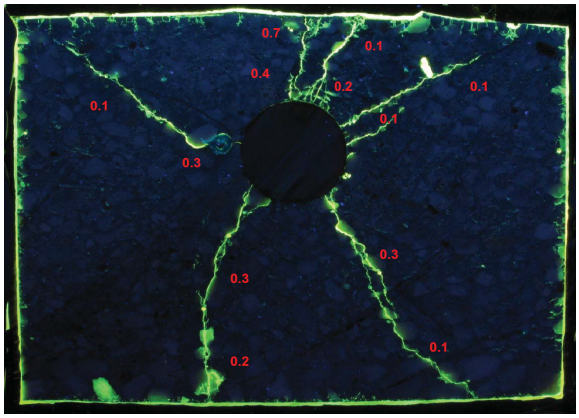

(b) 30 mm depth, UV light

(c) 100 mm depth, normal light

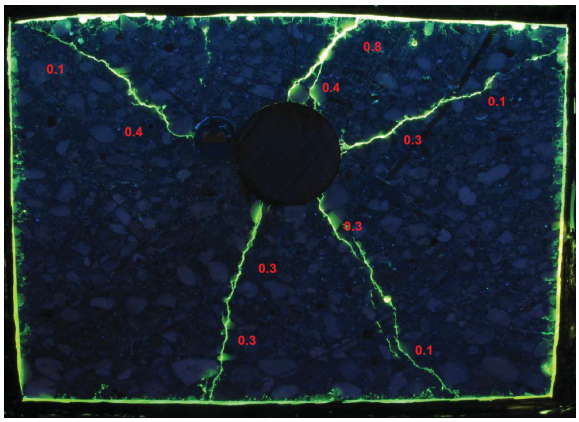

(d) 100 mm depth, UV light

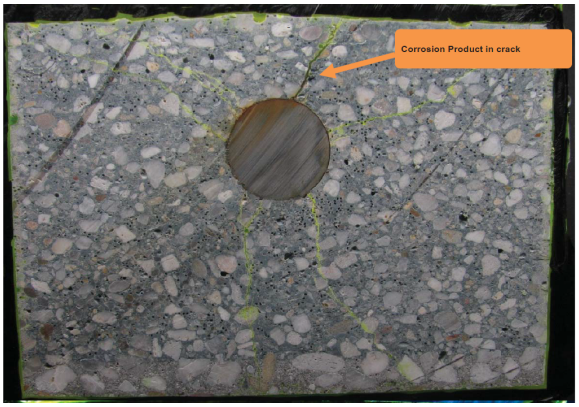

(e) 200 mm depth, normal light

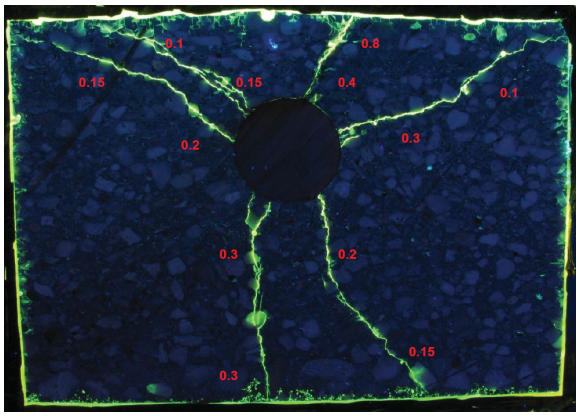

(f) 200 mm depth, UV light

Figure B.12: Crack Pattern of Material M4

The crack pattern of material M5 is shown in Figure B.13.

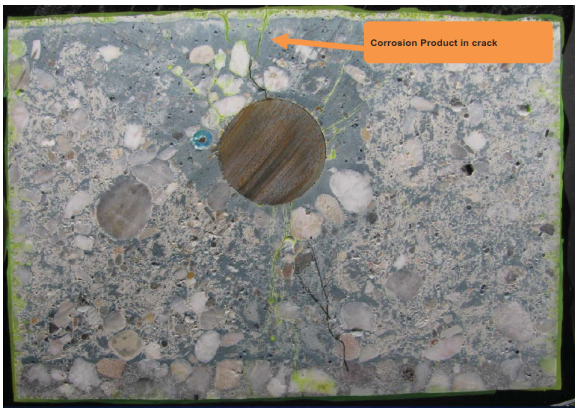

(a) 30 mm depth, normal light

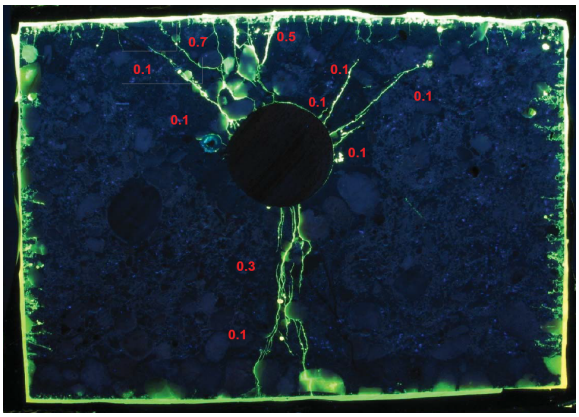

(b) 30 mm depth, UV light

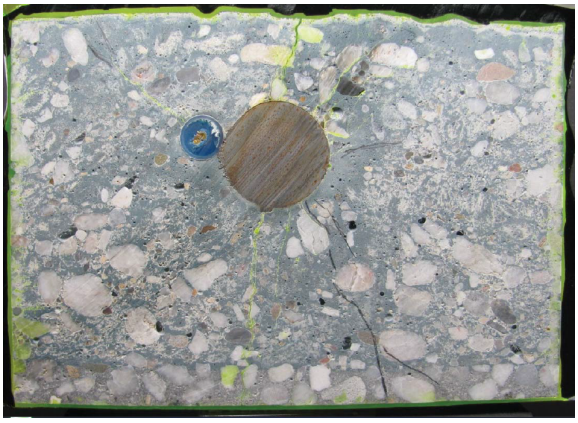

(c) 100 mm depth, normal light

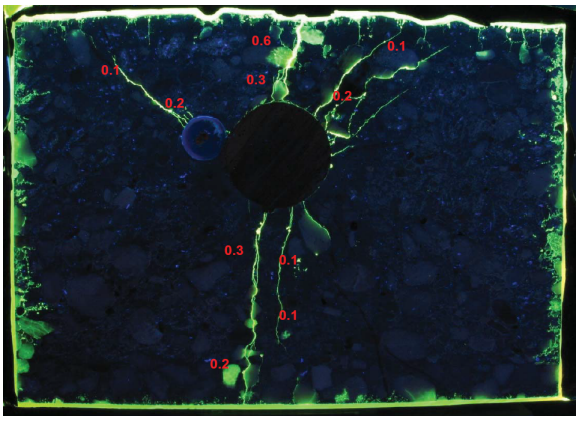

(d) 100 mm depth, UV light

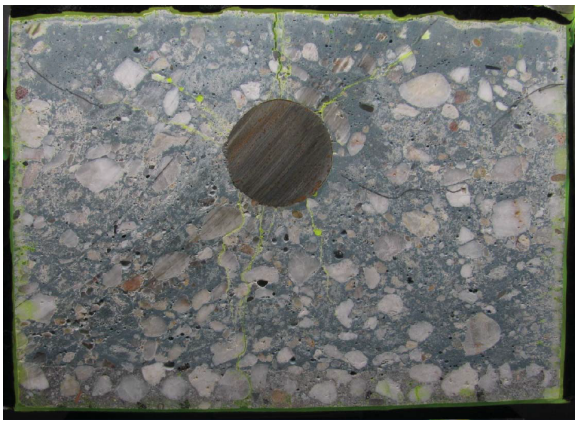

(e) 200 mm depth, normal light

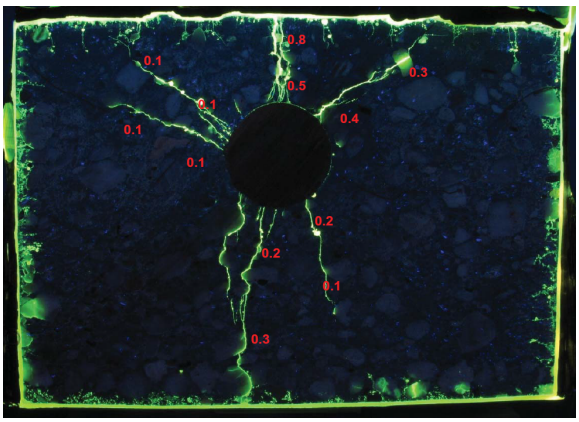

(f) 200 mm depth, UV light

Figure B.13: Crack Pattern of Material M5

C

INFLUENCE OF MESH SIZE IN THE LATTICE MODEL

In Section 4.1, it has been noticed that the model with $5mm$ mesh size shows more fracture energy than the model with $2mm$ mesh size in the direct tension test. The fracture energy is closely connected to the cracking behavior damage of a model. This means that mesh size can influence the cracking behavior of accelerated corrosion model. In this section, it is important to investigate for a proper mesh size that can describe the cracking behavior accurate enough.

C.1. MODEL WITH $2mm$ MESH SIZE

Due to the built-in randomness of lattice model, the detail crack pattern of models with different node distribution cannot be the same. However, if the mesh size is small enough, the general cracking behavior and rebar pressure should be similar. In this section, two other models with $2mm$ mesh size are built. All material properties, boundary conditions and loads are identical to the accelerated corrosion model in Section 4.1.2. Both of these two models are calibrated in element radius following the process mentioned in Section 4.1.1. The radius of lattice beams is respectively $1.007267mm$ and $1.006538mm$. Then the results of these three models are compared with each other.

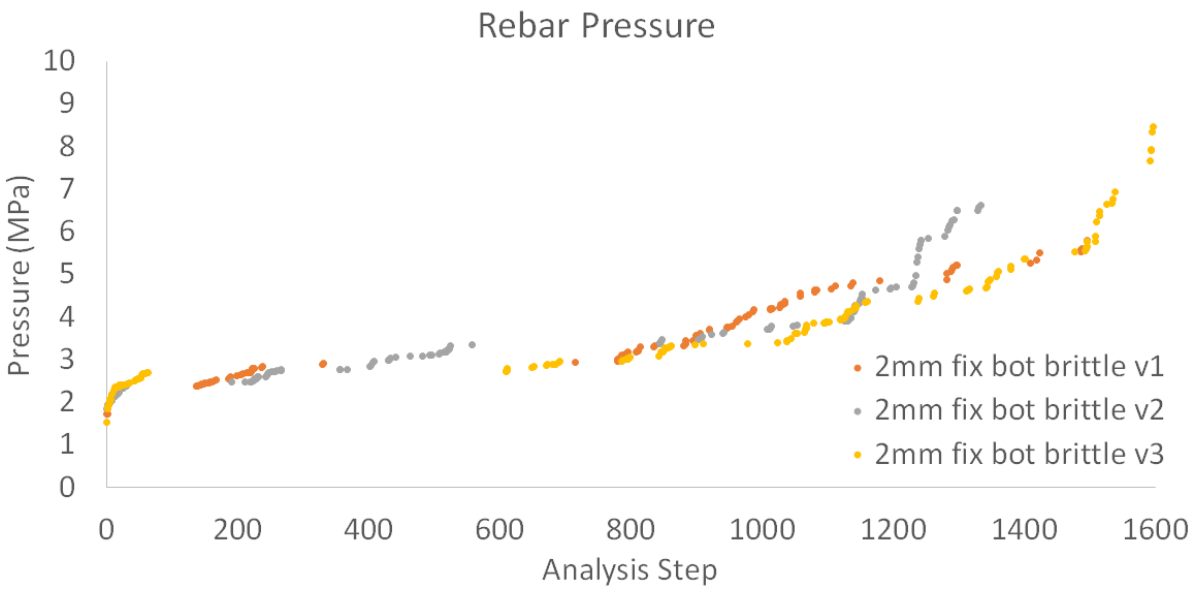

Figure C.1: Rebar Pressure Accelerated Corrosion Model 2 mm Mesh Size

Figure C.1 shows that the steel rod pressure in all three models are roughly at the same level and have the same trend in increasing. This implies that these $2mm$ models are damaged similarly and the $2mm$ mesh size is small enough to produce stable results. Moreover, two other steps: step 744 from model v2 and step 785 from model v3 are selected for investigation. The rebar pressure at these two steps is close to step 715 from the preliminary model.

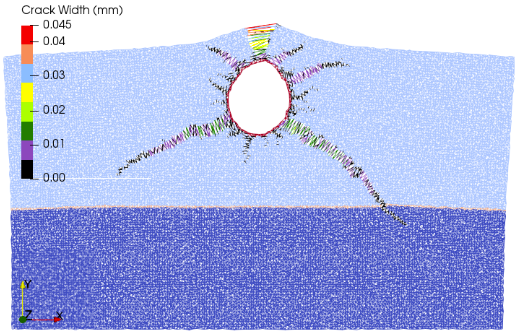

(a) Step 715, Model v1

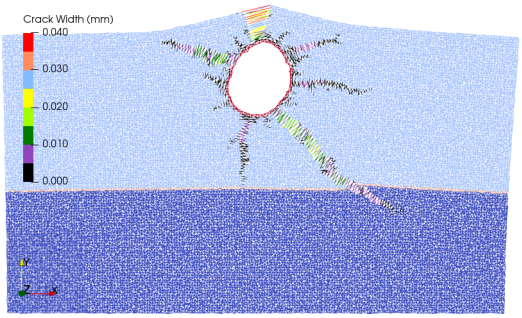

(b) Step 744, Model v2

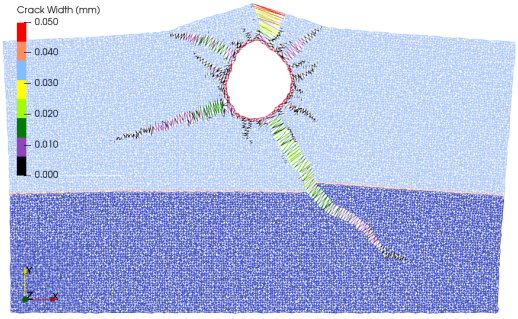

(c) Step 785, Model v3

Figure C.2: Crack Pattern of Models with $2mm$ Mesh Size

For all three models, there is one major crack at the top with a maximum crack width at the level of 0.04mm - 0.05mm. Also, there are secondary cracks along 11, 1 and 4 o'clock direction in all three models. Meanwhile, the secondary crack along 8 o'clock (6 o'clock in model v2) varies a bit in its developing direction. This can be explained by the difference in the distribution of lattice beams in these three models. As known from Section 3.2, this bottom crack is very sensitive in elongation. Therefore, the distribution of lattice beams can influence its direction. In general, the crack pattern of these three models at the same pressure level is similar.

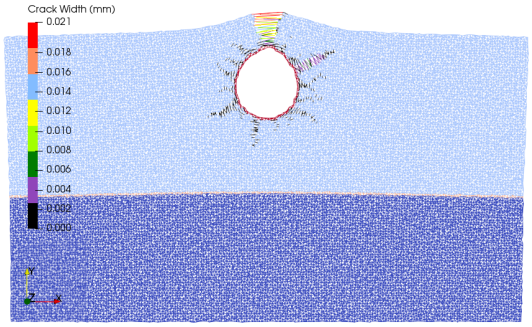

(a) Model v1

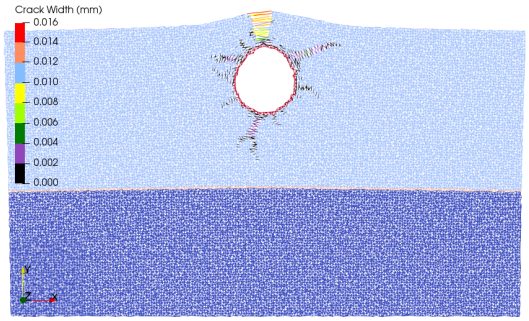

(b) Model v2

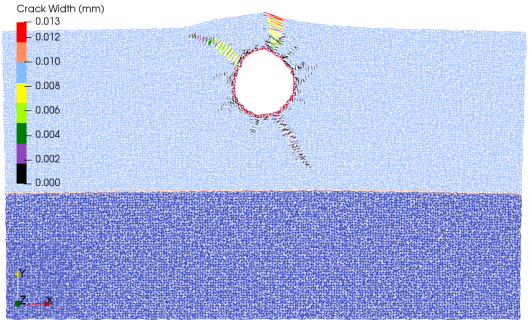

(c) Model v3

Figure C.3: Model with 2mm Mesh Size Crack Pattern, Step 300

Besides, the damage of these models at step 300 is also printed in Figure C.3. The maximum crack width of these models at step 300 has some difference. This is due to the difference in rebar pressure at this step. In general, the rebar pressure has a positive correlation with maximum crack width. Therefore, the rebar pressure has to be increased to have a crack width comparable to experiments. Meanwhile, the crack pattern of these models at starting stages is still similar. However, divergence can be observed in Figure C.1 after around step 750. This implies that the damage pattern grows differently after this step. This is due to

the development of the bottom crack. The bottom crack at this step in three models is getting close to the boundary. Therefore, the boundary condition starts showing a stronger influence on the damaging of the model. Due to the difference in the orientation of existing damage, the influence of the boundary results in different damage pattern afterward. Thus, the cracking behavior of model with $2mm$ mesh size is quite stable before certain steps. This also implies that when using the lattice model, the authenticity of the simulated results has its limit step, which has to be scrutinized.

C.2. MODEL WITH $5mm$ MESH SIZE

In order to investigate the influence of mesh size, a group of four models with $5mm$ mesh size is set up. The modelling process follows the method mentioned in Section 4.1.2. Material properties, boundary conditions and loading conditions are identical to model with $2mm$ mesh size in Section C.1. The radius of lattice beams in the four models are calibrated first. They are $2.506224mm$, $2.502264mm$, $2.503375mm$ and $2.512957mm$ respectively. A schematic view of these models is shown in Figure C.4.

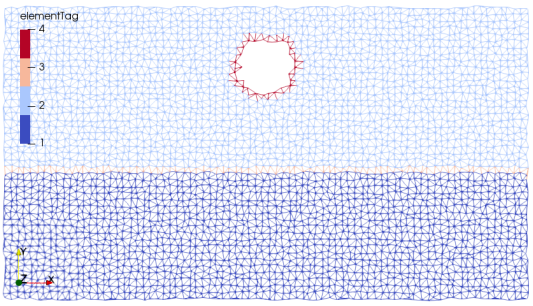

(a) Model v1

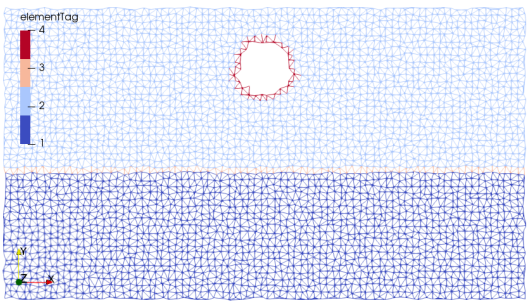

(b) Model v2

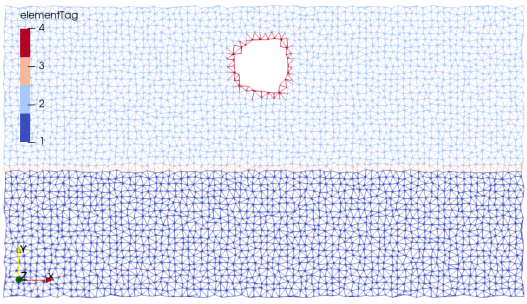

(c) Model v3

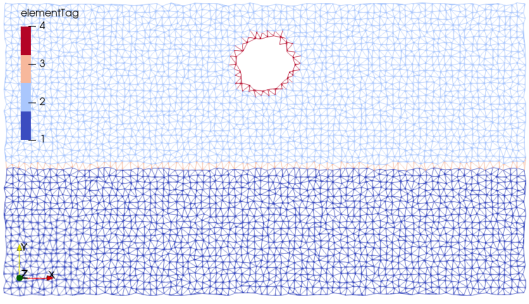

(d) Model v4

Figure C.4: Model with $2mm$ Mesh Size Crack Pattern, Step 300

Figure C.5 shows the rebar pressure with analysis steps of these four models. These models have a similar increase in rebar pressure at the beginning 300 steps. However, these models show huge variance in pressure afterward. This implies that the results from the model with 5mm mesh is very unstable after this step. The same behavior can also be observed in the previous group of 2 mm mesh size models.

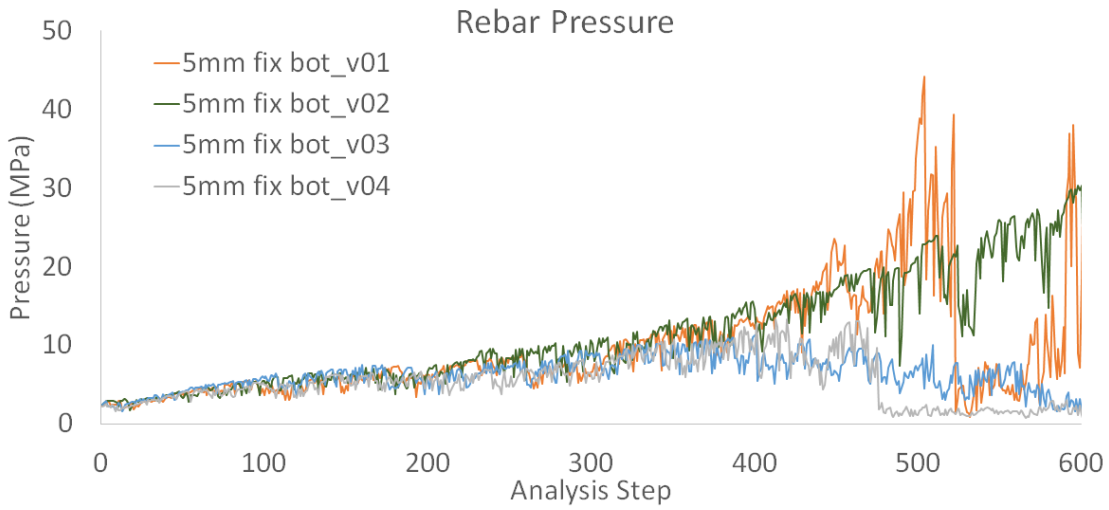

Figure C.5: Rebar Pressure Accelerated Corrosion Model 5 mm Mesh Size

Figure C.6 shows the damage pattern of each model at one step which is at the peak before a drop in pressure (similar pressure level): step 522 of model v1, step 524 of model v2, step 509 of model v3 and step 400 of model v4. These are the steps after the divergence in pressure happens. The four models at this pressure level are showing different damage mechanism. There is a huge tangential crack around the steel rod in model v1 and v3, in which the steel rod is pulled out from surrounding concrete. In model v2, the maximum crack width is located at the top crack. For model v4, the maximum crack width is not even at the top. It is located at one element at 3 o'clock direction without any localized crack. Theoretically, the maximum crack width should always happen at the top, because the concrete cover at the top is thinnest. Moreover, all the bottom cracks in four models get close to the edge of the model before showing divergence in behavior. Therefore, the damage pattern that these four models show after around step 350 is completely unreasonable, which verifies the assumption that the boundary condition has a strong influence on the damage of lattice model when a crack gets close.

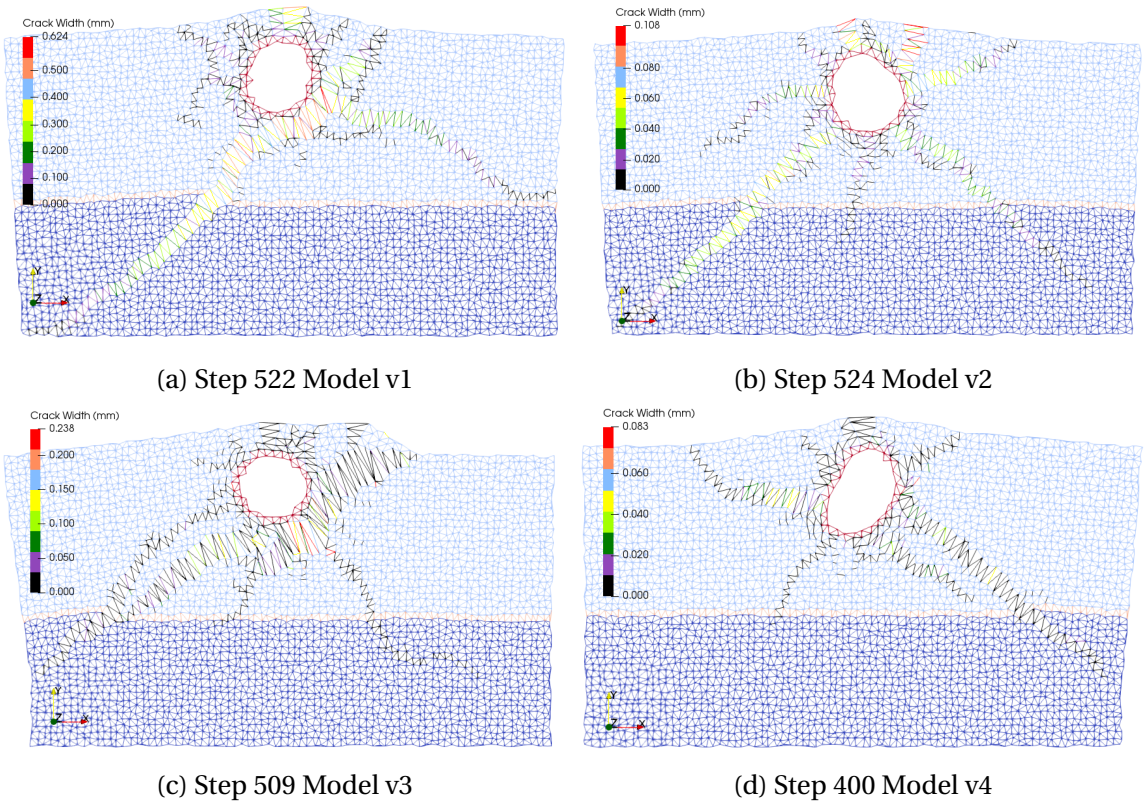

(a) Step 522 Model v1

(b) Step 524 Model v2

(c) Step 509 Model v3

(d) Step 400 Model v4

Figure C.6: Model with 5mm Mesh Size Crack Pattern

Another thing can be observed in Figure C.5 is that with 5 mm mesh size, the models can reach the pressure level of around 10 MPa before showing unstable results. This value of 2 mm mesh size model is only around 3 MPa. This is the influence brought by mesh size. Comparing the step 300 of 5 mm mesh model v1 and the step 715 of 2 mm mesh model, the maximum crack width of these two models has a difference of 7.55%. However, the pressure added has the difference of 50.47%. This indicates the considerable influence brought by mesh size. With increasing mesh size, fewer elements are generated. Thus, the influence of the built-in randomness is higher. Because less but longer elements need to be damaged to perform a crack. Then the orientation of the lattice beams is becoming more important to decide the tensile strength of an area, which results in the much higher pressure to produce crack with width at the same level.

However, it is also not a good idea to decrease the mesh size too small. One of the advantages in the lattice model over the continuum model is its built-in randomness. This "imperfection" of the model can help the lattice model to localize cracks and simulate the heterogeneity of concrete. That is one of the reasons why the lattice model has outstanding

performance in material research [40]. However, by decreasing mesh size, shorter lattice beams are performed in the model. This actually can be regarded as decreasing the built-in randomness in the lattice model. There is even a threshold that mesh smaller than this size will behave like models without randomness. Besides, from a structural point of view, a fine mesh is also limited by the computation power. Moreover, when up-scaling lattice model from micro to macro level, all composite in the concrete mix are regarded as together one integrated material. If a too fine mesh is applied, the up-scaling of the lattice model will be meaningless. Moreover, built-in randomness and mesh size are representing the heterogeneity of material in the lattice model. This should also depend on the composite and property of the material. Therefore, the mesh size cannot be defined without any limitation. However, this is not an important objective for this project. Therefore, a 2 mm mesh size is chosen for further models in order to balance the accuracy and the computing time.

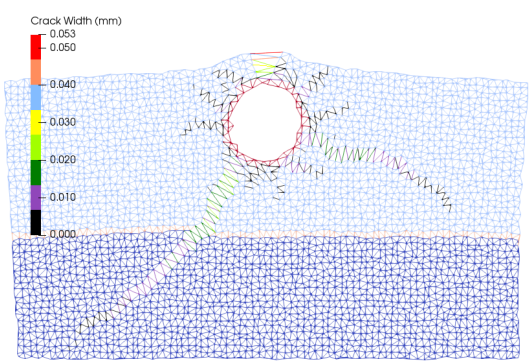

(a) Step 300, 5 mm Model v1

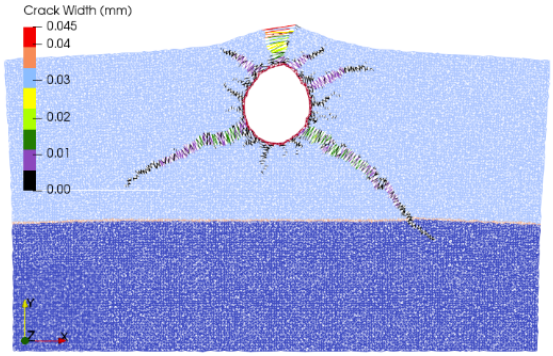

(b) Step 524, 2 mm Model v1

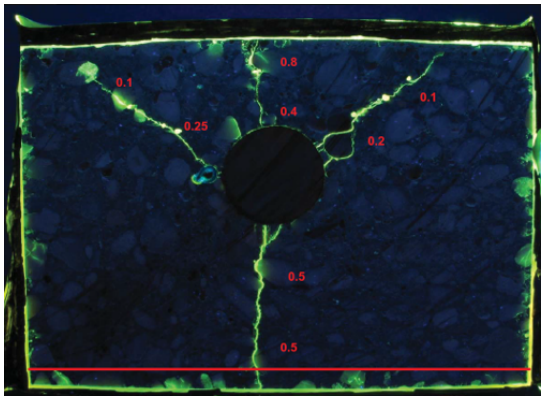

(c) Experimental Damage Pattern, Specimen ON06

Figure C.7: Crack Pattern of Models with Different Mesh Size and Experiment

Figure C.7c shows the damage of specimen with ON06 as repair mortar in the experiment. In experimental results of material ON06, the direction of bottom crack is along 6 o'clock direction. However, bottom crack is inclined towards the bottom corner in the lattice model. This shows clearly the influence of the bottom edge boundary condition. In the experiment, the bottom edge was kept free. However, with the constrained bottom in the lattice model, the stress is concentrated towards the bottom corner which results in the difference in bottom crack direction. The crack pattern obtained from the 2 mm and 5 mm model is similar to each other. This implies that the lattice model can produce the crack pattern that is independent of mesh size.